Final Report

Las Vegas Field Measurements of Volatile Chemical Product and Mobile Source Emissions: OZONE FORMATION AND ITS SENSITIVITY TO NOx AND VOCS

Point of Contact: Carsten Warneke
Contributors in-situ: Matthew Coggon, Chelsea Stockwell, Jeff Peischl, Jessica Gilman, Aaron Lamplugh, Lu Xu, Brian McDonald, Kristen Zuraski, Steven Brown
Contributors remote sensing: Sunil Baidar, Richard Marchbanks, W. Alan Brewer
Contributors modeling: Meng Li, Colin Harkins, Jian He, Bert Verreyken, Congmeng Lyu, Brian McDonald
Data manager: Ken Aikin
NOAA Chemical Sciences Laboratory (NOAA CSL), Boulder, CO
CIRES, University of Colorado Boulder

Table of Content

List of Figures & Tables

Figure 5-13. (Top) Map of Las Vegas area with the NOAA CSL mobile laboratory drive track colored by measured methane (CH_4), ethane (C_2H_6), and the methane/ethane ratio (bottom) Correlation of ethane with methane color coded by the methane/ethane ratio.

Pasadena, CA (bottom). Pasadena has nearly 10 times higher isoprene than mixing ratios observed at Jerome Mack.
Figure 10-2. Diurnal profile of isoprene and methyl vinyl ketone+methacrolein at the ground site in Jerome Mack (top) compared to the ground site in Pasadena, CA (bottom).
Figure 10-3. Drive tracks of the mobile laboratory color coded by isoprene in Las Vegas and the Los Angeles Basin.
Figure 10-4. Time series (top) and composition (bottom) of the monoterpenes at the ground site in Jerome Mack and during the drives.
Figure 10-5. Comparison of the monoterpene composition in downtown Las Vegas and at the Jerome Mack site.
Figure 10-6. Diurnal profiles of various monoterpenes measured at the Jerome Mack ground site.
Figure 10-7. Map of the canisters sampled during the mobile laboratory drives sized by the sum of the monoterpenes and color coded by the fractional contribution of d-limonene.
Figure 10-8. Map of the canister sampled during the mobile laboratory drives sized by the sum of the monoterpenes and color coded by the fractional contribution of d-limonene.
Figure 10-9. (top) The contribution of biogenics to ozone formation estimated from the box model. (bottom) The base case simulation of ozone production at Jerome Mack (blue trace) overlaid with ozone production when biogenic VOCs are excluded (green trace). The uncertainty bands reflect 20% changes to the modeled dilution rates.

Figure 11-1. Map of WRF-Chem model domains, including of the contiguous US (D1: 12 km x 12 km) that feeds an inner domain (D2: 4 km x 4 km) of the Western US.
Figure 11-2. Map of anthropogenic NO_x and VOC emissions used in WRF-Chem for the contiguous US (D1) domain (12 km x 12 km). Emissions are specific to July 2021.
Figure 11-3. Map of anthropogenic NO_x and VOC emissions used in WRF-Chem for the California/Nevada (D2) domain (4 km x 4 km). Emissions are specific to July 2021.
Figure 11-4. Trend of VCP emissions tracers in Boulder, CO due to COVID-19 pandemic. Bottom right panel shows trend in monthly sales of coatings and personal care products according to US Census Bureau data.
Figure 11-5. VOC/CO correlation of PTR-ToF-MS measurements at Jerome Mack (Las Vegas) and CalTech (Los Angeles) for a mobile source, VCP and cooking tracer.
Figure 11-6. VOC/CO correlation of measurements at Jerome Mack (Las Vegas) and CalTech (Los Angeles) for ~40 VOC species in mobile source and VCP emissions.
Figure 11-7. Map of biogenic isoprene and monoterpene emissions simulated in WRF-Chem for the California/Nevada (D2) domain (4 km x 4 km). Emissions are specific to July 2021.
Figure 11-8. Map of RAVE wildfire emissions input into WRF-Chem for the contiguous US (D1) domain (12 km x 12 km) for (top left) NO, (top right) CO, (bottom left) VOC, and (bottom right) $PM_{2.5}$. Emissions are specific to July 2021.
Figure 11-9. Evaluation of WRF with PBL height retrieved from Doppler Lidar located at North Las Vegas airport (July 1 to August 4, 2021). Model predicted boundary layer height is shown in red and observations in black. Distribution of absolute bias is shown to the right.
Figure 11-10. Evaluation of WRF wind profiles with the Doppler Lidar located at North Las Vegas airport.
Figure 11-11. Evaluation of WRF surface temperature at 2 m (pink line) with Airnow (black line) over Clark County. Solid black box shows period simulated for ozone sensitivity

simulations (7/5 to 7/12) capturing a heatwave event. Dashed black box outlines the highest MDA8 ozone days during this period.

Figure 11-12. Evaluation of WRF-Chem (red lines) versus NOAA measurements (black lines) for CO, NO_y, VOCs and O_3 at the Jerome Mack ground site. Error bars reflect one standard deviation.

Figure 11-13. Evaluation of WRF-Chem (red lines) versus NOAA measurements (black lines) for CO, NO_y, VOCs and O_3 at the CalTech ground site. Error bars reflect one standard deviation.

Figure 11-14. Evaluation of WRF-Chem hourly surface ozone (pink line) with Airnow (black line) over (top) California/Nevada domain and (bottom) Clark County. Solid black box shows period simulated for ozone sensitivity simulations (7/5 to 7/12) capturing a heatwave event. Dashed black box outlines the highest MDA8 ozone days during this period.

Figure 11-15. Evaluation of WRF-Chem MDA8 ozone (pink line) with Airnow (black line) over (top) California/Nevada domain and (bottom) Clark County. Solid black box shows period simulated for ozone sensitivity simulations (7/5 to 7/12) capturing a heatwave event. Dashed black box outlines the highest MDA8 ozone days during this period.

Figure 11-16. Evaluation of WRF-Chem ozone (red line) with ozonesonde profiles (black line) at Trinidad Head, CA (7/1, 7/9, 7/15, 7/22, and 7/30). Uncertainty bands reflect the 95% confidence interval of the mean.

Figure 11-17. Evaluation of WRF-Chem (top left) with satellite TROPOMI tropospheric NO_2 VCD with (top right) for July 2021. Linear regression of WRF-Chem model versus TROPOMI NO_2 for (bottom left) California-Nevada domain and (bottom right) Clark County box shown as a black outline.

Figure 11-18. Evaluation of WRF-Chem (red lines) versus NOAA measurements (black lines) at the Jerome Mack ground site for NO_x and NO_2. Error bars reflect one standard deviation.

Figure 11-19. Evaluation of WRF-Chem (blue markers) versus NOAA mobile lab observations (yellow markers) in the vicinity of Las Vegas. Markers are sized according to their concentrations.

Figure 11-20. Evaluation of WRF-Chem (blue markers) versus NOAA mobile lab observations (yellow markers) on the Las Vegas-Los Angeles transit drives. Markers are sized according to their concentrations.

Figure 11-21. WRF-Chem model sensitivity cases of anthropogenic and biogenic VOC emissions on MDA8 ozone. Maps show the average of MDA8 ozone for July 9 and 10, 2021. Max values are shown for Clark County and South Coast air basin. Differences are calculated relative to the base case simulation shown.

Figure 11-22. WRF-Chem model sensitivity cases of local Las Vegas and NO_x emissions on MDA8 ozone. Maps show the average of MDA8 ozone for July 9 and 10, 2021. Max values are shown for Clark County and South Coast air basin. Differences are calculated relative to the base case simulation shown.

Figure 11-23. WRF-Chem model sensitivity case of RAVE wildfire emissions on MDA8 ozone. (top) WRF-Chem model without wildfires, and (bottom) with wildfire emissions. Maps show MDAO3 averaged over the month of July, 2021.

Executive Summary

The main goal of this project was to determine the ozone formation and its sensitivity to volatile organic compounds (VOCs) and nitrogen oxides (NOx) in the Las Vegas region. The main components of this work are (1) detailed VOC, NOx, and related measurements at the Jerome Mack site and with a mobile laboratory, (2) determining biogenic and biomass burning influence, (3) VOC enhancement ratios and determining the weekday-weekend effect, (4) quantify cooking emissions, (5) VOC source apportionment of the measurements for anthropogenic compounds, (6) box modeling the ozone formation and its sensitivities based on the measurements, and (7) regional 3D air quality modeling with WRF-Chem.

For this project, a detailed set of trace gases was measured on the NOAA Mobile Laboratory (10 days of driving) and at the Jerome Mack site (4 weeks). Measurements of VOCs, CO, CO_2, CH_4, H_2O, NO, NO_2, NO_y, and ozone were performed in summer 2021. In addition, atmospheric profiles of wind speed and direction, vertical wind velocity variance, and aerosol backscatter were measured at the North Las Vegas airport to provide complementary dynamic data to improve model representations of urban meteorology.

Isoprene and methyl vinyl ketone+methacrolein (MVK+MACR), two oxidation products of isoprene, were observed at the Jerome Mack site at moderate mixing ratios and their relative abundances showed that isoprene was very locally emitted. The mobile laboratory showed some isoprene enhancements inside the urban core, but outside Las Vegas in the desert, isoprene was very low, less than 10 ppt. Speciated monoterpenes at Jerome Mack were dominated by a-pinene followed by b-pinene and d-limonene. The highest mixing ratios and the highest d-limonene fraction were generally observed around the Las Vegas Strip area, demonstrating the strong influence of anthropogenic monoterpene emissions from fragrance use on the Las Vegas Strip. Mixing ratios of all monoterpenes outside the city were low. The biomass burning tracers, acetonitrile and furfural, were low throughout the measurement period indicating minor influence from biomass burning on local VOC enhancements.

Cooking emissions of VOCs and aerosol are poorly understood. In previous work, cooking emissions were not distinguished from VCP emissions due to an incomplete understanding of the molecular markers that are characteristic of cooking emissions. Here, long-chain aldehydes were identified as cooking markers due to the high mixing ratios observed on the Las Vegas Strip. Generally, higher mixing ratios of the cooking tracer compounds were found in regions with higher restaurant density. This information was needed for the source apportionment to determine the contribution of cooking emissions to total anthropogenic VOCs observed in Las Vegas.

In this report enhancement ratios of VOCs emitted from anthropogenic sources versus an inert compound (e.g., CO) were determined for the Jerome Mack data and were used for comparing to inventory estimates, as inputs for positive matrix factorization (PMF), the box modeling, and the 3D chemical transport modeling (WRF-Chem). Due to changes in truck traffic and behavior, emissions and therefore photochemical processing are different on weekends compared to weekdays. A small weekend effect observed by changes in the enhancement ratio was found in Las Vegas, but due the large variability in the data and the low number of weekend observations no definite conclusions can be drawn.

In this report, source apportionment for the anthropogenic VOCs was done using Positive Matrix Factorization (PMF) analysis of PTR-ToF-MS data measured at Jerome Mack and the mobile laboratory around the Las Vegas Strip. PMF analysis determined the contribution of VOCs emitted from mobile sources, VCPs, and cooking and showed that VCPs account for the majority of the primary emissions (57%). Cooking emissions are an important contributor to the total VOC mass (16%), while mobile sources make up the remaining 27%. These results are consistent with the previous observations showing that VCPs are a dominant source of primary carbon in urban atmospheres, but quantified cooking for the first time.

We constructed a Eulerian box model to evaluate the chemical processes impacting air quality at the Las Vegas ground site, where model inputs were taken from all the measurements in this project. The model showed that daily O_3 enhancement, taken as the maximum O_3 produced midday is approximately 30 ppb. The O_3 sensitivities to VOCs and NO_x showed that reductions in both would reduce O_3 production. Reducing NO_x or VOCs by half would reduce O_3 by 10.5 ppb and 11.5 ppb, respectively. Reducing both NO_x and VOCs in half would decrease O_3 by 15 ppb. At the VOC and NO_x levels estimated on the Las Vegas Strip, O_3 remains sensitive to both NO_x and VOCs and falls into a similar chemical regime as predicted at the Jerome Mack ground site. The O_3 contribution from biogenic VOCs was ~3.5 ppb, which is about 10% of the total produced O_3.

WRF-Chem simulations for July 2021 were performed, where the most notable features are the use of the FIVE-VCP + NEI17 inventory and RACM-ESRL-VCP (updated oxy-VCP chemistry) chemical mechanism. The simulations showed that transported regional/background ozone remains a significant source of Las Vegas ozone during high heat events (~60 ppb MDA8 ozone). The model also showed that halving NO_x emissions can be effective at reducing MDA8 ozone by ~10 ppb, and WRF-Chem results are consistent with the box model. The effectiveness of controlling anthropogenic VOC emissions is mixed, and WRF-Chem results were inconsistent with the box model. WRF-Chem modeling also suggests that wildfires in the Western US are potentially a significant source of ozone pollution in Clark County that requires further research and attention.

1. ***Goals: Emissions, air quality, and climate in urban areas***

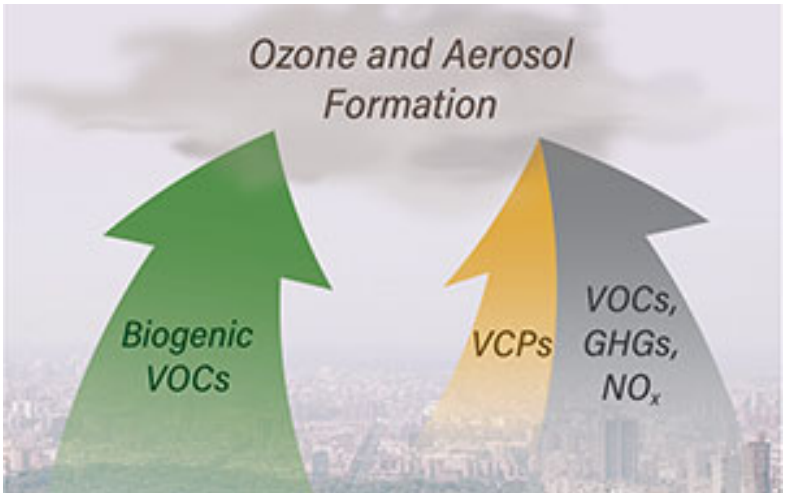

VOCs = volatile organic compounds
GHGs = greenhouse gases

Figure 1-1. Concept of the ozone formation and its sensitivity to NOx and VOCs study

This study determined **organic emissions and chemistry**, including of understudied volatile chemical products (VCPs).

1. How well do current emission inventories quantify the flux of anthropogenic VOC emissions in Clark County, including VCPs, mobile sources, cooking, and industrial facilities?

2. How does the relative distribution of VOC emissions vary by population density, influencing the ratio of VCPs to mobile source emissions?

3. What chemical tracers can be used to source apportion VOCs amongst VCPs, energy-related, cooking, and biogenic sources in Clark County?

4. What is the composition of gas- and aerosol phase organics in the urban atmosphere, including aromatics, alkanes, terpenes, cycloalkanes, oxygenated VOCs (including water-soluble organics such as alcohols, esters, glycols, and glycol ethers), and organic aerosol?

5. How well do current emission inventories quantify the flux of anthropogenic nitrogen oxides (NO_x = NO + NO_2) over Clark County, including from mobile sources, buildings, industrial facilities, and outlying agricultural regions and power generation?

2. ***Field-intensive July-September 2021***

2.1. Measurement overview

To understand ozone formation and the VOC/NO_x sensitivity in the Las Vegas area, trace gases were measured on the NOAA Mobile Laboratory and at the Jerome Mack site. Measurements of a comprehensive list of VOCs, CO, CO_2, CH_4, H_2O, NO, NO_2, NO_y, and ozone (O_3) were performed. Atmospheric profiles of wind speed and direction, vertical wind velocity variance, and aerosol backscatter were measured at the North Las Vegas airport to provide complementary dynamic data to improve model representations of urban meteorology. The dates for the respective measurements were:

- **Ground site at Jerome Mack**: 6/30/2021-7/25/2021
- **Lidar at North Las Vegas airport**: 2021/06/21-08/04
- **Mobile Laboratory Measurements:** 2021/06/27-29 (4 drives)
  2021/07/28-31 (4 drives)
  2021/09/07-08 (2 drives)

2.2. Instrumentation overview

The list of instruments and the key species observed during the Las Vegas field measurements are shown in Table 2-1. The Mobile Laboratory layout is shown in Figure 2-1. A comprehensive suite of VOCs was measured on the **NOAA CSL Mobile Laboratory** using a proton transfer reaction time of flight mass spectrometer (PTR-ToF-MS, Tofwerk Inc.) equipped with a custom gas chromatography (GC) front-end along with other trace gases (NO, NO_2, NO_y, O_3, CO, CO_2, and CH_4). In addition, whole air samples were collected on-demand and subsequently analyzed at NOAA CSL with a GC-MS instrument to resolve VOC isomers including monoterpene distributions, determine mixing ratios of alkane and alkene hydrocarbons, and verify compound-specific identities attributed to the masses measured by PTR-ToF-MS. The measured VOCs included tracers for various sources such as gasoline and diesel engines, volatile chemical products, biogenic emitters, and wildfires/domestic burning. Similar measurements with the same successful strategy have been conducted in New York City [*Coggon et al.*, 2021; *Gkatzelis et al.*, 2021a; *Gkatzelis et al.*, 2021b]. For the ground site measurements at Jerome Mack, the instruments were transferred from the Mobile Laboratory to the enclosure at the site.

The drives are used to determine the spatial distribution and characterize local sources, such as the Las Vegas Strip, cooking emissions downwind of restaurants, paving, painting, and industrial sources. The stationary in-situ measurements are used to determine diurnal profiles, VOC and NO_x emission ratios to CO, and photochemical impacts on observed trace gases. The stationary remote sensing measurements are used to determine the urban meteorological dynamics. The combination of the three strategies is needed to successfully

update emission inventories and initialize box and 3D modeling efforts for understanding air quality impacts in Clark County.

Table 2-1. The instrument package of the NOAA Mobile Laboratory, at Jerome Mack, and North Las Vegas Airport.

PI	Instrument/Package	Observed Species
Chelsea Stockwell Matt Coggon Lu Xu	Proton Transfer Reaction Time-of-Flight Mass Spectrometer (PTR-ToF-MS)	Fast in-situ VOCs (~100 species: incl. oxyVOCs, nitriles, alkenes, aromatics, etc)
Kristen Zuraski Steve Brown	NOx Cavity Ring Down (NOxCaRD)	NO, NO_2, NOy, O_3
Jeff Peischl	4-channel Picarro	CO, CO_2, CH_4, H_2O
Jessica Gilman Aaron Lamplugh	whole air canisters with offline analysis via GC-MS	Off-line VOCs (~30 species: incl. alkanes, nitriles, alkenes, aromatics, etc)
Lu Xu	GC front end add-on to PTR-ToF	Speciated VOC isomers
Clark County DES		CO, O_3, NO_x, NO_y, PM1, PM2.5 and 10, SO_2, auto-GC
Clark County DES		wind profile
Remote sensing instrumentation at the North Las Vegas Airport site		
Sunil Baidar Alan Brewer	Stationary [200S] Doppler lidar On a Trailer (StaDOT)	Horizontal Wind, Turbulence, and Aerosol Backscatter Intensity Profiles

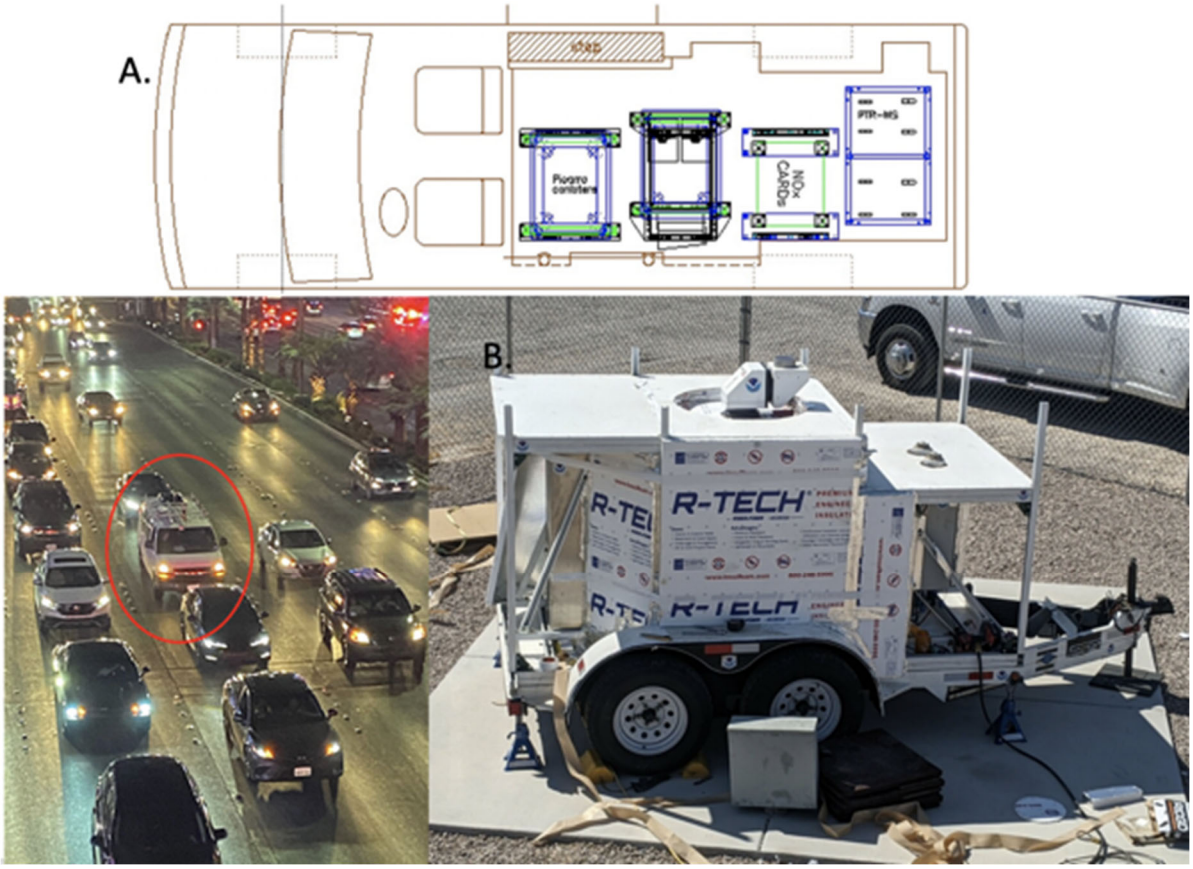

Figure 2-1. (A) The layout and aerial photo of the NOAA Mobile Laboratory on Las Vegas Boulevard. (B) A photo of the stationary [Leosphere 200S] Doppler lidar On a Trailer (StaDOT) at the North Las Vegas Airport site.

2.3. Calibration and final data for all NOAA instruments

PTR-ToF-MS

Mixing ratios of VOCs were determined using a proton-transfer-reaction time-of-flight mass spectrometer (PTR-ToF-MS) [*Yuan et al.*, 2017]. The PTR-ToF-MS measures a large range of aromatics, alkenes, nitrogen-containing species, and oxygenated VOCs. Instrument backgrounds were determined every 2 h for ground site experiments and every ~30 minutes during drives by passing air through a platinum catalyst heated to 350°C. Data were processed following the recommendations of Stark et al. [2015] using the Tofware package in Igor Pro (WaveMetrics). The PTR-ToF-MS was calibrated using gravimetrically-prepared gas standards for typical VOCs such as acetone, methyl ethyl ketone, toluene, and C8-aromatics. Many compounds not stable in gas standards were calibrated by liquid calibration methods as described by [*Coggon et al.*, 2018]. All other compounds that are not calibrated for are quantified using the method described by Sekimoto et al [2017], but have larger uncertainties.

The limits of detection and accuracy for each reported compound will be listed in the final data file provided to Clark County. The calibrations are summarized in Figure 2-2.

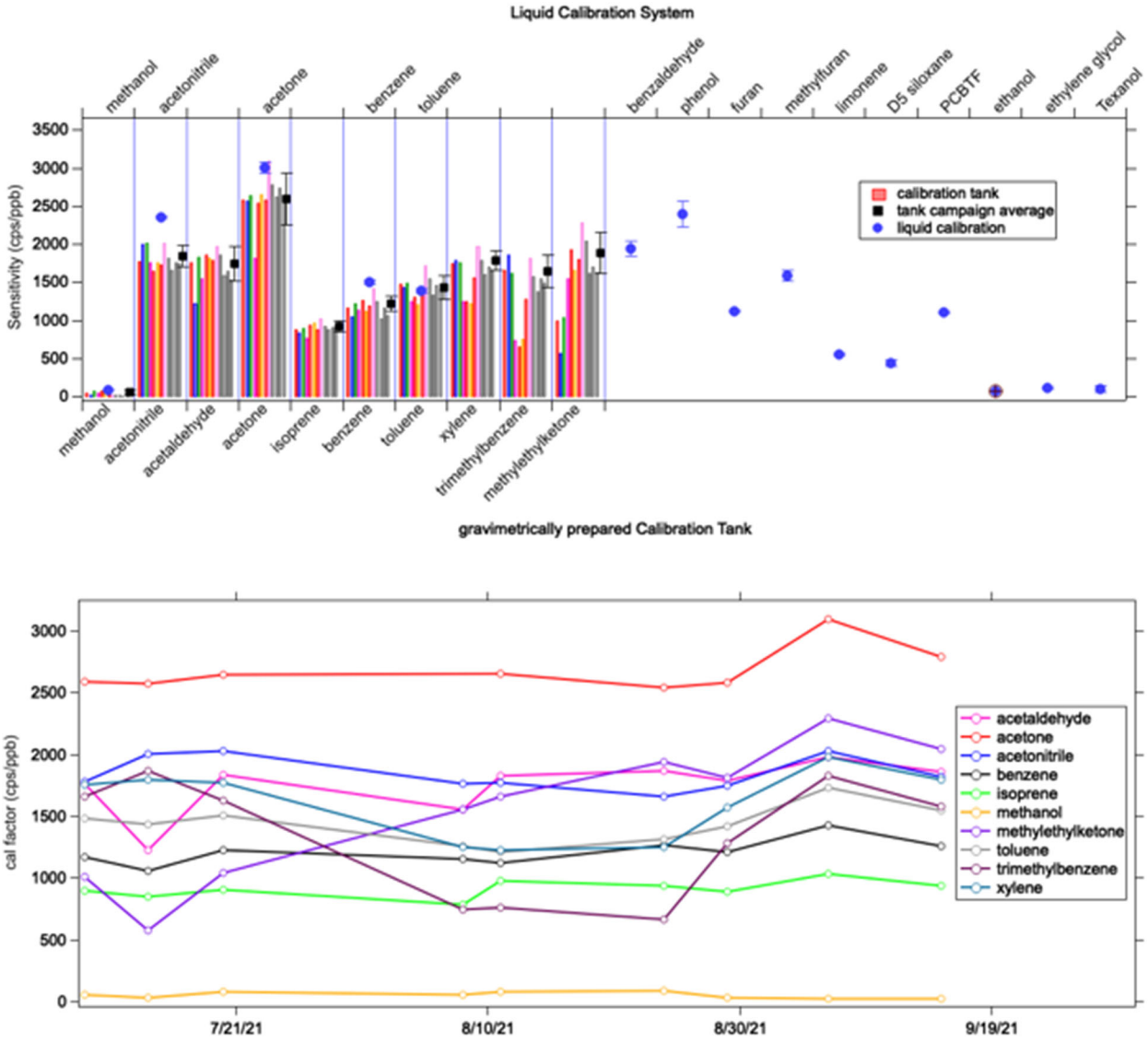

Figure 2-2. (top) The summary of the PTR-ToF-MS calibration using gravimetrically prepared calibration tanks and a liquid calibration system. (bottom) Time series of the calibrations performed throughout and post field measurements.

GC-PTR-ToF-MS

PTR-ToF only resolves VOC molecular formulae. Gas chromatography (GC) pre-separation has been used previously to identify structural isomers [*Yuan et al.*, 2017]. Here, a custom-built GC was used during the Jerome Mack measurements as a PTR-ToF front end to separate structural isomers [*Stockwell et al.*, 2021]. The GC consists of a DB-624 column (Agilent Technologies, 30 m, 0.25 mm ID, 1.4 µm film thickness) and oven combination

identical to the system described by Lerner et al. (2017), a liquid nitrogen cryotrap, and a 2 position 10-port valve (VICI) to direct gas flows. The column was selected to measure polar and nonpolar VOCs in the approximate range of C3-C10. The effluent of the GC column is injected into the PTR-ToF-MS inlet. Depending on the application, 1-5 minute samples can be collected and chromatogram lengths of 10-20 minutes can be chosen such that the total trapping and analysis time is between 15 and 30 minutes. LabVIEW (National Instruments) software controls the sequence of events, hot and cold trap temperatures, valve switching, sample flow and carrier gas flow. The detection limit for commonly detected VOCs (e.g., isoprene, benzene, xylenes) using this cryofocusing system is ~ 5 pptv.

WAS-GC-MS

The WAS-GC-MS provides chemically-detailed, isomer-specific identification of a wide-range of VOCs including alkanes, alkenes, and halocarbons that cannot be measured by PTR-ToF-MS, as well as molecules that are commonly measured by both techniques. WAS-GC-MS measurements are primarily used to resolve monoterpene and aromatic distributions, determine mixing ratios of alkane and alkene hydrocarbons, and verify compound-specific identities attributed to the masses measured by PTR-ToF-MS. The WAS sampling system consists of a stainless-steel bellows compressor, up to 24 canisters in series, a pneumatics system, and computer control. Each 2.7L electropolished stainless steel canister is initially cleaned, evacuated, and filled to 10 Torr of water vapor before shipping to the field. During sampling, each evacuated canister is opened electronically by pneumatically-actuated stainless-steel bellows valves on each canister. The compressor is upstream of the samplers and is used to pressurize each canister to approximately 45 psig. Each canister sample is analyzed off-line on a custom, two-channel GC-MS with a duty cycle of 20 minutes per sample [*Lerner et al.*, 2017].

For mobile lab sampling, canisters were filled “on-demand” using real-time information from the on-line gas-phase measurements in order to sample specific sources of interest or collect “clean” background air samples. A total of 152 samples were collected in the mobile lab with average fill times of 50 seconds. For the Jerome Mack site, a total of 297 WAS were collected approximately every 2 hours via automatic timer with an average fill time of 10 seconds. Calibrations of the GC-MS were conducted pre- and post-field measurements using several commercially-available and custom-made gravimetrically-prepared gas standards for typical VOCs such as C2-C10 hydrocarbons and simple oxygen- and nitrogen-containing VOCs and select halocarbons. The limits of detection and accuracy are compound dependent [*Lerner et al.*, 2017] and will be listed in the final data file provided to Clark County.

Picarro

CO, CO_2, CH_4, and H_2O were measured with a 4-channel Picarro cavity ring down spectrometry (CRDS) instrument. Precision at 5 seconds, 5 minutes, and 60 minutes is 15, 1.5, and 1 ppb for CO; 50, 20, and 10 ppb for CO_2; and 1, 0.5, and 0.3 ppb for CH_4. Maximum

drift at standard temperature and pressure (STP) over 24 hours was 10 ppb for CO; 100 ppb for CO_2; and 1 ppb for CH_4. The instrument was calibrated weekly in the field using tanks that were calibrated before and after the field project using standards obtained from NOAA's Global Monitoring Laboratory. These standards are tied to the WMO standard for greenhouse gases with known uncertainties. The field tanks were connected to the Picarro sample inlet and the calibration flow was sufficient to replace the entire sample flow of the instrument. The total uncertainty for the project is estimated to be ±(16 ppb + 2%) for CO, ±(0.2 ppm + 1%) for CO_2; and ±(2 ppb + 1%) for CH_4.

NOxCaRD

NO_x (=NO + NO_2) and ozone (O_3) were measured by a custom-built, four channel Cavity Ring Down Spectroscopy (CRDS) instrument that had a nominal sensitivity and precision of 20 ppt at one second. The CRDS instrument provides true NO_2 from direct absorption at 405 nm. It measures total NO_x through conversion of NO to NO_2 in excess O_3, and total reactive nitrogen (NO_y) through thermal conversion to NO and NO_2 in a quartz inlet heated to 650 °C. It measures O_3 through conversion to NO_2 in excess NO. Calibrations are done in the laboratory via standard additions of O_3 that are subsequently converted to NO_2 using the same conversion in excess NO used to measure O_3 in ambient air. In-field calibrations are done via standard additions from an NO_2 cylinder, which is compared to the laboratory calibration standard. Measurements are also compared to other NO_x and O_3 instruments, including the monitoring grade chemiluminescence NO_x instruments available at the Jerome Mack field station, a custom NO laser induced fluorescence (LIF) instrument with a photolytic converter for NO_2, and O_3 monitors based on UV absorption. The accuracy of final data has 3-5% accuracy for NO, NO_2 and O_3, and 12% accuracy for NO_y. The NO_x data will be used to critically evaluate emission inventories and emission factors from different sources, such as vehicles. It will also be used to evaluate monitoring instruments and in modeling studies of the NO_x sensitivity of O_3 photochemistry.

StaDOT

The bottom panel of Figure 2-3 shows the Stationary Doppler lidar On a Trailer (StaDOT) system deployed at the North Las Vegas Airport site. It consisted of a scanning 200S Leosphere lidar mounted on a trailer which ran continuously from 2021/06/21 - 2021/08/04. The operational mode consisted of a repeating 15-minute scan sequence. During the first 5 minutes of each sequence, the system performed azimuthal scans (used to calculate horizontal wind profiles) and the last 10 minutes were used to stare vertically (in order to calculate profiles of vertical velocity variance and aerosol backscatter intensity). Figure 2-3 shows 15-minute wind, aerosol, and vertical velocity variance profiles for a twelve-hour period starting at 12:00 (UTC) on 2021/08/03. An estimate of the boundary layer height (BLH) is shown as a magenta line superimposed on the data in the right two plots [Bonin et al., 2018].

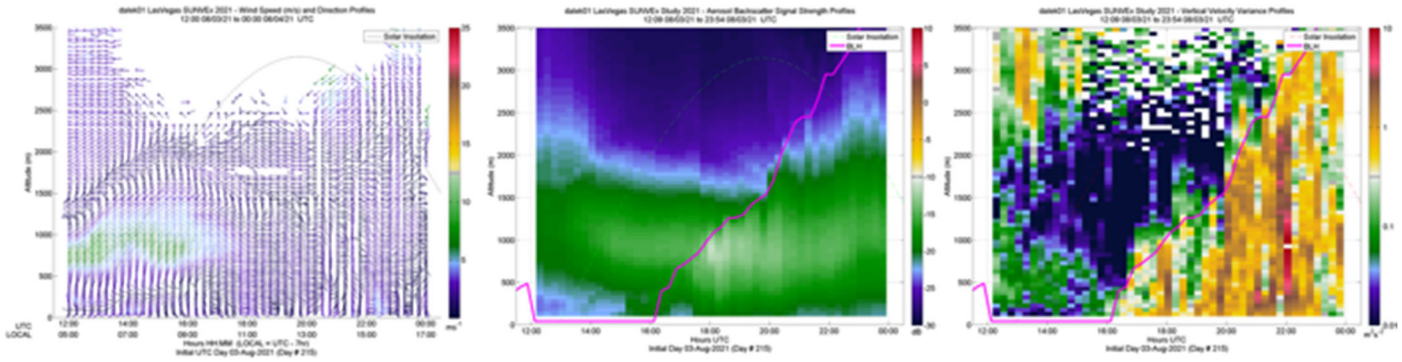

Figure 2-3. Data examples from the StaDOT Doppler lidar. The plots show continuous 15-minute profiles of the horizontal wind (left), aerosol backscatter intensity (middle), and vertical velocity variance (right). An estimate of the boundary layer height is shown as a magenta line superimposed on the right two plots.

3. Data availability

All the calibrations and Q&A for all instruments have been finalized and final data are posted on the password protected NOAA CSL website in ICARTT and Igor format. The final data are 1-minute for the Jerome Mack site and 1-second for the Mobile Laboratory drives. After the project is concluded, the password will be removed and the data will become public. The data can be provided to Clark County in a different format on request.

https://csl.noaa.gov/groups/csl7/measurements/2021sunvex/GroundLV/DataDownload/
https://csl.noaa.gov/groups/csl7/measurements/mobilelab/MobileLabSUNVEx/DataDownload/
https://csl.noaa.gov/groups/csl3/measurements/2021sunvex/dalek01/

Username: sunvex
Password: LV&LA21d@T@

4. Inter-comparison

4.1. NO_x and ozone

The final data from NOAA CSL averaged onto a 1-hour time base are inter-compared with the routine monitoring data from Jerome Mack for NO_y, NO, NO_2, CO, and O_3 in Figure 4-1. The time series comparison is shown on the left and the correlation plots together with the correlation coefficient (R^2) and fit parameters ($y = a + bx$) are shown on the right. The data gap in the middle of the project from 07/09/2021 to 07/13/2021 was caused by the overheating of the enclosure due to air-conditioning failure. The NO and NO_y measurements from the Jerome Mack site did not come online again until after the end of this project. All of the inter-comparisons have correlation coefficients of ≥ 0.90 and agree within 25%, but show discrepancies in the instrument backgrounds, which can be seen in the offsets.

The NO_y intercomparison only covers a rather short time period, but the correlation plot still has a statistically significant slope and intercept. The slope was 1.13 and the offset was over 3 ppb, which means that at low mixing ratios the NOAA NO_y instrument was about 3 ppb higher. This could indicate a low conversion efficiency of the NO_y converter used by the data monitoring instrument at the Jerome Mack site compared to the NOAA instrument. However, the negative concentration values reported by the Jerome Mack site instrument also implies a need to recalibrate the instrument to correct for the baseline offset.

The NO_2 intercomparison showed a high bias of the Jerome Mack data for the part of the inter-comparison before the re-start and was in excellent agreement after the restart.

The NO instruments also only were compared for a short time, during which the Jerome Mack instrument had a low bias of about 1.6 ppb and a slope of 1.24, but with and excellent correlation coefficient of 0.98.

This was also the case for the ozone mixing ratio comparison, where the agreement between the two instruments was much better after the restart and had a low bias in the first part of the experiment. The ozone measurements were also in better agreement at lower concentrations than at higher concentrations, where differences of >20 ppb were observed during mid-day/high-ozone concentration times with the Jerome Mack data consistently reporting lower values.

Overall, the inter-comparisons showed good agreement with good slopes and correlation coefficients ($R^2 \geq 0.90$, slope difference < 25%), but some Jerome Mack instruments, most notably the CO analyzer, seem to have drifting baselines and low bias, as discussed in the next section.

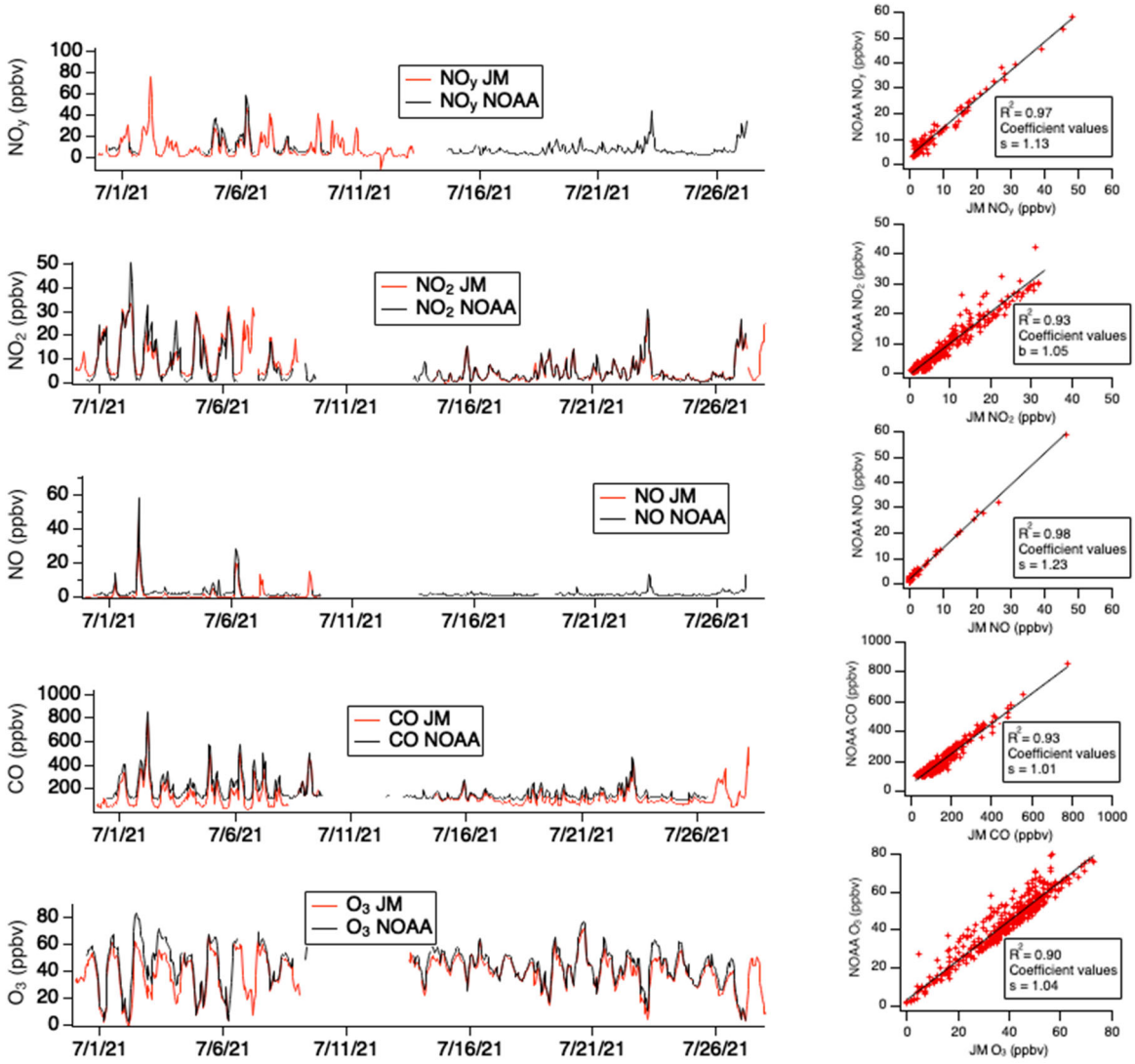

Figure 4-1. Inter-comparison of the Jerome Mack monitoring data with the NOAA CSL measurements.

4.2.Carbon Monoxide Comparison

The Jerome Mack instrument seemed to suffer from a low and varying baseline for the reported CO concentrations. In the clean daytime periods the reported values are as low as 25 ppb, which is clearly below the northern hemispheric summertime background values. After the restart, the two instruments had an excellent agreement, after which the baseline drifted lower again. This caused a relatively large offset of 47.5 ppb. Nevertheless, the slope was close to one at 1.01.

CO was measured with a Picarro model 2401 by NOAA CSL, which also measured carbon dioxide, methane, and water vapor. The instrument was deployed during the SUNVEx field

project, which consisted of the measurements in Las Vegas and in afterwards Pasadena, California. The instrument was calibrated before and after the campaign using standards tied to the United Nations World Meteorological Organization standard. During the Pasadena, California phase of the SUNVEx the Picarro compared well with a Los Gatos Research N_2O/CO analyzer (Figure 4-2). Over 35000 minutes of data were collected at the Pasadena ground site from a ~10 m tower and correlated with an R^2 of 0.999 and a slope of 1.0012 ± 0.0002. One-minute measurements of CO were greater than 100 ppb for the entire project, which is typical for an urban background even in summer.

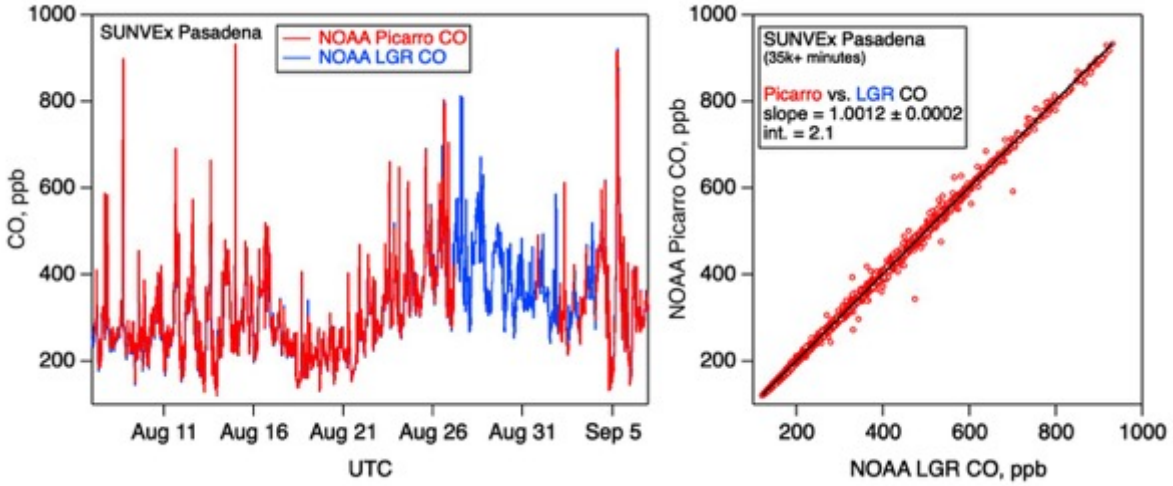

Figure 4-2. One-minute averaged CO data from the Pasadena, California ground site are plotted (left) as a time series for both the Los Gatos Research (LGR) and Picarro CO analyzers, and (right) as a correlation plot. The Picarro instrument was used in the mobile laboratory in late August, which is the reason for the data gap at the ground site.

The same NOAA Picarro instrument was used the previous month in Las Vegas, Nevada at the Jerome Mack ground site. The hourly-averaged CO measured by the Picarro were also always greater than 100 ppb for the entire project. The measurements did not compare as well with the Clark County CO monitor (Figure 4-3), which frequently measured below 100 ppb and for several days even below 60 ppb.

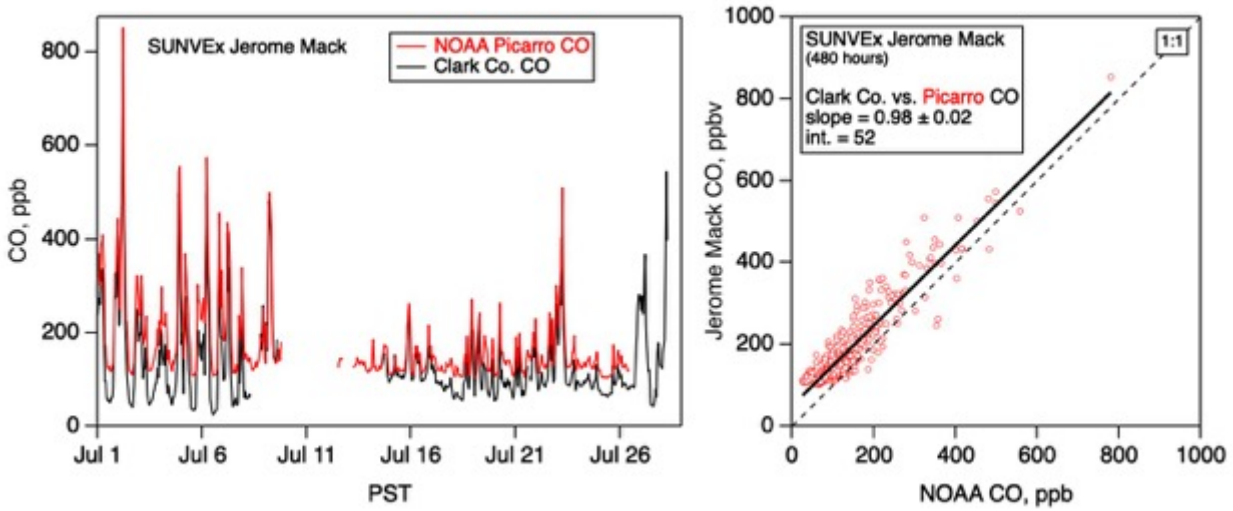

Figure 4-3. One-hour averaged CO data from the Jerome Mack ground site are plotted as (left) a time series and (right) a correlation plot.

In the following, we examine the differences in the measurements more closely. In July the Clark County measurements were approximately 70 ppb lower than the NOAA measurements (Figure 4-4). On July 8, the Clark County measurements agreed well with the NOAA measurements after a period of no reported data. Note that the NOAA measurements reported approximately the same urban background values as the previous days, i.e., greater than 100 ppb. On July 9 the measurements were shut down due to the air conditioners breaking at the Jerome Mack site. When the measurements were both back online, the Clark County measurements were again similar to the NOAA measurements, but drifted to lower mixing ratios over the next few days.

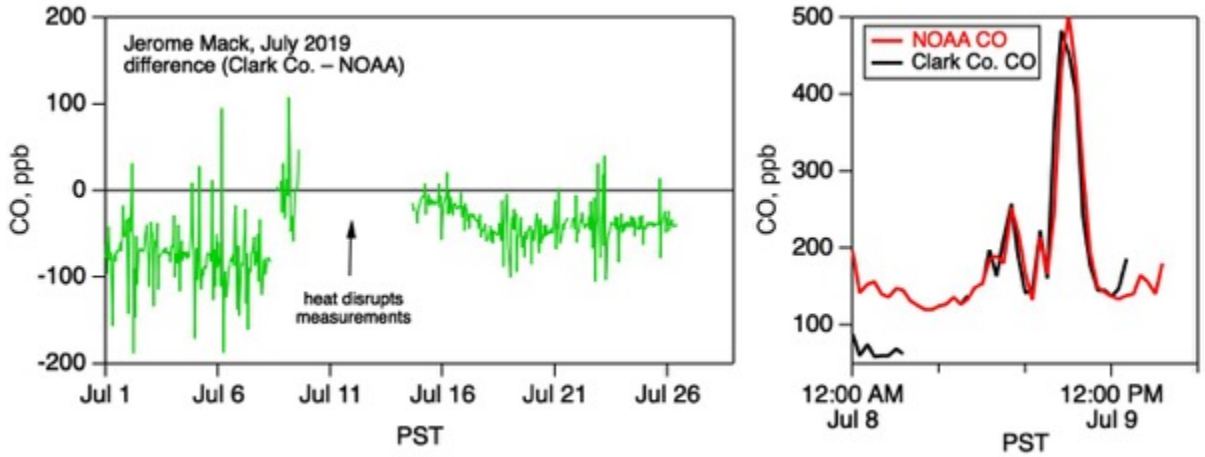

Figure 4-4. (Left) The differences in the one-hour averaged data from the Clark County and NOAA measurements are plotted as a time series. (Right) Measurements from Clark County were approximately 70 ppb lower than the NOAA measurements in the early morning hours

of July 8, went offline for a few hours, then came online later that day and compared well with the NOAA measurements.

We have no insight into why the Clark County measurements are drifting to lower mixing ratios than can be explained by northern hemispheric background air in summer. Typically, background CO reaches a minimum in summer due to its destruction by OH radicals, which are most concentrated during summer when water vapor, ozone, and incident solar radiation are highest. At the Mauna Loa Observatory far from CO sources, CO has not been measured below 60 ppb during the past three summers (Figure 4-5).

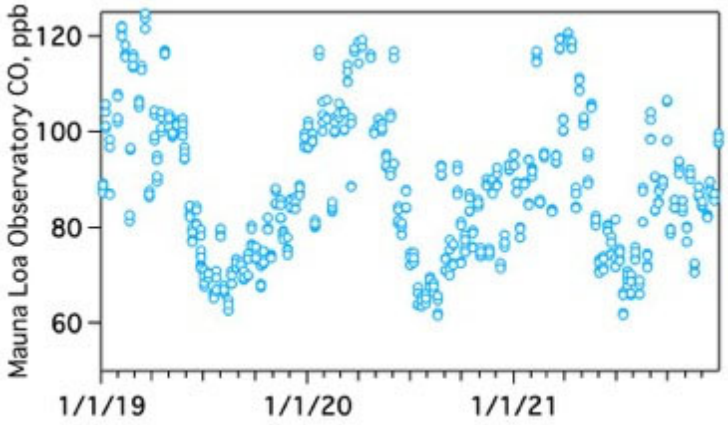

Figure 4-5. Measurements of CO from the Mauna Loa Observatory. Data provided by the NOAA Global Monitoring Laboratory.

The Clark County measurements were below 60 ppb for 10 days in July 2019. We consider it unlikely that an urban site in the U.S. would have lower CO than the clean background conditions of Mauna Loa. Furthermore, preliminary data from today, Sept. 13, 2022, show measurements below 10 ppb (Figure 4-6). Although these data have not been through the Quality Control phase of the data processing, it suggests there is some drift and/or offset affecting the Jerome Mack CO measurement. If the reason for the re-aligning of the CO measurements on July 8 was a calibration and/or zeroing on the Clark County monitor, we recommend calibrating every 4–5 days and diagnose whether this reduces instrument drift.

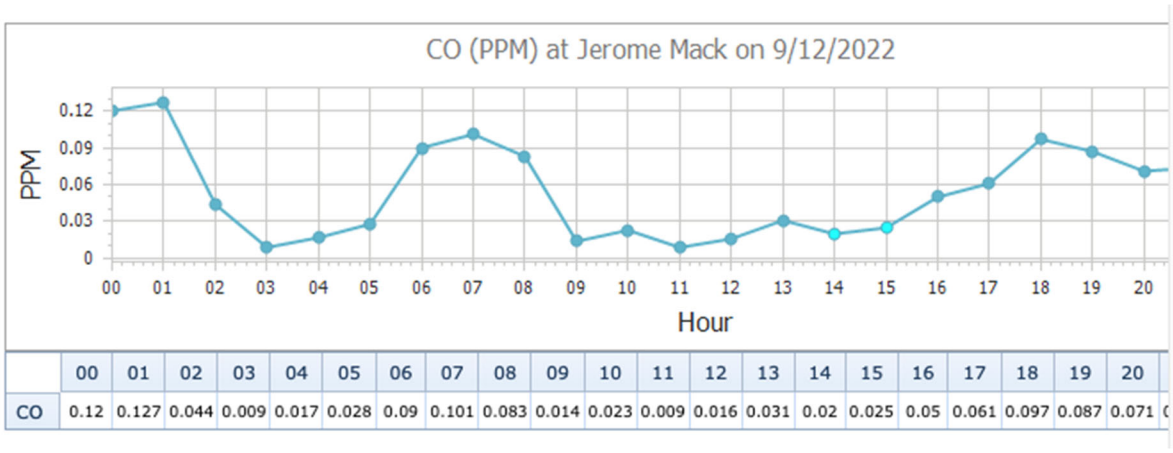

	00	01	02	03	04	05	06	07	08	09	10	11	12	13	14	15	16	17	18	19	20
CO	0.12	0.127	0.044	0.009	0.017	0.028	0.09	0.101	0.083	0.014	0.023	0.009	0.016	0.031	0.02	0.025	0.05	0.061	0.097	0.087	0.071

Figure 4-6. Live data before the Quality Control portion of data processing show CO below 10 ppb for the 3rd and 11th hours of the day on Sept. 12, 2022.

4.3. Accounting for measurement interferences on PTR-ToF-MS

Proton-transfer-reaction time-of-flight mass spectrometry (PTR-ToF-MS) is a technique used in atmospheric science to measure a wide spectrum of VOC functionality, including oxygenates, aromatics, furanoids, nitriles, and biogenic species such as isoprene and monoterpene isomers [*Yuan et al.*, 2017]. PTR-ToF-MS measurements in urban regions enable the determination of VOC mixing ratios resulting from a wide spectrum of emission sources, including fossil fuels, solvent evaporation from volatile chemical products (VCPs), residential wood burning, cooking, and urban foliage [*Coggon et al.*, 2021; *Coggon et al.*, 2018; *Coggon et al.*, 2016; *Gkatzelis et al.*, 2021a; *Gkatzelis et al.*, 2021b; *Karl et al.*, 2018; *Koss et al.*, 2018; *Stockwell et al.*, 2021]. The fast-time resolution and broad selectivity of PTR-ToF-MS measurements enables source apportionment, flux calculations, and spatial mapping on mobile platforms that yield important information about urban VOC source strengths.

In this chapter, we investigate interferences that impact fast time response PTR-ToF-MS isoprene measured in Las Vegas, NV.

VOC detection by PTR-ToF-MS relies on VOC reaction with protonated water (Reaction 1).

$$\mathrm{VOC} + \mathrm{H_3O^+} \rightarrow \mathrm{VOC \cdot H^+} + \mathrm{H_2O} \qquad \text{(Reaction 1)}$$

Proton-transfer is exothermic and spontaneous for VOCs with a proton affinity that is higher than water. For many VOCs, including ketones, aromatics, and nitriles, the protonated product ($\mathrm{VOC \cdot H^+}$) is the primary signal detected by PTR-ToF-MS. For other VOCs, other

products from dehydration, fragmentation, and water clustering can complicate mass spectral interpretation. Pagonis et al. [2019] summarizes the key studies that have investigated VOC fragmentation. Fragmentation is most prevalent in alcohols, aldehydes, and other species with long-chain alkane functionality. Small alcohols and aldehydes (C < 3) primarily react to form protonated products following Reaction 1. At higher carbon numbers, a large fraction of the reactions results in dehydration and subsequent fragmentation (Reactions 2-3).

$$(\mathrm{R-OH, RH=O}) \cdot \mathrm{H^+} \rightarrow \mathrm{R^+} + 2\,(\mathrm{H_2O}) \quad \text{(Reaction 2)}$$

$$\mathrm{R^+} \rightarrow \mathrm{R_1}^+ + \mathrm{R_2} \text{ (Reaction 3)}$$

Where R is the carbon backbone of an alcohol (R-OH) or aldehyde (RH=O), R+ is the dehydration product, R_1^+ is a fragment, and R_2 is a neutral product. Fragmentation may also result from protonation of cycloalkanes or alkyl aromatics. PTR-ToF-MS is not sensitive to small alkanes (C < 5). Larger cycloalkanes are detected at low sensitivity and subsequently fragment to produce ions that often overlap with the dehydration and fragmentation product of alcohols and aldehydes [Arnold et al., 1998; Gueneron et al., 2015; Jobson et al., 2005]. The degree of dehydration and fragmentation is partially dependent on the strength of the drift field (characterized by the E/N ratio), which impacts ion kinetic energy [*Arnold et al.*, 1998; *Krechmer et al.*, 2018; *Yuan et al.*, 2017]. Lower E/N results in lower fragmentation, but higher clustering with neutral water, which also complicates the mass spectra.

In the atmosphere, complex mixtures of emissions may result in PTR-ToF-MS mass spectra where dehydration and fragmentation products interfere with the quantification of important atmospheric VOCs. For example, PTR-ToF-MS measurements in regions with significant oil and natural gas development show that substituted cycloalkanes fragment to produce significant signal at m/z 69 [*Koss et al.*, 2017; *Warneke et al.*, 2014]. These fragments overlap with the ions typically associated with protonated isoprene and prevent accurate measurement of isoprene in these regions.

Assessments of interferences on PTR-MS-ToF measurements in urban atmospheres have been conducted previously [e.g., Warneke et al., 2003]. The sources that contribute to urban VOCs change on decadal timescales as fossil fuel emissions steadily decline [*Kim et al.*, 2022; *Warneke et al.*, 2012]. Consequently, PTR-ToF-MS spectra once dominated by motor vehicle emissions now include a higher proportion of oxygenates, solvents, and other VOCs from sources such as VCPs and cooking [*Coggon et al.*, 2018; *Gkatzelis et al.*, 2021b; *Karl et al.*, 2018; *Stockwell et al.*, 2021]. Furthermore, significant advances in PTR-ToF-MS detectors (quadrupole vs time-of-flight mass spectrometers) and drift tube designs (e.g. Vocus and PTR3) have enhanced instrument capabilities to acquire mass spectra with greater resolution and sensitivity [*Breitenlechner et al.*, 2017; *Krechmer et al.*, 2018; *Yuan et al.*, 2016]. These technological advances enable better identification and quantification of the interferences that impact PTR-ToF-MS spectra.

Biogenic VOCs are commonly reported by PTR-ToF-MS, including isoprene and the sum of monoterpene isomers. In urban environments, monoterpenes consist of naturally emitted species, such as alpha- and beta-pinene, along with isomers predominantly emitted from anthropogenic sources, such as limonene resulting from fragranced consumer products and degreasing agents [*Coggon et al.*, 2021; *Gkatzelis et al.*, 2021a; *Hurley et al.*, 2021]. In very densely populated regions, anthropogenic monoterpenes can outweigh emissions from natural sources [*Coggon et al.*, 2021]. Isoprene is the dominant biogenic VOC emitted by urban foliage and is a major contributor to urban OH reactivity and ozone production [*Calfapietra et al.*, 2013].

Figure 4-7 shows GC-PTR-ToF-MS chromatograms of the masses typically assigned to monoterpene isomers (m/z 137, $C_{10}H_{16}H^+$) and isoprene (m/z 69, $C_5H_8H^+$). As expected, monoterpenes are the sole contributors to the signal measured at m/z 137 (Figure 4-7). Limonene is the dominant isomer measured on the Las Vegas Strip, which is consistent with previous observations in densely populated regions [*Coggon et al.*, 2021]. In New York City, limonene mixing ratio correlates with population density and is predominantly associated with the use of fragranced VCPs [*Coggon et al.*, 2021; *Gkatzelis et al.*, 2021a]. Fragranced VCPs are the likely source of limonene shown in Figure 6-7.

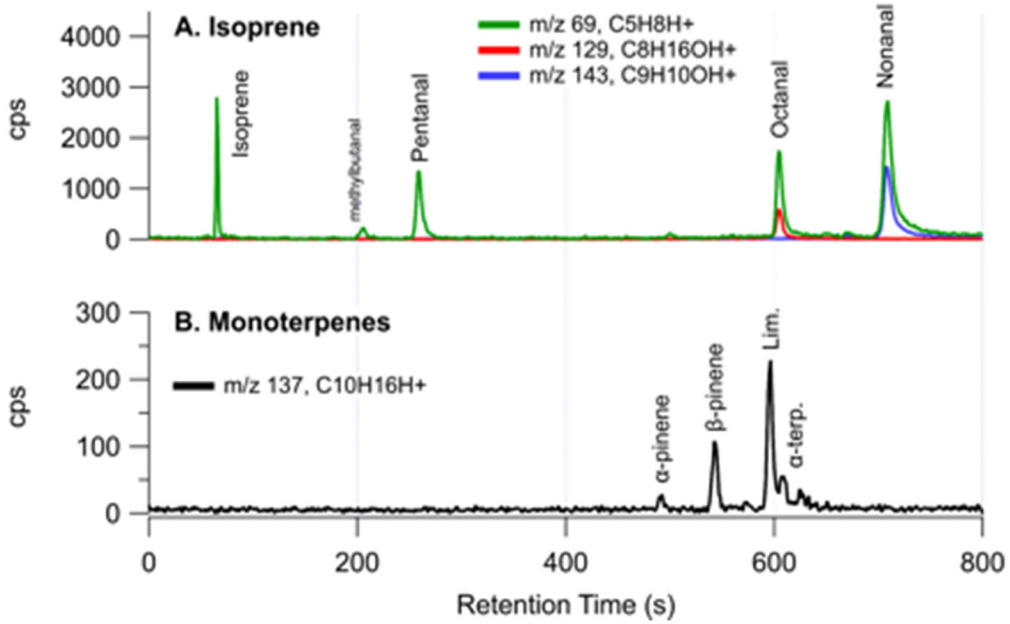

Figure 4-7. GC-PTR-ToF-MS chromatogram from the Las Vegas Strip showing the contributions of isomers and fragments to ions typically assigned to biogenic VOCs. The labels highlight the traditionally assigned isomers for (A) isoprene and (B) the sum of monoterpenes including alpha-pinene, beta-pinene, limonene, and alpha-terpinene.

Figure 4-7 shows that isoprene is only a small contributor to the signal at m/z 69 on the Las Vegas Strip. GC-PTR-ToF-MS measurements suggest that significant interferences result from the dehydration and fragmentation of saturated aldehydes, including methylbutanal,

pentanal, octanal, and nonanal (Figure 4-7 A). For reference, we show the chromatograms of the parent ions attributed to octanal and nonanal. The assignment of the parent ions to aldehydes, and not ketone isomers, is confirmed by comparing ambient observations with GC-PTR-ToF-MS measurements of aldehyde and ketone standards. These measurements show that the ambient observations are best explained by the retention times and fragmentation patterns of aldehydes. The source of these aldehydes is likely a result from meat char boiling and the use of cooking oils [*Arata et al.*, 2021; *Karl et al.*, 2018; *Klein et al.*, 2016; *Schauer et al.*, 1999a]. Their significant presence around the Las Vegas Strip is reflected by the high density of restaurants along Las Vegas Boulevard.

The isoprene interference results from the production of the $C_5H_9^+$ ion, which is a common fragment for higher-carbon aldehydes (> C5), as well as alkenes and cycloalkanes [*Buhr et al.*, 2002; *Gueneron et al.*, 2015; *Pagonis et al.*, 2019]. Previous studies have characterized isoprene interferences from alkenes and cycloalkanes, which are emitted from fossil fuel use along with oil and natural gas production [*Gueneron et al.*, 2015; *Warneke et al.*, 2014]. For example, *Gueneron et al.* [2015] showed that substituted cyclohexanes and cyclohexenes produce fragmentation patterns that consist largely of m/z 111, m/z 125, m/z 69, m/z 83, m/z 57, and other lesser-abundant hydrocarbon fragments. In regions with significant oil and natural gas development, these compounds may produce interferences at m/z 69 which can mask the signal resulting from biogenic sources of isoprene.

Figure 4-8 supports this inference, and shows how the sum of m/z 111 and m/z 125 (termed the "isoprene interference") varies relative to the signal at m/z 69 measured at the ground sites in Los Angeles and Las Vegas. In both cities, the isoprene interference is highest at night and is well-correlated with m/z 69. In Los Angeles, high daytime emissions of isoprene drive much of the observed variability in the m/z 69 diurnal pattern between 6:00 - 19:00. In Las Vegas, isoprene emissions are much lower, and the diurnal pattern of m/z 69 primarily follows the trend exhibited by the isoprene interference. There is also clear daytime variability in m/z 69 in Las Vegas that suggests small influence from local biogenic sources. Figure 4-8 demonstrates the degree to which aldehyde and cycloalkane fragmentation influences the inferred temporal pattern of m/z 69 in regions with varying isoprene emissions.

We evaluate the isoprene interference in Las Vegas and Los Angeles and apply corrections to the signal at m/z 69 in order to derive improved estimates of isoprene mixing ratios. We apply these corrections based on the observed fragmentation patterns of aldehydes. Octanal and nonanal are detected as protonated ions, but a large fraction of the signal is also detected at dehydrated products, $C_8H_{15}^+$ (m/z 111) and C_9H_{17}+ (m/z 125). In contrast, pentanal and methylbutanal almost entirely dehydrate to $C_5H_9^+$, and therefore have no unique markers to quantify their interference. Given that these aldehydes likely result from a common source (e.g., cooking emissions), we assume that pentanal and methylbutanal correlate with octanal and nonanal, and that the overall impact of aldehydes on isoprene mixing ratios can be assessed using the signals associated with m/z 111 and m/z 125.

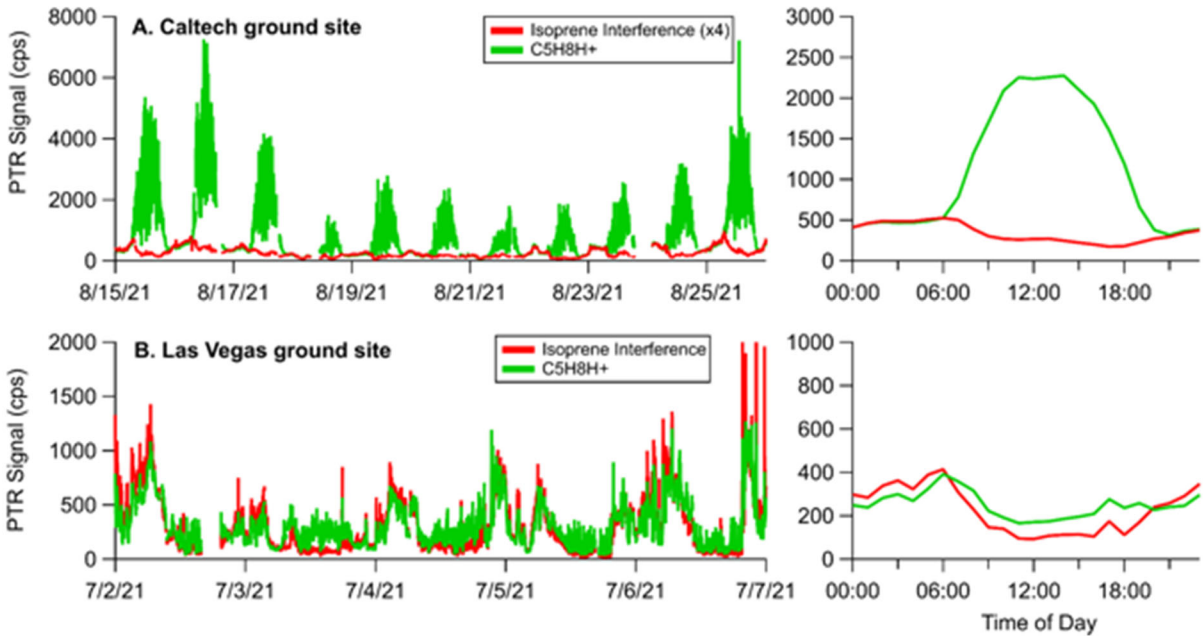

Figure 4-8: Time series and diurnal pattern of the signal at m/z 69 ($C_5H_8H^+$) and the isoprene interference (m/z 111 + m/z 125) measured at the (A) the Caltech ground site and (B) Las Vegas ground site. The time series data are shown for select periods to illustrate correlations between the isoprene interference and m/z 69. The diurnal patterns are averages over the entire campaign.

It is expected that isoprene emissions are lowest in the evening and at night [e.g., *Guenther et al.*, 2012]; therefore, we determine the contribution of the isoprene interference to m/z 69 based on nighttime data. We analyze data between 00:00 - 04:00 Local Time, and when daytime isoprene is lowest in order to minimize the influence of residual isoprene from previous days. We then determine the ratio of m/z 69 to the sum of m/z 111 + m/z 125, and apply this ratio (f69/(111+125)) to the full dataset to determine a corrected isoprene (Method 1).

$$\mathrm{Isoprene}_{\mathrm{Corrected}} = S_{C5H9+} - S_{111+125} \cdot f_{69/(111+125)} \quad \text{(Method 1)}$$

The nighttime ratio is calculated to be 6.9 in Las Vegas and 7.9 in Los Angeles. The differences between the cities may reflect variations in the distribution of aldehydes and cycloalkanes, or possibly a contribution from nighttime isoprene.

Figure 4-9 shows how isoprene changes as a result of this correction and compares the corrected isoprene mixing ratios to GC-MS samples co-located with the PTR-ToF-MS. In Los Angeles, the correction largely impacts isoprene mixing ratios at night. The diurnal pattern shows that average mixing ratios approach zero in the evenings, though increases in nighttime isoprene mixing ratios are observed during some periods (e.g., August 22 - 24). Corrections to m/z 69 during the daytime lead to a ~10% decrease in reported isoprene mixing ratios. This

shows that even when isoprene emissions are high, VOC fragmentation can have a significant impact on the signal at m/z 69.

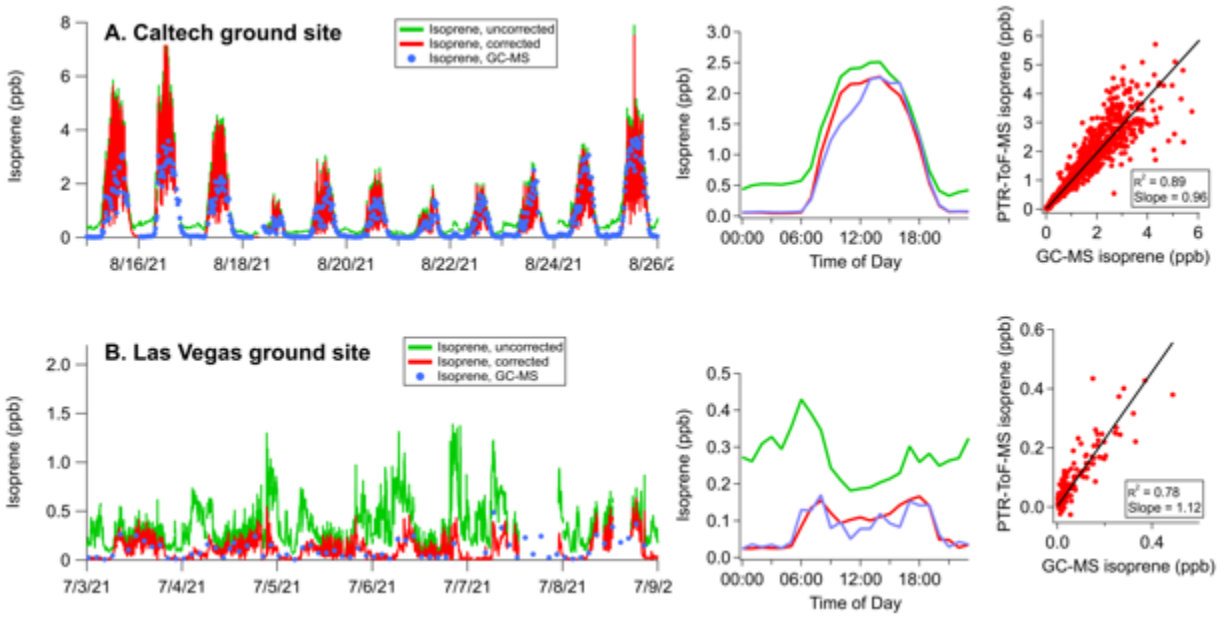

Figure 4-9. Isoprene interference correction on the reported time series and diurnal pattern of isoprene at (A) the Caltech and (B) Las Vegas ground sites. GC-MS measurements are compared against the corrected isoprene mixing ratios.

The corrected isoprene measurements are correlated with GC-MS measurements with R^2 = 0.89 and agree to within 4%. At high isoprene mixing ratios, the measurements exhibit larger variability. This variability results from the differences in sampling timescales (10s for PTR-ToF-MS, ~120 s for GC-MS) along with the high variability of isoprene from local sources. When averaged diurnally, the daytime mixing ratios also agree to within 4%. Both instruments show that average isoprene declines to low mixing ratios at night (< 0.05 ppb). The GC-MS observed a number of periods of enhanced isoprene. After accounting for the large nighttime isoprene interference, the corrected isoprene mixing ratios exhibit good correlation with the GC-MS measurements. These results further demonstrate that the correction described by Method 1 is sufficient to resolve isoprene mixing ratios, even during hours when the interference dominates the total signal at m/z 69.

The isoprene correction is most impactful to the Las Vegas measurements where isoprene emissions are low and aldehydes + cycloalkanes are high. Without correction, the variability in m/z 69 across all daytime hours is driven by the isoprene interference (Figure 4-8). When the interference is subtracted, corrected isoprene mixing ratios approach zero at night and are 0.1 - 0.15 ppb during the day. The resulting diurnal pattern changes substantially and exhibits a daytime peak that is consistent with the expected pattern for isoprene and consistent with the GC-MS measurements. Though the number of cannister samples in Las Vegas was limited

(total 275), a comparison between the corrected PTR-ToF-MS and GC-MS samples agree to within 15% and an R^2=0.78.

5. *VOC, NO_x, and ozone measurements*

In this chapter, the observed mixing ratios from all the instrument are shown as spatial distributions, time series, and diurnal profiles to provide an overview of the observations in Las Vegas and the Jerome Mack ground site. The biogenic VOCs are described in a separate chapter below.

5.1. Spatial distribution of VOCs from Mobile Laboratory drives

Figure 5-1 shows daytime drive tracks from 2021/06/27-28-29 and Figure 5-2 from 2021/07/28-29-30. The tracks are on the map of Las Vegas and are color coded with ethanol and benzene. Ethanol is a good general marker for volatile chemical product (VCP) emissions, because it is an ingredient of many products such as personal care, cleaning, and coatings products. Benzene is regarded as a good tracer for mobile source emissions. The maps show that VCPs are most strongly enhanced around the Las Vegas Strip and the downtown area, while mobile sources are much more spread out over the metropolitan area. All VOCs quickly reach low concentrations outside the populated areas and it is clear that there was no transport of any VOCs into the city on any of the drives.

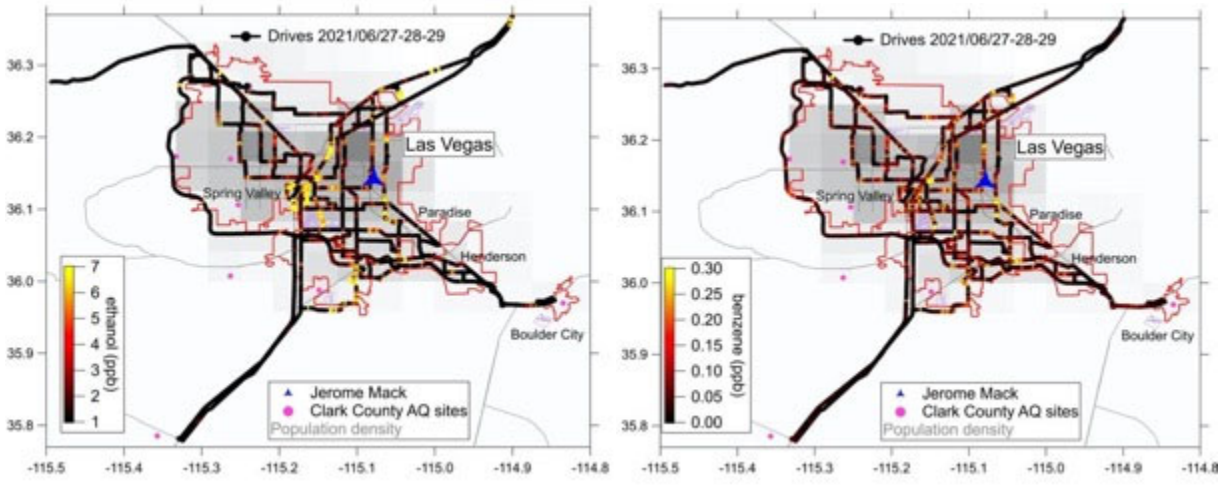

Figure 5-1. The drive tracks of the NOAA Mobile Laboratory from the daytime drives on 2021/06/27-28-29 color coded with ethanol (VCP tracer) and benzene (mobile source tracer).

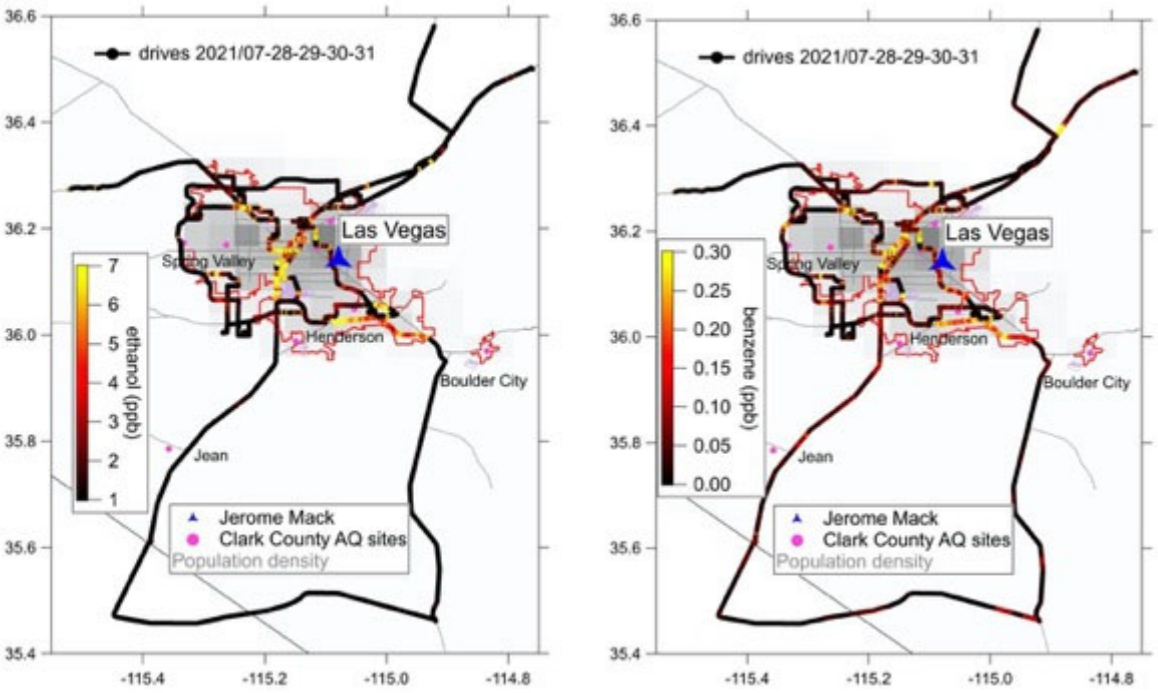

Figure 5-2. The drive tracks of the NOAA Mobile Laboratory from the daytime drives on 2021/07/28-29-30 color coded with ethanol (VCP tracer) and benzene (mobile source tracer).

The nighttime drives on 2021/06/28 and 2021/07/31 show very high mixing ratios of most VOCs around the Las Vegas Strip (Figure 5-3). This area is subjected to emissions from multiple VCPs, mobile, cooking, cleaning, and other sources, which are larger at night due to greater activity (i.e., higher emissions) and lower atmospheric mixing and lower boundary layer height (i.e., less dilution). The difference in mixing ratios between night and day are also highlighted in Figure 5-4 that show the time series of a few select compounds from the daytime and the nighttime drive on 2021/06/28, where the period driving on the Las Vegas Boulevard is indicated. VOCs that are emitted from VCPs had very high mixing ratios all along Las Vegas Boulevard. During the daytime, large spikes are observed on the Las Vegas Boulevard; however, nighttime mixing ratios are sustained throughout the whole area. Here, ethanol exceeded 1 ppm, D5 siloxane from personal care products was over 1 ppb, and monoterpenes that are mostly from fragrances at night were over 5 ppb. These are some of the highest mixing ratios detected by the Mobile Laboratory across other major urban areas, such as New York, Los Angeles, and Chicago. Only a small distance away from Las Vegas Boulevard, mixing ratios were more typical for urban areas.

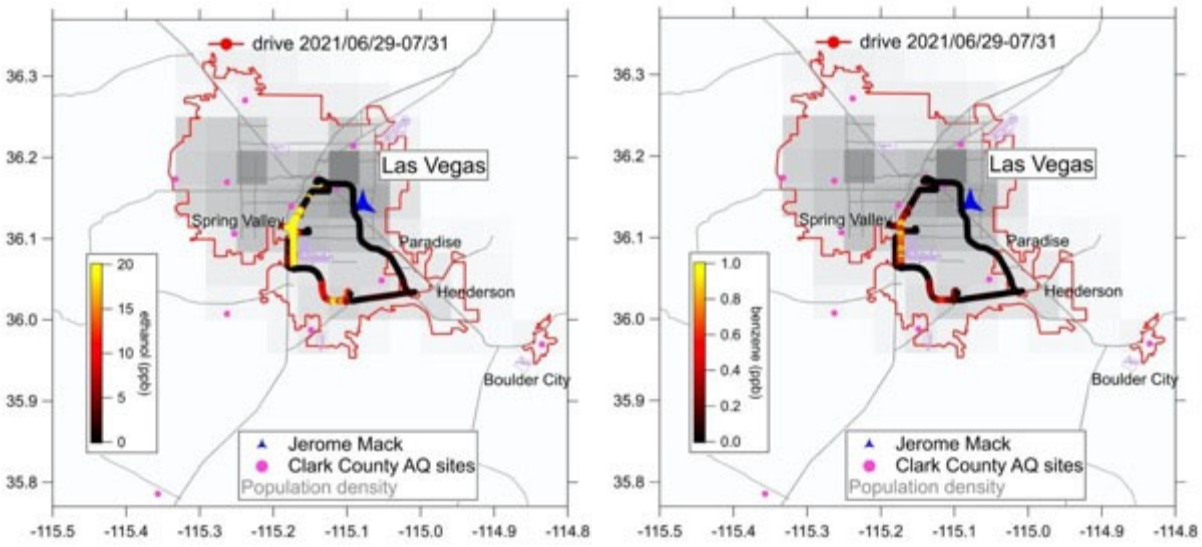

Figure 5-3. The drive tracks of the NOAA Mobile Laboratory from the nighttime drives on 2021/06/28 and 2021/07/31 color coded with ethanol (VCP tracer) and benzene (mobile source tracer). Note the change in scale compared to daytime.

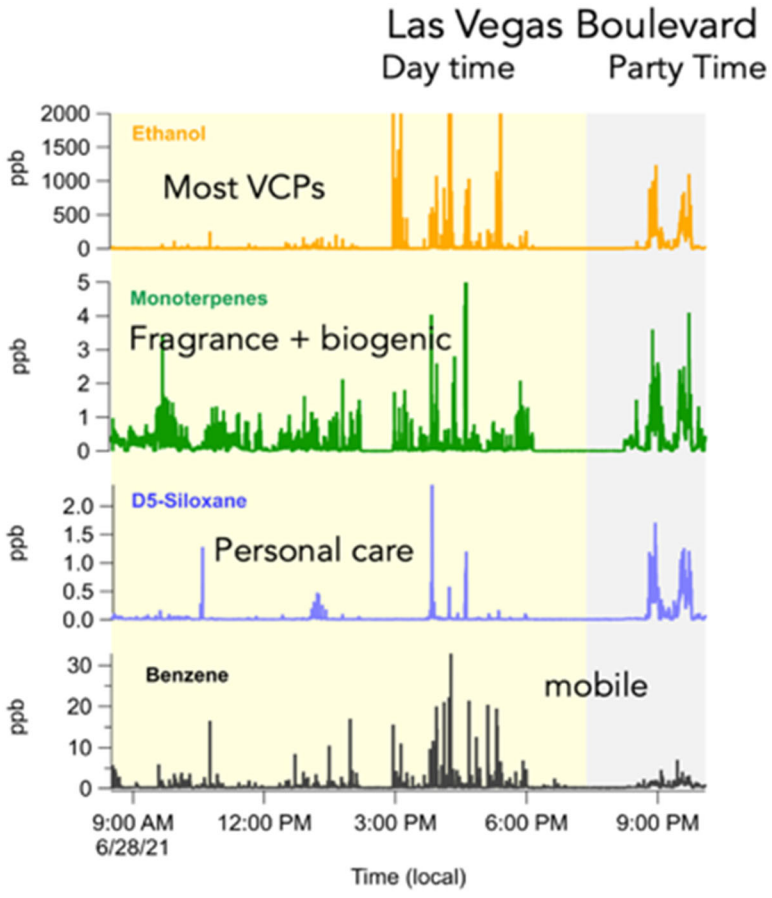

Figure 5-4. Comparison of the daytime and nighttime mixing ratios from the drive on 2021/06/28 on the Las Vegas Strip.

As mentioned above, the PTR-ToF cannot separate structural isomeric compounds. To better understand the complicated VOC mix around the Las Vegas Strip, we have also deployed the GC-PTR-ToF method on the Mobile Laboratory for the drive on 2021/07/31. Figure 5-5 shows chromatograms for some selected VOCs that were sampled and analyzed with the GC-PTR-ToF system on Las Vegas Strip at night. The chromatogram demonstrates that many VOCs, such as the aromatics, ketones, PCBTF (parachlorobenzotrifluoride, which is a tracer for solvent borne coating [*Stockwell et al.,* 2021]), or benzaldehyde can be measured with PTR-ToF without significant interference, even in areas with complicated VOC mixtures.

The chromatogram also shows that limonene is the dominant monoterpene isomer with alpha- and beta-pinene in much smaller amounts. This indicates that in this area the monoterpenes are mostly not biogenic, but from the use of fragrances in personal care or cleaning products. This is consistent with our previous observations in NYC, which showed that fragranced VCPs are a major source of urban monoterpenes [*Gkatzelis et al.*, 2021a], *Coggon et al.* 2021]. Limonene is the most commonly used ingredient in fragrances, and alpha-pinene is generally the largest biogenic emission. In addition, monoterpene emissions are at a minimum at night and likely will not accumulate to such large mixing ratios.

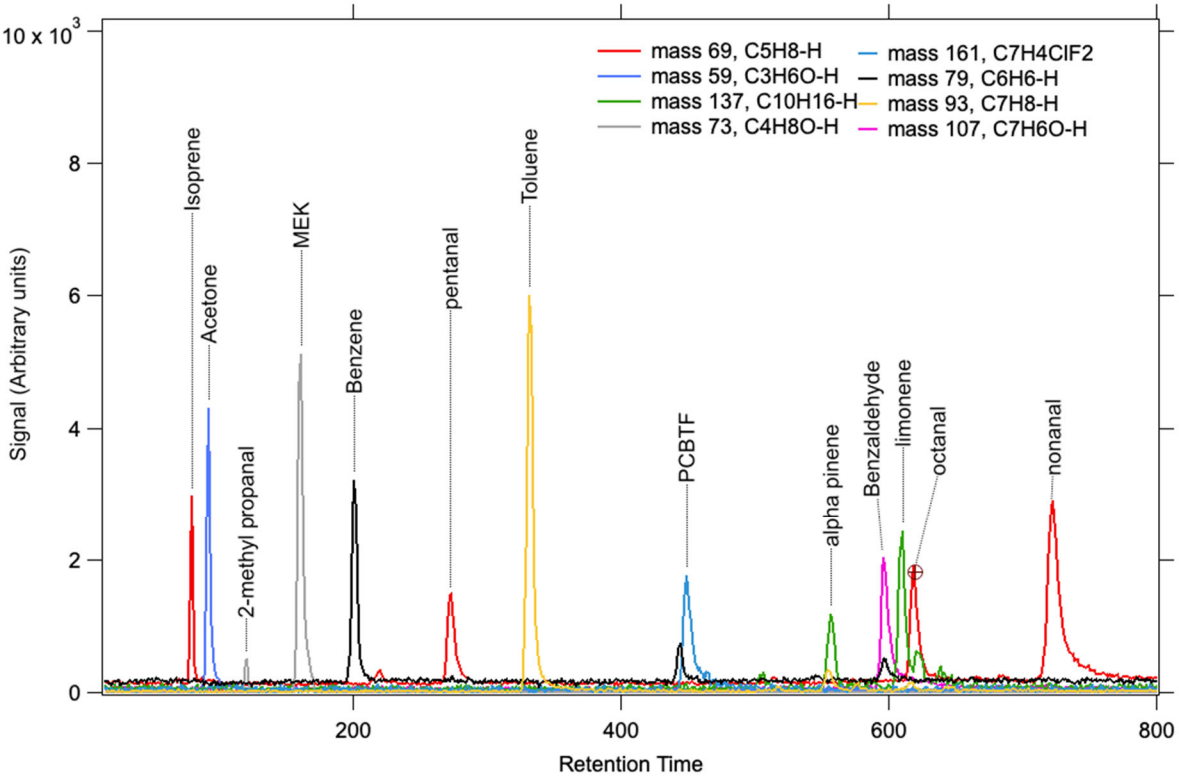

Figure 5-5. Chromatograms for some select VOCs from the GC-PTR-ToF combination sampled on the Las Vegas Boulevard on 2021/07/31 at night.

The time series of NO_x, NO, NO_2, and O_3 at Jerome Mack were shown in Figure 4-1 and Figure 5-6 shows the daytime drive tracks color coded by NO_x. With the mobile laboratory, the measured mixing ratios of NO_x are heavily dominated by on-road emissions of individual vehicles such that a regional distribution cannot be measured and Figure 5-6 shows high NO_x throughout all the drives. Emission ratios of NO_x from vehicles will be discussed below.

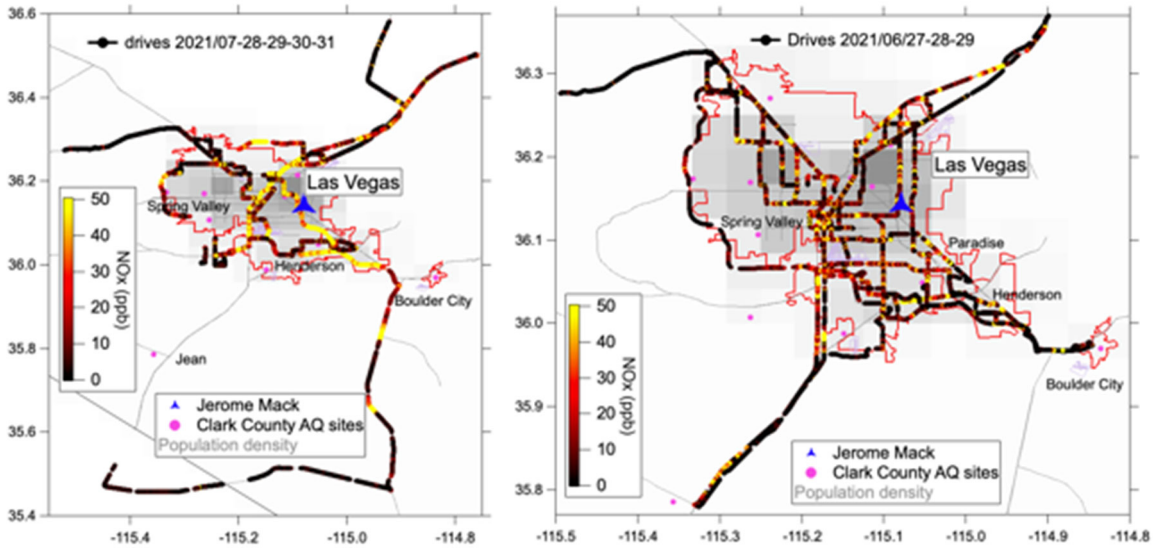

Figure 5-6. The drive tracks of the NOAA Mobile Laboratory from the daytime drives color coded with NO_x.

5.2. Time series of VOCs at the Jerome Mack site

The time series of some select VOCs measured by PTR-ToF-MS for 1-minute average data are shown in Figure 5-7 together with ozone. Most of the VOCs show significant influence of local sources indicated by very large short-term spikes. Most notably is a local source from solvent-based coatings that happened frequently throughout several days. This source is characterized by large spikes of PCBTF, acetone, toluene, other larger aromatics, and alkanes. Most likely emission source was a cabinet making company located within a few hundred yards of the Jerome Mack site. These spikes in several select compounds were added on top of the more sustained mixing ratios and will increase the observed average mixing ratios, but are easy to account for by either removing them or by simply averaging for longer time periods as will be shown below.

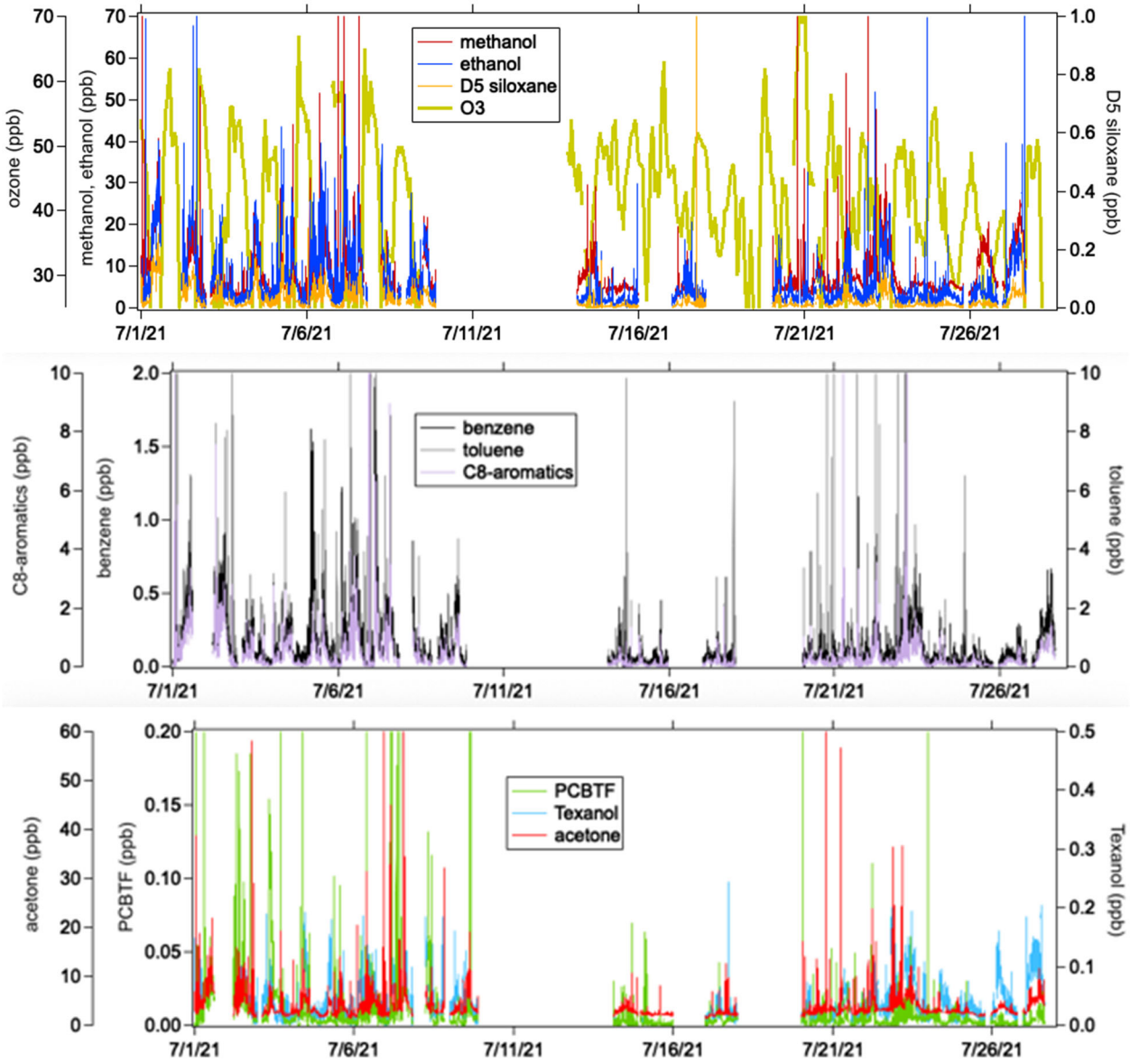

Figure 5-7. Time series of some select VOCs measured by PTR-ToF-MS at the Jerome Mack site.

Selected small alkanes and alkenes measured by WAS GC-MS are shown in Figure 5-8. These compounds are emitted in significant amounts from mobile sources and oil and natural gas production and usage. High mixing ratios were observed throughout the campaign, which result in a large contribution of the total OH reactivity that has a significant influence on ozone formation as will be discussed in a later chapter.

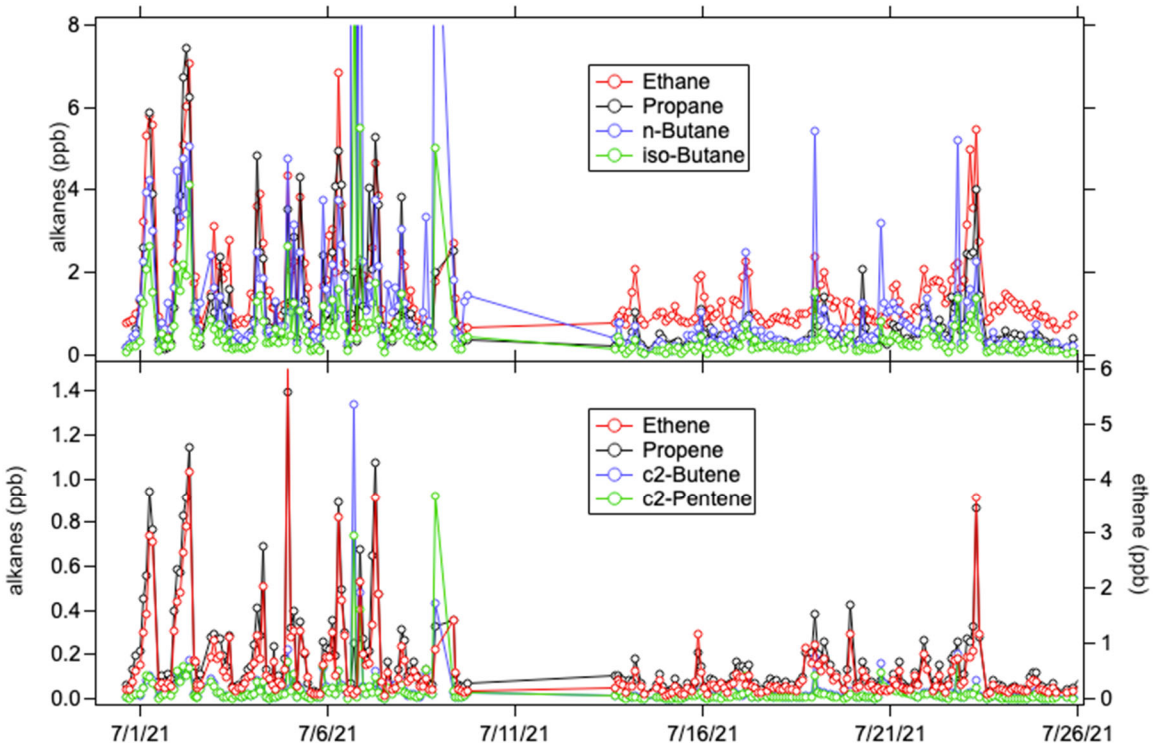

Figure 5-8. Time series of alkanes and alkenes measured by canister analysis with GC-MS at the Jerome Mack site.

Benzene, toluene, and some other VOCs were measured by both WAS GC-MS and PTR-ToF-MS as shown in Figure 5-9. This figure demonstrates that the combination of these two instruments for VOC measurements is providing good data coverage; the PTR-ToF-MS has a very fast time resolution and is sensitive to many VOCs, including oxygenated and N-containing VOCs, which cannot be detected from canister samples and subsequent GC-MS analysis. But PTR-ToF-MS only measures the mass of the various compounds, which often means that only the sum of VOCs with the same mass are detected. The WAS GC-MS is dependent on the number of canister samples that can be collected, but is very specific to each compound and can detect alkanes and alkenes that are not measured by PTR-ToF-MS.

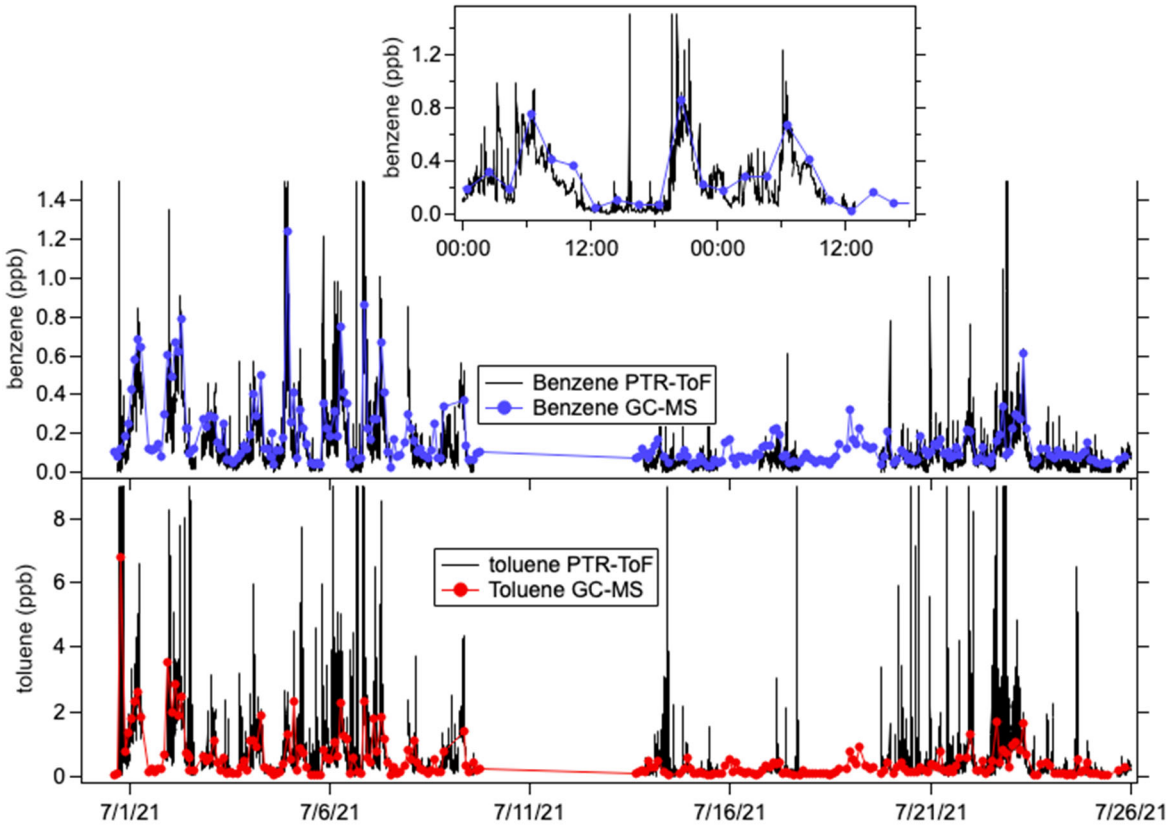

Figure 5-9. Time series of benzene and toluene measured by PTR-ToF-MS and canister analysis with GC-MS at the Jerome Mack site.

5.3. Diurnal Profiles at Jerome Mack

The diurnal profiles of the small alkanes and alkenes are shown in Figure 5-10 and some other select VOCs, CO, NO_x, and ozone are shown in Figure 5-11. VOCs, CO, and NO_x are high at night in the nocturnal stable layer and have their maximum in the early morning hours before the daytime boundary layer gets established and oxidative losses decease mixing ratios during the day. A diurnal profile of the boundary layer height (BLH) measured by StaDOT is also shown in Figure 5-10. Ozone as a secondary photochemistry product has the maximum during the day as expected. The atmospheric dynamics measurements from the StaDOT instrument will be used to understand the interactions between mixing, transport, and photochemistry determining the VOC mixing ratios at the Jerome Mack site. These dynamics measurements will also be used to set up the box model determining the VOC/NO_x sensitivity and ozone formation pathways.

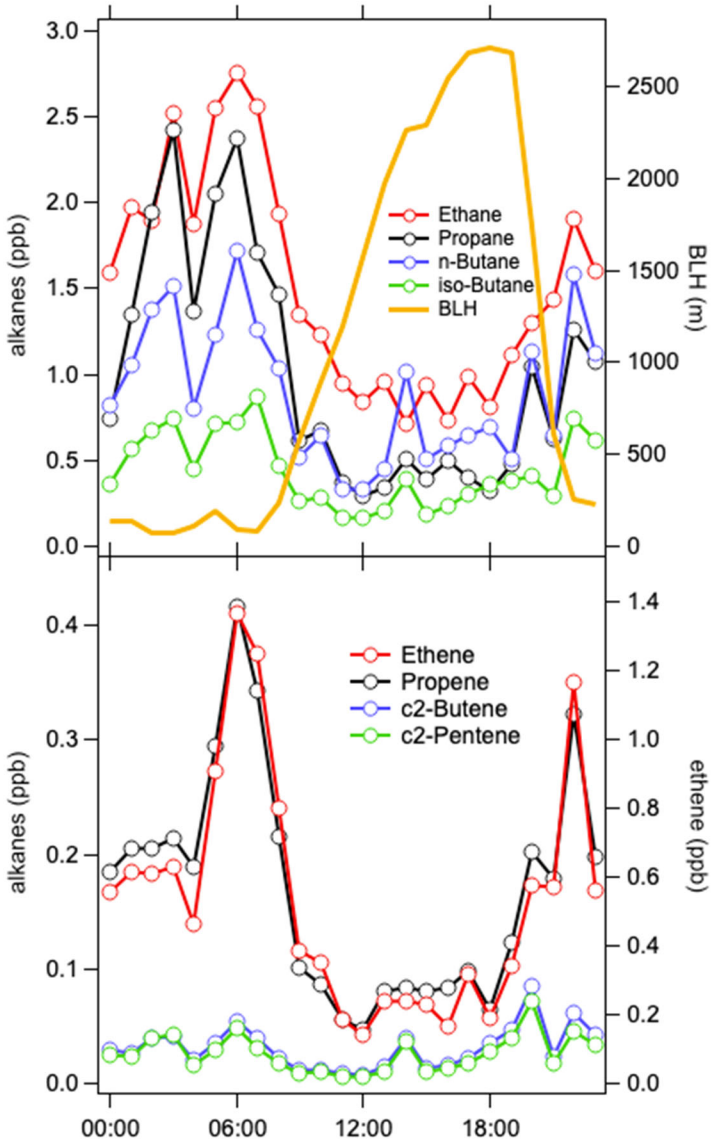

Figure 5-10. Diurnal profiles of small alkanes, alkenes together with the boundary layer height (BLH).

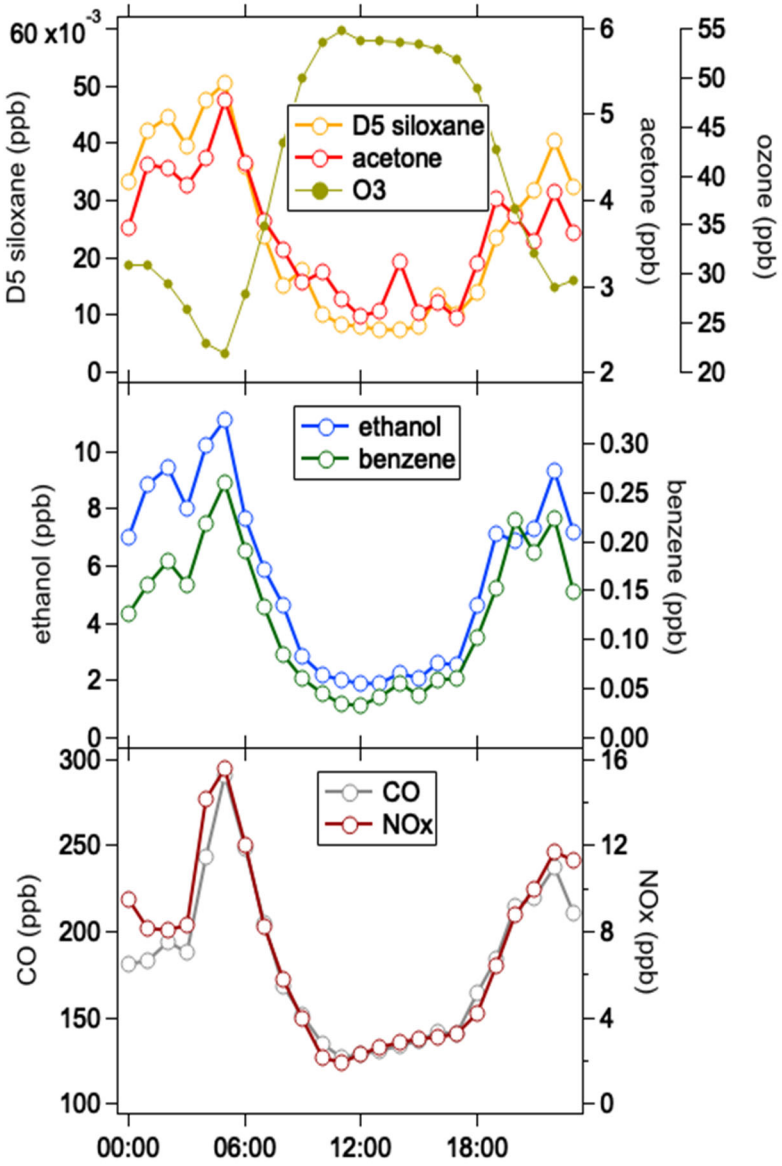

Figure 5-11. Diurnal profiles of some selected VOCs, CO, NOx and ozone.

5.4.Methane distribution in Las Vegas

The methane spatial distribution was measured on the mobile laboratory and the drive track is shown on the map of Las Vegas area colored by measured methane (CH_4) mixing ratio (Figure 5-12). The largest regional enhancements were typically measured around the Las Vegas Strip and the Apex Landfill was observed to be the largest point source in the area. Note that on 2021/07/28, winds were from the southwest and the mobile laboratory was not able to drive downwind of the landfill. Las Vegas Strip enhancements were possibly due to on road emissions and/or natural gas emissions. Analysis of whole air samples provides

additional information to constrain the likely source of these emissions as shown in Figure 5-13. The canister samples collected during the drives of the mobile lab are shown on top of the Las Vegas map, color coded with methane, ethane, and the methane/ethane ratio respectively. Also shown in Figure 5-13 is the correlation plot of ethane versus methane color coded by the methane/ethane ratio. Previous measurements have found a ~2% ethane/methane ratio in urban areas due to emissions from natural gas usage and vehicles [*Peischl et al.*, 2013; *Wennberg et al.*, 2012], which is similar to what was observed in the Las Vegas urban area. The only exception is the sample collected downwind of the Apex Landfill, which does not have significant ethane enhancements as can be expected from biogenic emissions from a landfill [*Peischl et al.*, 2013].

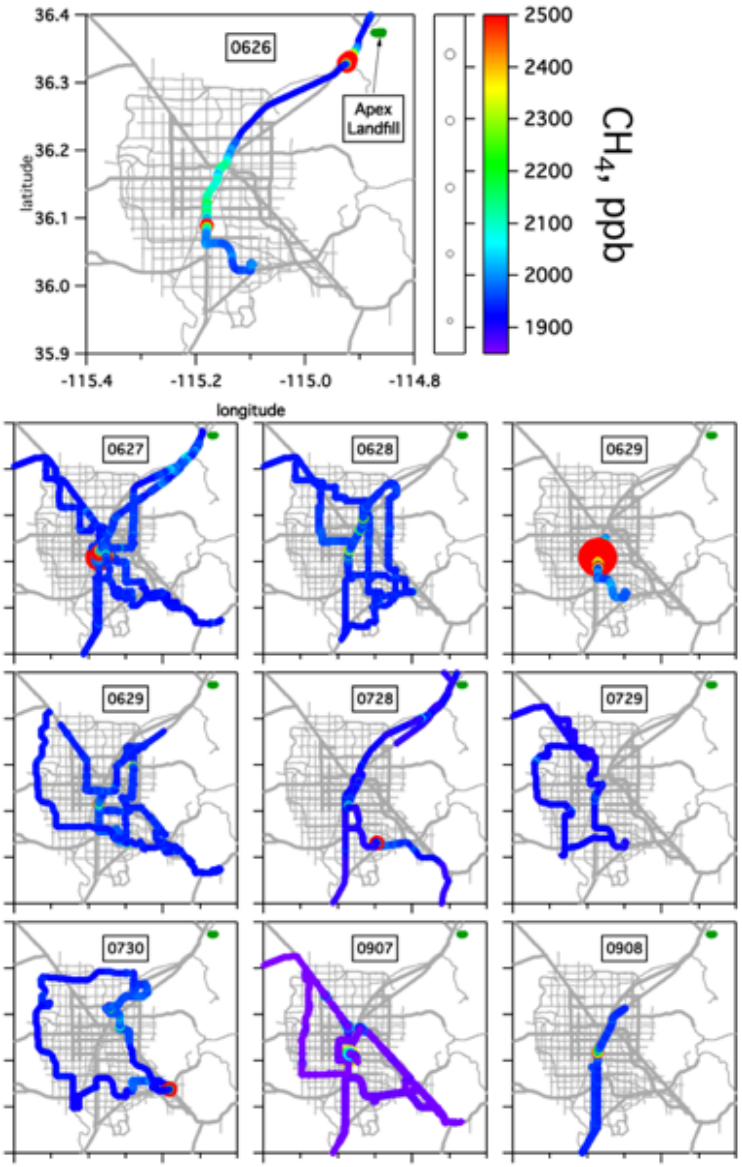

Figure 5-12. Map of Las Vegas area with the NOAA CSL mobile laboratory drive track colored by measured methane (CH_4) mixing ratio.

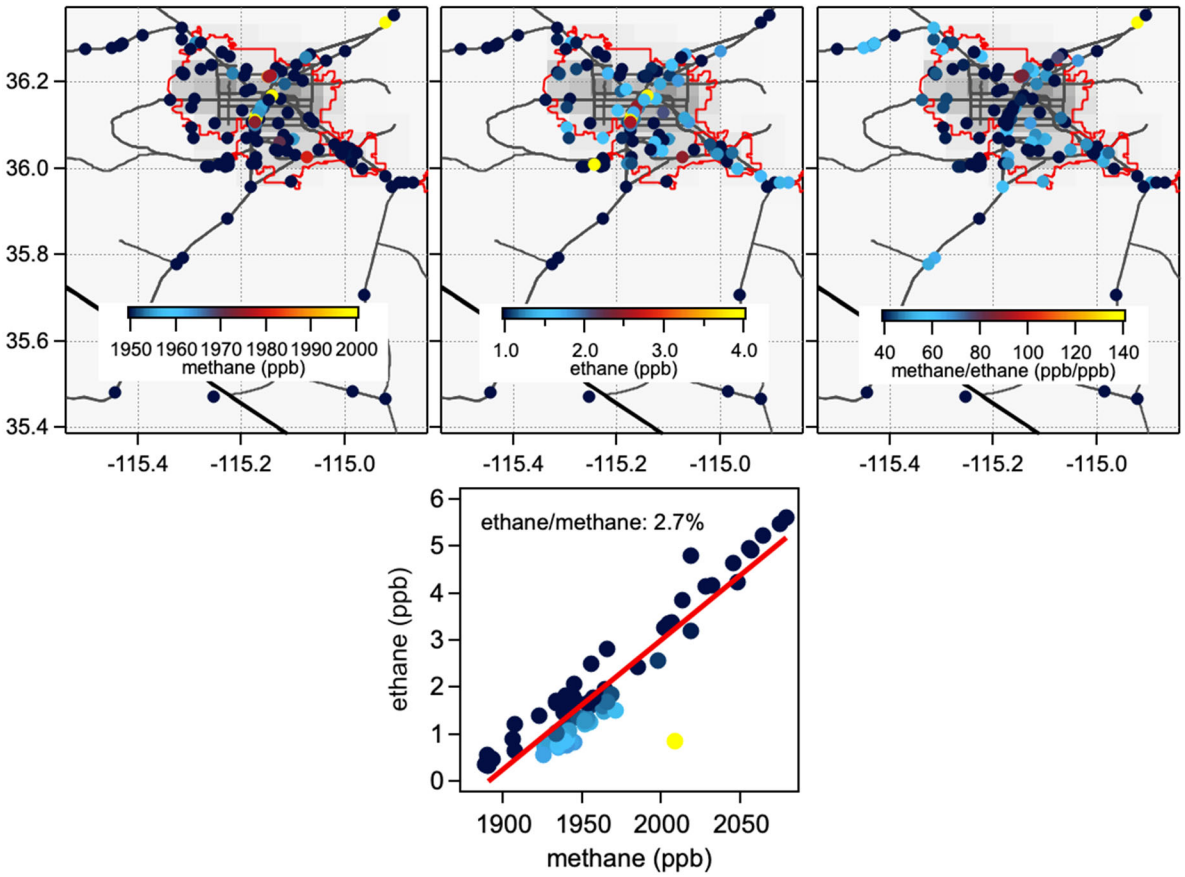

Figure 5-13. (Top) Map of Las Vegas area with the NOAA CSL mobile laboratory drive track colored by measured methane (CH_4), ethane (C_2H_6), and the methane/ethane ratio (bottom) Correlation of ethane with methane color coded by the methane/ethane ratio.

5.5. Weekend effect

Significant weekday to weekend differences in traffic patterns exist in urban areas such Los Angeles: gasoline powered passenger vehicles show different peak hours but overall have similar total activity on weekends, whereas the heavy-duty diesel truck traffic is significantly reduced on weekends [Harley et al., 2005]. The lower ambient NO_x mixing ratios can result in faster photochemical processing during the weekends such that short-lived VOCs are reduced in the weekends [Warneke et al., 2013].

To investigate this effect in Las Vegas, the Jerome Mack data are segregated into weekday and weekend days, and even further into day (12-6 PM) versus night (1-5 AM) for weekends and weekdays as shown in Figure 5-14. There were only three weekend data sets

available, one weekend was missed because of the air condition failure. The diurnal profiles for the whole period are shown together with the weekday and weekends profiles of CO, NO_x, ozone, benzene, D5-siloxane, and ethanol are shown in Figure 5-15. The weekday and weekend data for this time period during the daytime are very similar, but the early morning data are higher on the weekdays. This time period also has the largest variability. NO_x has similar reductions as all the other compounds and it is not clear at least from the Jerome Mack data that there is a larger reduction in NO_x compared to VOCs as is observed in Los Angeles.

The weekday and weekend data are further separated into day (12-6PM) and night time (1-5AM) in Figure 5-16 to investigate the influence of potential faster photochemistry on the weekends. The scatter plots of various aromatics versus benzene are shown. The main sink of aromatic compounds is reactions with OH radicals, where benzene is the longest lived followed by toluene, then C8-aromatics, and C9-aromatics. If OH-initiated photochemistry is faster, shorter-lived compounds such as the C8- and C9-aromatics are more reduced during the daytime compared to longer lived compounds such as benzene. The scatter plots of benzene with toluene, C8-aromatics, and C9-aromatics for the nighttime data are shown on the right side of Figure 5-16. The slopes of the correlation are similar on weekday and weekends, which is expected during a time when photochemical processing with OH is at its minimum. The slopes for the C8- and C9-aromatics versus benzene are smaller on the weekends, which might indicate faster photochemical loss rates on the weekends during transport to Jerome Mack. It should be here that the variability of the aromatics to benzene ratio during the day was large, causing a significant uncertainty in the slopes.

In summary, there may be a small weekend effect in Las Vegas, but due the large variability in the data and the small number of weekend observations no definite conclusions can be drawn.

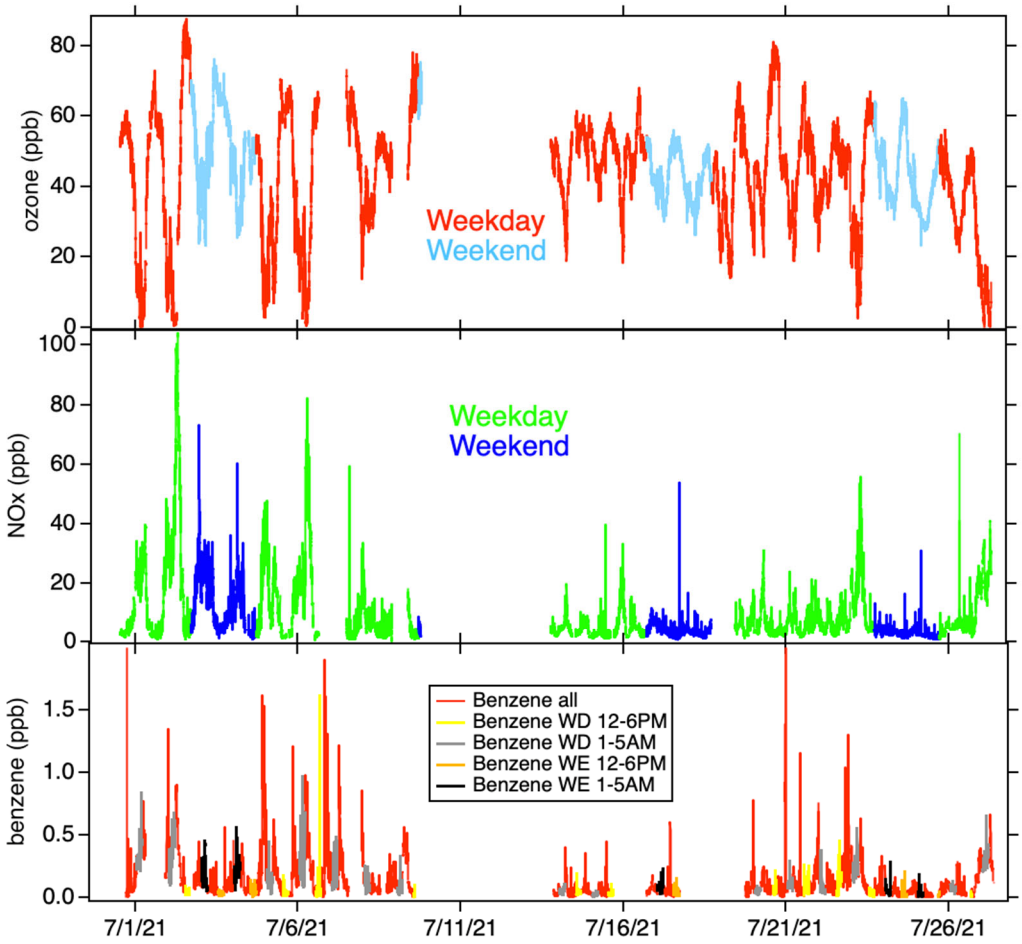

Figure 5-14. Ozone and NOx time series color coded by weekends and weekdays and night and day.

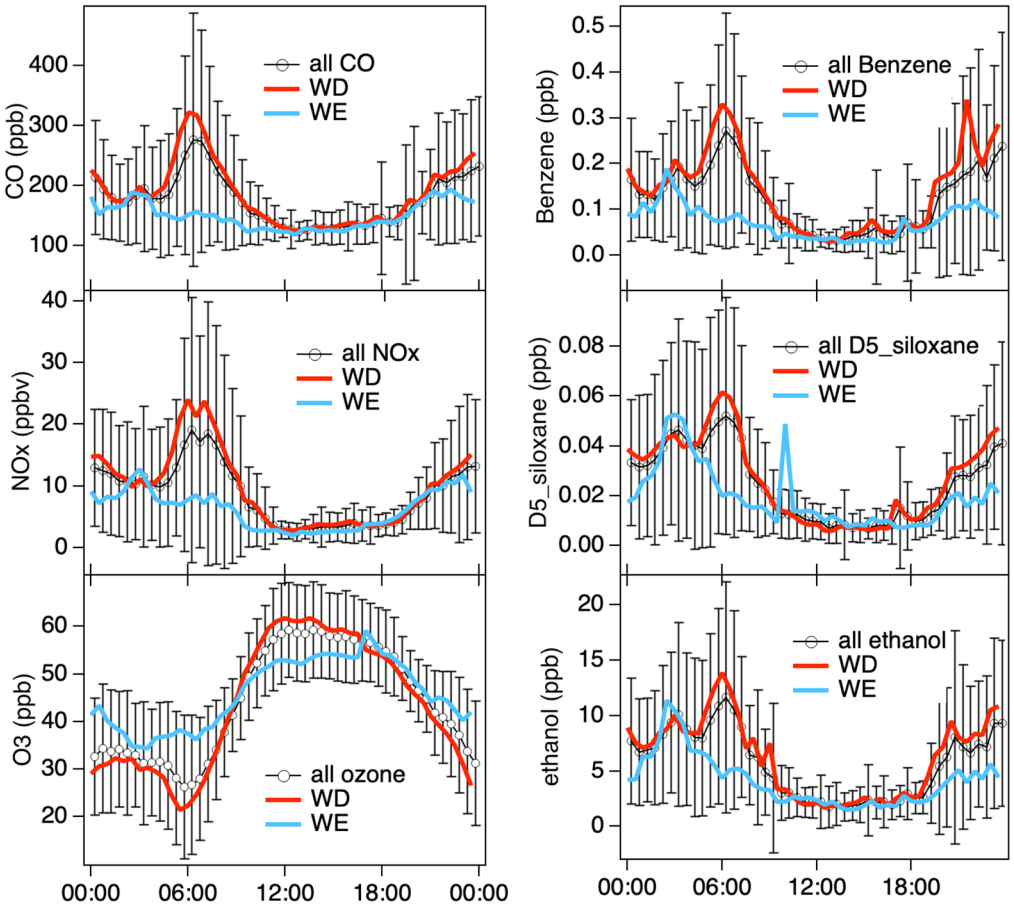

Figure 5-15. Diurnal profiles of some selected VOCs, CO, NOx, and ozone separated into weekdays and weekends.

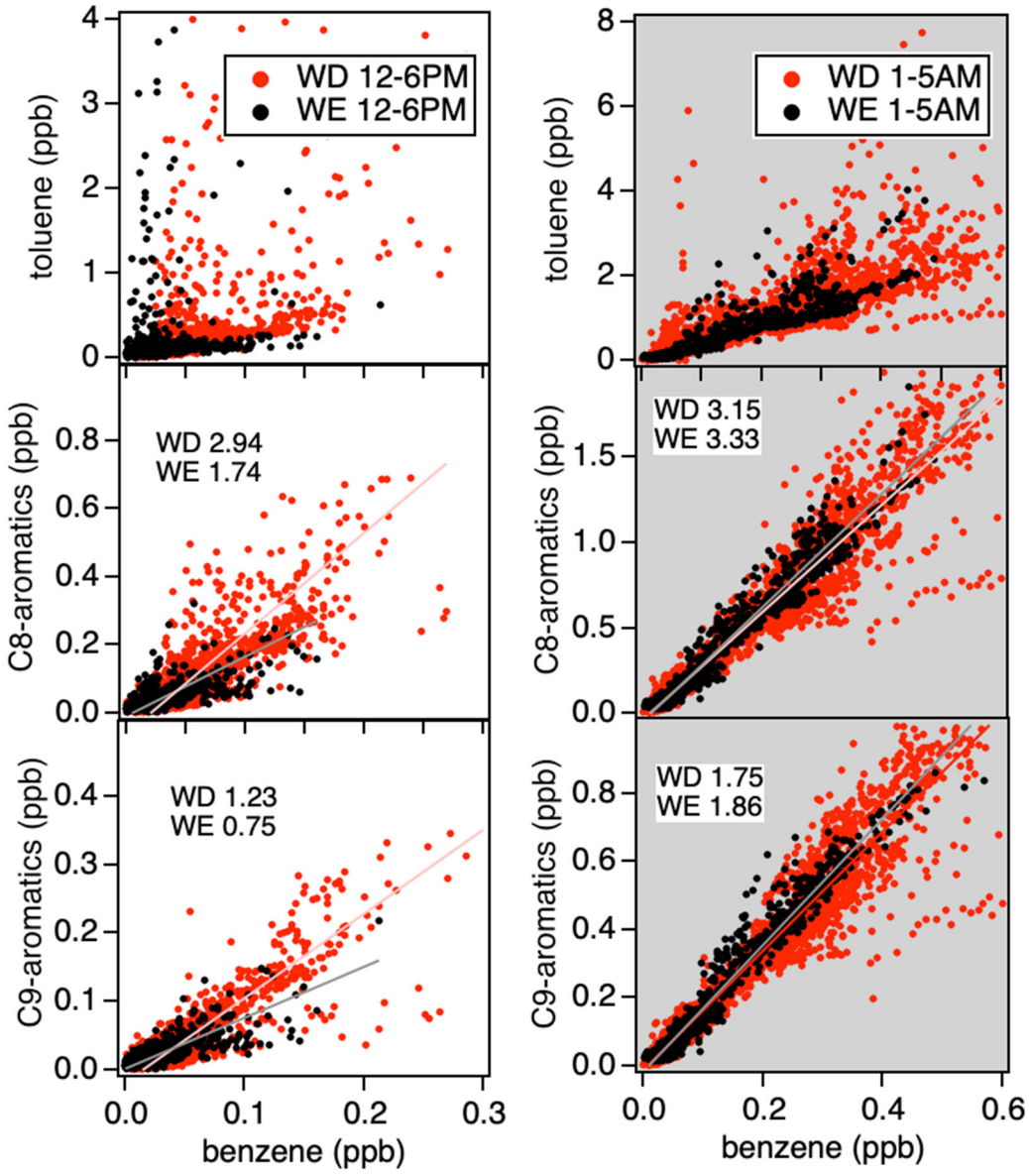

Figure 5-16. Slopes of aromatics on weekdays and weekend separated into daytime and nighttime.

5.6.Biomass burning impact

Acetonitrile and furfural are two VOCs that have been used as biomass burning and domestic burning tracers [*Coggon et al.*, 2016; *de Gouw et al.*, 2003]; both were measured by PTR-ToF at Jerome Mack and their time series and diurnal profile are shown in Figure 5-17. Acetonitrile likely has some smaller urban sources as a use in solvents. Small anthropogenic acetonitrile plumes not accompanied with any other VOCs have been observed in Boulder, CO [*Coggon et al.*, 2016], similar to what is observed at Jerome Mack in the acetonitrile time

series. Furfural has only very small enhancements throughout the measurement period. Both acetonitrile and furfural are not strongly correlated with carbon monoxide (R^2= 0.18 and 0.0006, respectively). The only period, where acetonitrile and furfural were enhanced significantly at the same time was on July 04, 2021 from around 10 PM to midnight. The large enhancement of the shorter-lived furfural compared to acetonitrile shows that this plume has not aged significantly and we speculate that this plume was related to 4th of July fireworks instead of transported biomass burning emissions.

Overall, there is no evidence that biomass burning had a significant impact on the results presented below.

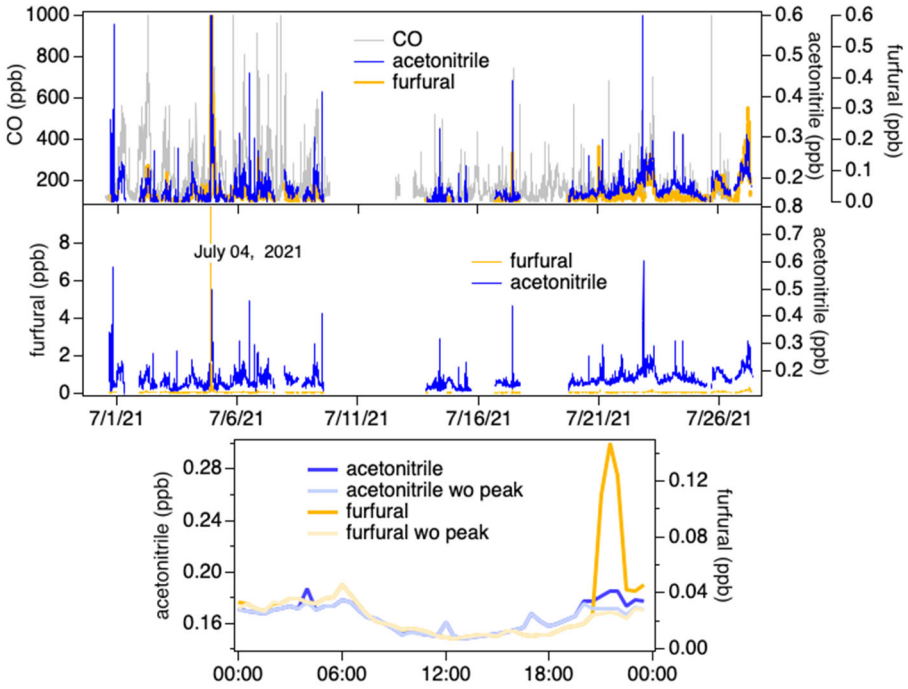

Figure 5-17. The time series of the two biomass burning tracers acetonitrile and furfural and their diurnal profiles at the Jerome Mack.

6. ***Enhancement Ratios***

6.1. Enhancement ratios at Jerome Mack and during drives

The top of Figure 6-1 shows correlation plots of D5-siloxane and benzene with ethanol for the 1-minute and for 1-hour average data. Correlation plots like these, often done with CO, are used to determine emission ratios that can be compared with emission inventories in order to update the inventory for a specific city such as Las Vegas. In addition, in a previous publication we used D5-siloxane emission ratios with CO to estimate total emission of D5 siloxane in Boulder and New York City [*Coggon et al.*, 2021; *Coggon et al.*, 2018]. The FIVE emissions inventory has been validated for CO on several occasions and found to be accurate to within 30%. The emission ratio of the VOC and the CO inventory can then be used to estimate VOC emissions.

There are a large number of data points with significant scatter from the local sources as described above, but nevertheless the emission ratios can be determined from both the 1-minute and the 1-hour data as shown in the top panels of Figure 6-1. D5-siloxane and ethanol are both expected from VCP emissions [*Gkatzelis et al.*, 2021a] and are indeed well correlated in the Jerome Mack data. Benzene, the marker for mobile sources, is also well correlated with ethanol, which indicates that VCP and mobile sources readily mix before they are measured at Jerome Mack and that changes in mixing ratios are mostly determined by transport and dynamics. The local solvent-based coatings source is an exception as the transport time is very short.

The bottom of Figure 6-1 compares the correlation of D5-siloxane and benzene with ethanol from the ground site to the mobile laboratory drives. Benzene and ethanol are not well correlated during the drives, and the D5-siloxane and ethanol correlation is significantly diminished compared to the ground site. This shows that emissions ratios from local sources, such as restaurant cooking (as will be described in Section 7), can be determined with the Mobile Laboratory measurements, while the aggregate emission ratios needed for emission inventory updates can be determined from the Jerome Mack data.

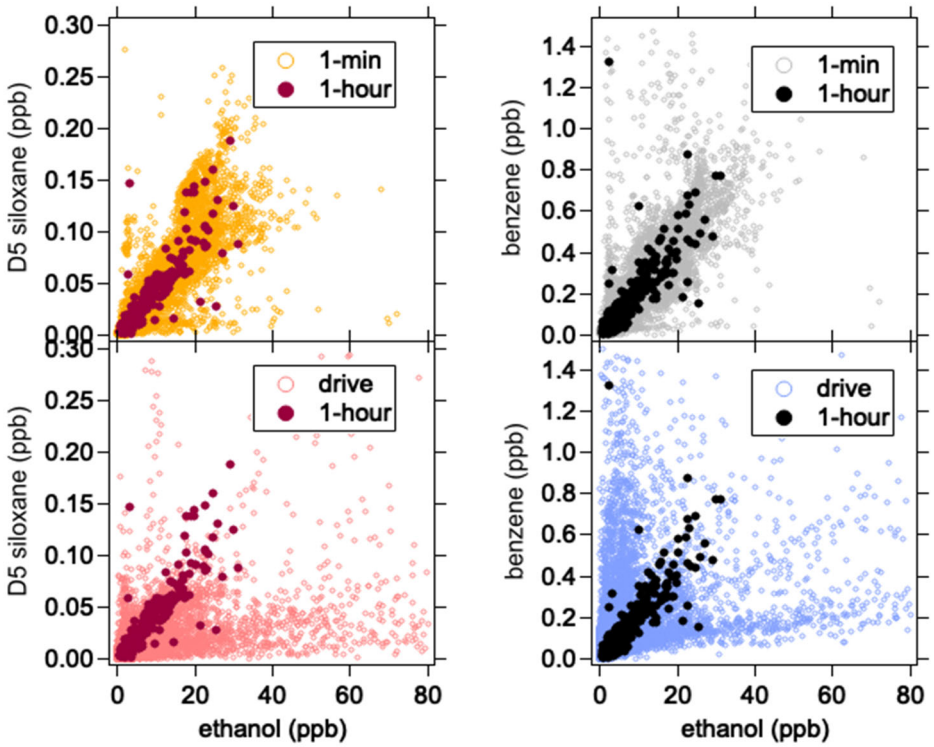

Figure 6-1. Correlation of ethanol with benzene and D5-siloxane for the Jerome Mack ground site for data that were averaged for (top) 1-minute and 1-hour averaged data and (bottom) correlations from the Mobile Laboratory drive on 2021/07/28 for 1-second data.

6.2. All VOCs

Enhancement ratios (ERs) of VOCs emitted from anthropogenic sources (e.g., VCPs and mobile sources) versus an inert compound (e.g., CO) are critical for comparing to inventory [*Gkatzelis et al.*, 2021b] estimates and are key inputs for positive matrix factorization (PMF), box modeling, and 3D chemical transport modeling (WRF-Chem) as was shown by *Coggon et al.* [2021]. ERs are often calculated from nighttime data, when mixing ratios are highest as local emissions accumulate in a shallower boundary layer and photochemical production and loss are at a minimum [*Borbon et al.*, 2013; *de Gouw et al.*, 2018; *Warneke et al.*, 2007].

Typical scatter plots used to estimate ERs are shown in the left panels of Figure 6-2 for benzene, acetaldehyde, and the sum of the C9-aromatics. In these plots, all measurements by the PTR-ToF-MS (grey markers) were sorted by daytime (1-6 PM; yellow markers) and nighttime (12-6 AM; black markers), with linear fits for each relative to CO shown. Benzene is a primary emission predominantly resulting from mobile sources, and it is not significantly impacted by photochemistry on short timescales; therefore, ERs (*i.e.*, the slope of the linear fit) estimated for the day and nighttime data are very similar. Acetaldehyde has a short lifetime

(highly reactive) during the day, and it can be rapidly formed due to significant photochemical production [*de Gouw et al.*, 2018] resulting in a slope to CO that is larger during the day than at night. The sum of C9-aromatics has a short lifetime during the day and no photochemical sources [*Warneke et al.*, 2013] and the slopes with CO are smaller during the day than at night.

An ER for each PTR-ToF-MS species was calculated by determining the slope to CO using an orthogonal distance regression. The results for each ER estimated for daytime (1-6 PM) are plotted versus those calculated at night (12-6 AM) and are shown in the upper right panel of Figure 6-2, where each point represents a single compound or mass measured by PTR-ToF-MS. Several compounds included in this Figure are from emissions from mobile sources and VCPs. The nighttime versus daytime comparison shows significant scatter (R^2=0.49), which is expected to result from varying daytime reactivity and photochemistry as demonstrated by the plots in the left panels for acetaldehyde and C9-aromatics. In order to minimize photochemical impact and secondary chemistry, the nighttime measurements will be used in the WRF-Chem modeling as they better describe primary emissions.

ERs can vary by city as each municipality can have different emission sources with varying contributions to total VOC and NO_x emissions [*Warneke et al.*, 2007]. The lower right panel of Figure 6-2 compares the 2021 Las Vegas nighttime ER estimates with measurements in August 2021 from Pasadena, which is a receptor site of air impacted by downtown Los Angeles. On average, the ERs were about 60% higher in Pasadena, but the reasons for this difference are subject to further study.

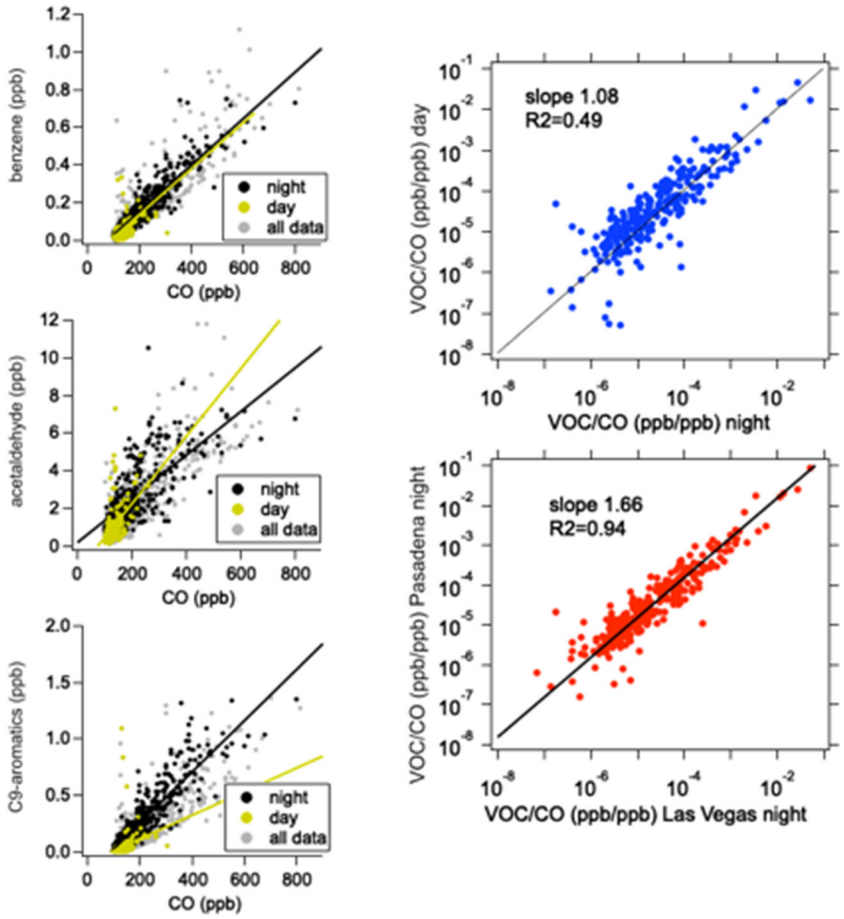

Figure 6-2. Individual VOC measurements (benzene, acetaldehyde, C9-aromatics) versus CO used to calculate enhancement ratios for nighttime (black markers) and daytime (yellow markers) data (left). ERs estimated for each VOC measured by the PTR-ToF-MS comparing day versus nighttime (upper right) and Las Vegas versus Pasadena (lower right).

6.3. On-road emission ratios

In this chapter we look at on-road measurements of vehicle exhaust, as shown in Figure 5-6. These data are utilized here to determine emission ratios for NO_2/NO_x, NO_x/CO, NO_x/CO_2, and $VOCs/NO_x$. Two methods are used for determining the emissions ratios: (1) a total oxidant approach for NO_2/NO_x and (2) an integral ratio approach for NO_x/CO, NO_x/CO_2, and $VOCs/NO_x$.

NO_2/NO_x

The ratio of NO_2/NO_x is an important indicator of control technology implementation motivated to reduce the direct emission of NO_2 by diesel vehicles. Light-duty vehicles emit NO_x mostly in the form of NO, but diesel vehicles tend to emit higher NO_2 fractions.

Additionally, catalytic converters used in heavy-duty diesel trucks convert much of the NO formed during combustion to NO_2. This exhaust is used to oxidize particles and continuously clean particle filters, partially converting the NO_2 back to NO.

If NO_x is emitted as NO, it will locally titrate ozone via the reaction

$$(1)\ NO + O_3 \rightarrow NO_2 + O_2,$$

and must react with a species other than O_3 to form NO_2 before net ozone production can occur. Direct NO_2 emission is immediately available for O_3 production via

$$(2)\ NO_2 + h\nu \rightarrow NO + O$$
$$(3)\ O + O_2 + M \rightarrow O_3 + M.$$

This pathway results in ozone production closer to the NO_x emission source and a higher final O_3 concentration subsequent to oxidation of all the emitted NO_x.

Figure 6-3 shows time series of NO, NO_2, and O_3 of two example vehicle plumes observed during the drives in Las Vegas: one from a single vehicle and one from overlapping vehicle plumes. The plumes were 15s and 22s wide, respectively. The challenge in determining NO_2/NO_x ratios is the rapid photochemical cycling between NO and NO_2 from the reactions between NO and O_3 and the daytime photolysis of NO_2 and from Figure 6-3a it is clear that O_3 is titrated in both plumes. The total oxidant approach determines the NO_2/NO_x ratio from the slope of the enhancement of O_x ($=O_3+NO_2$) to NO_x [*Wild et al.*, 2017], where the total NO_x and O_x measured are conserved during the photochemical cycling. The simultaneous measurement of total NO_x and O_x bypasses this problem since both are conserved during these conversions. The NO_2/NO_x emission ratio then is the slope of the relationship between O_x and NO_x in each plume, regardless of how much NO has reacted with O_3 [*Peischl et al.*, 2010]. The relationship is valid because total NO_x and total O_x are conserved during rapid interconversion of NO, NO_2 and O_3 just after emission.

The derived ratios from the slope of the correlation plots are shown in Figure 6-3d and this method was used to analyze over 700 plumes in Las Vegas. The average NO_2/NO_x ratio for the region during the time of the mobile laboratory measurements was found to be 0.059 ± 0.004, which is similar to the values reported by *Wild et al.* [2017] of 5.9%.

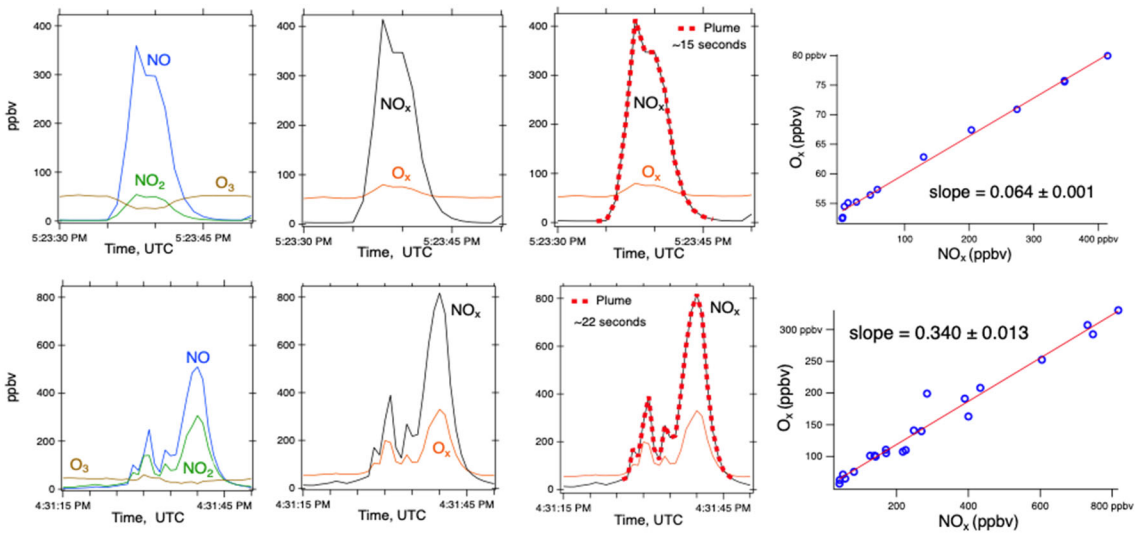

Figure 6-3 (a) NO, NO_2, and O_3 mixing ratios in an on-road vehicle plume. (b) The corresponding NO_x and O_x concentration levels measured in the same plume. (c) The sizes of the plume used to generate the (d) correlation plots.

<u>NO_x/CO, NO_x/CO_2, and VOCs/NO_x</u>

The integral approach is used to determine the NO_x/CO, NO_x/CO_2, and VOCs/NO_x emission ratios. The NO_2/NO_x ratio provides a measurement of the composition of the NO_x emissions, the NO_x/CO and NO_x/CO_2 ratios provide a measurement of the total on-road NO_x emissions and relates them to total fuel consumption. The VOC/ NO_x ratios might allow for the characterization of the fuel used (gasoline versus diesel) and might provide a tracer for measuring VOC emissions from on-road vs. off-road sources. Figure 6-4 and Figure 6-5 show examples of vehicle emission plumes observed on a highway and non-highway road, respectively. Five VOCs were selected, including benzene, toluene, and C8-C10 aromatics, based on their abundance in vehicle emissions. The backgrounds for each observed chemical species are subtracted prior to integrating the area under the plume to isolate the on-road emissions from emissions in the surrounding area. Correlation plots are also shown for five of the correlated VOCs reported. The ratios for the example plumes shown in Figure 6-4 and 6-5 are reported in Tables 6-1. Significant differences in emission ratios are observed for these two example plumes for all species.

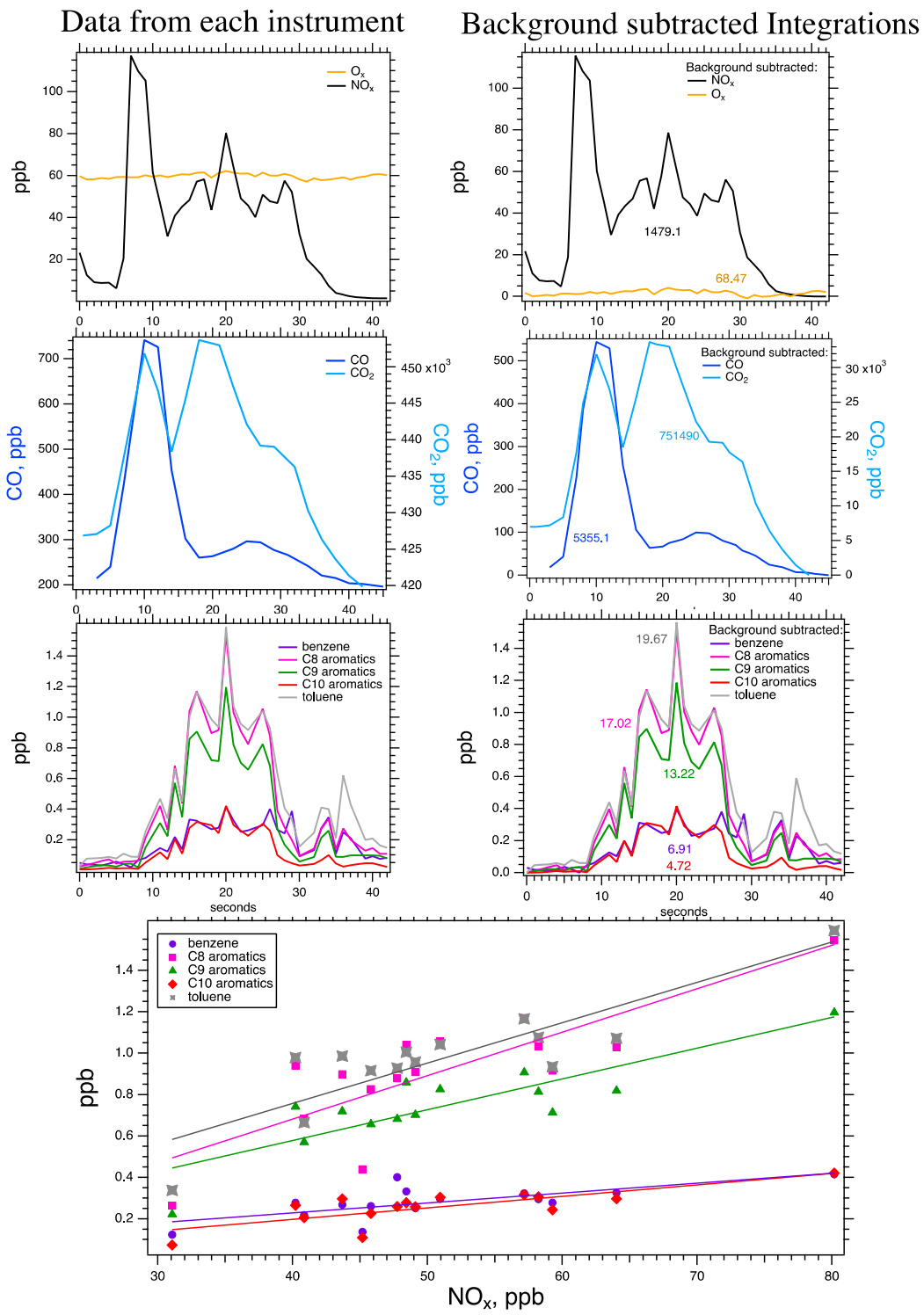

Figure 6-4. Vehicle plume observed on a highway road. Integral values for each species are displayed on the background subtracted plume traces on the right. The lower plot shows the correlation between select VOCs and NO_x.

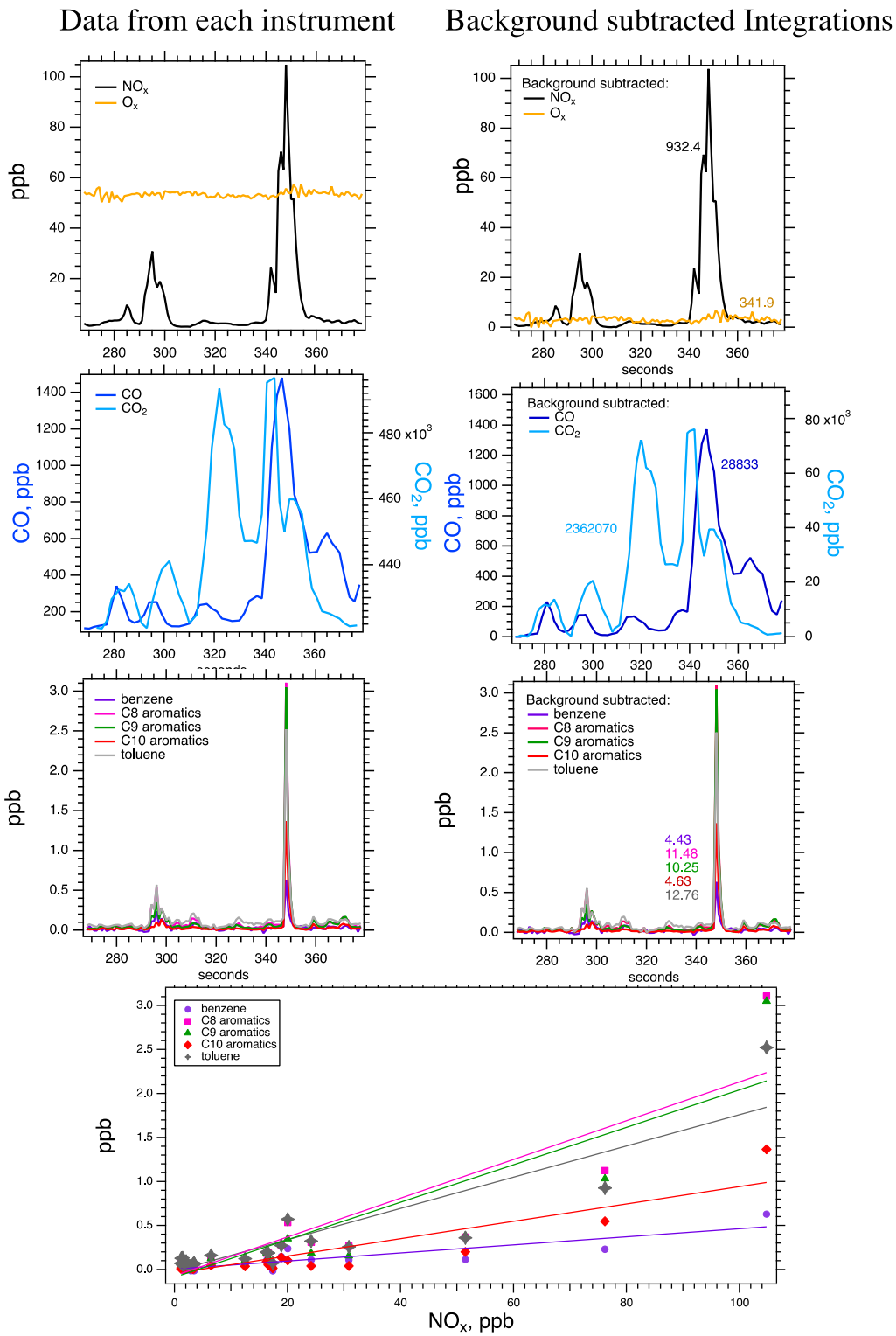

Figure 6-5. Vehicle plume observed on a non-highway road. Integral values for each species are displayed on the background subtracted plume traces on the right. The lower plot shows the correlation between select VOCs and NO_x.

Table 6-1 NO_x/CO, NO_x/CO_2, and VOC/NO_x emission ratios for example highway and non-highway plumes.

Ratio	NO_x	O_x	Benzene	C8-aromatics	C9- aromatics	C10-aromatics	toluene
Highway							
CO	.276	.013	.0013	.0047	.0025	.0009	.0036
CO_2	.0020	9.1e-5	9.2e-6	2.3e-5	1.8e-5	6.3e-6	2.6e-5
NO_x	1	.046	.0047	.012	.009	.003	.013
Non-Highway							
CO	.032	.012	1.5e-4	4.0e-4	3.6e-4	1.6e-4	4.4e-4
CO_2	.0004	3.9e-4	1.9e-6	4.9e-6	4.3e-6	2.0e-6	5.4e-6
NO_x	1	.37	.005	.012	.011	.005	.014

7. Cooking emissions

Cooking emissions of VOCs and aerosol are poorly understood. In our previous work, we have not been able to distinguish cooking from VCP emissions due to an incomplete understanding of the molecular markers that are characteristic of cooking emissions [*Coggon et al.*, 2021; *Gkatzelis et al.*, 2021b]. By leveraging new sampling techniques, we are able to investigate the importance of cooking emissions on Las Vegas air quality. The following sections describe the work to quantify cooking VOCs.

7.1. Introduction to cooking emissions

Cooking influenced organic aerosol (CIOA) has been well studied, but relatively little has been done to measure and quantify cooking VOCs in ambient air. Since 2010, there have been > 40 studies focused on quantifying CIOA in ambient data sets and identifying CIOA tracers from aerosol mass spectrometers and aerosol filter samples. For example, Hayes et al. [2015] showed via PMF that CIOA makes up a large fraction of organic aerosol measured in Los Angeles, especially in the evening (Figure 7-1).

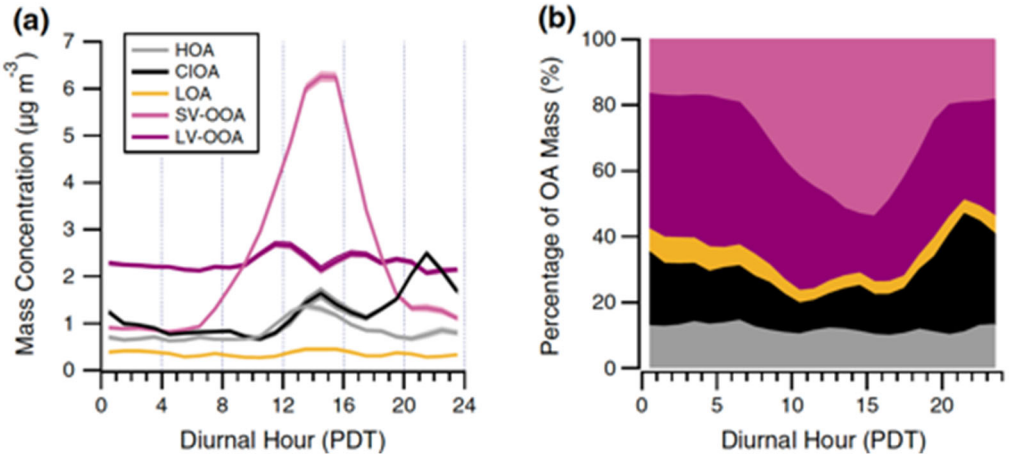

Figure 7-1. From Hayes et al. [2015]: Diurnal profiles of the composition of organic aerosol (OA) in Pasadena measured during CALNEX2010. CIOA = Cooking-influenced OA.

There have been ~ 10 studies on cooking VOCs; all studies were laboratory based and focused on quantifying cooking emissions factors and their impact on indoor air quality. One key study from Schauer et al. [1999b] quantified C1 through C29 organic VOCs from meat charbroiling, which was the first study that showed high emission rate of C1 – C11 aldehydes. Smaller aldehydes are common and abundant in the atmosphere, but larger aldehydes (C7 – C9) are emitted from cooking at high rates but are not significantly prevalent in VCP or mobile source emissions. Recently, Klein et al. [2016] showed the prevalence of aldehydes from

cooking. They performed an exhaustive series of laboratory experiments following recipes for frying and cooking vegetables and meat and found that saturated aldehydes are the dominant emissions observed by PTR-ToF-MS (Figure 7-2). They reported that emission factors from using oils and fatty meats are among the highest for cooking processes and that nonanal and octantal are key species emitted from oils and fatty foods.

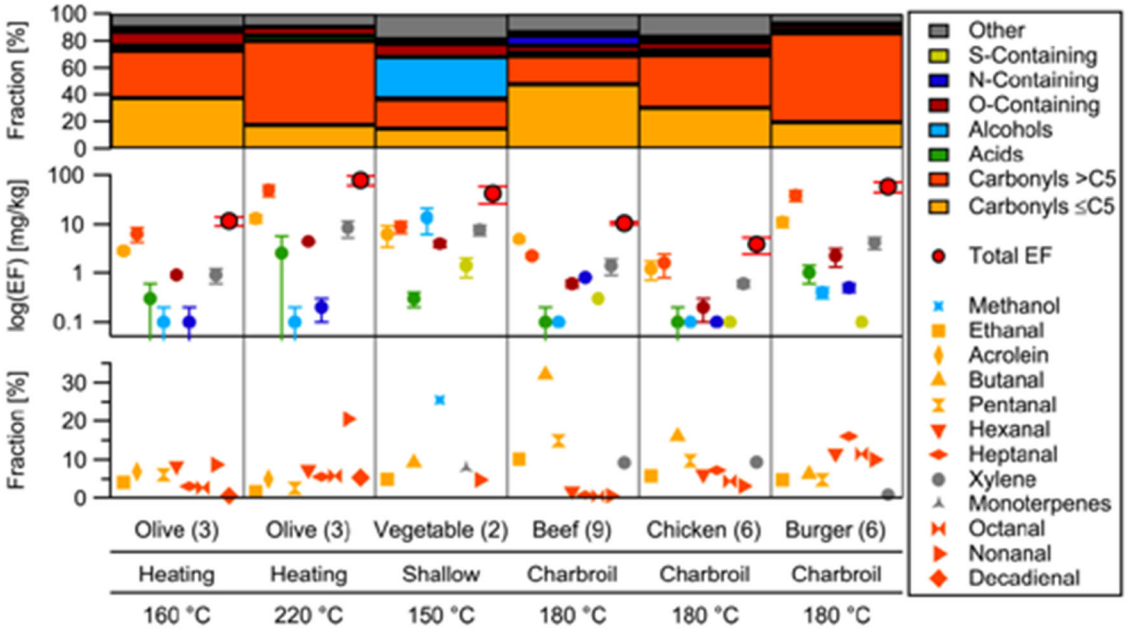

Figure 7-2. From Klein et al. [2016]: laboratory experiment of frying and cooking vegetables and meat showing the importance of nonanal and octanal emissions.

7.2. Identification of nonanal and octanal in Las Vegas with GC-PTR-ToF-MS

Long-chain aldehydes have not been regularly reported in ambient datasets. PTR-ToF-MS is sensitive to both aldehydes and ketones, and therefore it is possible that structural isomers, such as nonanal and nonanone, could be simultaneously detected by our instrumentation. To determine whether signals are aldehydes, ketones, or a mixture of isomers, we have used a gas-chromatographic pre-separation method (GC-PTR-ToF-MS) to separate structural isomers prior to detection by PTR-ToF-MS [*Stockwell et al.*, 2021]. The schematic is shown in Figure 7-3.

Figure 7-3. Pre-separation allows for identification of interferences and fragmentation patterns.

This setup was used regularly at the Jerome Mack ground site and was also deployed on the mobile laboratory during an evening drive to the Las Vegas Strip to collect samples close to several restaurants. The chromatograms from the Strip sample are compared to post-mission laboratory measurements of octanal, octanone (both $C_8H_{16}O$), nonanal, and nonanone (both $C_9H_{18}O$) in Figure 7-4. The fragmentation patterns and retention times show that the ambient signals detected at $C_8H_{16}O$ and $C_9H_{18}O$ primarily result from octanal and nonanal. Octanal is detected at masses 129, 111, and 69, while nonanal is detected at masses 143, 125, and 69. In contrast, octanone and nonanone are only detected at masses 129 and 143, respectively. The ambient chromatograms most resemble those of the aldehydes, confirming that these molecules are the dominant isomers detected by PTR-ToF-MS. Furthermore, the fragmentation pattern of mass 143 (nonanal or nonanone) versus its dehydration product in PTR-ToF-MS shows that no significant influence of nonanone was observed during any of the drives (Figure 7-5). These results confirm that nonanal and octanal, along with other long-chain aldehydes, are useful tracers for evaluating the impact of cooking emissions on urban air.

In addition, in the GC-PTR-ToF-MS sample on the Las Vegas Strip a whole suite of aldehydes was detected, which provides more evidence for a large aldehydes source related to cooking.

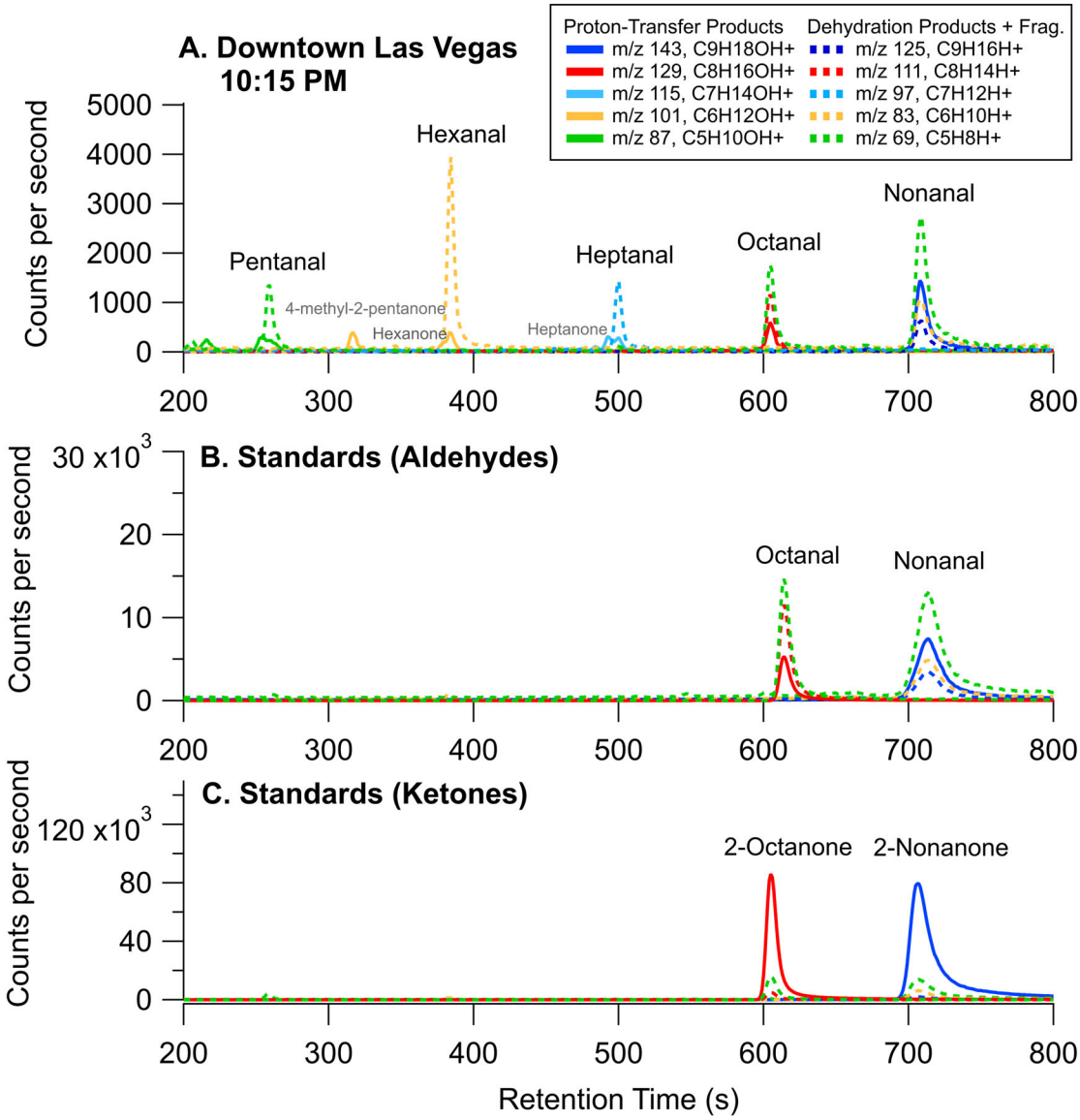

Figure 7-4. (A) Ambient sample on the Las Vegas Strip showing a suite of aldehydes. (B) GC-PTR-ToF of pure standards showing the retention times and the fragmentation pattern of octanal, octanone, nonanal, and nonanone. (C) A GC-PTR-ToF-MS sample taken on the Las Vegas Strip next to restaurants shows two peaks that correspond to octanal and nonanal.

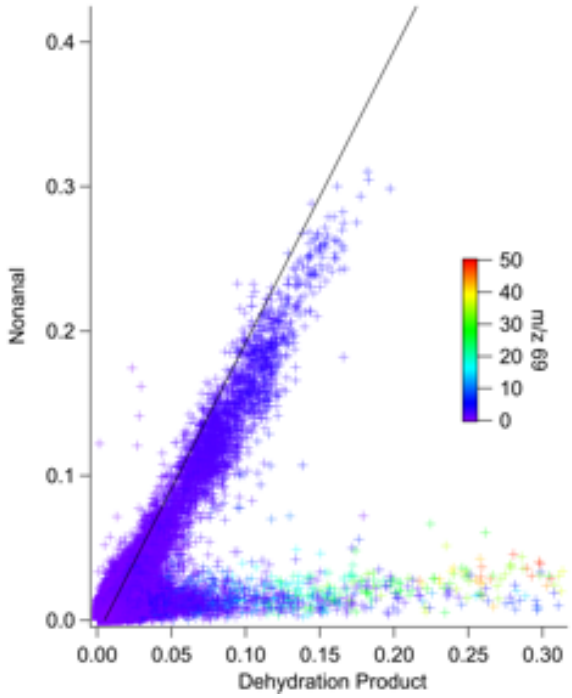

Figure 7-5. Fragmentation pattern for all the data measured on all drives is consistent with nonanal and not nonanone.

In summary, the laboratory measurements from Klein et al. [2016] and Schauer et al. [1999] together with the GC-PTR-ToF-MS measurements close to restaurants on the Las Vegas Strip indicate that octanal and nonanal are unique tracers for cooking emissions in urban areas.

7.3. Spatial distribution of restaurant density and nonanal

The mixing ratios for the nighttime drive on 2021/06/28 are shown in Figure 7-6, where the period driving on the Las Vegas Boulevard is indicated by the grey background. Traffic emissions, indicated by benzene, are significant throughout the region and the signals are highest during the day and along major roads, as expected. The pattern for personal care products, indicated by D5-siloxane, is different and the highest signals were on the Las Vegas Strip and mostly at night when population density is very high. Sustained mixing ratios of 500 ppt of D5 were observed during nighttime sampling and exceeded ppb levels at times. Our other VCP tracers were also high; very clear enhancements of anthropogenic monoterpenes from fragrances (> 1 ppb) and sustained ethanol mixing ratios (> 500 ppb) were observed on the strip at night. In addition to the VCP and traffic emissions, high mixing ratios of nonanal were observed, which indicates significant emissions from cooking.

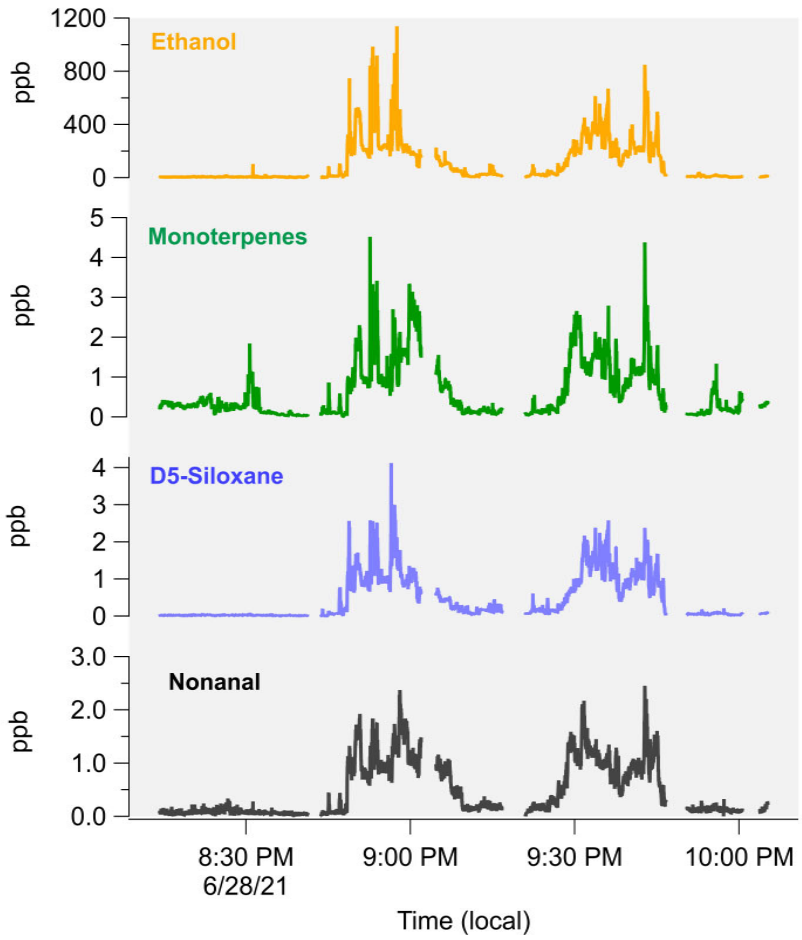

Figure 7-6. Nighttime mixing ratios from the drive on 2021/06/28 to the Las Vegas Strip.

The diurnal pattern of nonanal measured at the Jerome Mack site (Figure 7-7) shows the highest concentrations at night, which shows that nonanal is a primary species with no significant secondary photochemical sources. The high variability at noon and several peaks in the evening suggest cooking activity influencing the Jerome Mack site. The observed increase at night is likely the result of emissions into the shallow nighttime mixing layer, but may also reflect build-up of emissions from evening cooking. This is supported by the drives, where we saw that the emissions are highest on the Strip at night relative to the surrounding area.

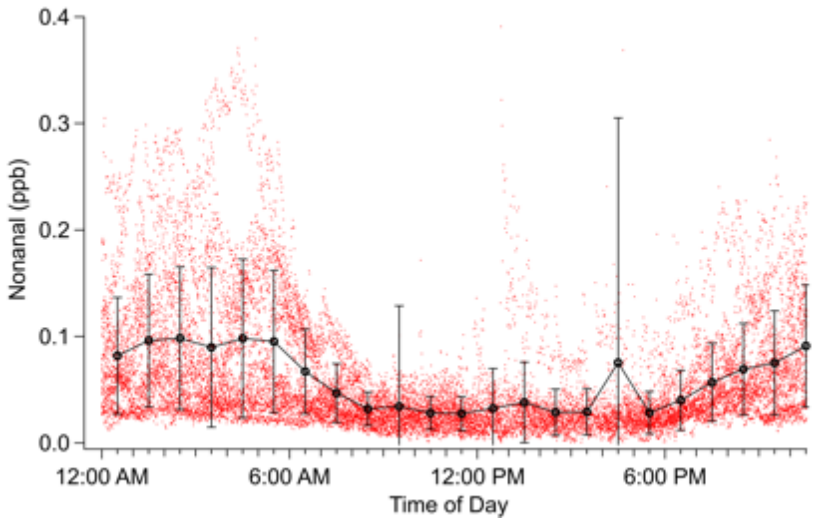

Figure 7-7. Diurnal profile of nonanal at the Jerome Mack site.

Restaurant inspection data are available online at a Las Vegas open data website (https://opendataportal-lasvegas.opendata.arcgis.com/datasets/restaurant-inspections-open-data/explore). The information includes the name, location, type (restaurant, snack bar, bar, tavern, etc.), the current inspection grade, and date of last inspection. The restaurant data are shown in Figure 7-8 as individual locations and binned on a 0.5km grid indicating the restaurant density in a given area.

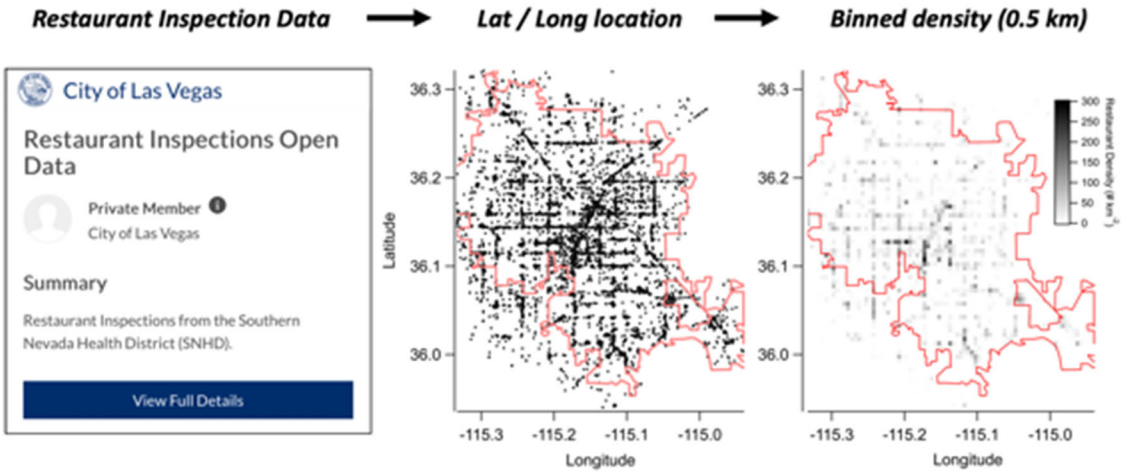

Figure 7-8. The restaurant data as individual locations and binned on a 0.5 km grid.

The spatial distribution of the restaurant density is shown together with nonanal in Figure 7-9. The drive tracks have good coverage across the Las Vegas valley and sampled regions with a range of restaurant density. The coincidence of higher mixing ratios of nonanal in regions with greater restaurant density further supports the identification of this molecule as a cooking tracer. The restaurant density has some correlation with population density (more

restaurants, more people), which means that the spatial distribution of cooking emissions is likely similar to VCPs. Consequently, a full determination of cooking emission impacts must be done using source apportionment techniques in order to separate observations of cooking from those of VCPs.

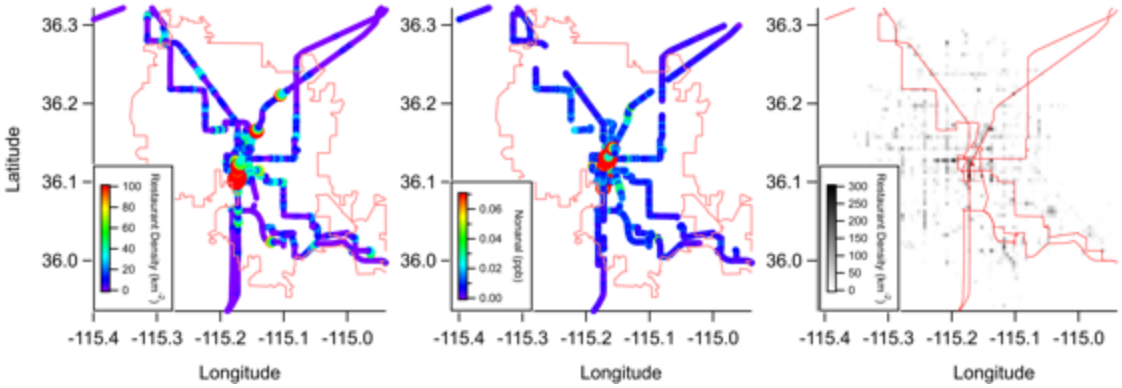

Figure 7-9. The drive tracks in Las Vegas color coded by the restaurant density and nonanal.

The time series of nonanal and the restaurant density for three drives are shown in Figure 7-10. Similar to Figure 7-9, this plot shows how nonanal mixing ratios respond in regions with higher restaurant density. No clear difference in the correlation between daytime and nighttime was observed, but the urban enhancement seems higher during the evening drive, which is consistent with the likelihood of higher emissions at night owing to more cooking (e.g., Figure 7-10).

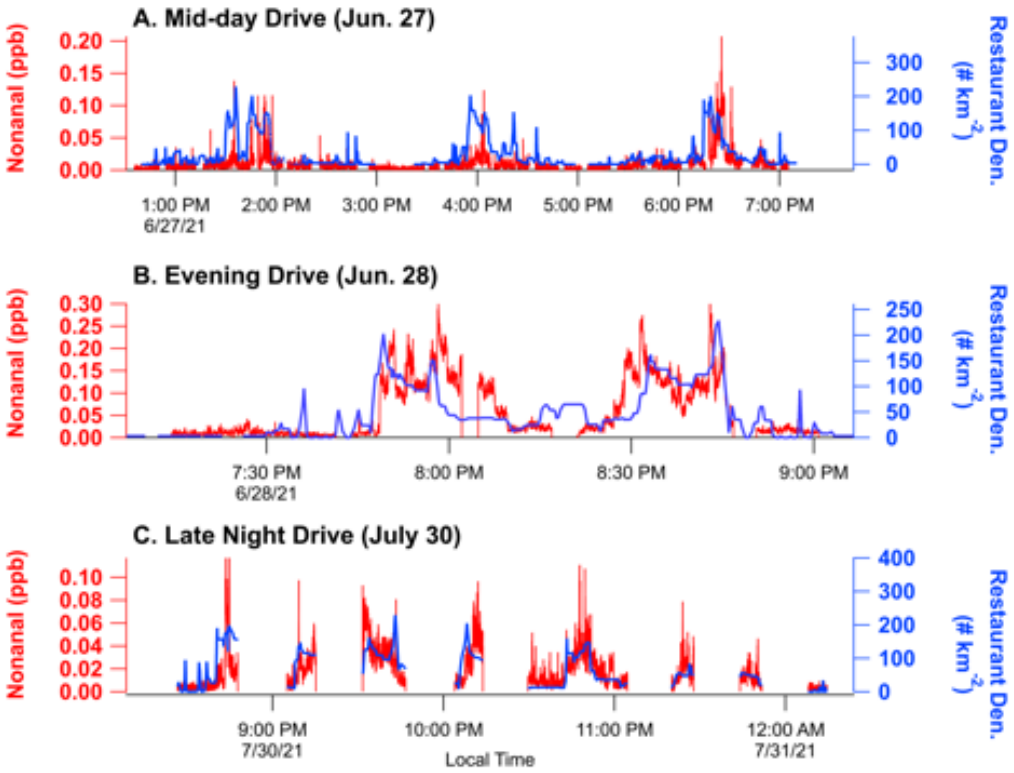

Figure 7-10. Comparison of the daytime and nighttime mixing ratios from the drive on 2021/06/28 around the Las Vegas Strip area.

In summary, clear evidence of cooking emissions was observed in Las Vegas ambient measurements, where mixing ratios were the highest in the area of the highest restaurant density. The identification of long-chain aldehydes as cooking markers can be used in source apportionment to determine the contribution of cooking emissions to total anthropogenic VOCs observed in Las Vegas.

8. VOC Source Apportionment

8.1. Background information

Elevated urban VOC mixing ratios result from the emissions of anthropogenic and biogenic sources. Biogenic emissions are dominated by reactive hydrocarbons such as isoprene, monoterpene isomers, and small oxygenates [Guenther et al., 2012], whereas anthropogenic emissions impact a large suite of chemical species, including aromatics, alkanes, oxygenates, and nitrogen-containing molecules. The total emissions of anthropogenic VOCs have implications on ozone and secondary aerosol formation, and determining the sources of these emissions is important for evaluating strategies that might reduce the burden of anthropogenic VOCs.

Positive Matrix Factorization (PMF) is a powerful tool for conducting VOC source apportionment. PMF is commonly used by the aerosol community to identify the key contributors to organic aerosol formation [e.g., Zhang et al., 2019], and it was recently used by our group to identify sources of VOC mixing ratios in urban areas [*Gkatzelis et al.*, 2021b]. As illustrated in Figure 8-1, PMF is a statistical tool that deconvolves an input matrix of data (X) into the linear combination of a user-defined number of source contributions (p), described by a factor time series (matrix G) and factor profile (matrix F). The factor profile is interpreted to represent a source "fingerprint", while the factor time series reflects the total signal attributed to that profile. PMF may be conducted without any knowledge about source profiles (termed "unconstrained" PMF), or may be guided with input of VOC factor profiles that determine the fingerprint of one or more sources (termed "constrained" PMF). The number of factors employed to solve the matrix is determined by the user and relies on statistical assessment of model residuals, comparison to chemical tracers, and expert judgement.

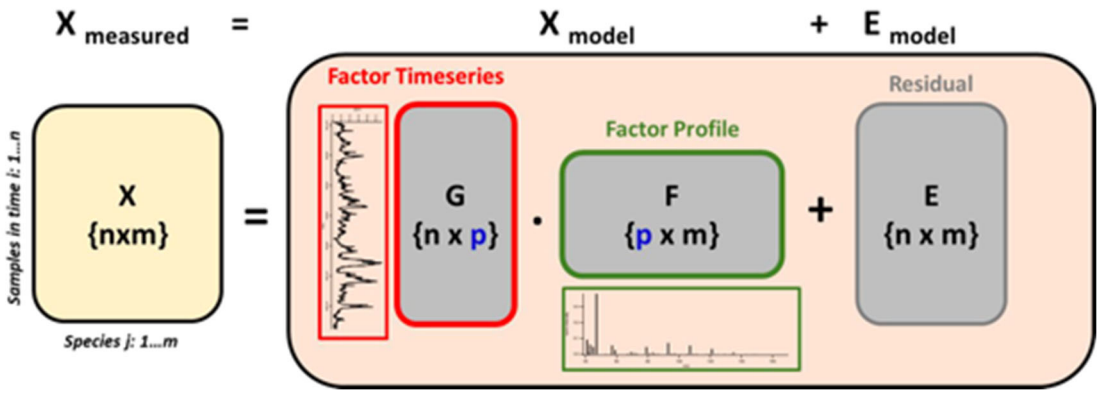

Figure 8-1. Schematic demonstrating the relationship between PMF input (X) and resulting factor time series (G) and factor profiles (F). Figure reproduced from *Gkatzelis et al.* [2021b].

In New York City, we determined that VOC mixing ratios measured by our proton-transfer-reaction mass spectrometer (PTR-ToF-MS) at a ground site in Manhattan could be explained by a combination of four factors: (1) emissions from mobile sources, (2) emissions from volatile chemical products (VCPs), (3) VOCs emitted or produced by chemical oxidation during daytime hours, and (4) a morning factor that represented emissions and chemical oxidation of monoterpenes (Figure 8-2). Mobile sources were constrained based on an observationally-derived factor profile, while all other factors were resolved by the PMF algorithm and assigned to a given sources based on the abundance of VOC tracer molecules. For example, the VCP factor was observed to contain D5-siloxane, methyl ethyl ketone (MEK), parachlorobenzotriflouride (PCBTF), and monoterpenes, which are known to be prominent ingredients of consumer and industrial products. The daytime factor contained isoprene, acetone, methyl vinyl ketone, and methacrolein, which are molecules known to be emitted or formed by chemical oxidation during daytime hours. The morning factor reflected a buildup of VOCs during morning hours, which is often observed for biogenic species (e.g., monoterpenes) in urban regions.

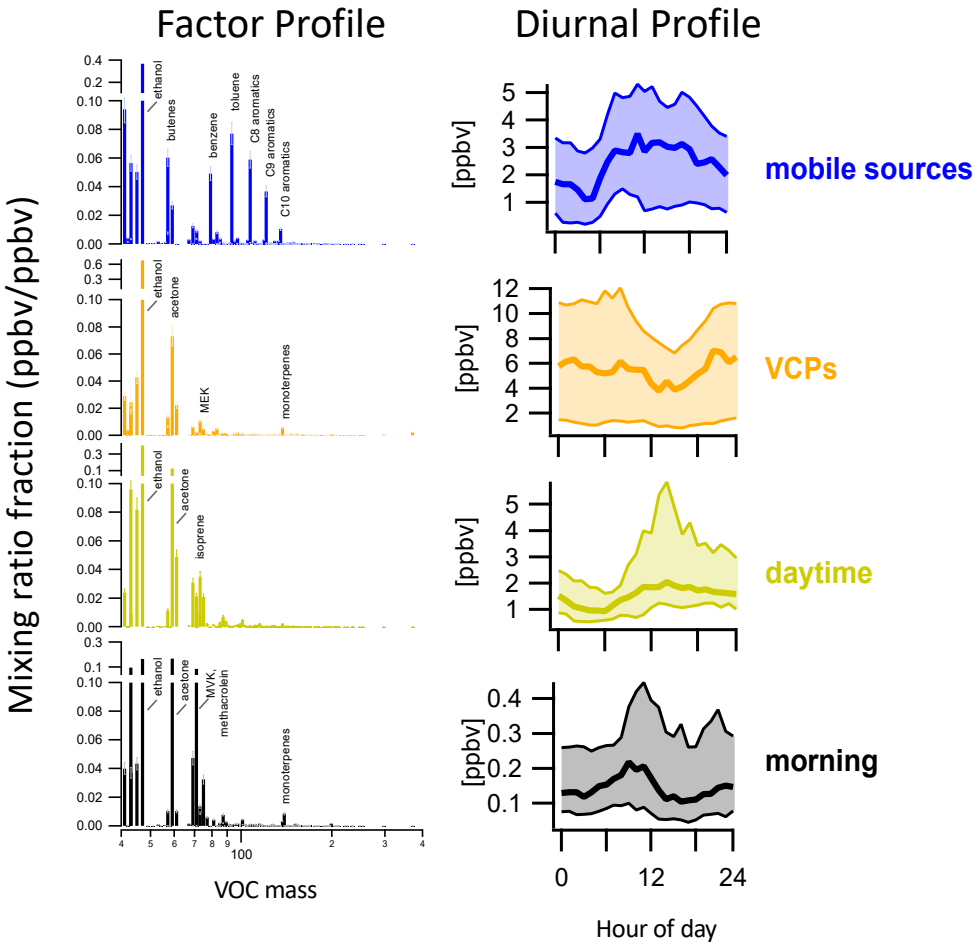

Figure 8-2. PMF results from New York City showing contribution of mobile sources, volatile chemical products, and secondary VOCs to ground site measurements conducted in Manhattan [*Gkatzelis et al.*, 2021b].

8.2. PMF Setup in Las Vegas

In this report, we present a PMF analysis on PTR-ToF-MS data measured at the Jerome Mack ground site, with a focus on apportioning anthropogenic VOCs. We supplement this analysis with a PMF analysis on PTR-ToF-MS data measured by mobile laboratory around the Las Vegas Strip area. A key goal of this PMF analysis is to determine the contribution of VOCs emitted from mobile sources, VCPs, and other non-fossil fuel sources such as cooking.

PMF applied to the Ground Site and Mobile Laboratory Data

PMF was conducted on two periods during ground-site sampling (7/1 – 7/9/2021 and 7/19 – 7/27/2021) using the Source Finder (SoFi) software package in Igor Pro [Canonaco et al., 2013]. SoFi utilizes the Multilinear Engine (ME-2) to perform source apportionment following the algorithms described by Paatero [1999]. Traditional PMF analysis requires a user input of a signal matrix, which consists of the time series for each species considered for source apportionment, and an error matrix which represents the uncertainty of each measurement. For this analysis, we supply a signal matrix that represents the 10 min average mixing ratios of 270 ions measured by PTR-ToF-MS. The error matrix reflects the uncertainty of each measurement and is calculated as 2 times the standard deviation in background mixing ratios.

PMF solutions were determined for 1-10 factors. Increasing the number of factors improves the model characterization of the measurements, but can result in solutions that are non-physical. It is typical to report a solution where the number of factors minimize model residuals, and each factor can be justified by chemical tracers or known chemical processes. In this report, we present solutions that comprise factors representative of (1) mobile sources, (2) VCPs, (3) cooking emissions, and (4) regional chemical oxidation.

A key function of ME-2 is that it allows a user to input a factor profile that describes the relative distribution of VOCs associated with a given source. The extent to which this constraint is enforced is dictated by a scalar termed the “a-value”, which represents the fraction by which the profile is allowed to vary beyond its constraint, as demonstrated by Equation 1.

$$g_{i,solution} = g_i + a \cdot g_i \quad \text{(Eq 1)}$$

Where $g_{i,solution}$ is the factor solution, g_i is the factor profile constraint, and a is the a-value. When the a-value = 0, $g_{i,solution}$ is fully constrained to g_i. Positive values allow the software to

solve for $g_{i,solution}$ within uncertainty bounds dictated by the term $a \cdot g_i$. In this analysis, we constrain PMF with a mobile source profile and vary the a-value from 0.1 – 0.75. For this report, we present a solution to the ground site data with a-value = 0.75. Details describing the mobile source constraint are provided in the following section.

We also conduct a PMF analysis on the mobile drive data conducted around the Las Vegas Strip. This region was identified previously as the location in the Las Vegas Valley with the highest mixing ratios of VOCs and CO, and likely reflects a hotspot of VOC emissions from mobile sources, consumer products, fragrances, and cooking. Figure 8-3 shows the region considered for this analysis. We supply the data matrices on a 10s average and constrain the mobile source profile with an a-value = 0.1. We exclude mixing ratios of ethanol in this analysis of the mobile lab data. Ethanol in excess of 200 ppb was observed on the Las Vegas Strip and PMF solutions that included ethanol in this area resulted in an abundant factor that was solely composed of ethanol, which indicates that the variability of this molecule could be explained by a factor other than mobile sources, VCPs, or cooking. We can only postulate the source of this factor, and therefore exclude it from our analysis.

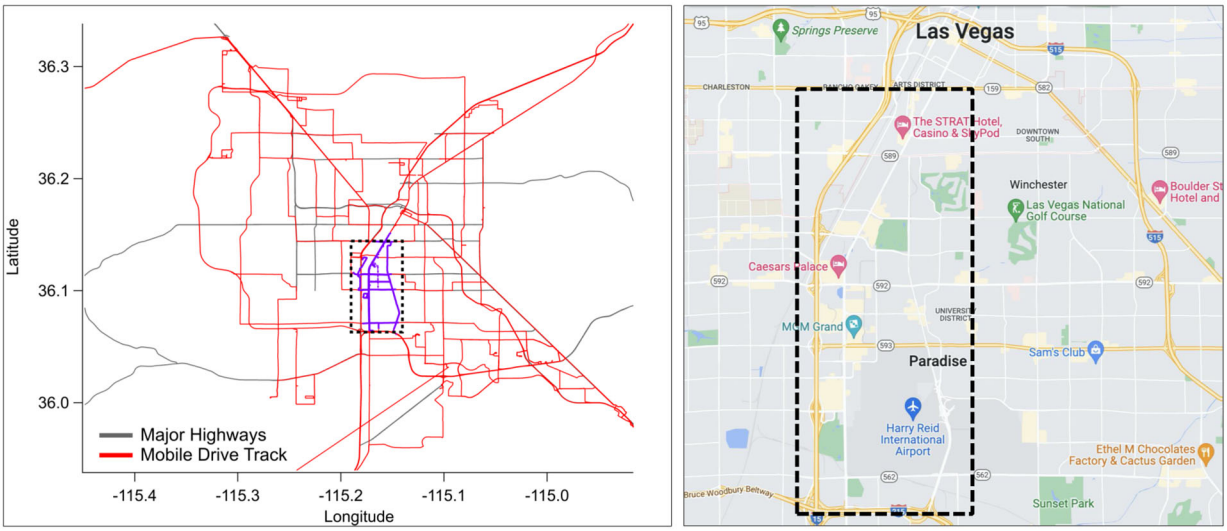

Figure 8-3. Map showing the location of mobile laboratory data analyzed by PMF. The region encompasses Las Vegas Boulevard from I-215 to Route 159, along with surrounding streets extending as far east as Harry Reid International Airport.

Mobile Source Constraint

Mobile sources and other uses of fossil fuels are traditionally considered a dominant source of VOCs in urban areas. However, years of regulation have resulted in major declines in fossil fuel VOC mixing ratios [*Bishop and Haugen*, 2018; *Warneke et al.*, 2012]. These declines present challenges for resolving mobile source contributions to urban VOCs, as even molecules previously assigned to mobile sources, such as aromatics and ethanol, can have significant contributions from solvent sources such as paints and coatings [*Gkatzelis et al.*,

2021a; *Gkatzelis et al.*, 2021b; *McDonald et al.*, 2018a]. For example, Figure 8-4 shows the time series of benzene, toluene, and the sum of C8-aromatics measured at the Jerome Mack ground site. Benzene is often attributed to fossil fuels since it is banned from consumer products, while toluene and C8-aromatics can result from both mobile sources and emissions from solvent-borne products [*McDonald et al.*, 2018a]. At the Jerome Mack ground site, there are periods when aromatics correlate well (likely mobile source emissions), and there are periods when toluene and C8-aromatics are significantly higher than benzene (likely due to a solvent source). *Gkatzelis et al.* [2021b] made similar observations in NYC, and it was found that an unconstrained PMF analysis resulted in a source apportionment that mixed the contributions from VCPs and mobile sources.

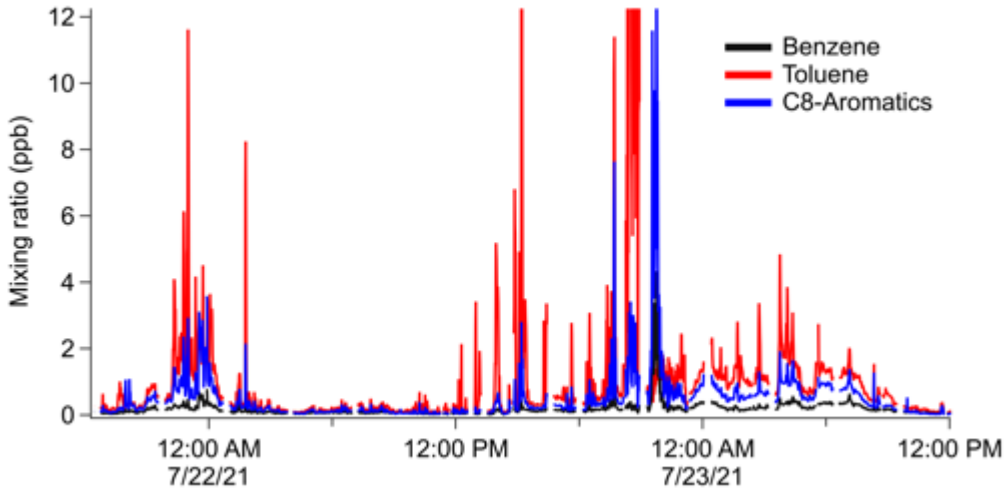

Figure 8-4. Time series of aromatic species measured at the Jerome Mack ground site.

To help separate mobile sources from VCPs, *Gkatzelis et al.* [2021b] constrained PMF with a mobile source profile that was representative of the fossil fuel emissions in the NYC area. This profile was determined using on-road VOC measurements measured by the mobile laboratory, which can be used to identify and separate VOC plumes resulting from tailpipe emissions from other plumes resulting from sources such as VCPs, cooking, etc. We follow the methods by *Gkatzelis et al.* [2021b] , and determine a mobile source profile for Las Vegas using the mobile laboratory data collected throughout the Las Vegas Valley. Figure 8-5 illustrates our methods. Briefly, we identify periods when on-road mixing ratios of aromatic species, such as benzene, toluene, and C8-aromatics, are enhanced above background mixing ratios by at least a factor of five (stringency criteria). We screen these plumes to exclude periods when VCP tracers are enhanced (e.g., monoterpenes, D5-siloxane). These on-road plumes must also be enriched in CO and NOx, which further differentiates mobile source enhancements of aromatics from solvent-borne emissions. We subtract out the local VOC background just outside of the plume to correct for VOCs with large regional mixing ratios (e.g., acetone, ethanol, etc.), then normalize plume-enhanced VOC mixing ratios by the total VOCs measured by PTR-ToF-MS. The mobile source profile is calculated as the average of

these normalized plume profiles. In total, 100 plumes were identified and included in this analysis.

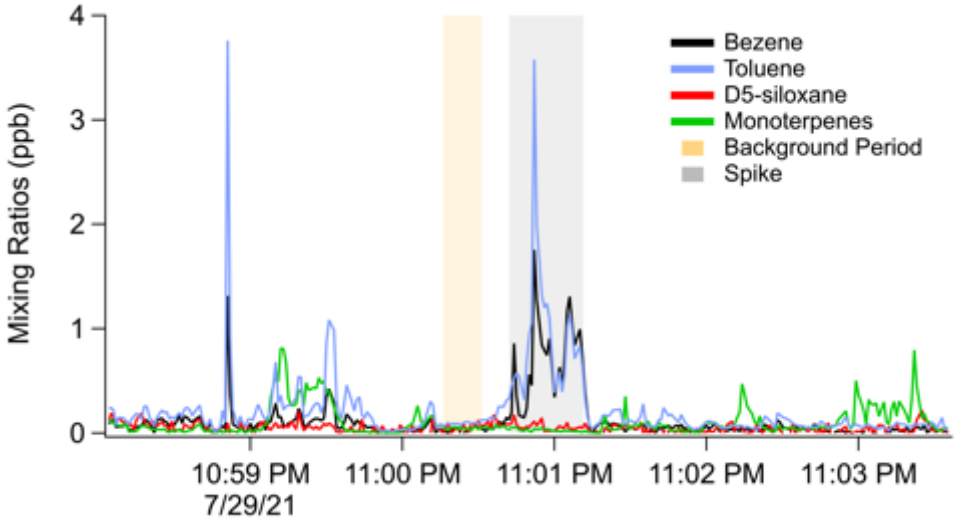

Figure 8-5. Mobile laboratory data showing the methods for screening for on-road mobile source emissions. Plumes are identified based on enhancements of aromatics and combustion tracers (not shown), and screened to exclude periods when VCP tracers, such as monoterpenes and D5-siloxane, are enhanced.

The resulting VOC profile is shown in Figure 8-6. The derived profile is very similar to the mobile fingerprint determined by *Gkatzelis et al.* [2021b]. The profile demonstrates that ethanol is the dominant VOC from mobile sources measured by PTR-ToF-MS, followed by aromatics. Ethanol is also an important contributor to VCP emissions and therefore it is important to constrain ethanol for quantitatively apportioning VCP and mobile source emissions.

A series of sensitivity analyses were conducted to assess how the derived mobile source profile changes under different stringency criteria. Panels A, B, C, and D show sensitivity analyses when benzene is enhanced over background (BG) by varying amounts. Benzene enhancements above 2 ppb are considered "high emitters" and represent the upper 30% of all plumes identified in this analysis. Plumes averaged within the upper 74% of all emitters exhibit a similar mobile source profile as those averaged within the upper 94%. High emitters exhibit a significantly larger fraction of ethanol, but relatively similar proportion of aromatics. These results demonstrate that the fraction of ethanol in mobile source emission is likely between 0.5 – 0.6 ppb/ppb.

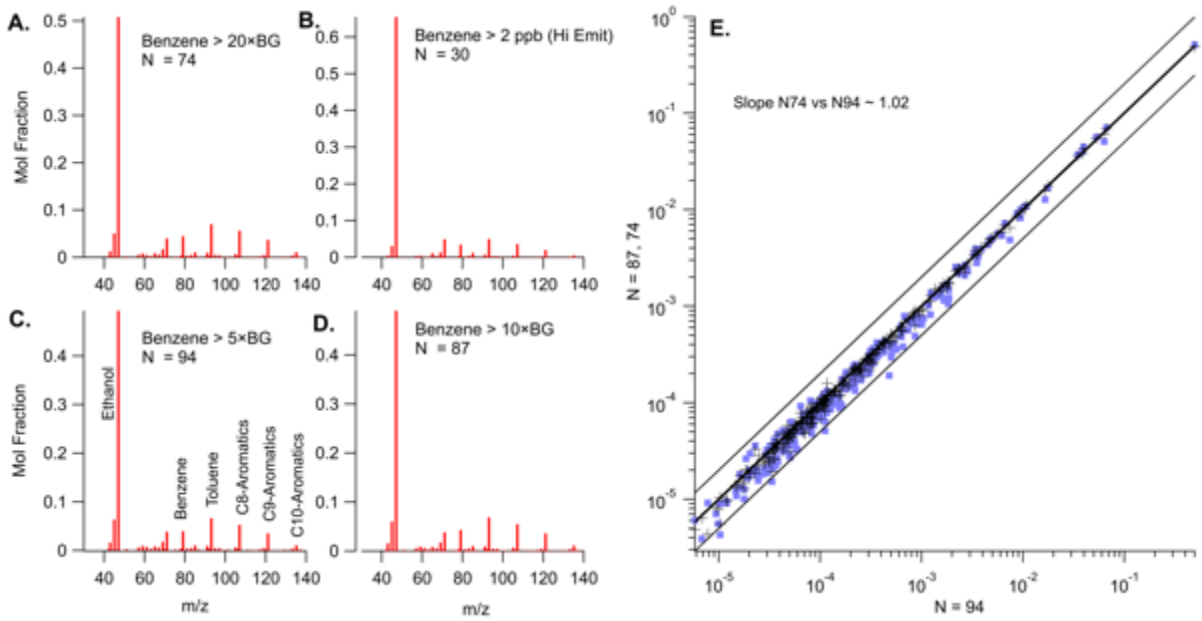

Figure 8-6. The derived mobile source profile based on mobile laboratory data screening processes shown in Figure 10. Panels A-D shows the derived profile under different stringency criteria, and panel E shows that screening the data to include the upper 74% of all plumes changes the derived mobile source profile by ~2 %.

8.3. PMF Results – Jerome Mack

Figures 8-7 and 8-8 show the PMF solution for the ground site data. Here, we present a 5-factor solution that includes ethanol. VOCs apportioned to primary emissions from (1) mobile sources, (2) VCPs, (3) cooking, (4) a local solvent source and (5) secondary oxidation processes. The **mobile source factor** is apportioned based on the constraints described earlier and is largely composed of ethanol and C6-C10 aromatics. The **VCP factor** is primarily composed of ethanol (EOH), but also contains D5-siloxane, monoterpenes, and acetone, which are common ingredients in consumer products. Both factors resemble the solution presented by *Gkatzelis et al.* [2021b]. The VCP factor had two differences from the NYC measurements. First, the VCP factor contained a series of other VCP markers, including PCBTF and D4-siloxane. These molecules are largely associated with construction activity due to industrial coatings and adhesives [*Gkatzelis et al.*, 2021a; *Stockwell et al.*, 2021]. At the Jerome Mack ground site, PCBTF variability was largely attributed to the local solvent factor, which appeared to come from a point source near the ground site measurements. The exact source of this solvent factor is still unknown. Second, the VCP factor reported by *Gkatzelis et al.* [2021b] also contained methyl ethyl ketone (MEK), which is a prominent solvent in consumer and industrial VCPs. MEK was excluded from this analysis due to interferences imposed by our instrumental setup.

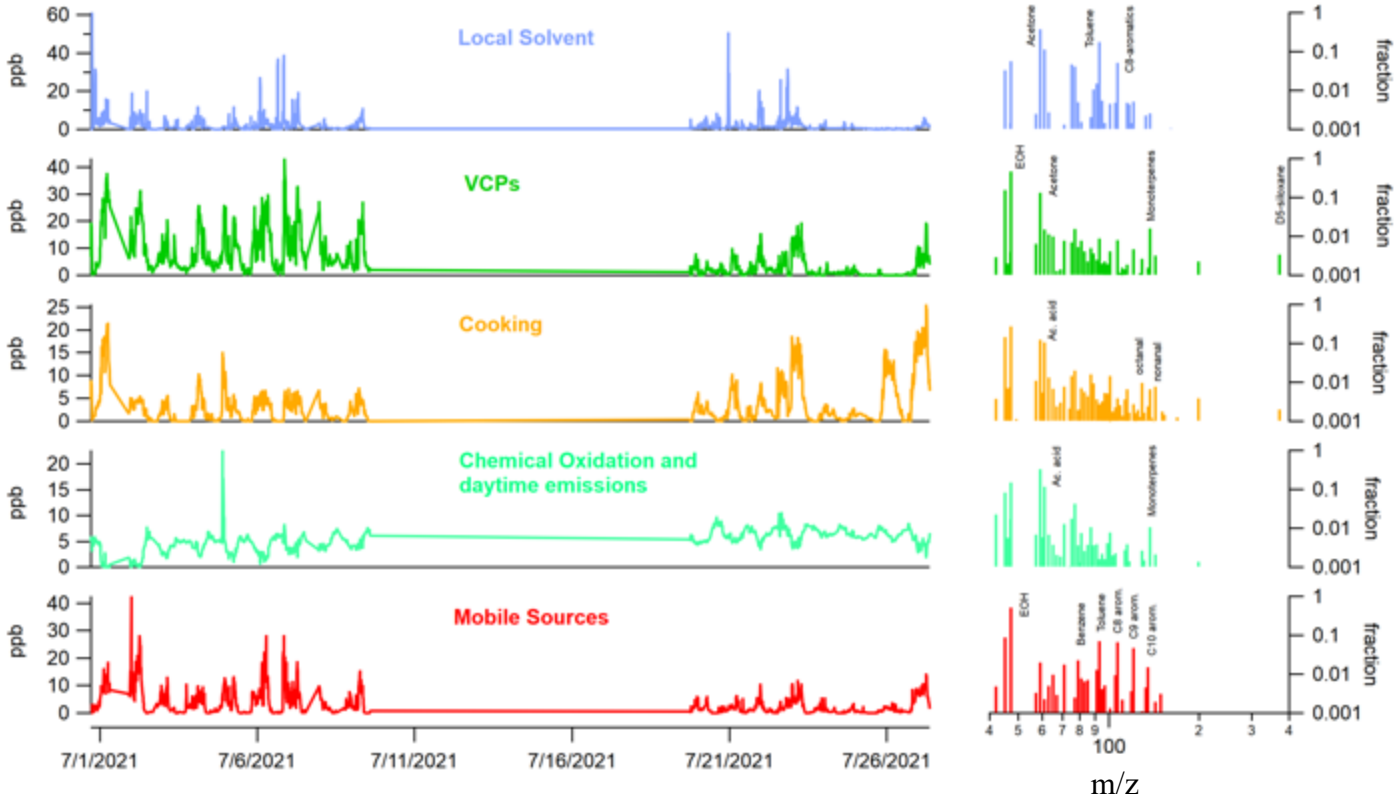

Figure 8-7. PMF results for the Jerome Mack ground site. To the right are mass spectra showing the distribution of VOCs represented by each factor time series (left). Key VOCs are highlighted, which indicate various tracers.

A key difference from *Gkatzelis et al.* [2021b] is that PMF analysis on Jerome Mack has led to the resolution of a distinct cooking emission factor, which has not been readily reported in previous datasets. Cooking VOC emissions in urban regions have been understudied, but as demonstrated previously, we have observed that long-chain aldehydes, such as nonanal and octanal, are well-correlated with the restaurant density in the Las Vegas region. Nonanal and octanal are primarily resolved alongside other aldehydes, including acrolein and other unsaturated aldehydes such as decenal and undecanal. The general grouping of these aldehydes agrees with the expected emissions from meat cooking and oil evaporation [*Klein et al.*, 2016; *Schauer et al.*, 1999a] as shown in Figure 8-8.

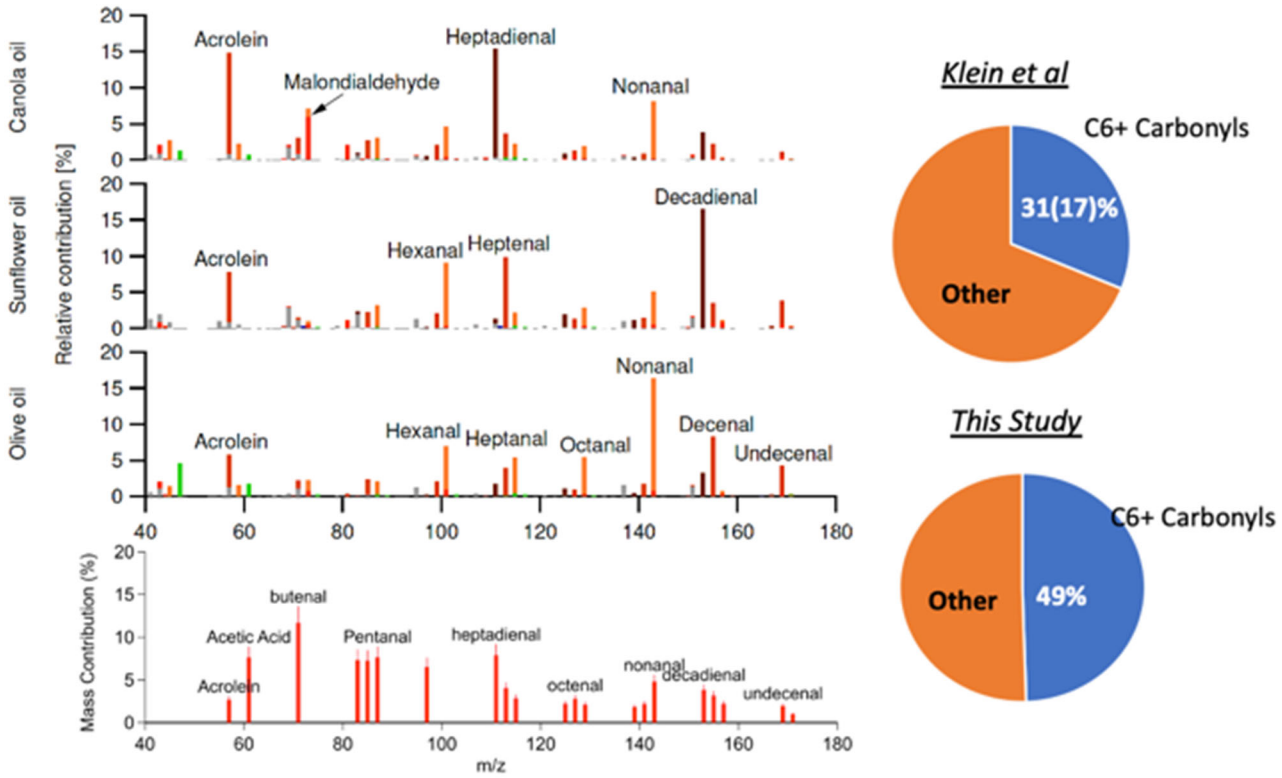

Figure 8-8. Comparison of the cooking fingerprint from this work to the laboratory work from Klein et al [2016].

Gkatzelis et al. [2021b] also derived a chemical oxidation / daytime emission factor, which results from the OH oxidation of VOC precursors. The key species observed in this factor generally agree with the secondary VOCs observed in Las Vegas, and mainly correspond to multiply oxygenated carbon-containing molecules.

Figure 8-9 shows the 24-hr diurnal pattern of each factor. The black circles show the hourly averages, while the dots show the PMF solution at each data point. Atmospheric chemistry drives the diurnal pattern in the chemical oxidation factor (panel C), and this factor dominates the observed VOC mixing ratios during daytime hours. These results are consistent with observations by *Gkatzelis et al.* [2021b], and demonstrate that atmospheric chemistry plays an important role in controlling the mixing ratios during the day in the Las Vegas region. For all of the primary emission sources (mobile source, VCP, cooking, and solvent), mixing ratios are highest at night when boundary layer heights are low. The mobile source factor exhibits a peak in the morning and evening that likely correspond to rush hours emissions. Both the VCP and cooking factor exhibit highest mixing ratios in the evening, but the cooking factor shows variability during midday hours that likely correspond to lunchtime emissions. The solvent factor exhibits significant variability (Figure 8-7), which is also reflected in the diurnal pattern. This behavior is consistent with a local source, and is unlikely to reflect an emission source that impacts the entire Las Vegas Valley.

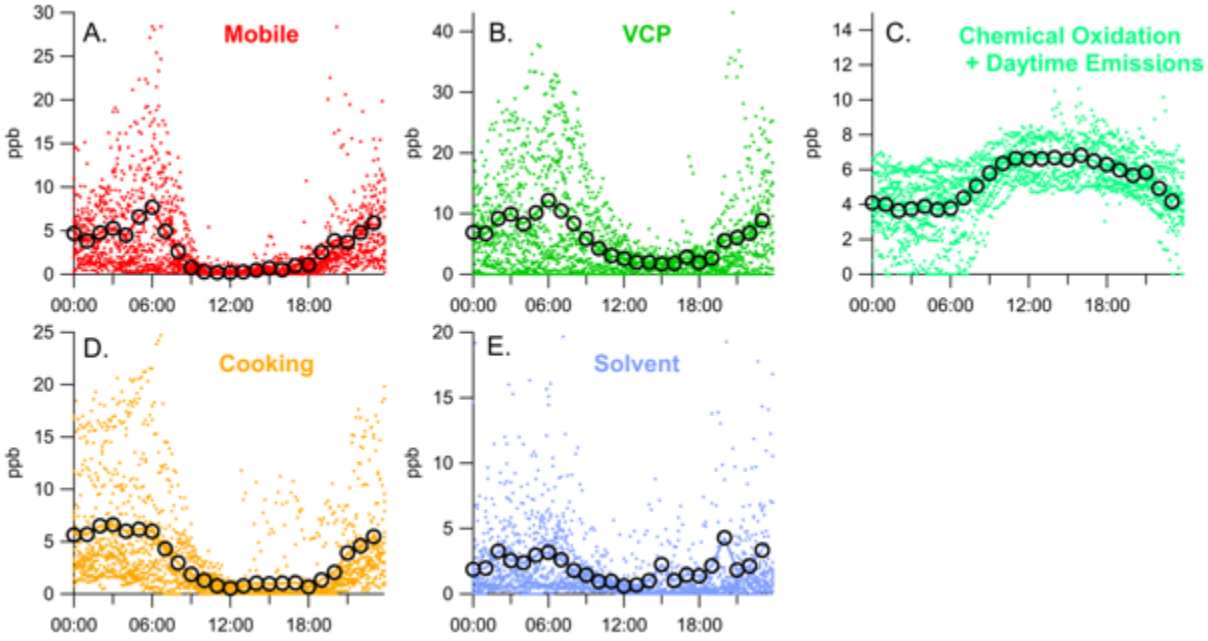

Figure 8-9. (A-E) 24 hourly average patterns for the 5 factors resolved by PMF of PTR-ToF data.

The results shown in Figure 8-9 show PMF for molecules detected by PTR-ToF-MS. There are a number of other molecules that are not measured by PTR-ToF-MS, including alkanes, alkenes, and hydroflourocarbons. *Gkatzelis et al.* [2021b] found that ~53% of the mass associated with mobile source emissions and ~50% of the mass associated with VCPs results from emissions that cannot be resolved by PTR-ToF-MS. To account for these missing VOCs, we calculate the mass measured by PTR-ToF-MS in Figure 8-9 and adjust the VCP and mobile source profiles to account for this unresolved fraction associated with alkanes, alkenes, and hydroflourocarbons. We do not adjust the cooking, solvent, or oxidation factor, as we expect that the mass detected by PTR-ToF-MS represents the majority of these emissions.

Figure 8-10 shows the resulting diurnal profile of mass emissions by factor. Each factor contributes to the total anthropogenic emissions at different times of day depending on the emission patterns. Figure 8-10 shows the fraction that each factor contributes to total anthropogenic emissions (= VCP + mobile source + cooking). Overall, VCP emissions play an important role in the total VOC emissions in Las Vegas. On a mass basis, PMF suggests that VCPs constitute 40 – 80% of the VOCs. These mixing ratios are largely driven by the high emissions of solvents, such as ethanol and acetone, which is consistent with observations by *Gkatzelis et al.* [2021b]. VCP emissions exhibit the highest relative abundances in the morning hours (8:00 -11:00 AM), then decrease in relative abundance throughout the day. This behavior is consistent with the diurnal pattern of personal care product emissions observed in cities such as Boulder, CO where the emissions of D5-siloxane from deodorants and hair products peaked during morning hours [*Coggon et al.*, 2018].

Cooking emissions play an important role in the VOC mixing ratios observed by PTR-ToF-MS. Over the entire course of the day, the cooking factor represents 10-20% of the total observed VOC mixing ratios. The relative fraction of cooking emissions peak during lunchtime hours, as well as in the evenings when cooking is expected to be highest. Similar behavior has been observed in the relative abundance of primary cooking organic aerosol in cities such as Los Angeles [Hayes et al., 2013].

During evening and rush hour periods, mobile sources constitute ~ 30-40% of the total primary VOC mixing ratios, but then decrease during midday due to both a large enhancement of VCPs, but also lower emissions from mobile sources. This analysis is consistent with previous observations in cities such as New York City, Los Angles, and Boulder, CO and demonstrates the declining importance of mobile source emissions on total urban anthropogenic VOC emissions [*Bishop and Haugen*, 2018; *Coggon et al.*, 2018; *Gkatzelis et al.*, 2021a; *Gkatzelis et al.*, 2021b; *McDonald et al.*, 2018a; *McDonald et al.*, 2013; *Warneke et al.*, 2012].

The daily average mass fraction of VCPs, mobile sources, and cooking are shown in the pie chart in Figure 8-10. We find that VCPs account for the majority of the primary emissions (57%). Cooking emissions are an important contributor to the total VOC mass (16%), while mobile sources make up the remaining 27%. These results are consistent with the observations by *Gkatzelis et al.* [2021b] that VCPs are a dominant source of primary carbon in urban atmospheres.

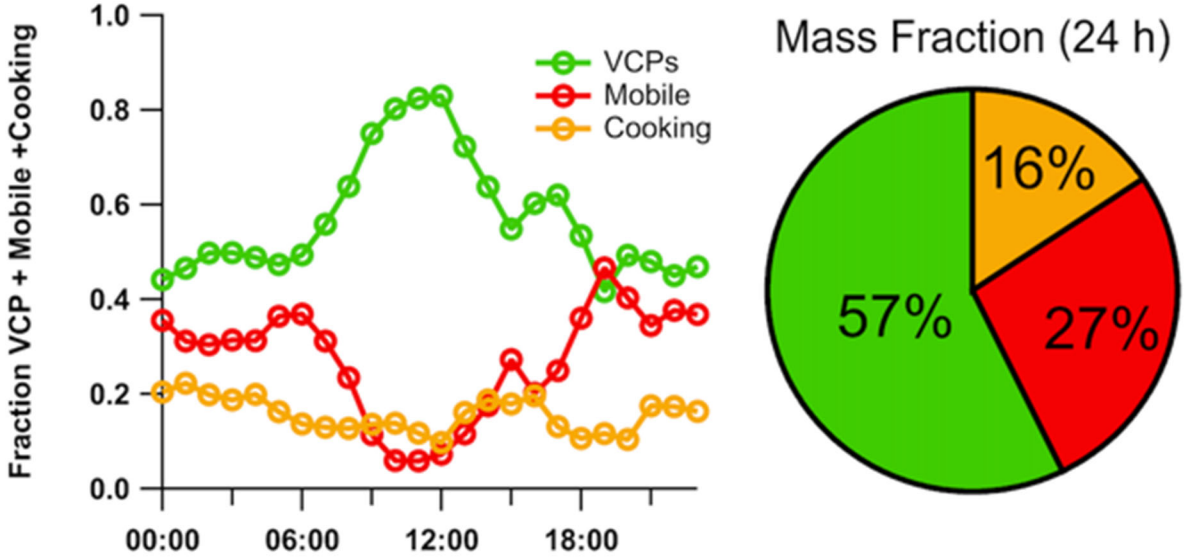

Figure 8-10. Contribution of VCP, mobile sources, and cooking factors to the sum of primary emissions (= VCP + mobile source + cooking) as diurnal profile and pie chart.

8.4. PMF Results – Mobile Drives around the Las Vegas Strip

Figures 8-10 and 8-11 present PMF results for the mobile laboratory data collected around the Las Vegas Strip. In this analysis, a 4-factor solution was needed to describe the VOC variability. Three factors were linked to primary emissions representing mobile sources, cooking, and VCP emissions. The profile of each factor resembled the corresponding factors identified at Jerome Mack and included the corresponding tracers, such as D5-siloxane for VCPs, aromatics for mobile sources, and nonanal and octanal for cooking. A fourth factor, identified as a regional background factor, was observed that resembled the chemical oxidation factor. The solvent factor was not observed, supporting our conclusions that the observations of this factor at the ground site were linked to a local source.

Figure 8-10 shows that mobile sources were highly variably throughout the region, which is expected since the mobile laboratory sampled along major roadways. The VCP and cooking factors were primarily enhanced along Las Vegas Boulevard. This is consistent with the previous chapter, which showed that personal care product and cooking tracers, such as D5-siloxane and nonanal, were well-correlated with population and restaurant density, which are highest along the Las Vegas Strip.

Figure 8-11 further compares the varying contributions of each source on a 24-hr average. Around the Las Vegas Strip, the mobile source factor peaked during rush hour periods, while the VCP and cooking factor were largest in the evenings. The higher nighttime contributions of VCPs and cooking in this region likely reflect larger emissions from dining and recreation. We note that ethanol is a major component of each factor, but was excluded from this analysis due to significant contributions from sources other than VCPs, fossil fuels, and cooking.

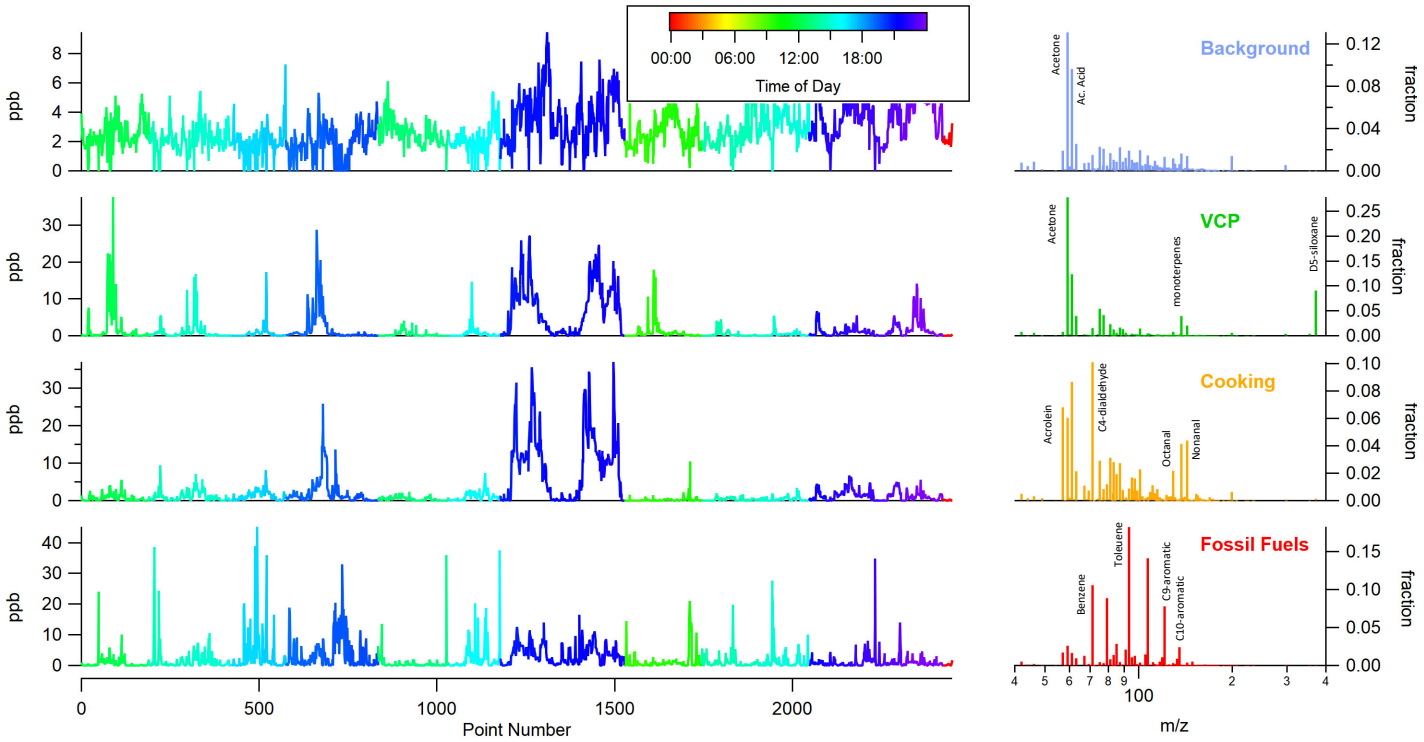

Figure 8-10. Time series of a 4-factor solution for all of the samples measured around the Las Vegas Strip. The timeseries for each factor is colored by the time of day to show when mixing ratios are highest.

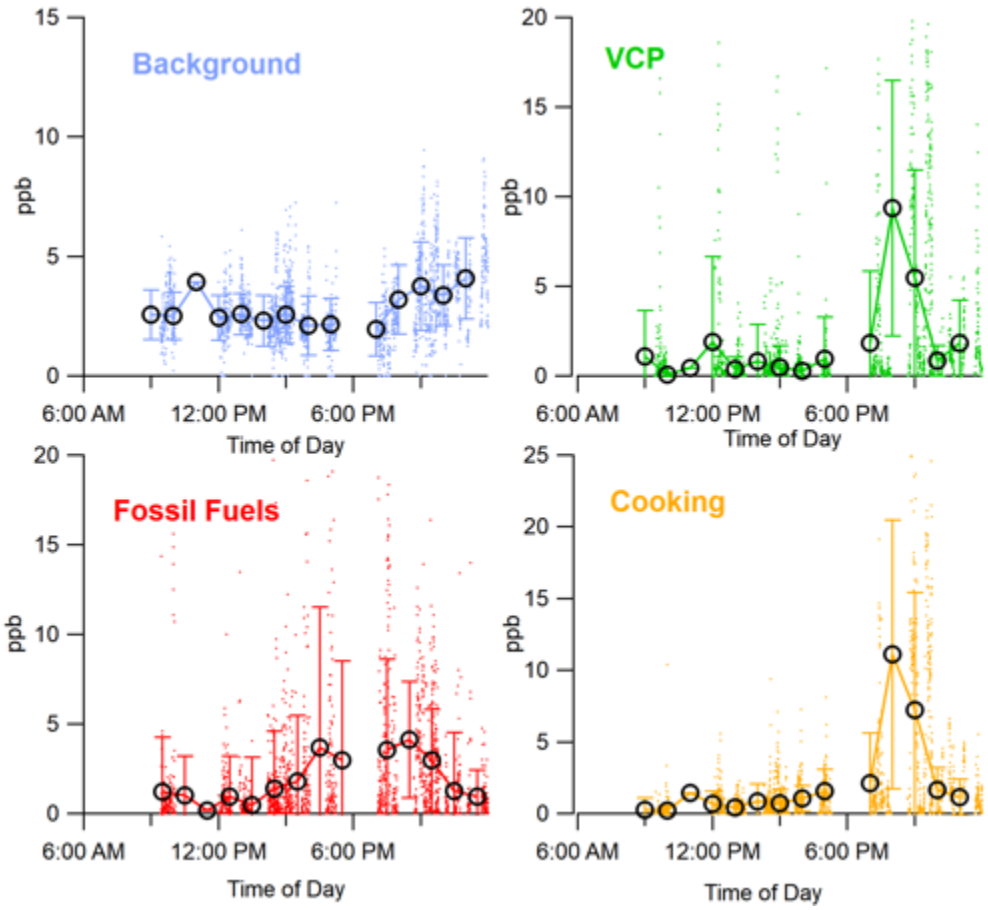

Figure 8-11. 24 hourly average patterns for the 5 factors resolved by PMF around the Las Vegas Strip.

9. ***Box modeling for ozone sensitivity***

9.1. Model setup

In-situ measurements at the Jerome Mack site were conducted from July 1st to July 27th in 2021. Due to the air conditioner failure at the site and following instrument instabilities, we utilize measurements from two distinct periods in the following analysis: July 1st- July 8th and July 19th - July 27th. The suite of VOCs was quantified using PTR-ToF-MS and WAS-GC-MS. The planetary boundary layer height (PBL) was measured with the Stationary Doppler lidar On a Trailer (StaDOT) and is shown overlaid with WRF-Chem model PBL estimates in Figure 9-1. The time-series of several representative VOC tracers that were measured are shown in Figure 9-2. Additional meteorological measurements included temperature, pressure, wind speed, and wind direction, which were measured by Clark County DES at Jerome Mack.

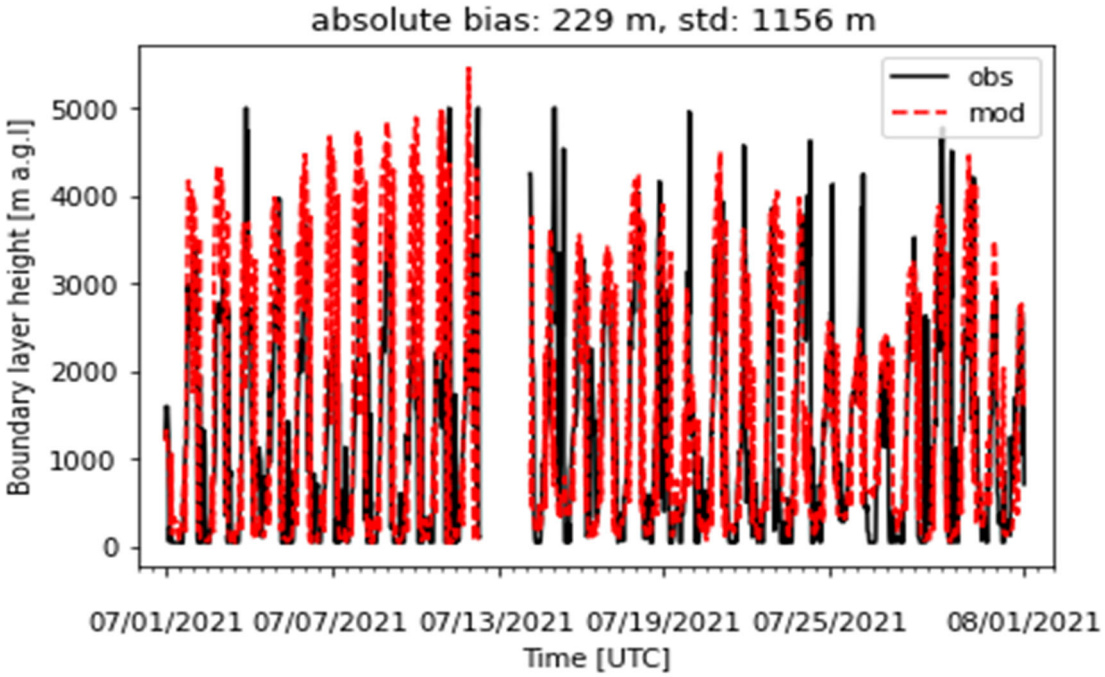

Figure 9-1. Time series of PBL height from Doppler Lidar (black line) and the WRF-Chem model (red dashed line).

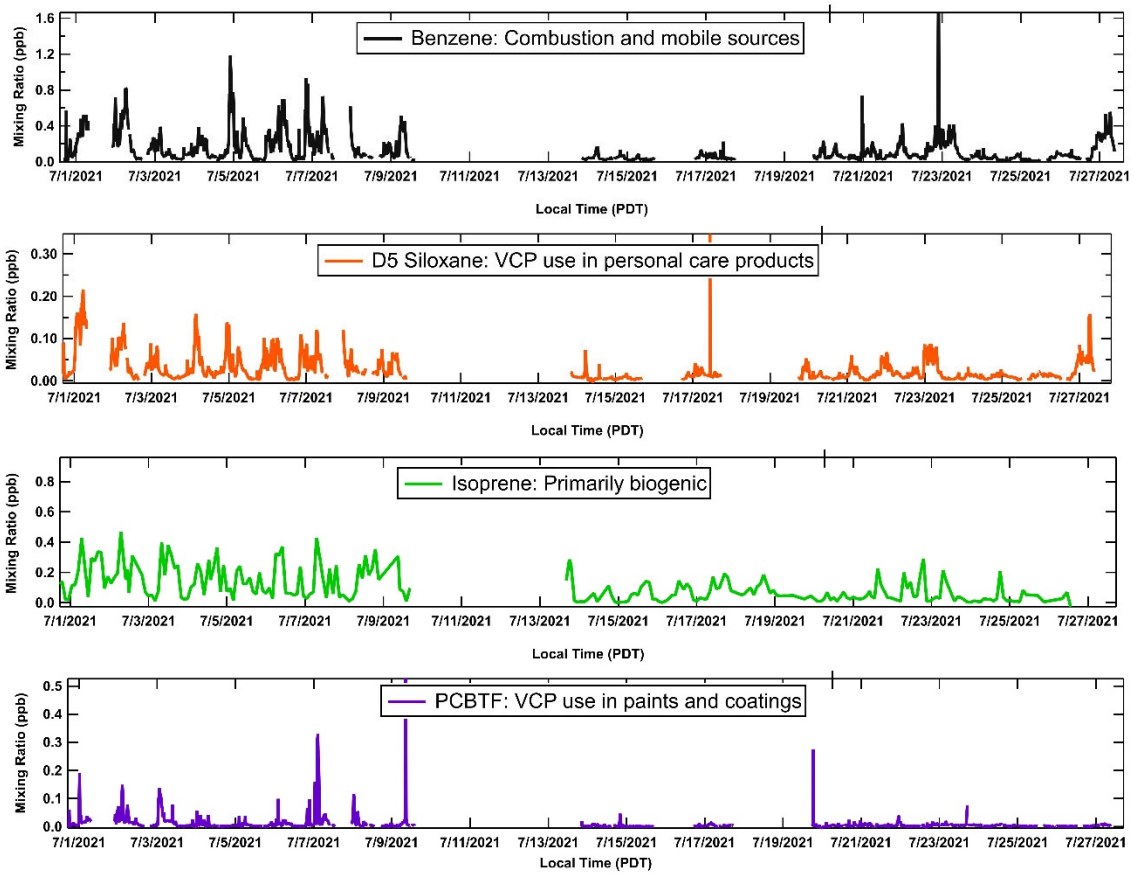

Figure 9-2. Ambient time series of various VOCs sampled at the Jerome Mack site. A mobile source (benzene, black trace), VCP personal care tracer (D5-siloxane, orange trace), biogenic species (isoprene, green trace), and a paints/coatings tracer (PCBTF, purple trace) are shown.

We constructed a Eulerian box model to evaluate the chemical processes impacting air quality at the Las Vegas ground site (Figure 9-3). Meteorological inputs were taken from on-site measurements and included pressure, temperature, relative humidity, and planetary boundary PBL. Photolysis frequencies for key chemical species were retrieved from the Weather Research Forecasting with Chemistry (WRF-Chem) model. The Framework for 0-D Atmospheric Modeling (F0AM) was used to analyze O_3 production during the July time period. The gas-phase chemical oxidation mechanisms were modified previously for the Master Chemical Mechanism (MCMv3.3.1) to include additional biomass burning oxygenated VOCs (OVOCs) and these updated mechanisms are used in this analysis. The MCM is a near-explicit mechanism used to characterize gas-phase chemical processes involved in the tropospheric degradation of hundreds of VOCs and a complete inorganic mechanism scheme (Jenkin et al., 2015).

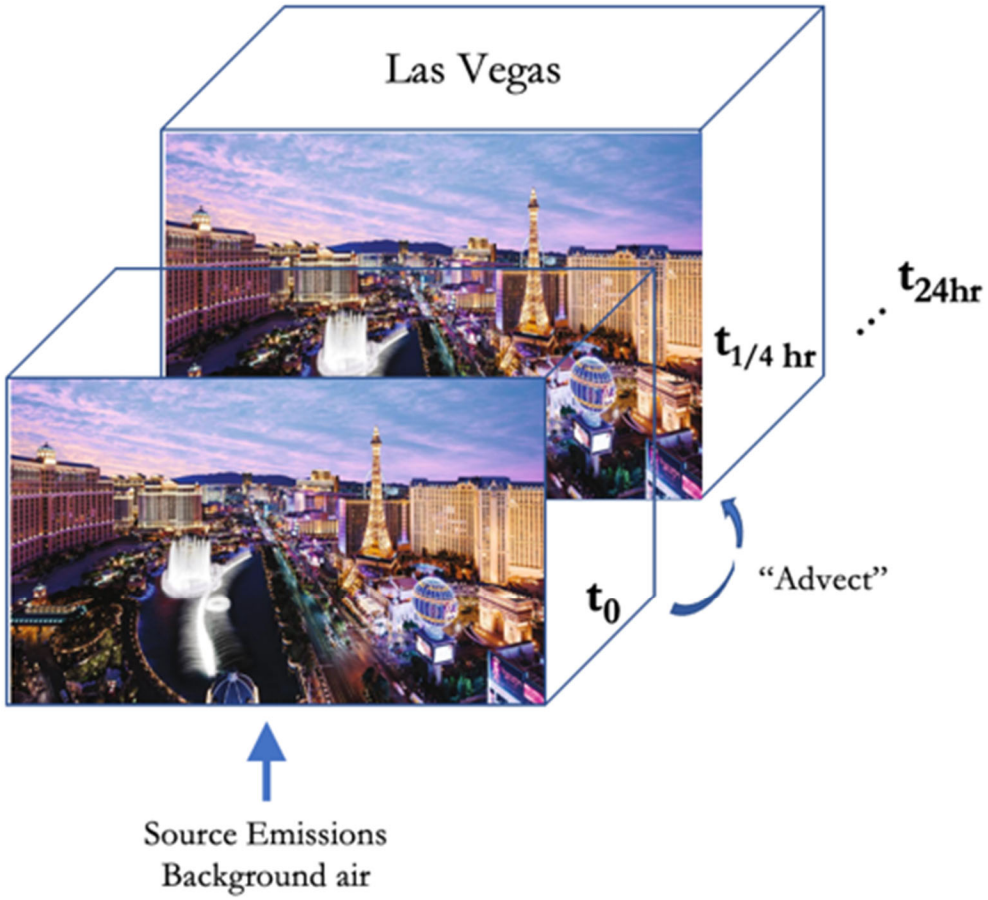

Figure 9-3. The Eulerian model concept simulates emissions, chemistry, and dilution in an array of fixed computational boxes. Chemical species are removed by advection, chemical reaction, and deposition.

In this analysis, we focus on model simulations between 6:00 and 17:00 local time when photochemical processes drive O_3 formation. In-situ chemical and meteorological measurements and WRF-Chem photolysis rates were incorporated into the model on quarter hour intervals. VOC mixing ratios, meteorological parameters, and photolysis frequencies were fully constrained to the diel median observations for the selected time period (7/1-7/8; 7/19-7/27) as shown for selected profiles in Figure 9-4. Medians were selected to reduce the impact of local point sources. The compounds used to constrain the model grouped by compound class and measurement method are identified in Table 9-1. The model was also constrained to the diel observed median total NO_x ($NO+NO_2$) at the beginning of each modeled time step, but was then speciated to NO and NO_2 by allowing the model to calculate the NO/NO_2 ratio assuming a pseudo-steady state using jNO2, temperature, and O_3. This assumption mitigates model artifacts that are not representative of regional, well-mixed models (such as NO titration of O_3).

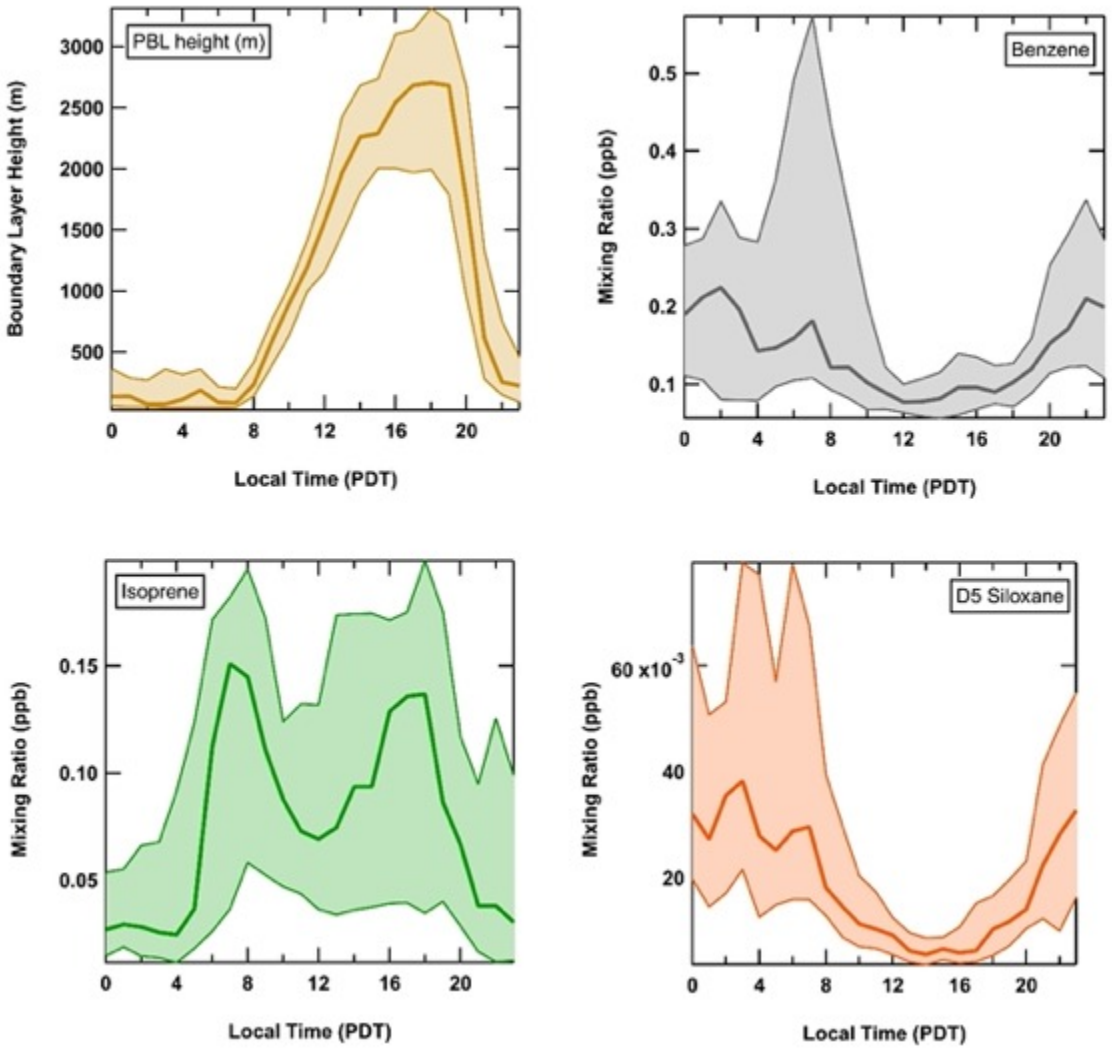

Figure 9-4. Median diel observations of planetary boundary layer height (m) and VOC measurements (ppbv) of benzene (mobile source), isoprene (biogenics), and D5 siloxane (personal care VCP). The median is indicated as a solid line with shaded regions showing the 25th and 75th percentiles.

Table 9-1. Compounds used to constrain the model simulation and the instrumentation used.

Group	Compound	Method
Inorganics	Nitric oxide, Nitrogen dioxide	NO_xCARD
	Carbon monoxide, Carbon dioxide	Picarro
Alkenes	Cis-2-Butene, Cis-2-Pentene, Ethene, Propene, Trans-2-Butene, Trans-2-Pentene, 1-Butene, 1-Pentene, 2-Methyl-1-Butene, 3-Methyl-1-Butene	GC-MS
Alkanes	Butane, Ethane, Isobutane, Isopentane, n-Decane, Propane, n-Hexane, n-Nonane, n-Octane, n-Pentane, Methylcyclopentane, Cyclohexane	GC-MS
Furans + Phenolics	Dimethyl furans, Furan, Guaiacol, Creosols, Methyl furan, Phenol, Xylenes, Ethylbenzene	PTR-ToF-MS

Aromatics	C8 aromatics, C9 aromatics, Furfural, Maleic anhydride, Benzaldehyde, Styrene	PTR-ToF-MS
	Benzene, Chlorobenzene, Isobutene, Methylcyclohexane, 2-Methyl-Pentane, Toluene, Tetrachloroethylene, Isopropyl nitrate, 2-Methyl-Pentane, 3-Methyl-Pentane	GC-MS
OVOCs	Acetaldehyde, Acrolein, Ethanol, Methanol, Formic Acid	PTR-ToF-MS
	Methyl acetate, Methyl ethyl ketone, Propanol, Methyl vinyl ketone, Methacrolein, Butanedione	GC-MS
Terpenes	Alpha-pinene, Beta-pinene, Isoprene	GC-MS

9.2. Model results

The calculated OH reactivity from the simulation indicated a maximum in the early morning near 10 s^{-1}. OVOCs, inorganics (CO & NO_2), and other VOC functionalities not measured on-site (labeled “Other”) make up the largest contributions to the calculated OH reactivity as shown in the top panel of Figure 9-5. The bottom panel of Figure 9-5 shows the simulated production and loss rates of OH due to individual compounds averaged over the diel cycle.

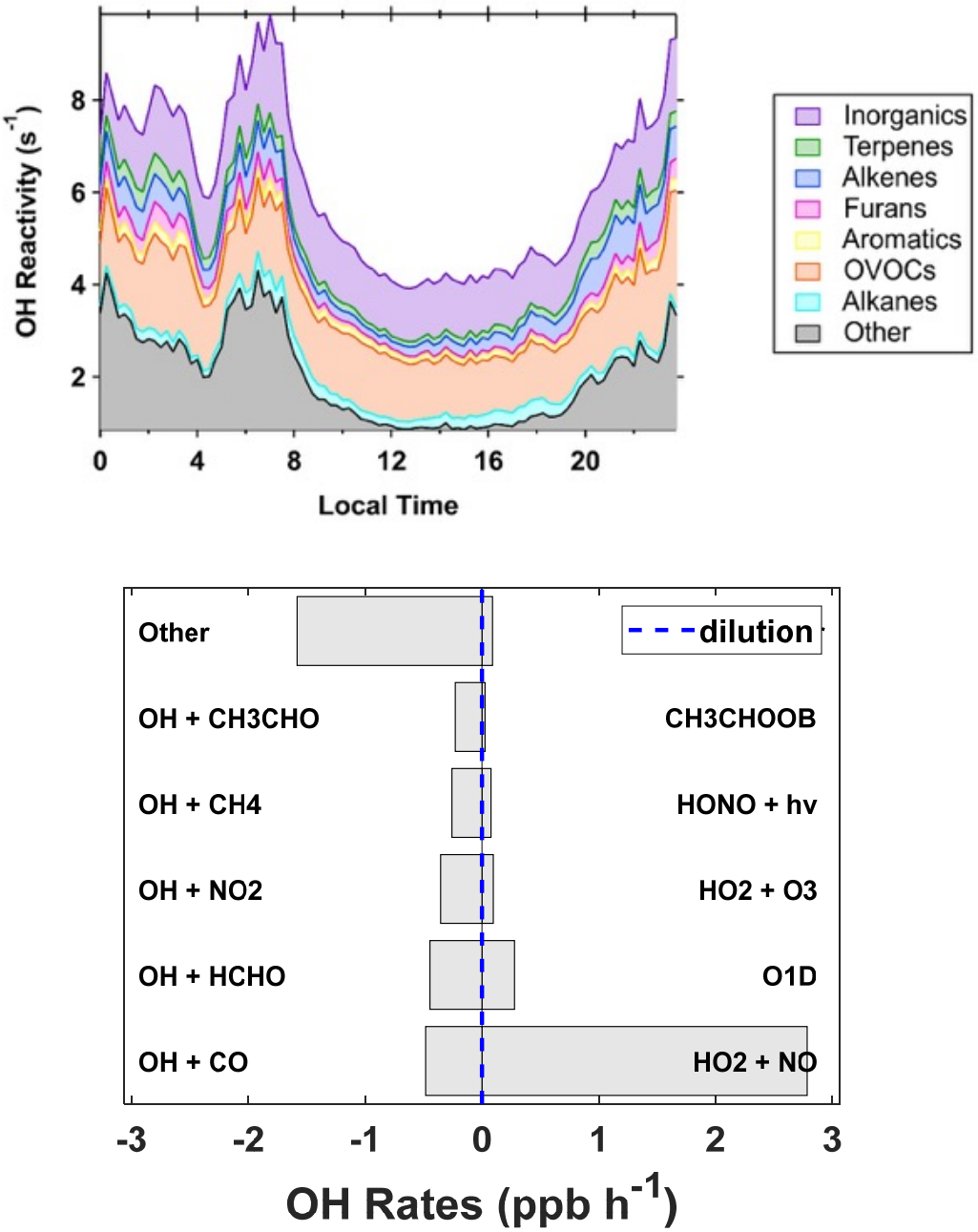

Figure 9-5. (top) Time series of the speciated contribution to calculated OH reactivity from the model simulation. (bottom) Production and loss rates of OH averaged over the day.

Ozone mixing ratios were not constrained and were initialized with mixing ratios measured overnight (38 ppb) and are shown in Figure 9-6. Physical losses of O_3 by dilution were estimated by multiplying a first-order dilution rate (k_{dil}) to the observed O_3 background taken as the minimum in the diel (27 ppb). The dilution rate was determined by varying k_{dil} until a best fit was observed between the model and measured O_3. The resulting dilution rate determined by this analysis was 8×10^{-5} s^{-1}. A sensitivity analysis was performed by varying

the dilution rate by ±20% to account for the uncertainty in this approach. The periods of sampling used to estimate the O_3 median diel that the model is compared to are highlighted in the time series of Figure 9-6.

The model simulation of O_3 overlaid with NOxCARD O_3 measurements is shown in Figure 9-6. The daily O_3 enhancement, taken as the maximum ozone produced midday relative to the minimum during early morning is approximately 30 ppb and the simulation reasonably captures the O_3 enhancements during the primary O_3 production time period (6:00-17:00 LT), but slightly underestimates O_3 in the late evening and at night.

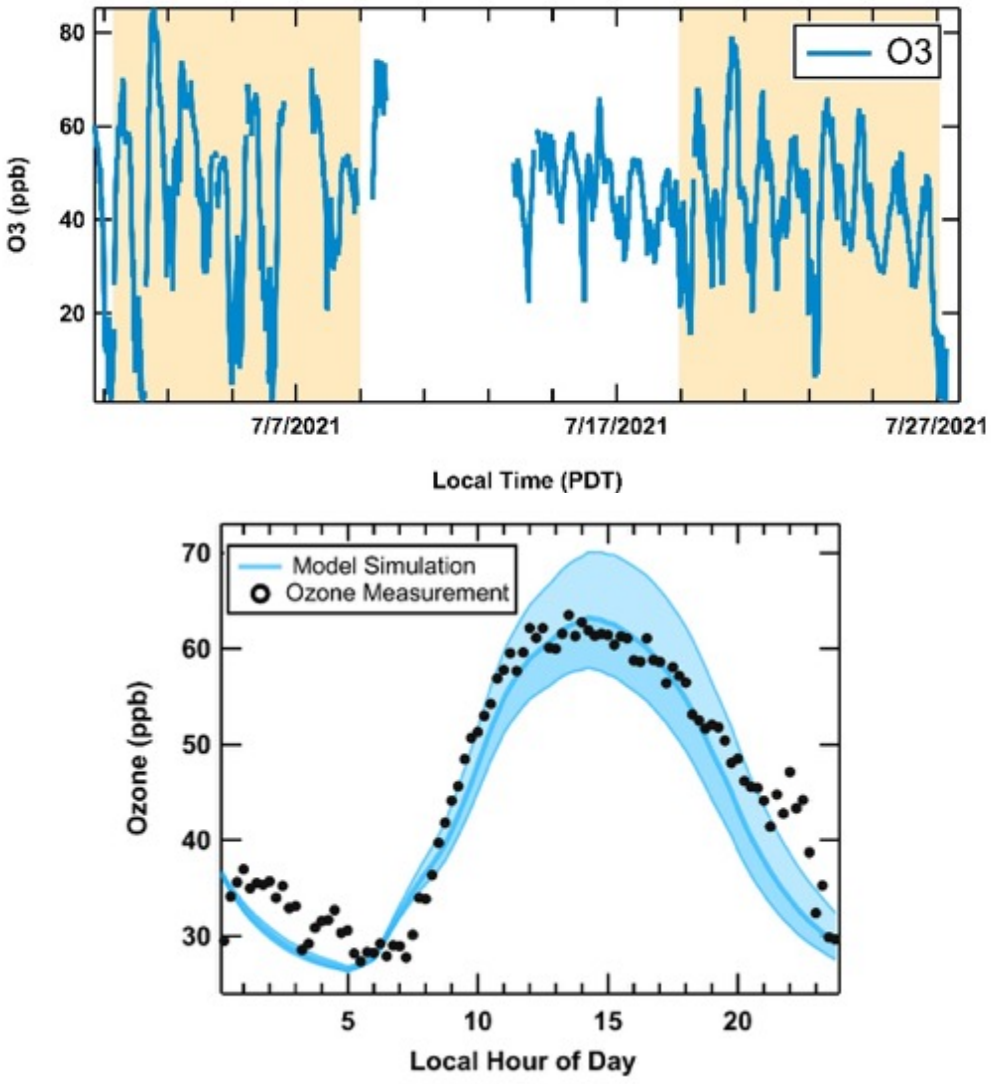

Figure 9-6. (top) Time series of ozone with time periods used to initialize the model simulation highlighted in yellow. (bottom) Median diel O_3 measurement profile (black dots) with modeled results (blue) overlaid. The uncertainty bands reflect 20% changes to the modeled dilution rates.

The O_3 isopleth in Figure 9-7 shows simulated O_3 at the daily maximum (14:00 LT) as a function of NO_x and VOC scaling, where the base case from Figure 9-6 is indicated as a value of one shown as the yellow marker. This isopleth shows that O_3 production is still in the NO_x sensitive regime, but lies very close to the transition region. The bottom panels of Figure 9-7 also show ozone sensitivities with changing (a) NO_x or (b) VOC emissions. The black marker represents the ambient condition observed at the Jerome Mack ground-site. Ambient conditions at maximum O_3 production were close to the transition region and an increase of approximately 1 ppb of NO_x would push O_3 production into a NO_x saturated regime. In other regions of Las Vegas, where urban NO_x might be larger than at Jerome Mack, O_3 production could be NO_x saturated. The O_3 sensitivities to VOCs show that reductions in VOCs would also reduce O_3 production. Reducing NO_x or VOCs by half would reduce O_3 by 10.5 ppb and 11.5 ppb, respectively. Reducing both NO_x and VOCs in half would decrease O_3 by 15 ppb.

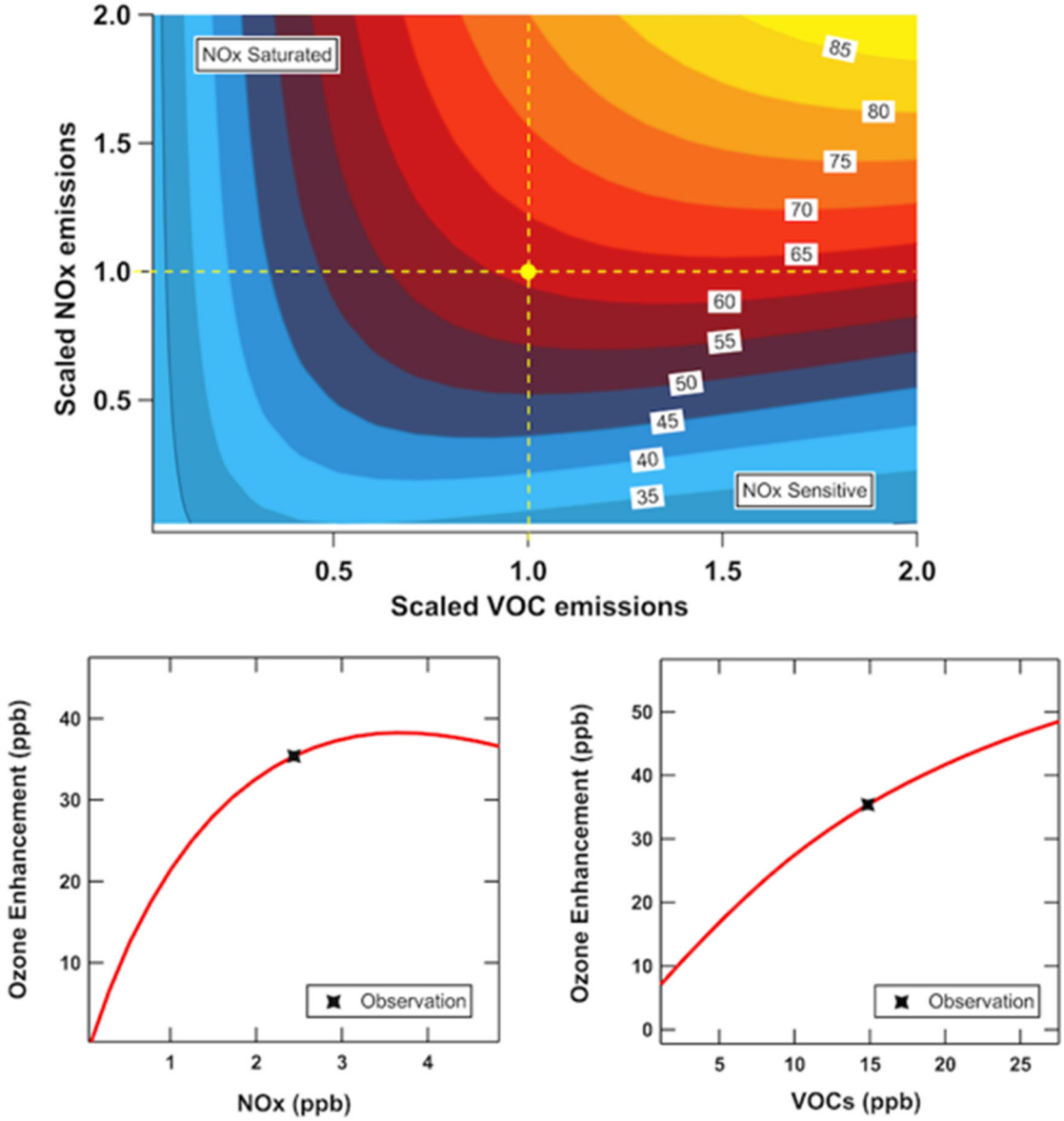

Figure 9-7. (top) Isopleths of modeled maximum ozone production (at 14:00 LT) as a function of scaled total NO_x and VOC emissions. The base case where NO_x and VOCs have not been adjusted are indicated by the yellow marker. (bottom) Modeled ozone enhancements as a result of changing NO_x (left) and VOCs (right). Ambient observations are indicated by the black marker.

Further sensitivity tests are shown in Figure 9-8. To evaluate the contribution of oxygenated VOCs (OVOCs) to peak ozone formation, sensitivity tests were performed by removing groups of VOCs based on their functionality. The results show that OVOCs are the largest ozone contributor (~15 ppb) followed by alkanes/alkenes, aromatics, and biogenics (each < 2 ppb), which is consistent with the OH reactivity shown in Figure 9-5. The results of removing all OVOCs is shown with the green line in Figure 9-8. Without OVOCs, the overall ozone production decreases and is pushed into a NO_x saturated/transitional regime at observed

NOx levels, where only significant changes in NO_x would drastically change ozone (Figure 9-8). This means that it is likely that regional transport of OVOCs contributes to ozone production in the Las Vegas basin, but the box model, which is constrained with OVOC observations, is not able to resolve regional background OVOCs from local anthropogenic sources.

In order to assess the NO_x/VOC sensitivity along the Las Vegas Strip, data from the mobile laboratory drives were used to estimate VOCs and NO_x levels. Only data from within the perimeter defined for the mobile laboratory specific PMF analysis (Figure 8-3) were used. Significantly larger enhancements of VOCs were observed along the Las Vegas Strip compared to Jerome Mack, especially during drives in the evening and night. Most relevant for ozone formation is the time of peak ozone formation in the afternoon. During that time period, total VOC mixing ratios were estimated by averaging drive data, excluding measurements from the upper 75th percentile to remove on-road vehicle exhaust plumes and other local VOC sources. The total VOC concentration estimated to be representative for the Las Vegas Strip, were approximately 1.6 times higher than the Jerome Mack levels. The blue curve in Figure 9-8 is taken from the isopleth in Figure 9-7 at expected VOC levels along the Las Vegas Strip during the midafternoon.

In a similar way, NO_x levels were roughly estimated on the Las Vegas Strip during peak ozone production times. The caveat is that the mobile laboratory continuously measured during stop-and-go traffic along the Las Vegas Strip, which is not fully representative of the regional NO_x levels and therefore the upper 50th percentile of the NO_x data was removed to account for the local on-road vehicle exhaust. With this method, NO_x levels along the Las Vegas Strip were estimated to be ~4.5 ppb during the peak ozone production time period. This value is indicated with the black square on top of the blue curve in Figure 9-8. At the VOC and NO_x levels estimated on the Las Vegas Strip, ozone remains sensitive to both NO_x and VOCs and falls into a similar chemical regime as predicted at the Jerome Mack ground site.

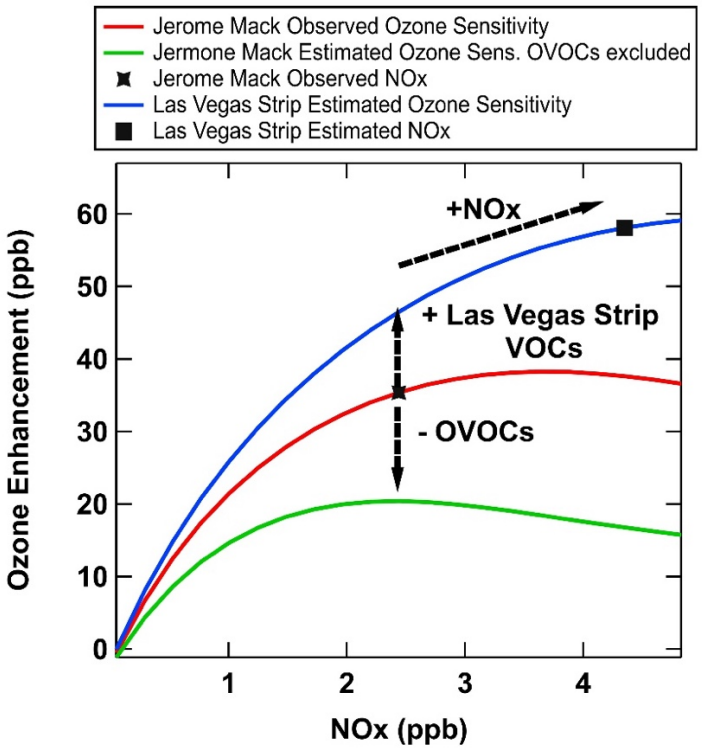

Figure 9-8. Modeled ozone production as a function of NO_x mixing ratios for the base simulation at Jerome Mack (red) at observed NO_x concentrations (black cross marker), at Jerome Mack when excluding oxygenated VOCs (green), and for the Las Vegas Strip (blue) at estimated VOC and NO_x (square marker) mixing ratios.

10. Biogenics

In this chapter, the observations and modeling of the biogenics are described in detail. Isoprene emissions are temperature and light dependent, while monoterpenes are temperature dependent emissions from biogenic sources such as urban vegetation. The Jerome Mack site is near a grass field with some trees that likely emit isoprene and potentially monoterpenes. Additionally, as described above, monoterpenes are emitted as VCPs from fragranced products, where limonene is the major contributor, while a-pinene usually dominates biogenic emissions [*Coggon et al.*, 2021].

10.1. Isoprene

The time series of isoprene and methyl vinyl ketone+methacrolein (MVK+MACR), two oxidation products of isoprene, are shown in Figures 10-1 for the Jerome Mack site (top panel) and are compared to measurements in Pasadena (bottom panel) the following month. Isoprene was measured by the WAS GC-MS and MVK+MACR by the PTR-ToF-MS. While there are only a few trees near the Jerome Mack site, the Pasadena site was in close proximity to many trees. This difference in the amount of vegetation around each site resulted in nearly ten times higher isoprene and MVK+MACR mixing ratios in Pasadena compared to Jerome Mack.

The respective diurnal profiles of isoprene and MVK+MACR are shown in Figures 10-2. The shape of the diurnal profiles indicates that emissions observed at both sites are relatively fresh with Pasadena being less aged [*Warneke et al.*, 2010]. Since isoprene emissions are light and temperature dependent, they are at a maximum mid-afternoon. At Jerome Mack, boundary layer height and atmospheric oxidation also peak in the mid-afternoon causing the mixing ratios to drop at that time and instead concentrations peak late morning and early evening as was observed in other areas [*Warneke et al.*, 2004]. The ratio of MVK+MACR to isoprene at Jerome Mack (~1) and in Pasadena (~0.5) also indicates that isoprene was recently emitted, with Jerome Mack being slightly more aged. In aged air, the MVK+MAC isoprene ratio goes up to 10 [*Warneke et al.*, 2004].

The mobile laboratory drive tracks color coded by isoprene are shown in Figure 10-3 for Las Vegas and Los Angeles. Inside the urban core isoprene was observed in both cities with generally higher mixing ratios in Los Angeles. Outside Las Vegas in the desert, isoprene was very low, usually less than 10 ppt. The only canister sample outside the urban area during all the drives that had slightly elevated isoprene (246 ppt) was at a higher elevation near Angel Peak, a more forested area.

In summarizing the isoprene observations, we find that small but not insignificant emissions are expected from the vegetation inside the city, but no isoprene was observed immediately outside Las Vegas.

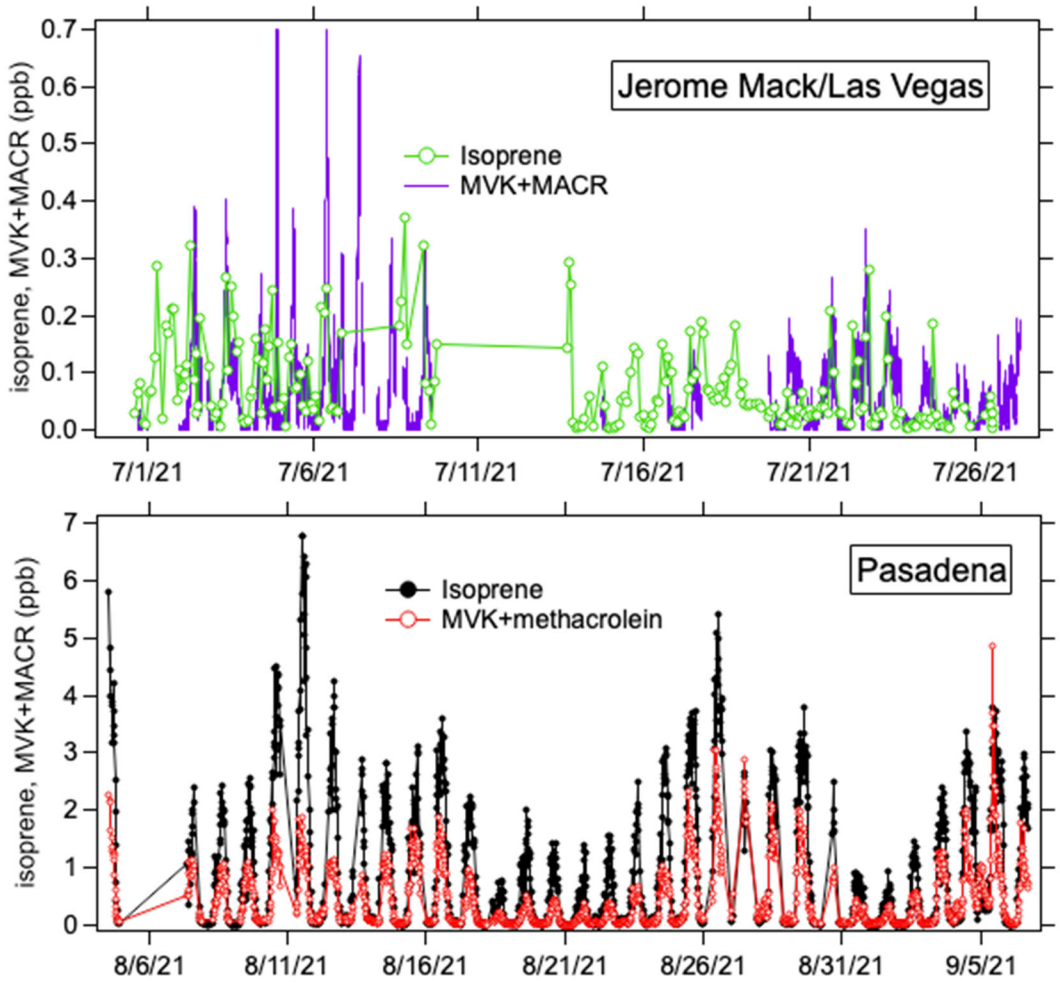

Figure 10-1. Time series of isoprene and its oxidation products (methyl vinyl ketone+methacrolein) at the ground site in Jerome Mack (top) compared to the ground site in Pasadena, CA (bottom). Pasadena has nearly 10 times higher isoprene than mixing ratios observed at Jerome Mack.

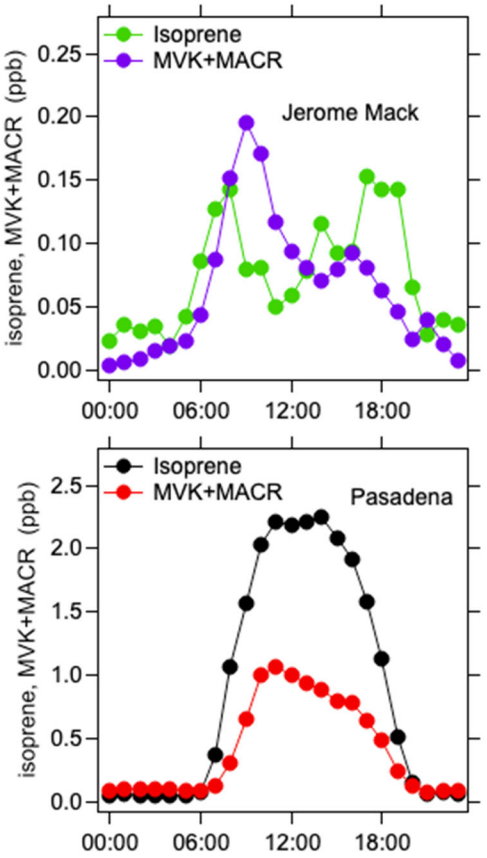

Figure 10-2. Diurnal profile of isoprene and methyl vinyl ketone+methacrolein at the ground site in Jerome Mack (top) compared to the ground site in Pasadena, CA (bottom).

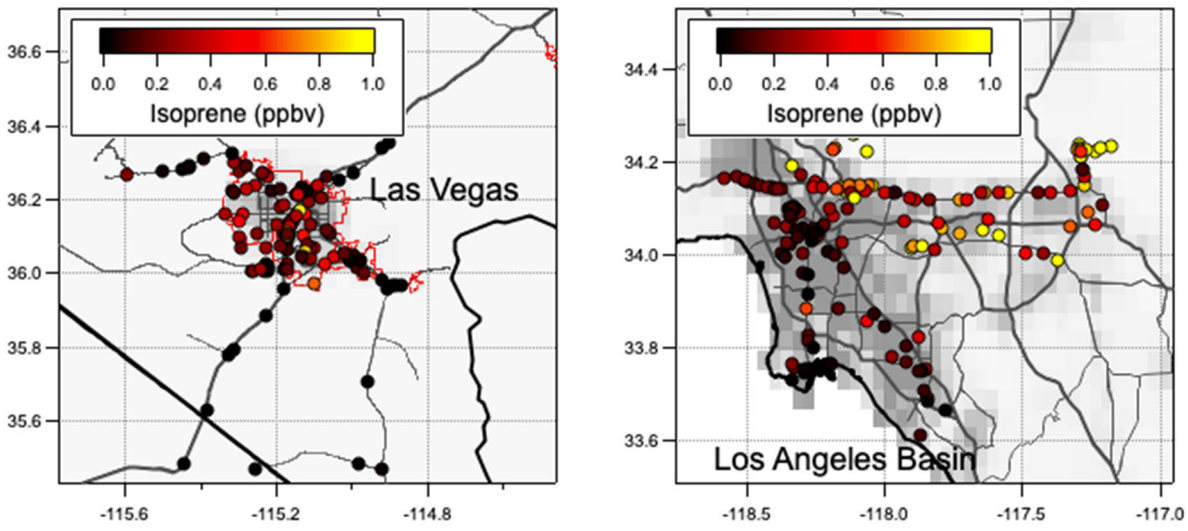

Figure 10-3. Drive tracks of the mobile laboratory color coded by isoprene in Las Vegas and the Los Angeles Basin.

10.2. Monoterpenes

The time series of the sum and speciated monoterpenes at Jerome Mack is shown in Figure 10-4. At Jerome Mack the distribution of the monoterpenes is dominated by a-pinene followed by b-pinene and d-limonene. A more detailed comparison of the composition of the monoterpenes between the Las Vegas Strip area and the Jerome Mack site is shown in Figure 10-5. During the mobile drives on the Las Vegas Strip, the distribution is dominated by d-limonene, which was also observed with the GC-PTR-ToF-MS measurements shown in Figure 4-7. This again shows that the Las Vegas Strip area is likely more influenced by anthropogenic monoterpenes than the Jerome Mack site.

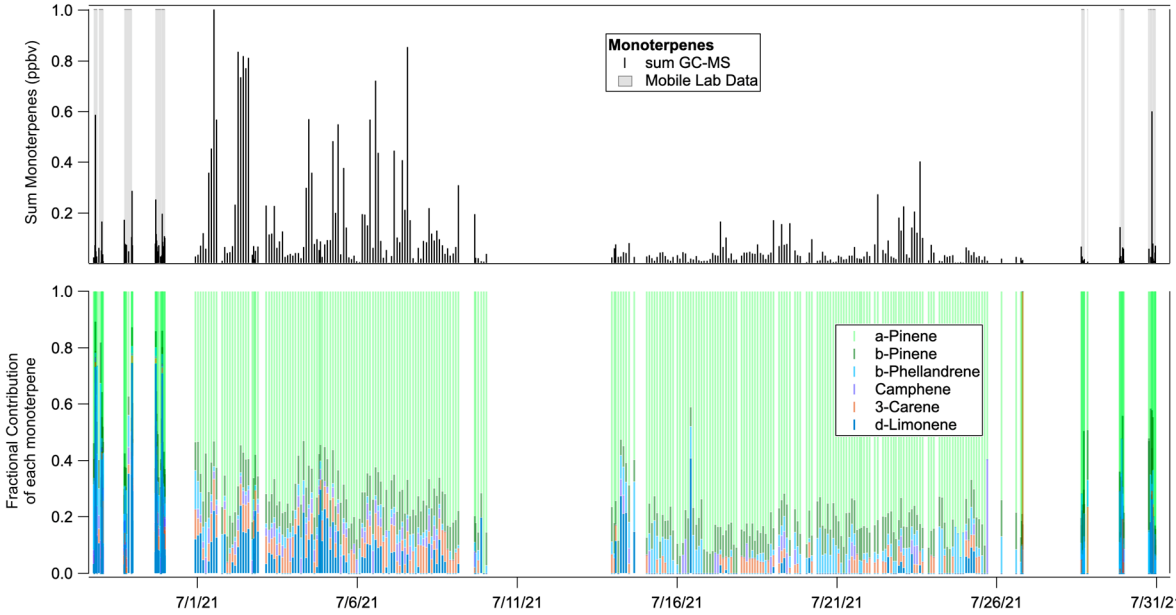

Figure 10-4. Time series (top) and composition (bottom) of the monoterpenes at the ground site in Jerome Mack and during the drives.

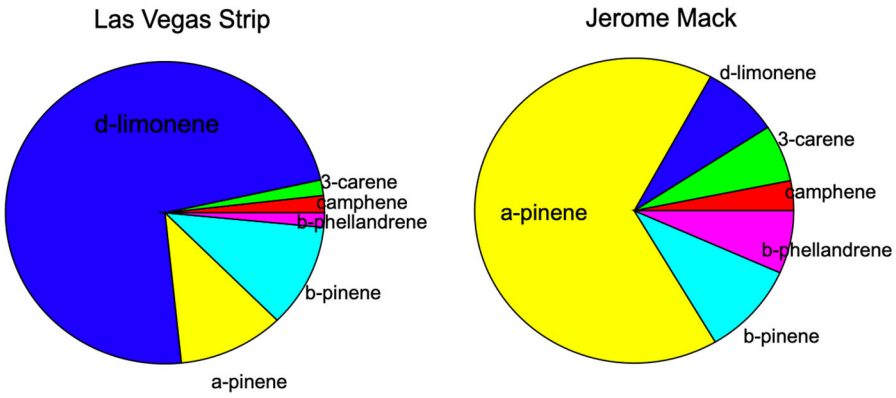

Figure 10-5. Comparison of the monoterpene composition around the Las Vegas Strip and at the Jerome Mack site.

The diurnal profile of several speciated monoterpenes is shown in Figure 10-6. Similar to many other compounds, the largest mixing ratios were observed at night. Monoterpene emissions are only temperature dependent; this means that monoterpene emissions peak during the day but are also emitted at night. Together with a short lifetime and the high boundary layer during the day, the daytime minimum is expected to be similar to monoterpene diurnal profiles in other areas [*Warneke et al.*, 2004].

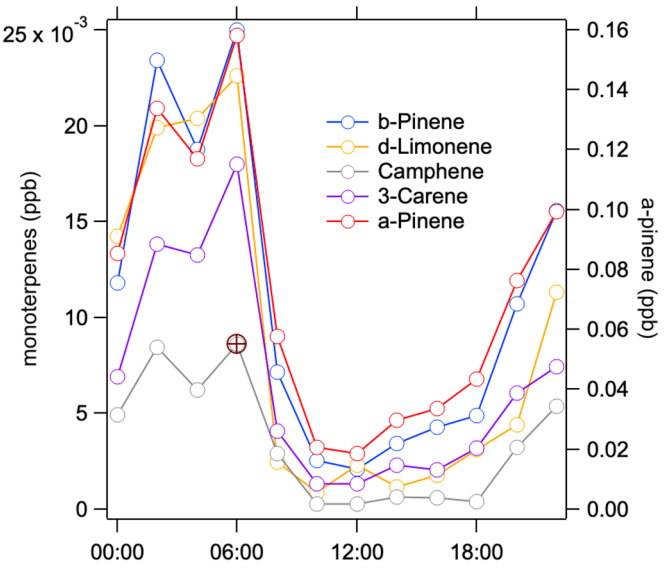

Figure 10-6. Diurnal profiles of various monoterpenes measured at the Jerome Mack ground site.

A map showing the location of each canister sampled during the mobile laboratory drives is shown in Figure 10-7. The points are sized by the mixing ratio of the sum of the monoterpenes and color coded by the fraction of d-limonene. The highest mixing ratios and the highest d-limonene fraction were generally observed around the Las Vegas Strip area, again demonstrating the strong influence of anthropogenic monoterpene emissions on the Las Vegas Strip. As was the case for isoprene, mixing ratios of all monoterpenes outside the city were relatively low.

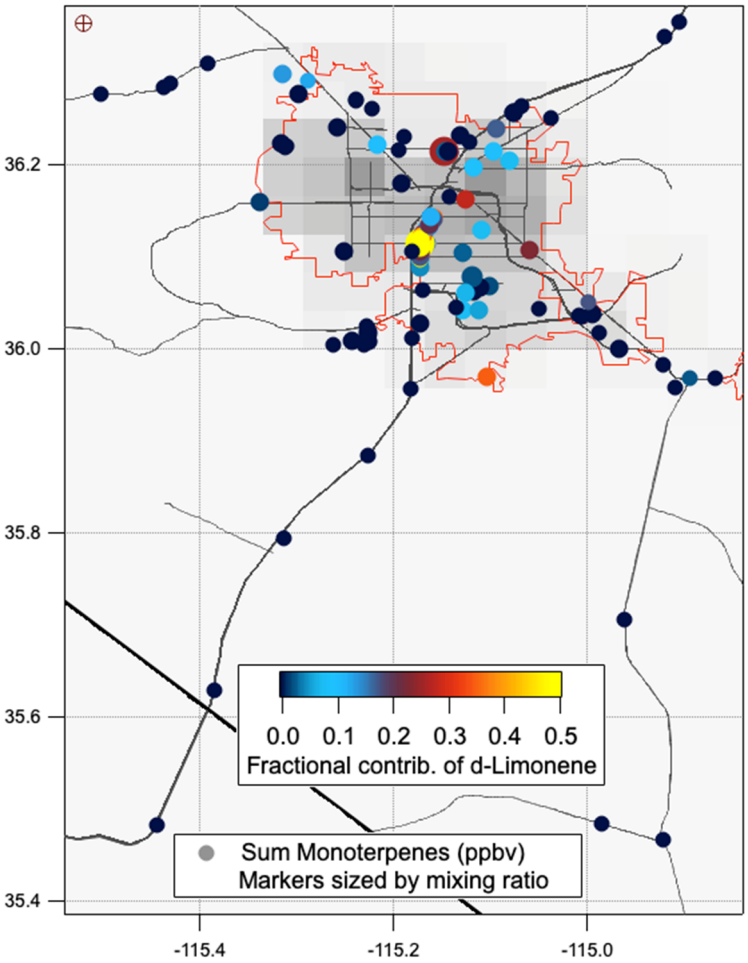

Figure 10-7. Map of the canisters sampled during the mobile laboratory drives sized by the sum of the monoterpenes and color coded by the fractional contribution of d-limonene.

10.3. Sesquiterpenes

Sesquiterpenes are detected by the PTR-ToF-MS on mass 205 ($C_{15}H_{24}H^+$) and the time series and diurnal profile of the mixing ratios are shown in Figure 10-8. No calibration was available for these compounds and therefore the mixing ratio was estimated using a method described previously [Sekimoto et al., 2017]. Unusually high mixing ratios from 6-9 AM were observed on almost all days for the sesquiterpenes. One explanation for this unusual behavior could be that the high mixing ratios coincided with the watering of the nearby grass field at the Jerome Mack school using an automated sprinkler system. More research needs to be done to understand this diurnal profile.

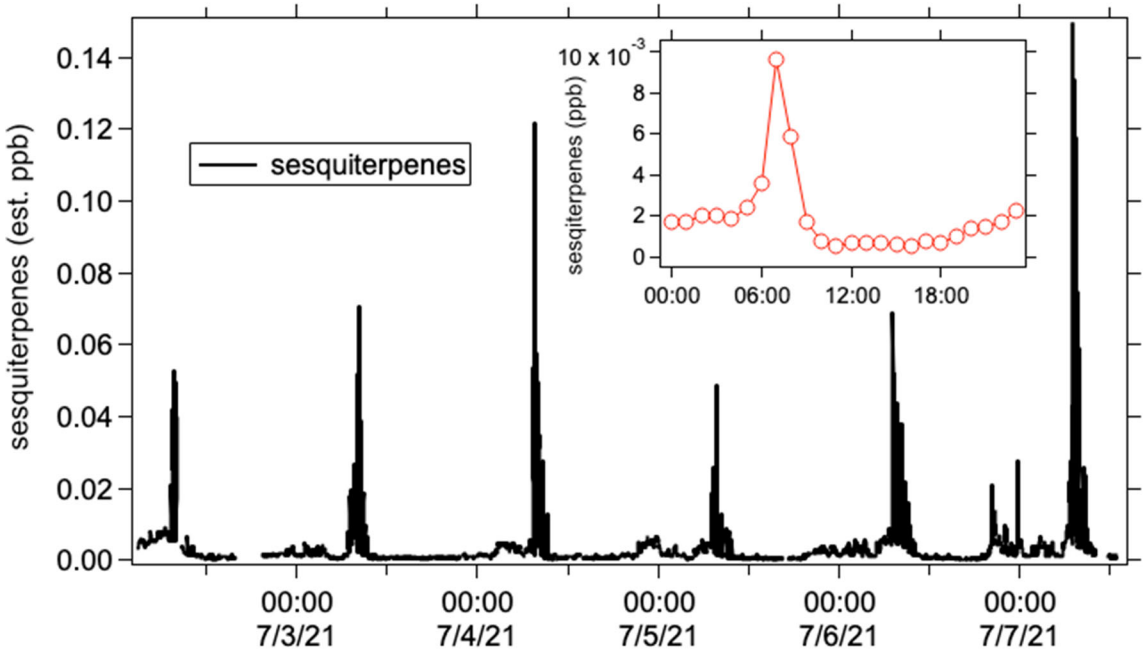

Figure 10-8. Map of the canister sampled during the mobile laboratory drives sized by the sum of the monoterpenes and color coded by the fractional contribution of d-limonene.

10.4. Contribution of biogenics to ozone in the box model calculation

The calculated OH reactivity shown in Figure 9-5 indicates the contribution from terpenes are relatively small. The box model simulation was repeated excluding isoprene, methacrolein, methyl vinyl ketone, and alpha/beta-pinene in order to evaluate ozone sensitivity to biogenic VOCs. The bottom panel of Figure 10-9 shows the base case simulation of ozone production at Jerome Mack (blue trace) overlaid with ozone production when biogenic VOCs are excluded (green trace). The top panel shows the absolute ozone contribution from biogenic VOCs as a function of time of day. At peak daily ozone production, the O_3 contribution from biogenic VOCs is ~3.5 ppb, which is about 10% of the total produced ozone. Anthropogenic isoprene and monoterpenes could not be separated from biogenics, and therefore ozone attributed to biogenics should be considered an upper bound.

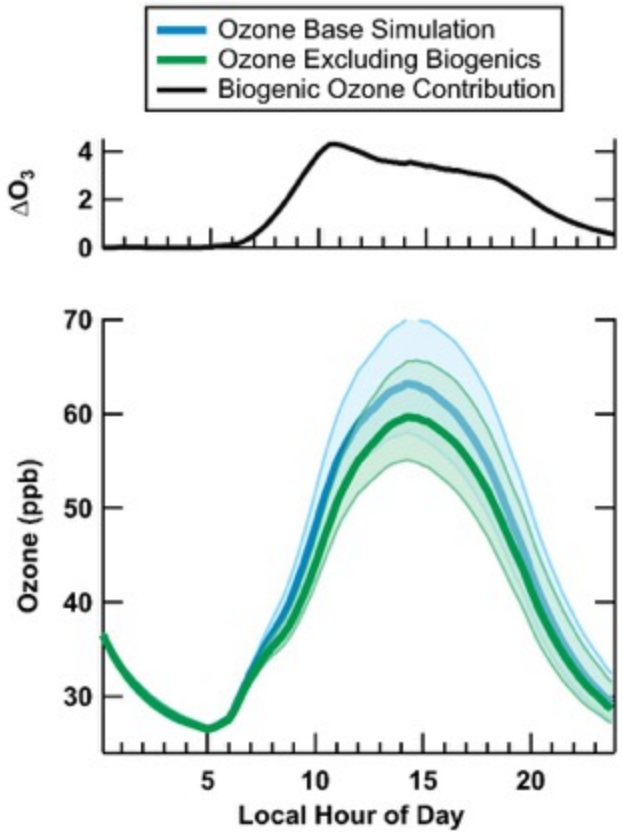

Figure 10-9. (top) The contribution of biogenics to ozone formation estimated from the box model. (bottom) The base case simulation of ozone production at Jerome Mack (blue trace) overlaid with ozone production when biogenic VOCs are excluded (green trace). The uncertainty bands reflect 20% changes to the modeled dilution rates.

11. WRF-Chem modeling for ozone sensitivity

11.1. 3D modeling overview

Three-dimensional chemical transport modeling is performed using the Weather Research Forecasting with Chemistry (WRF-Chem) model. The 3D modeling was performed to complement the box modeling described in section 9. The three-dimensional modeling allows for simulation of chemistry with meteorology, and to directly assess heatwaves, biogenic emissions, and interstate transport of air pollution on Las Vegas ozone. The objectives of the 3D modeling are outlined as follows:

(1) Perform meteorological simulations and evaluate with Doppler Lidar observations collected at North Las Vegas airport, including the evolution of the planetary boundary layer (PBL) and wind profiles over Clark County;

(2) Verify anthropogenic NO_x and VOC emission inventories with the NOAA CSL measurements collected at the Jerome Mack ground site;

(3) Evaluate biogenic VOC emissions in WRF-Chem with NOAA CSL ground site and mobile laboratory measurements of isoprene and monoterpenes;

(4) Perform ozone model sensitivity simulations to assess the role of biogenic and anthropogenic VOC emissions on ozone in the Las Vegas region, assess NO_x vs. VOC sensitivity, and assess the role of local versus long-range transport of ozone;

(5) Provide a preliminary assessment of the role of wildfires on transported ozone over Western US during the SUNVEx 2021 field campaign.

11.2. WRF-Chem model setup

WRF-Chem is a fully coupled meteorological and chemistry model [*Grell et al.*, 2005]. To address the research objectives outlined above, a contiguous US domain (D1) was simulated at 12 km x 12 km spatial resolution (Figure 11-1). The vertical resolution includes 50 levels that extend up to 50 hPa into the Upper Troposphere-Lower Stratosphere (UTLS). The meteorological IC/BC for the contiguous US domain (D1) are from the North American Mesoscale Model (https://www.ncei.noaa.gov/products/weather-climate-models/north-american-mesoscale). Chemical boundary conditions are provided from a global model developed by the University of Wisconsin called the Realtime Air Quality Modeling System (RAQMS, http://raqms-ops.ssec.wisc.edu/). The global air quality forecasts include data assimilation of satellite ozone and aerosol optical depth (AOD) products. Though more computationally expensive, the contiguous US simulation provides a more realistic representation of air pollutant concentrations than simply using a global model coupled directly with a high-resolution regional domain. First, the contiguous US simulation utilizes the most up-to-date bottom-up emission inventories for the US and described in Section 11.3, rather than a coarse global emissions inventory. Second, the spatial resolution of D1 (12 km

x 12 km) is significantly higher than for the global RAQMS model (1 degree x 1 degree), which is especially important for simulating ozone and its precursors, and non-linearities in chemistry. Third, the contiguous US domain is coupled to the global RAQMS model, taking advantage of the strength of RAQMS, which is to simulate long-range transport of air pollution and prediction of stratospheric intrusion events.

Figure 11-1. Map of WRF-Chem model domains, including of the contiguous US (D1: 12 km x 12 km) that feeds an inner domain (D2: 4 km x 4 km) of the Western US. Trinidad Head ozonesonde launch location denoted by red star.

For the inner model domain (D2), the geographic extent was chosen to be large enough to incorporate emissions and transport of air pollution from California to Clark County, while being computationally-feasible to perform numerous ozone sensitivity simulations with full gas and aerosol chemistry. A high-resolution domain over Clark County was investigated (1.3 km x 1.3 km) but deemed too computationally-expensive for full chemistry simulations. The 4 km x 4 km domain provides enough spatial resolution to capture ozone and precursor concentration gradients, sufficient for evaluating with the field-intensive observations. Prioritization was placed on capturing intra-Mountain West transport of air pollution (4 km x 4 km) over very high-resolution modeling (1.3 km x 1.3 km) focused on Clark County only. For the inner domain (D2), meteorological initial and boundary conditions come from the High-Resolution Rapid Refresh (HRRR) model (https://rapidrefresh.noaa.gov/hrrr/). This takes advantage of the extensive hourly meteorological assimilation by NOAA of commercial aircraft observations and GOES-16 satellite radiances. Chemical initial and boundary conditions are provided to the California/Nevada domain (D2) from the contiguous US domain (D1).

Other physics and chemistry options utilized in the NOAA CSL WRF-Chem setup are listed in Table 11-1. These settings have been well tested and evaluated previously in modeling over the Southeastern US [*McDonald et al.*, 2018b], Eastern US [*Coggon et al.*, 2021], and contiguous US [*Li et al.*, 2021]. Some notable updates include the use of the eddy diffusivity-mass flux (EDMF) scheme. The inclusion of EDMF has been shown to improve

forecast skill of the Mellor-Yamada Nakanishi and Niino (MYNN) PBL scheme (https://dtcenter.ucar.edu/GMTB/v5.0.0/sci_doc/MYNNEDMF.html), critical for simulating surface concentrations of air pollution accurately. The development of the RACM-ESRL-VCP mechanism described in Coggon et al. [2021] advances the previous RACM-ESRL chemistry option in WRF-Chem, and accounts for oxygenated VOC chemistry resulting from VCP emissions.

Table 11-1. NOAA CSL WRF-Chem Model Configuration.[a]

Settings	Description
Horizontal Resolution	12 km x 12 km + nested Western US 4 km x 4km domain
Vertical Resolution	50 levels (up to 50 hPa)
Meteorology	North American Mesoscale Model (D1) High-Resolution Rapid Refresh (D2)
Surface Layer	Mellor-Yamada Nakanishi and Niino
Planetary Boundary Layer	Mellor-Yamada Nakanishi and Niino Level 2.5 with Eddy Diffusivity Mass Flux (EDMF) Scheme
Cumulus Scheme	Grell-Devenyi (GD) Ensemble Cumulus
Land Surface	Noah Land Surface Model
Microphysics	WRF Single Moment 5-Class
Short- and Long-Wave Radiation	Rapid Radiative Transfer Model for General Circulation Models
Gas-Phase Chemistry	RACM-ESRL-VCP (updated oxy-VCP chemistry)
Photolysis	Madronich Photolysis (TUV)

a. See http://www2.mmm.ucar.edu/wrf/users/docs/user_guide_V3/contents.html for full description of model options.

11.3. Anthropogenic emissions

Table 11-2 summarizes anthropogenic CO, NO_x, and VOC emissions aggregated over Clark County utilized in WRF-Chem. The bottom-up inventory is a hybrid of NOAA CSL

developed bottom-up inventories and regulatory emissions provided by US EPA through the National Emissions Inventory (NEI) 2017. The NOAA CSL developed inventories, include for mobile source engines (**F**uel-based **I**nventory of **V**ehicle **E**missions), volatile chemical products (VCPs), and cooking. Power plant emissions are updated using Continuous Emissions Monitoring System (CEMS) data. Other point and areawide emissions are taken from the NEI 2017. The purpose of the NOAA CSL developed inventories is to benchmark and evaluate uncertainties in key emission sectors, and not intended to replace gridded emissions from US EPA's Sparse Matrix Object Kernel Emissions (SMOKE) processor for regulatory modeling. Emissions outside of the US for international shipping, Mexico, and Canada are from the Copernicus Atmospheric Monitoring Service (CAMS) [*Doumbia et al.*, 2021]. A description of how mobile source, VCP and cooking emissions are estimated and gridded for WRF-Chem is provided below. Gridded maps of NO_x and VOC emissions for the contiguous US (D1) and California/Nevada (D2) domains are shown in Figures 11-2 and 11-3, respectively. These gridded emission files will be made available on the SUNVEx 2021 website (https://csl.noaa.gov/projects/sunvex/).

Table 11-2. Sum of anthropogenic CO, NO_x and VOC emissions (metric tons/d) in Clark County for the FIVE-VCP + NEI17 inventory with comparison to NEI17.[a]

Sector	FIVE-VCP21 CO	NEI17 CO	FIVE-VCP21 NO_x	NEI17 NO_x	FIVE-VCP21 VOC	NEI17 VOC
Mobile	**290**	**480**	**51**	**68**	**31**	**39**
Onroad	103	250	33	36	14	21
Offroad	185	232	18	32	17	18
VCPs	--	--	--	**--**	**106**	**44**
Cooking	--	--	--	**--**	**29**	**<1**
Other Anthro.	24	29	16	19	21	16

a. FIVE-VCP emissions are for July 2021. NEI17 emissions are annual totals from: https://www.epa.gov/air-emissions-inventories/2017-national-emissions-inventory-nei-data

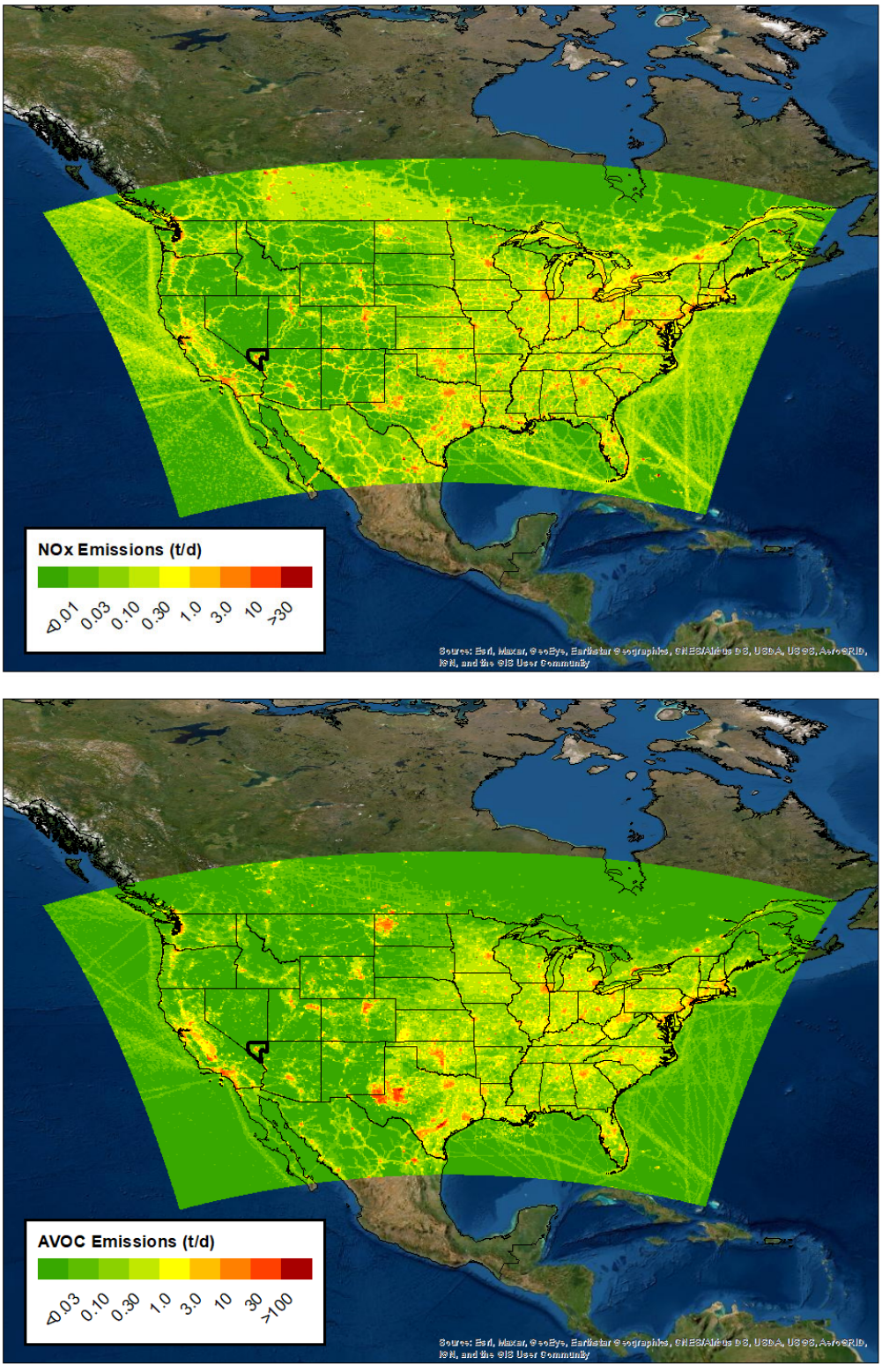

Figure 11-2. Map of anthropogenic NO_x and VOC emissions used in WRF-Chem for the contiguous US (D1) domain (12 km x 12 km). Emissions are specific to July 2021.

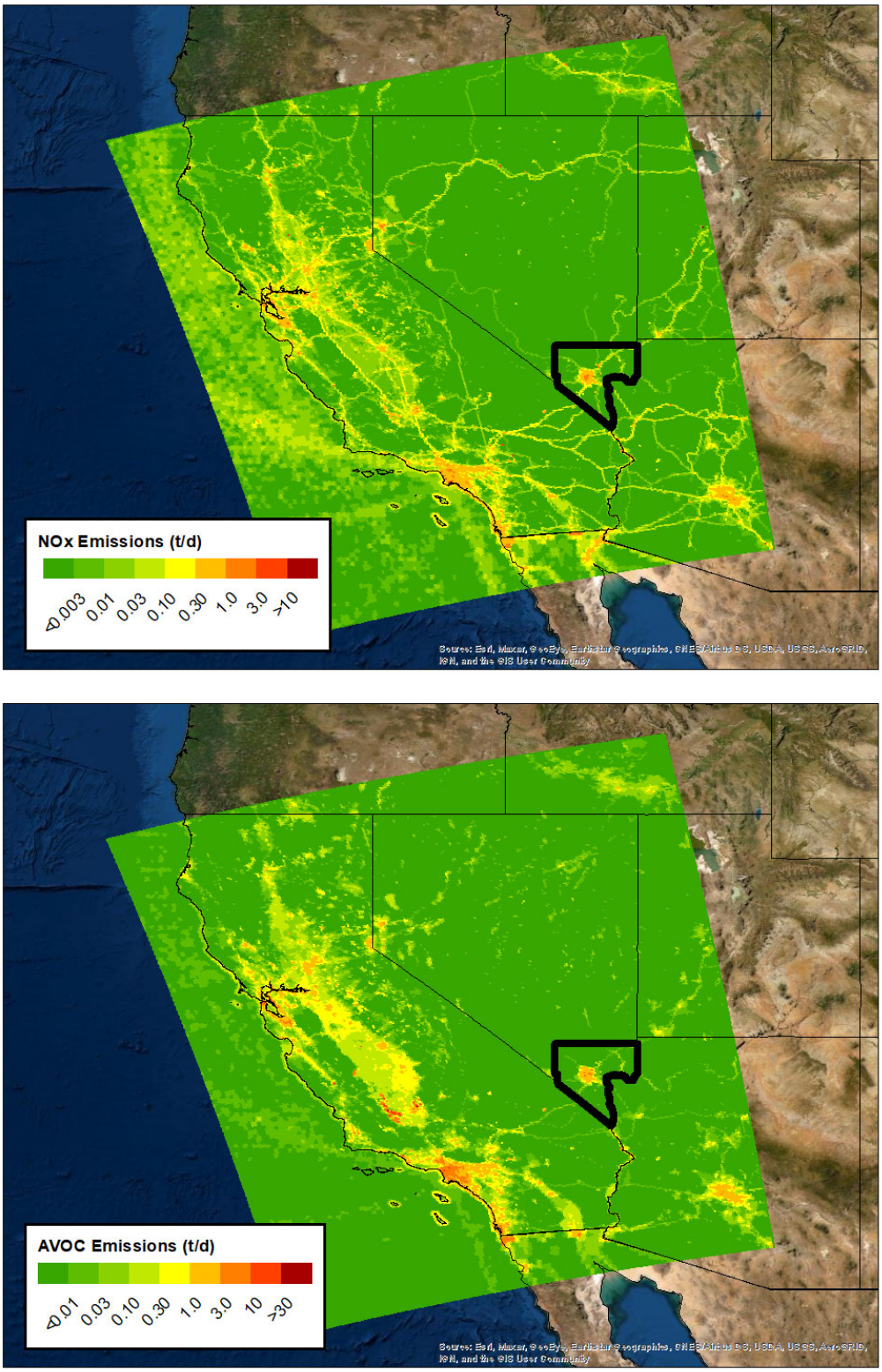

Figure 11-3. Map of anthropogenic NO_x and VOC emissions used in WRF-Chem for the California/Nevada (D2) domain (4 km x 4 km). Emissions are specific to July 2021.

Mobile Sources

The Fuel-based Inventory of Vehicle Emissions (FIVE) is utilized for mobile source engines [*McDonald et al.*, 2014; *McDonald et al.*, 2018b]. Briefly, fuel sales of on-road engines are reported by state by the U.S. Federal Highway Administration. Taxable gasoline and diesel fuel sales for road transportation are downscaled from the state-level to roadways using light- and heavy-duty vehicle count data from the Highway Performance Monitoring System (https://www.fhwa.dot.gov/policyinformation/hpms.cfm), respectively. Roadway-link specific data account for ~70% of gasoline and ~80% of diesel fuel sales nationally [*McDonald et al.*, 2014]. The remaining fraction of traffic is apportioned using population density as a spatial surrogate. Once fuel use is mapped, co-emitted air pollutant species can be estimated using fuel-based emission factors (e.g., g pollutant / kg fuel) derived from roadside measurements and laboratory studies. Fuel-based emissions factors have been published for light-duty gasoline and heavy-duty diesel vehicles for CO [*Hassler et al.*, 2016; *McDonald et al.*, 2013], NO_x [*McDonald et al.*, 2012; *McDonald et al.*, 2018b; *Yu et al.*, 2021], VOCs [*McDonald et al.*, 2018a; *McDonald et al.*, 2013], NH_3 [*Cao et al.*, 2022], and $PM_{2.5}$ [*McDonald et al.*, 2015]. An advantage of using fuel sales for on-road activity is that monthly fuel sales data are available for near real-time emissions adjustment [*Harkins et al.*, 2021]. Once the on-road emissions have been mapped, diurnal and day-of-week activity factors for light- and heavy-duty vehicles are applied separately to estimate hourly emissions [*McDonald et al.*, 2014]. The link-level traffic emissions from FIVE can be seen along major interstate corridors in Figures 11-2 (contiguous US) and 11-3 (California + Nevada).

FIVE also includes emissions for non-road engines in a similar manner. Off-road distillate fuel sales are reported by state by the Energy Information Administration (https://www.eia.gov/petroleum/fueloilkerosene/) and allocated to end uses following Kean et al. [2000]. Non-highway use of gasoline is reported by the Federal Highway Administration (https://www.fhwa.dot.gov/policyinformation/statistics/2020/mf24.cfm). Emission factors of co-emitted air pollutants (in g/kg fuel) are taken from the EPA NONROAD model [*EPA*, 2010]. Non-road engine emissions are mapped spatially and temporally using surrogates from the NEI 2017.

The VOC speciation profiles for gasoline and diesel engines are reported in McDonald et al. [2018a] and based on tunnel and laboratory studies, including profiles for liquid gasoline and headspace vapors distinct from exhaust [*Harley et al.*, 2000]. The FIVE mobile source inventory has been rigorously evaluated in previous modeling studies over Los Angeles [*Kim et al.*, 2016], Southeastern US [*McDonald et al.*, 2018b], and New York City [*Coggon et al.*, 2021], and with satellite NO_2 datasets [*Li et al.*, 2021]. Updates due to the COVID-19 pandemic are taken into account, including rebounding of traffic after lockdown efforts [*Harkins et al.*, 2021].

Table 11-2 shows that the FIVE CO, NO_x, and VOC emissions are lower than the NEI17 by 40%, 25%, and 21%, respectively. The larger discrepancies in CO are consistent with past comparisons between FIVE and MOVES [*McDonald et al.*, 2018b]. For Clark County, both FIVE and the NEI17 suggest that mobile source engines are the dominant source of NO_x emissions (>75%). For VOCs, the mobile source emissions in the bottom-up inventory contribute ~17% of the anthropogenic emissions in Clark County, consistent with the PMF results shown in Figure 8-10. The FIVE inventory simulated in WRF-Chem is further evaluated with ground measurements at both Jerome Mack (Las Vegas) and CalTech (Los Angeles) in Section 11.6.

Volatile Chemical Products

Following McDonald et al. [2018a], VCP emissions are estimated for coatings, inks, adhesives, personal care products, cleaning agents and pesticides. Briefly, VCP emissions were estimated by first performing a mass balance of chemical feedstocks and their distribution across a variety of products manufactured by the chemical industry. Average daily usage and VOC emission factors are reported in McDonald et al. [2018a] across the US. Long-term trends are taken into account using the same mass balance approach over time following Kim et al. [2022]. The VCP inventory reflects continuous efforts to lower the VOC content of chemical products, including architectural coatings and phasing out of solvent to waterborne formulations [*Stockwell et al.*, 2021].

Nationally, around ~60% of VCP emissions are for consumer uses and ~40% for agricultural and industrial uses [*McDonald et al.*, 2018a]. Agricultural pesticides are spatially and temporally allocated according to agricultural pesticide VOC emissions from the NEI17. Industrial uses are similarly spatially and temporally allocated according to the point source VOC inventory from the NEI17. Consumer product emissions are spatially allocated using population density. Past NOAA CSL measurements in New York City and elsewhere have shown a strong population density dependence of consumer VCP emissions [*Coggon et al.*, 2021; *Gkatzelis et al.*, 2021b]. Diurnal profiles for personal care product emissions are shown to peak in the morning and exponentially decay across the day [*Coggon et al.*, 2016]. Other VCP sectors use diurnal profiles from the NEI17, which exhibit a midday peak. Detailed VOC speciation profiles were compiled in McDonald et al. [2018a] and updated to the latest California Air Resources Board surveys of consumer products and architectural coatings in Coggon et al. [2021].

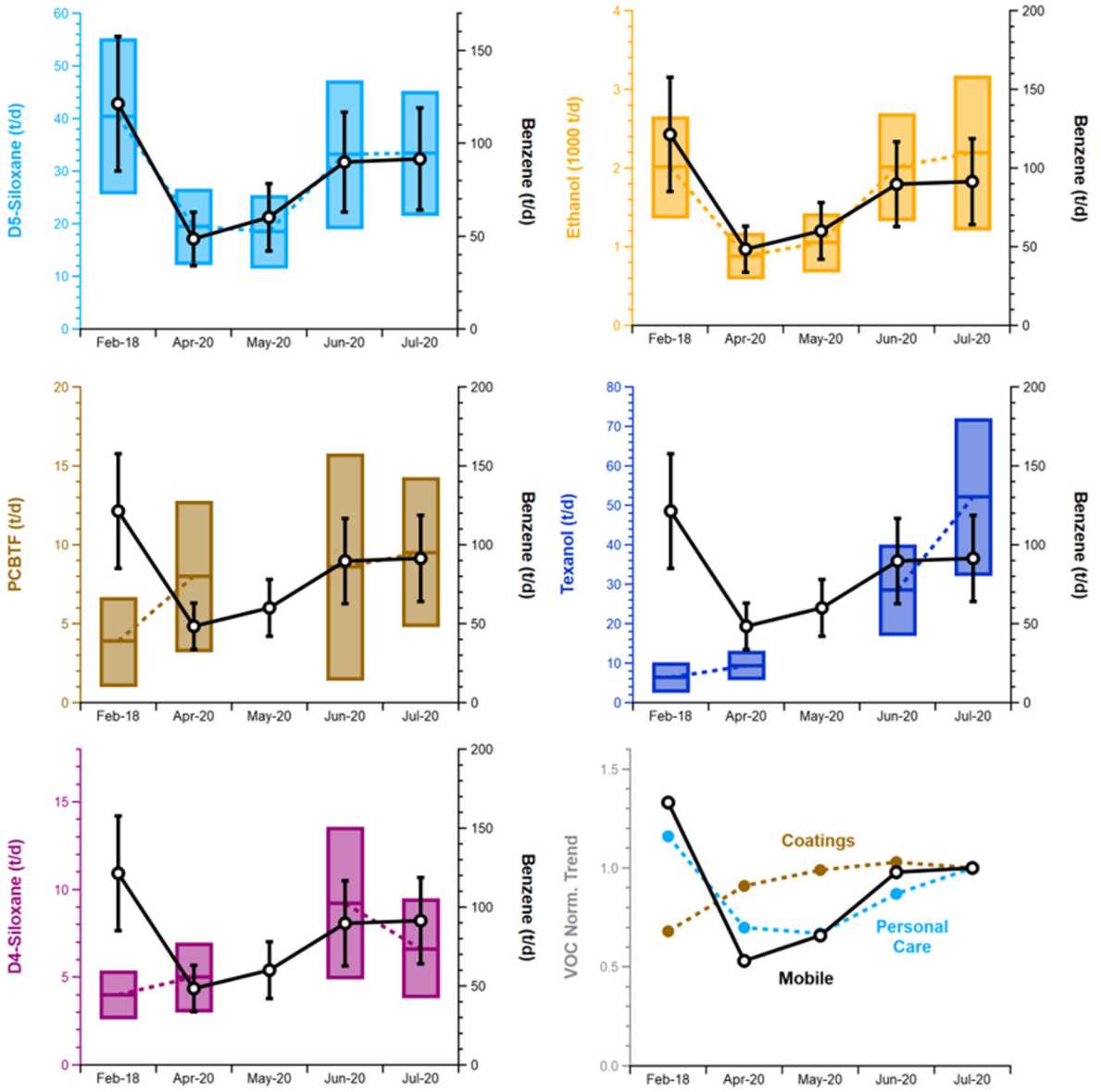

Figure 11-4. Trend of VCP emissions tracers in Boulder, CO due to COVID-19 pandemic. Bottom right panel shows trend in monthly sales of coatings and personal care products according to US Census Bureau data.

Current work in NOAA CSL include on generating near real-time (NRT) emission inventories, to address rapid changes in human activity due to the COVID-19 pandemic. Figure 11-4 shows trends in VCP emissions inferred from measurements in Boulder, CO (https://csl.noaa.gov/groups/csl7/measurements/2020covid-aqs/). VCP emissions are inferred from calculating enhancement ratios of VCP tracers relative to benzene for D5-siloxane (personal care), ethanol (personal care + cleaning), parachlorobenzotriflouride (solvent-borne coatings), Texanol (waterborne coatings), and D4-siloxane (adhesives). The enhancement ratios are multiplied by benzene emission trends from FIVE that account for COVID-19 [*Harkins et al.*, 2021]. The emission trends are consistent with monthly sales adjusted for

inflation of Health and Personal Care and Building Material stores reported by the US Census Bureau. The VCP emissions for this project have been adjusted using these monthly retail statistics adjusted for inflation through the summer of 2021.

Table 11-2 shows that the VCP VOC emissions are higher than the NEI17 by a factor of 2-3, which is consistent with McDonald et al. [2018a]. The dominance of VCPs as a source of anthropogenic VOC emissions in Clark County (~60%) is consistent with the PMF results shown in Figure 8-10, and inconsistent with the NEI17 (<50%).

Cooking

While cooking VOC emissions are included in the NEI17, they are at least an order of magnitude lower than reflected in the ambient measurements made in Las Vegas and Los Angeles as part of SUNVEx 2021 (Table 11-2). Figure 11-5 shows VOC/CO correlation plots for tracers of mobile sources (benzene), personal care products (D5-siloxane) and cooking (nonanal). Since it is expected that cooking emissions vary according to population density similar to VCPs, a per capita cooking emissions factor of ~8 g VOC/person/d is estimated using the D5-siloxane/CO and nonanal/CO enhancement ratios, and their corresponding mass fractions in VCPs and cooking, respectively. The cooking VOCs are then gridded according to population density and diurnally allocated using the NEI 2017. Lastly, the emissions are speciated according to the VOC cooking fingerprint shown in Figure 8-8.

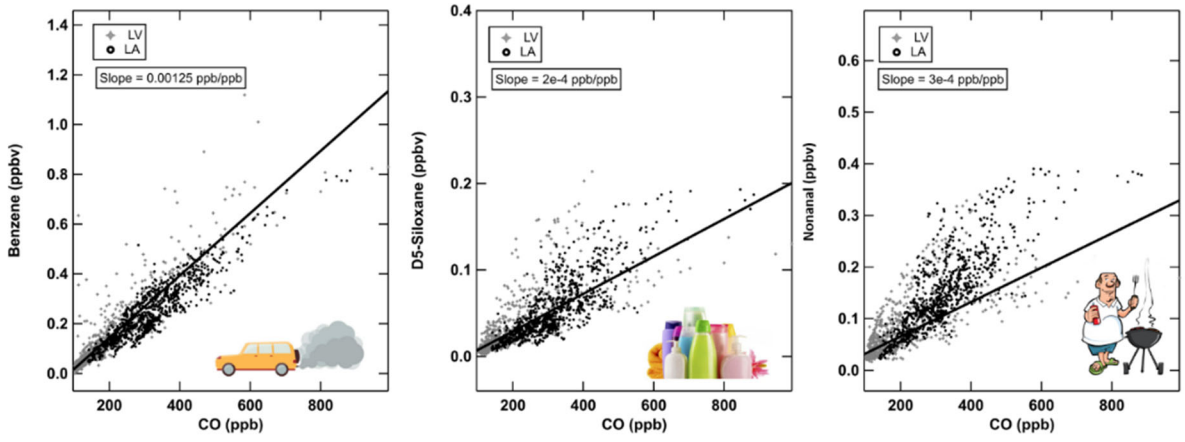

Figure 11-5. VOC/CO correlation of PTR-ToF-MS measurements at Jerome Mack (Las Vegas) and CalTech (Los Angeles) for a mobile source, VCP and cooking tracer.

Other Anthropogenic

Emissions from electricity generating units are updated to include Continuous Emissions Monitoring Systems (CEMS) data for July 2021. Stack parameters and plume-rise are taken into account in WRF-Chem. Other point and areawide emissions are taken from the NEI17 and applied with near real-time scaling factors similar to VCPs. Appendix Table A-1 lists how source sectors are subset by Source Classification Codes (SCC), and the datasets used to adjust individual sectors in near real-time. By summer of 2021, reduced human and economic activity due to COVID-19 lockdowns had largely rebounded. Table 11-2 shows that the other areawide and point source emissions when applied with the near real-time scaling factors are similar to those reported in the NEI17.

VOC/CO Analysis of FIVE-VCP

Because the FIVE-VCP inventory is developed across the contiguous US, the emissions can be evaluated using the detailed VOC and CO measurements made during SUNVEx in both Los Angeles and Las Vegas. Figure 11-6 shows the inventory VOC/CO ratio on the vertical axis and those observed at the ground sites on the horizontal axis. To minimize the effects of photochemistry on deriving emission ratios from observations, the inventory is compared with nighttime emission ratios. Nighttime emission ratios have been shown to be consistent with using daytime values corrected for photochemical aging [*Borbon et al.*, 2013], and does not result in inventory-observation mismatches. Overall, the agreement in the FIVE-VCP inventory and ambient observations is strong in both cities, increasing confidence in the anthropogenic VOC inventory over the California/Nevada domain. The species evaluated against are predominantly found in mobile source and VCP emissions, including alkanes (dark blue), cycloalkanes (light blue), alkenes (yellow), aromatics (green), oxygenates (red) and halocarbons (purple).

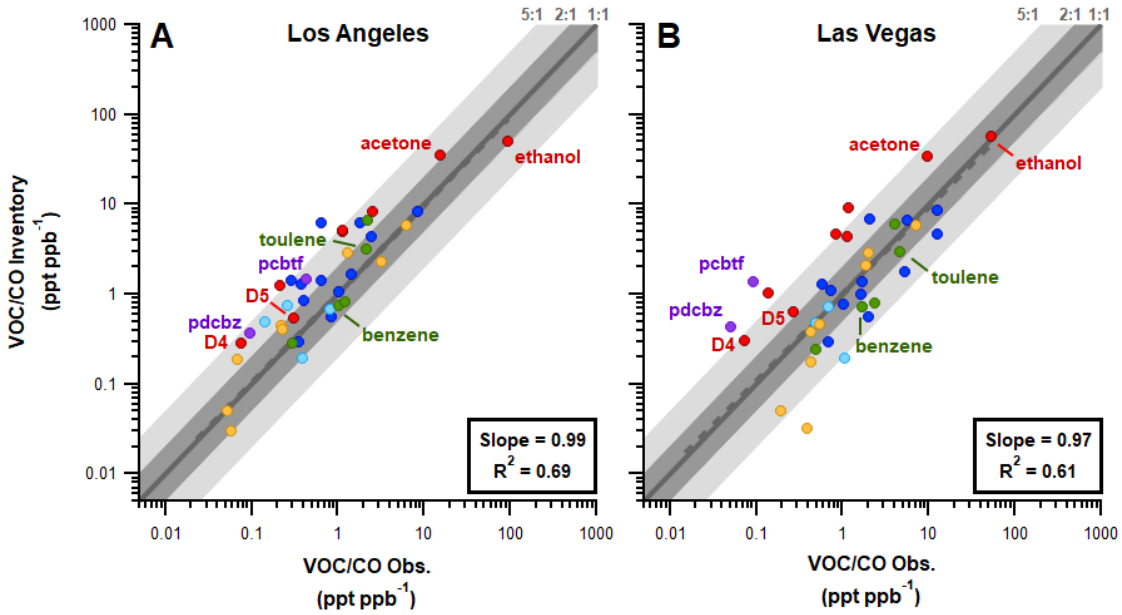

Figure 11-6. VOC/CO correlation of measurements at Jerome Mack (Las Vegas) and CalTech (Los Angeles) for ~40 VOC species in mobile source and VCP emissions.

11.4 Biogenic emissions

Biogenic emissions are simulated with the Biogenic Emissions Inventory System (BEIS) v3.14 [*Pierce et al.*, 2002]. While there are newer versions of BEIS available for other modeling platforms (e.g., CMAQ), v3.14 is currently the biogenic inventory coupled with WRF-Chem. While updating the BEIS inventory to newer versions is not feasible in the timeframe of this study, extensive evaluation with the NOAA CSL mobile laboratory is provided in Section 11.6 to provide a "top-down" observation-based constraint on biogenic VOC emissions. Isoprene and monoterpene emissions are added for urban vegetation based on a taxonomy of the South Coast air basin [*Benjamin et al.*, 1996]. Figure 11-7 shows a map of isoprene and monoterpene emissions generated from the simulations. Table 11-3 summarizes the biogenic VOC emissions using BEIS v3.14 with the addition of urban vegetation, whose emissions are calculated online with WRF-Chem meteorology (i.e., specific to July 2021). The top-down estimates are also provided here, which are ~3 times lower. The derivation of the top-down estimate is provided in Section 11.6, as well as discussion of discrepancies. We also checked the biogenic VOC emissions from BEIS v3.14 with summary tables of v3.61 released with the NEI 2017 (https://www.epa.gov/air-emissions-inventories/2017-national-emissions-inventory-nei-data). While the comparison is not direct since BEIS v3.61 was simulated with 2017 meteorology, and here we are simulating 2021 meteorology, the average temperature was similar across the two years in July (~35 ºC). To first order, the total amount of biogenic VOC emissions over Clark County is similar in BEIS v3.61 to what was simulated in WRF-Chem. It is unlikely that newer versions of BEIS will fix the factor of ~3 discrepancies shown in Table 11-3.

Table 11-3. Biogenic VOC emissions in Clark County for July 2021 (metric tons/d).

Species	**BEIS v3.14** (Jul 2021)	**Top-Down** (Jul 2021)	BEIS v3.61 (Jul 2017)
Isoprene	100	40	--
a-Pinene	160	65	--
Limonene	40	20	--
∑ =	300	125	330

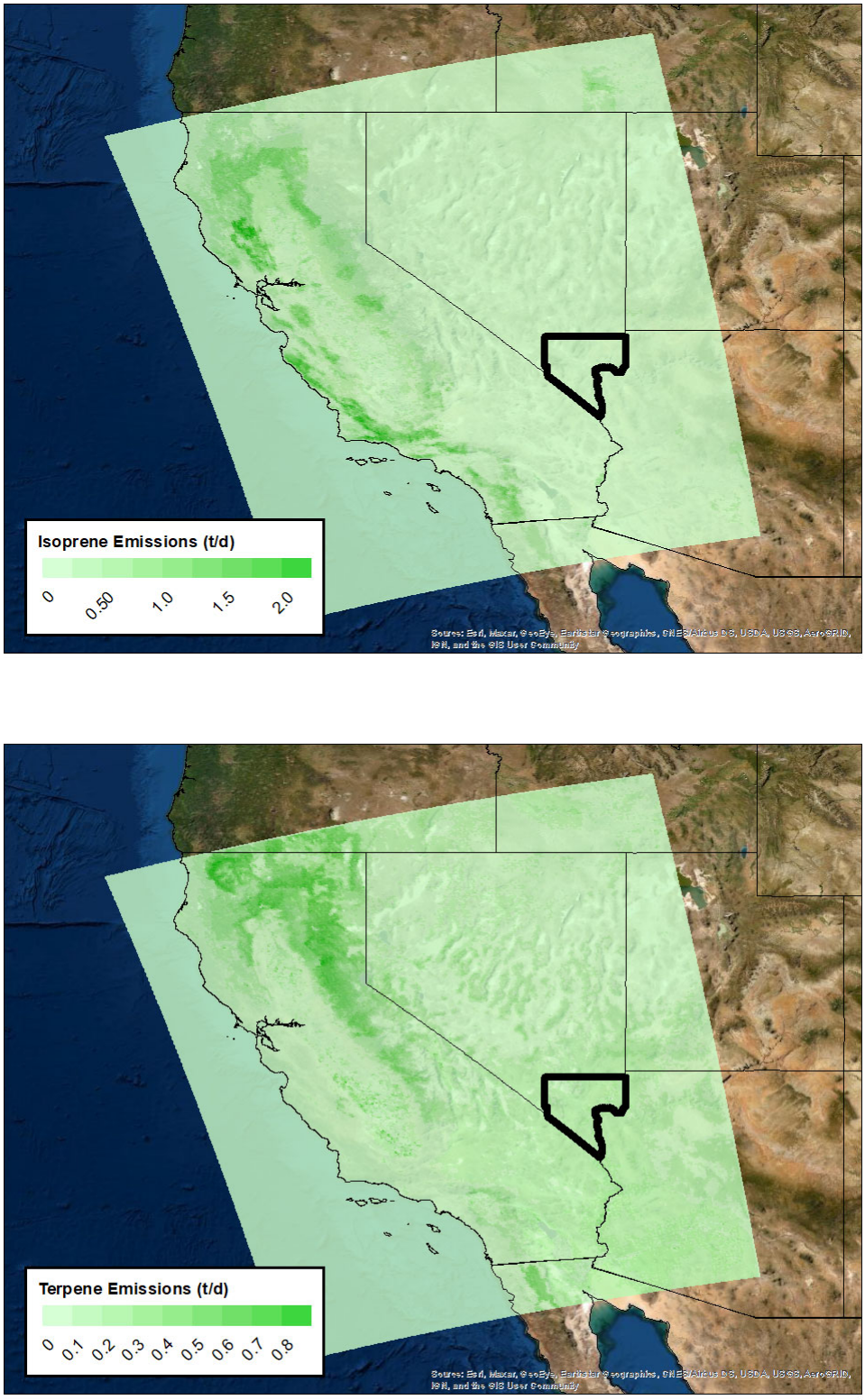

Figure 11-7. Map of biogenic isoprene and monoterpene emissions simulated in WRF-Chem for the California/Nevada (D2) domain (4 km x 4 km). Emissions are specific to July 2021.

11.5 Wildfire emissions

Model sensitivity cases are performed in the contiguous US (D1) domain using a newly developed wildfire emissions inventory called the Regional Hourly Advanced Baseline Imager (ABI) and Visible Infrared Radiometer Suite (VIIRS) Emissions, or RAVE [Li et al., 2022]. The ABI is onboard NOAA's GOES-16 and GOES-17 geostationary satellites, which detect the location of wildfires and their intensity with fire radiative power (FRP) over North America. The VIIRS onboard the NOAA-20 polar-orbiting satellite provides global coverage of FRP. The two satellite detectors of wildfires are blended together to create RAVE. The intensity of FRP provides a basis for estimating air pollutant emission factors. Here, wildfire emission factors compiled in the literature [Andreae, 2019] are combined with FRP from RAVE. Maps of wildfire emissions for July 2021, generated from RAVE with revised biomass burning emission factors, are shown in Figure 11-8.

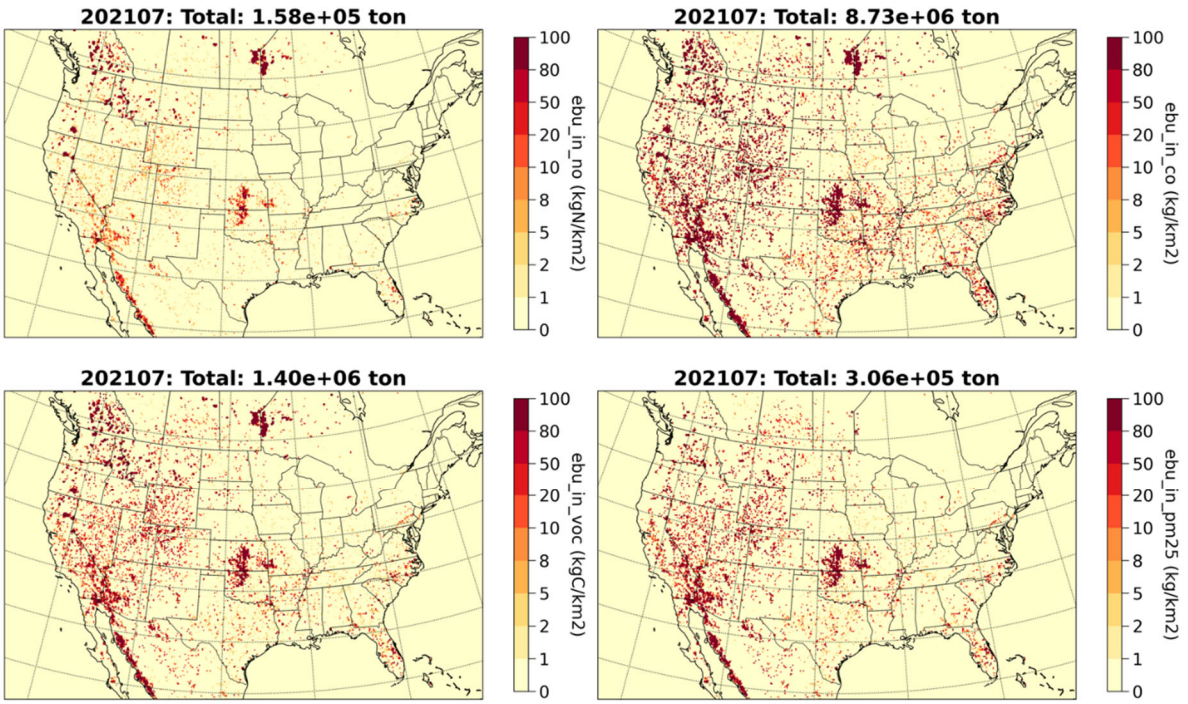

Figure 11-8. Map of RAVE wildfire emissions input into WRF-Chem for the contiguous US (D1) domain (12 km x 12 km) for (top left) NO, (top right) CO, (bottom left) VOC, and (bottom right) $PM_{2.5}$. Emissions are specific to July 2021.

11.6 Baseline WRF-Chem evaluation

To summarize, the baseline model simulation utilizes the meteorological and chemistry options listed in Table 11-1. Anthropogenic emissions are from the FIVE-VCP

inventory for mobile sources and VCPs. Cooking emissions are scaled relative to VCPs using the ambient ground site measurements. Other areawide and point source emissions are based on the NEI17 with near real-time adjustments. Anthropogenic emission totals for Clark County are summed in Table 11-2. In the base simulation, biogenic emissions are from BEIS v3.14 with added urban vegetation as summed in Table 11-3. Wildfires are excluded from the base simulation given large uncertainties in emissions, plume-rise and transport, and smoke chemistry. Sensitivity simulations are performed in Section 11.7 to assess the role and uncertainties of biogenic VOC and wildfire smoke on ozone concentrations in Clark County. The evaluation of the baseline simulation is performed for (1) meteorology, (2) ozone and its precursors, and (3) biogenic emissions using the California/Nevada (D2) domain.

Meteorological Evaluation

The Doppler Lidar located at North Las Vegas airport and described in Section 2 was used to evaluate the PBL height (Figure 11-9) and wind profiles (11-10) of WRF. In general, WRF was able to reproduce the strong growth in the PBL in the middle of the day (up to 5000 m) with a slight upward bias of ~200 m on average. While WRF generally performed well overall, the wide spread in the absolute bias suggests challenges with capturing the evolution of the PBL on specific days. The biases are most pronounced during a heatwave period that occurred between July 5th through 12th. Though the median bias in the PBL is similar at night, the percentage differences is large given the shallow nighttime boundaries observed. Figure 11-11 shows that WRF captures surface temperature (at 2 m) with a median bias of 0.1 K. The evaluation of surface temperature is performed with the MELODIES-MONET package (https://csl.noaa.gov/groups/csl4/modeldata/melodies-monet/), which is a tool that has been developed between NOAA and NCAR to systematically analyze model output (e.g., WRF-Chem) with surface observations, including Airnow/AQS.

Wind profiles from WRF are evaluated with the Doppler Lidar in Figure 11-10. Summary statistics of the model bias for wind speed and wind direction are in Table 11-4, and subset between the free troposphere (FT) and boundary layer (BL). The median bias in wind speed (-1.9%) and wind direction (+1.8 degrees) is small over the duration of the campaign. When data are subset between the boundary layer and free troposphere, there are persistent upward biases in wind speed in the boundary layer (+26%) that are compensated by lower wind speeds in the free troposphere (-8.6%). Overall, WRF captures the evolution of the PBL, temperature, wind speed and wind direction over the course of the field campaign. While there are areas for improvement in the representation of vertical mixing between the boundary layer and free troposphere, the model biases are within the uncertainties of other components of the model, including for anthropogenic and biogenic emission inputs.

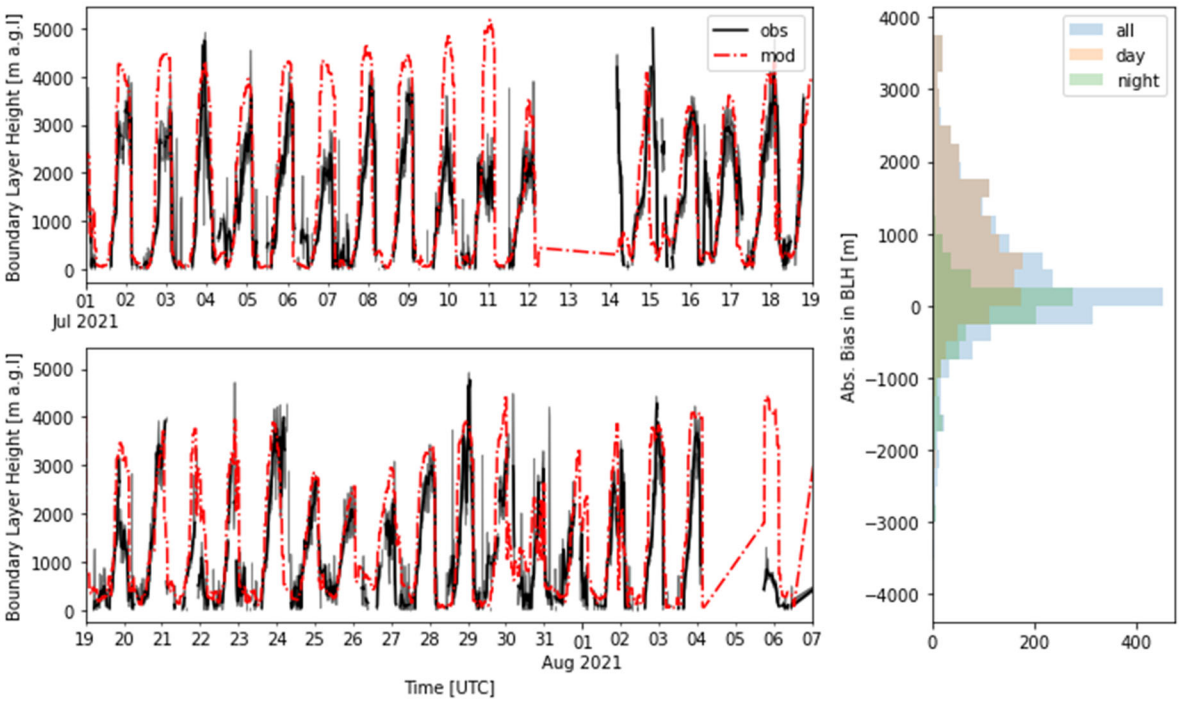

Figure 11-9. Evaluation of WRF with PBL height retrieved from Doppler Lidar located at North Las Vegas airport (July 1 to August 4, 2021). Model predicted boundary layer height is shown in red and observations in black. Distribution of absolute bias is shown to the right.

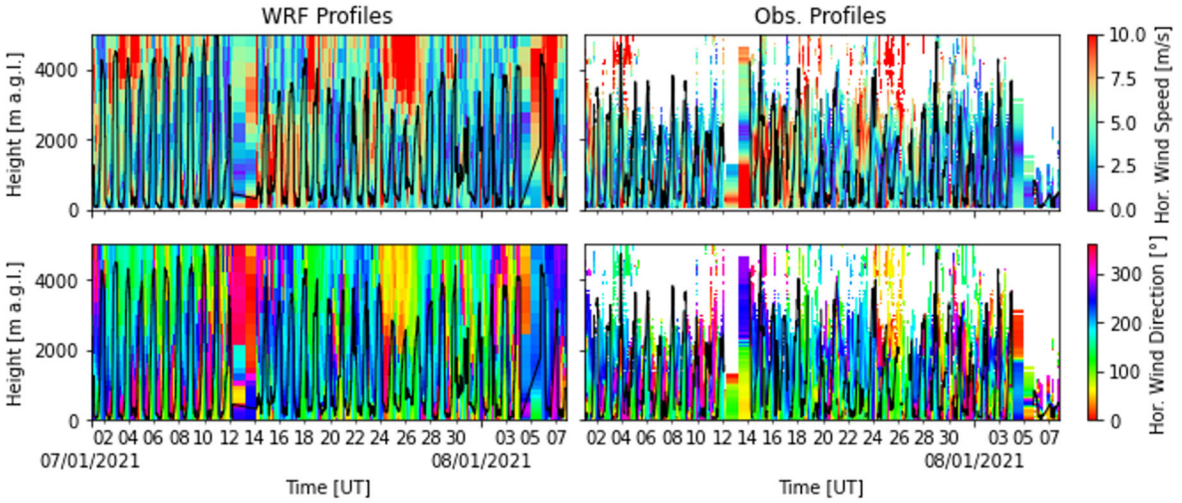

Figure 11-10. Evaluation of WRF wind profiles with the Doppler Lidar located at North Las Vegas airport.

Table 11-4. Bias of WRF-Chem Wind Speed and Wind Direction with Doppler Lidar

WSpd [%]	Median	Std	WDir [°]	Median	Std
All	-1.9	190	All	1.8	52
FT	-8.6	185	FT	-0.55	52
BL	26	206	BL	11.6	52
Day, all	2.1	180	Day, all	1.7	54
Day, FT	-11	176	Day, FT	-4.2	55
Day, BL	30	184	Day, BL	14	47
Night, all	-5.1	202	Night, all	1.9	51
Night, FT	-7.2	192	Night, FT	1.9	49
Night, BL	15	252	Night, BL	2.0	62

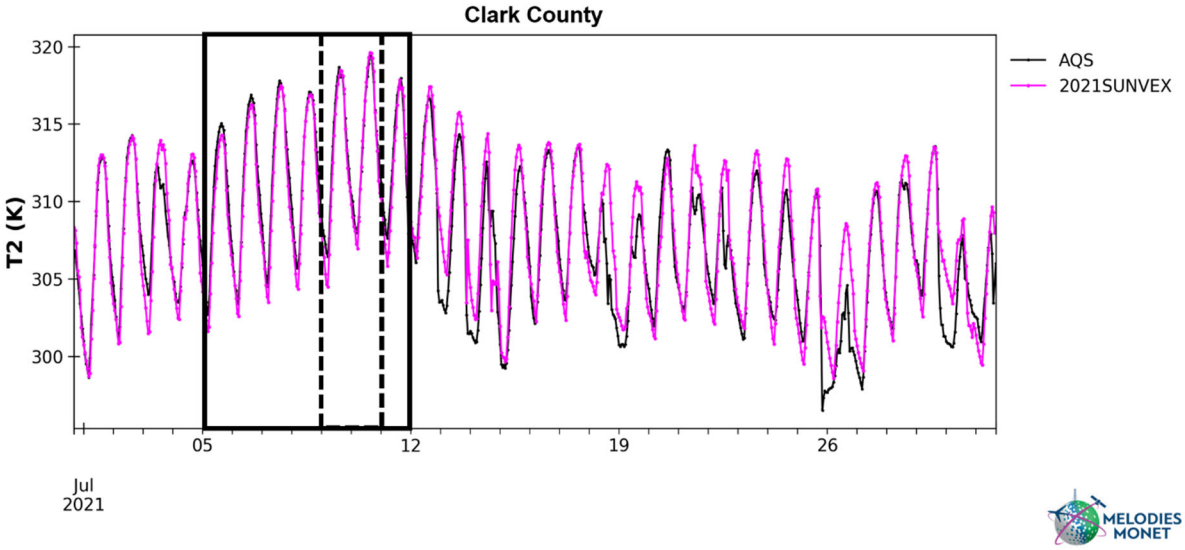

Figure 11-11. Evaluation of WRF surface temperature at 2 m (pink line) with Airnow (black line) over Clark County. Solid black box shows period simulated for ozone sensitivity simulations (7/5 to 7/12) capturing a heatwave event. Dashed black box outlines the highest MDA8 ozone days during this period.

Ozone and Precursors Evaluation

The baseline model is evaluated with several datasets to assess how well WRF-Chem captures ozone concentrations, and precursor emissions of NO_x and VOCs. The model is evaluated with both local measurements in Clark County, and across the broader California/Nevada domain. Satellite observations of nitrogen dioxide (NO_2) from the Sentinel-5P/TROPOMI provide a broader context for evaluating the model's performance of NO_x emissions [*Li et al.*, 2021].

Evaluation of WRF-Chem with NOAA measurements for the Jerome Mack (Las Vegas) and CalTech (Los Angeles) ground sites are shown in Figures 11-12 and 11-13, respectively. Evaluation of WRF-Chem is performed on both sites because the FIVE-VCP is constructed in the same way for both cities, and enhances confidence in regional transport of air pollution from California to Nevada. The differences in model biases also provide a range of uncertainty for the FIVE-VCP + NEI17 emissions inventory input into the model. The evaluations are limited to daytime hours (9 AM to 6 PM) due to large uncertainties with simulating the PBL height at nighttime.

CO is overestimated by 30 ppb in Las Vegas and underestimated by 46 ppb in Los Angeles. While the biases offset one another, the challenges with modeling CO suggest that it is becoming harder and harder to use CO as a tracer for anthropogenic air pollution. As Table 11-2 indicates, a major source of CO emissions is from off-road engines, predominantly 2-stroke and 4-stroke engines used in recreational vehicles, lawn equipment, etc., and whose emissions are highly uncertain. Oxidation of biogenic VOC emissions [*McDonald et al.*, 2018b] and wildfire smoke can further complicate evaluation of CO emission inventories with ambient observations. Note that wildfire emissions have not been included in the baseline simulation so CO concentrations could increase with inclusion of wildfire smoke. For total reactive nitrogen ($NO_y = NO_x$ + PAN + HNO_3 + organic nitrates), WRF-Chem agrees with the observations within -2% to +23%, suggesting NO_x emissions are well-represented across the California/Nevada domain.

Three VOCs are included in Figures 11-12 and 11-13, isoprene represents a biogenic VOC, monoterpenes have contributions from both biogenic and anthropogenic sources within cities [*Coggon et al.*, 2021], and ethanol is the most abundant anthropogenic VOC with contributions mainly from VCPs and mobile sources [*Gkatzelis et al.*, 2021a]. All three species are represented explicitly in the RACM_ESRL_VCP chemical mechanism utilized in WRF-Chem, rather than lumping of multiple VOCs. WRF-Chem isoprene is +50% in Las Vegas and -50% in Los Angeles, reflecting significant uncertainties in estimating urban vegetation emissions. Monoterpenes are slightly overestimated by +35% in Las Vegas and substantially underestimated in Los Angeles (by 2.6x). In both cities, the monoterpene

emissions input into WRF-Chem over urbanized land area are dominated by urban vegetation (>95%), and thus model-observation discrepancies also suggestive of uncertainties in estimating urban vegetation emissions. The WRF-Chem ethanol concentrations are within ±20% for both cities, and an indication that the FIVE-VCP inventory is well representing anthropogenic VOC emissions.

Taken together, the good representation of anthropogenic NO_x and VOC emissions, and reasonable representation of biogenic isoprene (+50%) and monoterpenes (+35%) lead to strong ozone performance in WRF-Chem over Clark County. The model is able to match ozone concentrations at the Jerome Mack ground site with a slight +2.7 ppb bias. Figure 11-14 shows the model performance of hourly ozone with respect to AQS monitors as a time series using the MELODIES-MONET package. The top panel shows is over the California/Nevada model domain (median bias = +2.8 ppb, R^2 = 0.63). The bottom panel shows the evaluation limited to AQS sites over Clark County (median bias = +1.8 ppb, R^2 = 0.60). Figure 11-15 shows the same for MDA8 ozone for the California/Nevada domain (median bias = +2.9 ppb, R^2 = 0.62) and Clark County (median bias = +2.9 ppb, R^2 = 0.62).

Though wildfire emissions were not included in the baseline simulation, we further examined why WRF-Chem had a slight over-prediction of ozone. To check whether the ozone bias is due to global background concentrations from RAQMS, we evaluated WRF-Chem with ozonesonde data at Trinidad Head, CA (see location in Figure 11-1). The Trinidad Head site is part of the NOAA Global Monitoring Laboratory network, and during the month of July 2021, there were five days with launches occurring between 18 and 20 UTC (https://gml.noaa.gov/aftp/data/ozwv/Ozonesonde/Trinidad%20Head,%20California/100%20Meter%20Average%20Files/). The results are shown in Figure 11-16. Below the tropopause (<10 km), WRF-Chem tends to under-predict background ozone by ~3 ppb, although the model concentrations are well within the uncertainty band of the observations. It is unlikely that background ozone is the cause for the slight over-prediction.

Another potential explanation is the fidelity of the meteorological simulations. As Figure 11-9 illustrates, during the first half of July, WRF-Chem tended to over-predict the PBL height. After 7/14, WRF-Chem had strong performance in predicting PBL height. If we restrict the model-observation of ozone at the Jerome Mack site to the second half of July versus the whole month, the ozone bias is cut in half from +2.7 ppb to +1.4 ppb. The deeper simulated boundary layer (up to 5 km) could lead to higher entrainment of ozone in the upper troposphere/lower stratosphere that gets mixed down to the surface, thus contributing to the high ozone bias. This suggests more research is needed to improve PBL dynamics in models, especially under high heat events, as well as better representation of the urban canopy.

Lastly, we suggest updating chemical mechanisms could help with improving photochemical formation of ozone in the model. Evaluations of NO_x emissions in WRF-Chem with satellite TROPOMI NO_2 is shown in Figure 11-17. The comparison is performed following Li et al. [2021] where to facilitate a more direct comparison of satellite tropospheric vertical column densities (VCD) with WRF-Chem, an air-mass-factor (AMF) correction is performed utilizing the WRF-Chem model output. The spatial distribution of NO_2 is generally consistent over anthropogenic source regions between TROPOMI and WRF-Chem (Figure 11-17, top row). However, over rural background regions, NO_2 tends to be under-predicted in WRF-Chem likely due to missing wildfire emissions that can contribute NO_x. Over anthropogenic source regions, the slope of the regression of WRF-Chem vs. TROPOMI NO_2 provides an indication of the bias (Figure 11-17, bottom row). Over the whole California-Nevada domain, WRF-Chem is within ~10% of TROPOMI NO_2. Over Clark County specifically, WRF-Chem tends to over-predict NO_2 by ~40%. Over polluted regions, Li et al. [2021] reports that TROPOMI systematically underestimates tropospheric NO_2 columns by ~20% when compared to the NASA Aura/OMI satellite. Thus part of the model bias could be due to systematic underestimation of TROPOMI NO_2 over cities. The model bias is also due to uncertainties in photochemistry. While Figure 11-12 showed strong agreement between the model and observations for NO_y, which is a more conserved tracer of NO_x emissions, the model tends to over-predict NO_x (+20%) and NO_2 (+48%) as shown in Figure 11-18. Updating to more recent versions of the Madronich Photolysis (TUV) scheme could help with better representing the photochemistry of reactive nitrogen species, as well as the simulation of ozone.

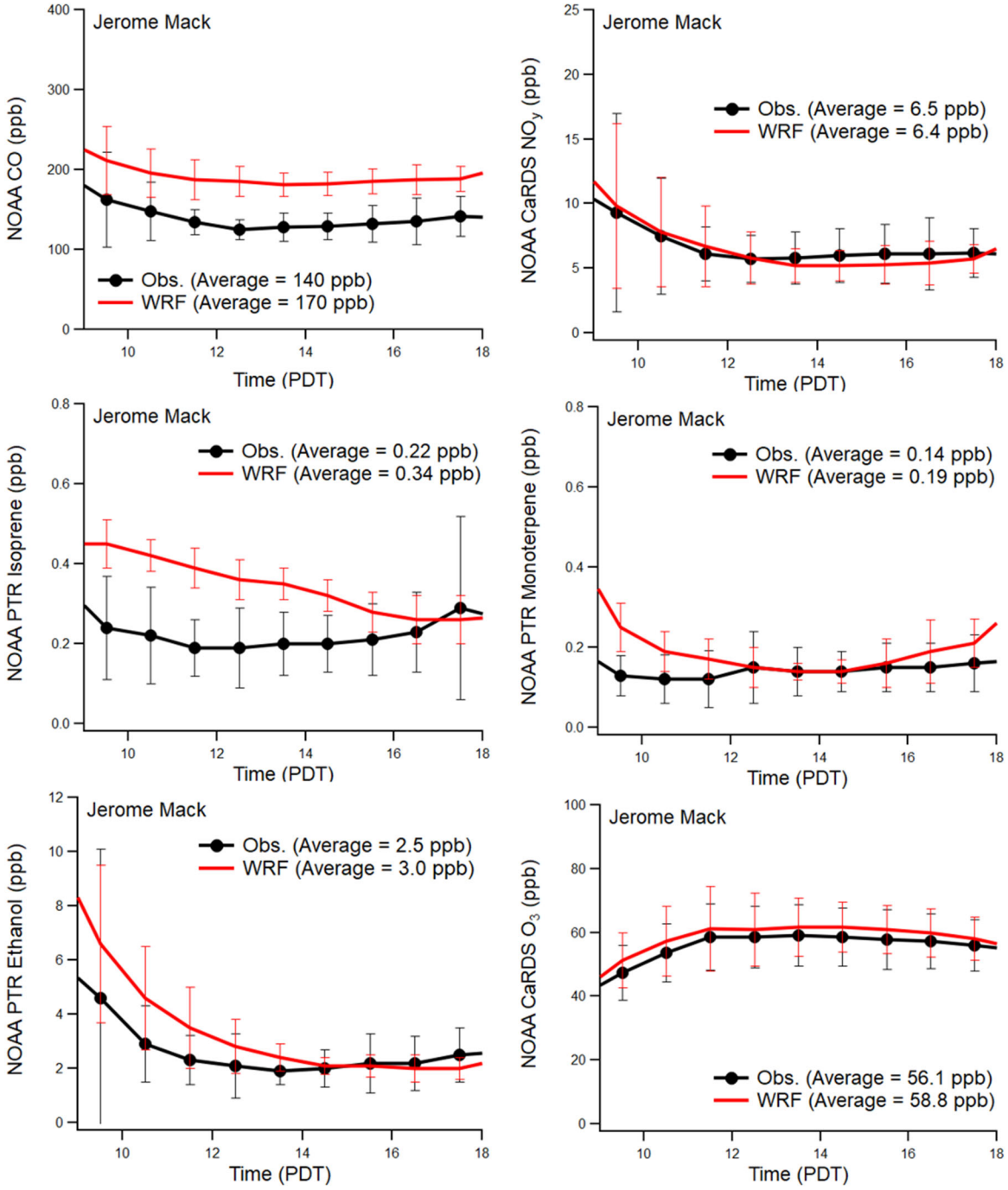

Figure 11-12. Evaluation of WRF-Chem (red lines) versus NOAA measurements (black lines) for CO, NO_y, VOCs and O_3 at the Jerome Mack ground site. Error bars reflect one standard deviation.

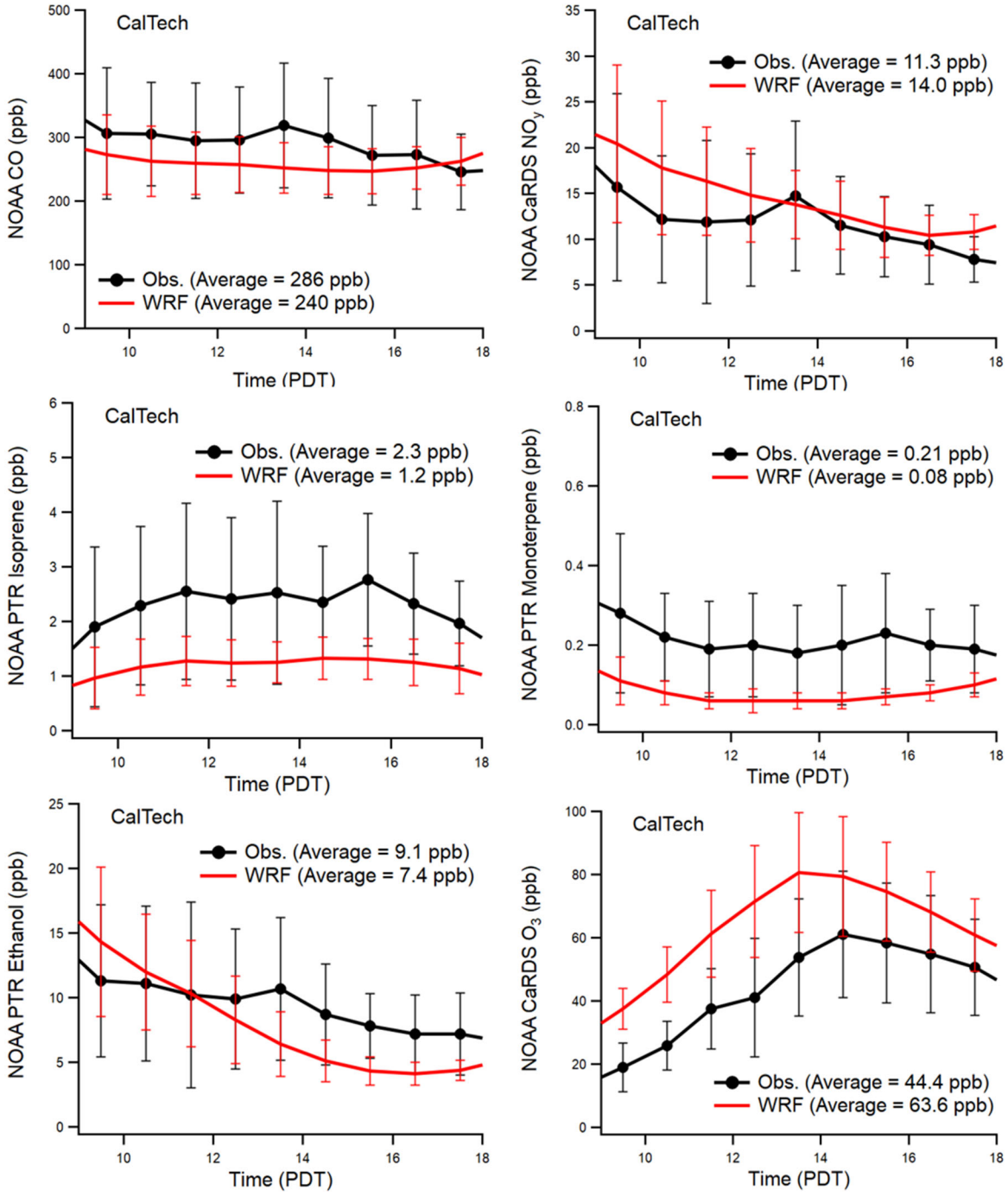

Figure 11-13. Evaluation of WRF-Chem (red lines) versus NOAA measurements (black lines) for CO, NO_y, VOCs and O_3 at the CalTech ground site. Error bars reflect one standard deviation.

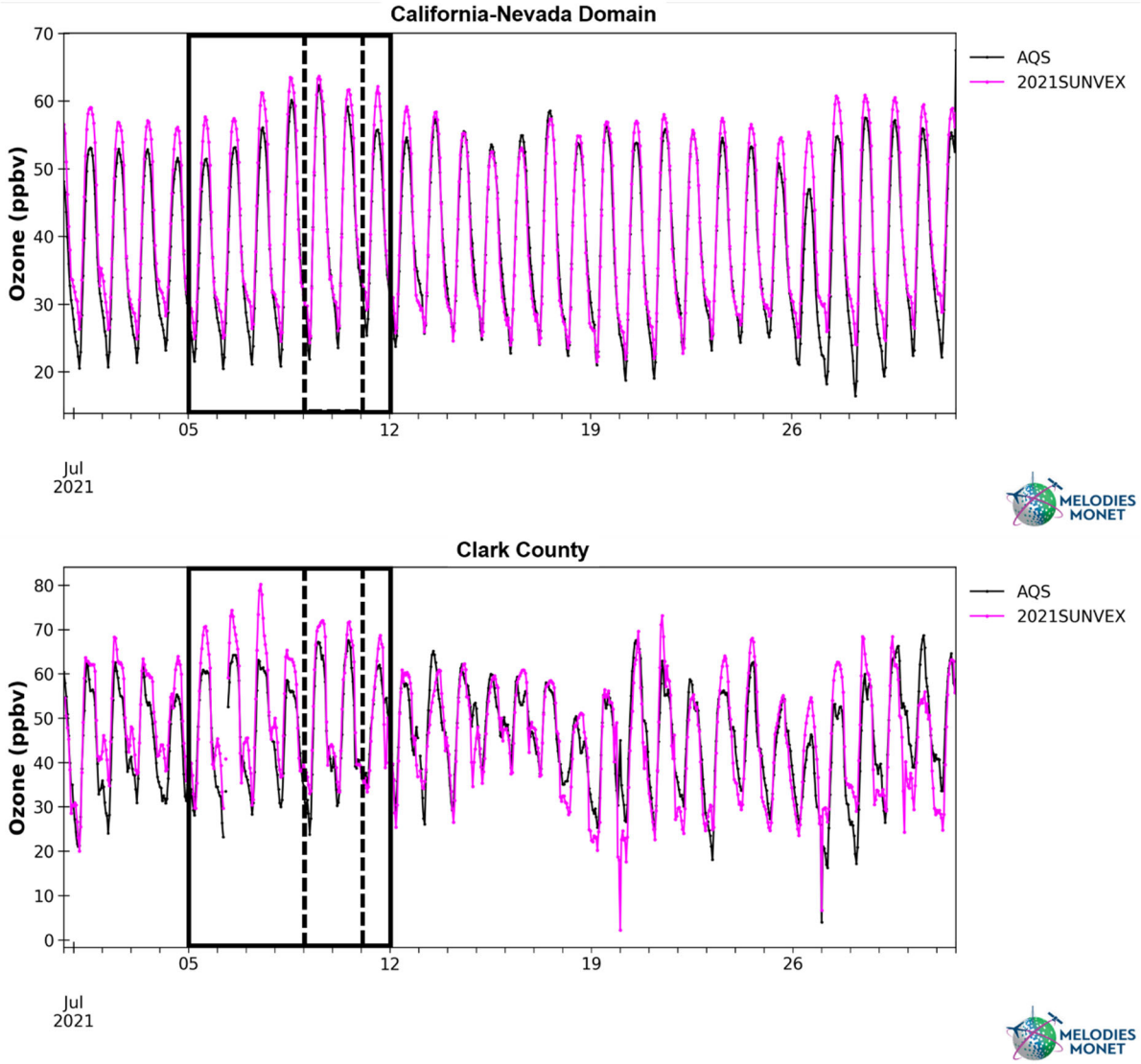

Figure 11-14. Evaluation of WRF-Chem hourly surface ozone (pink line) with Airnow (black line) over (top) California/Nevada domain and (bottom) Clark County. Solid black box shows period simulated for ozone sensitivity simulations (7/5 to 7/12) capturing a heatwave event. Dashed black box outlines the highest MDA8 ozone days during this period.

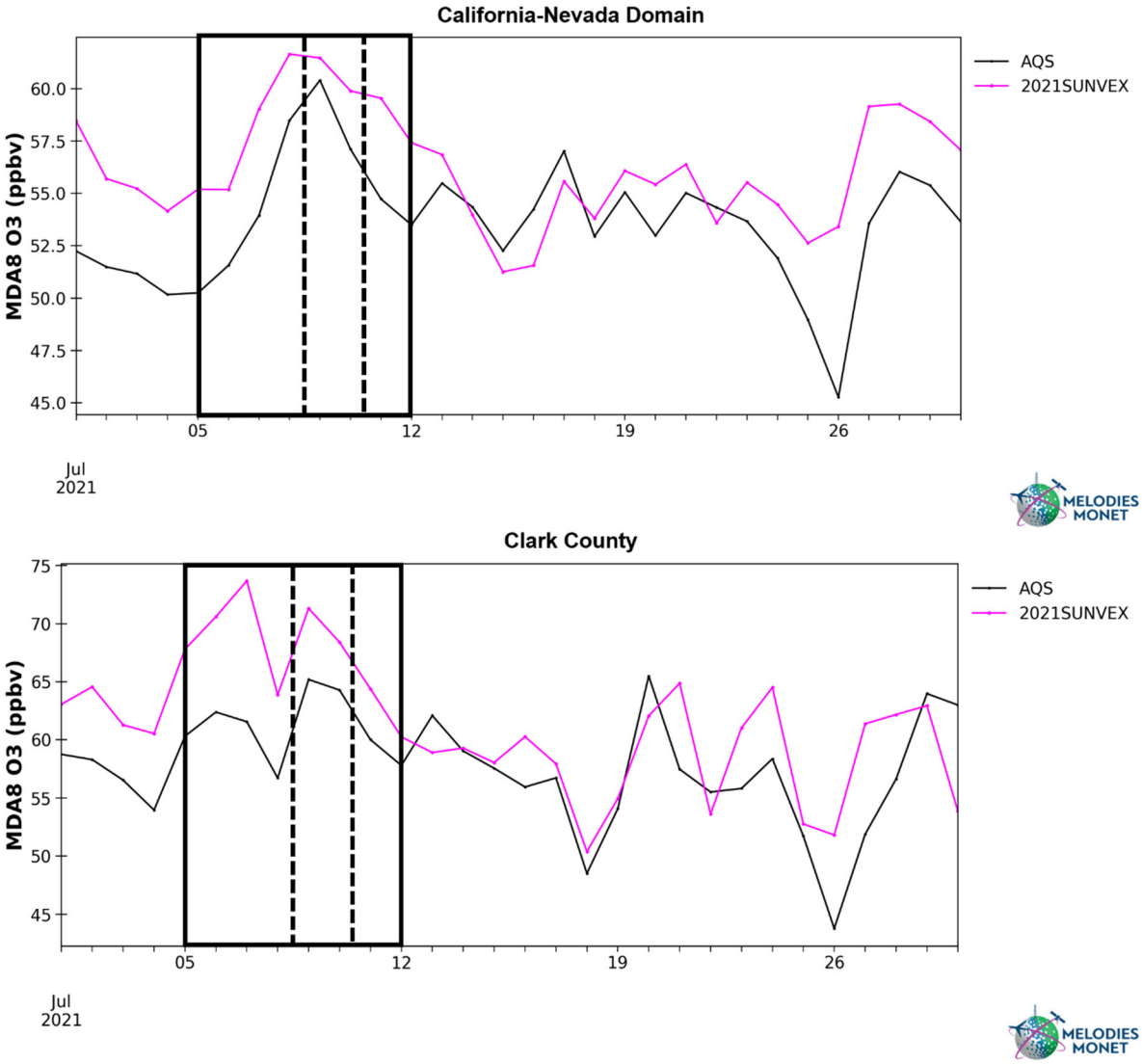

Figure 11-15. Evaluation of WRF-Chem MDA8 ozone (pink line) with Airnow (black line) over (top) California/Nevada domain and (bottom) Clark County. Solid black box shows period simulated for ozone sensitivity simulations (7/5 to 7/12) capturing a heatwave event. Dashed black box outlines the highest MDA8 ozone days during this period.

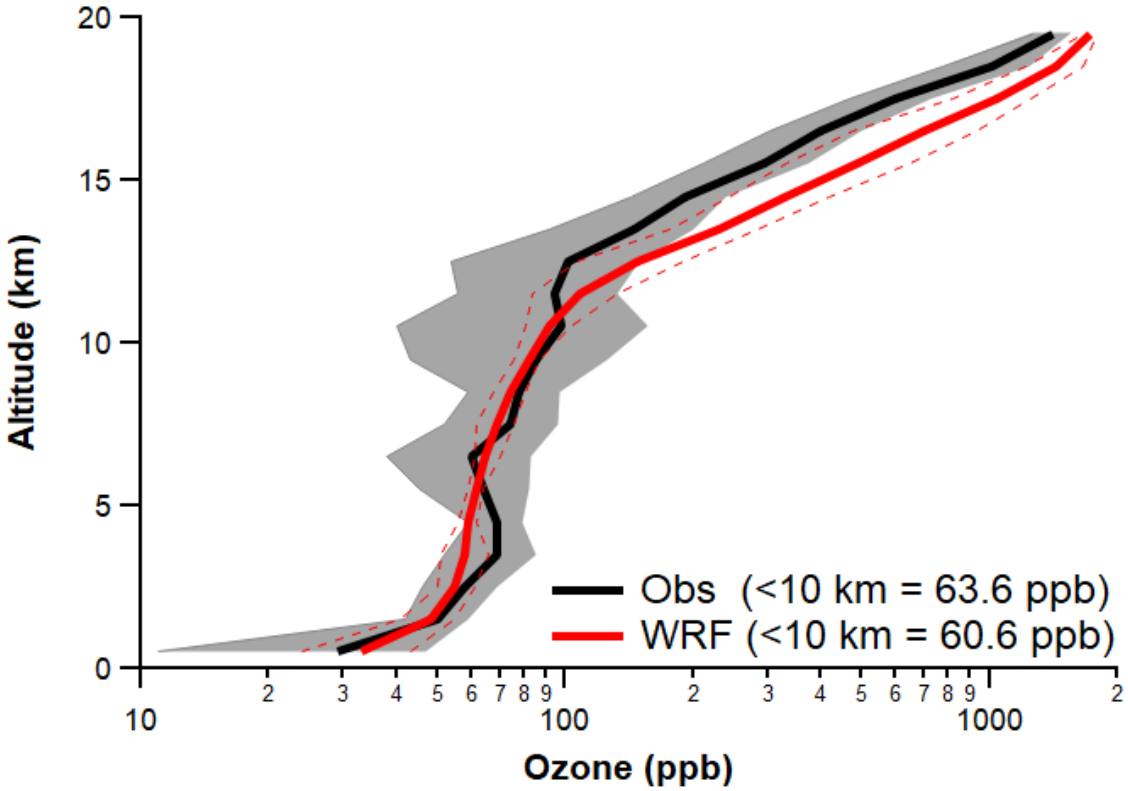

Figure 11-16. Evaluation of WRF-Chem ozone (red line) with ozonesonde profiles (black line) at Trinidad Head, CA (7/1, 7/9, 7/15, 7/22, and 7/30). Uncertainty bands reflect the 95% confidence interval of the mean.

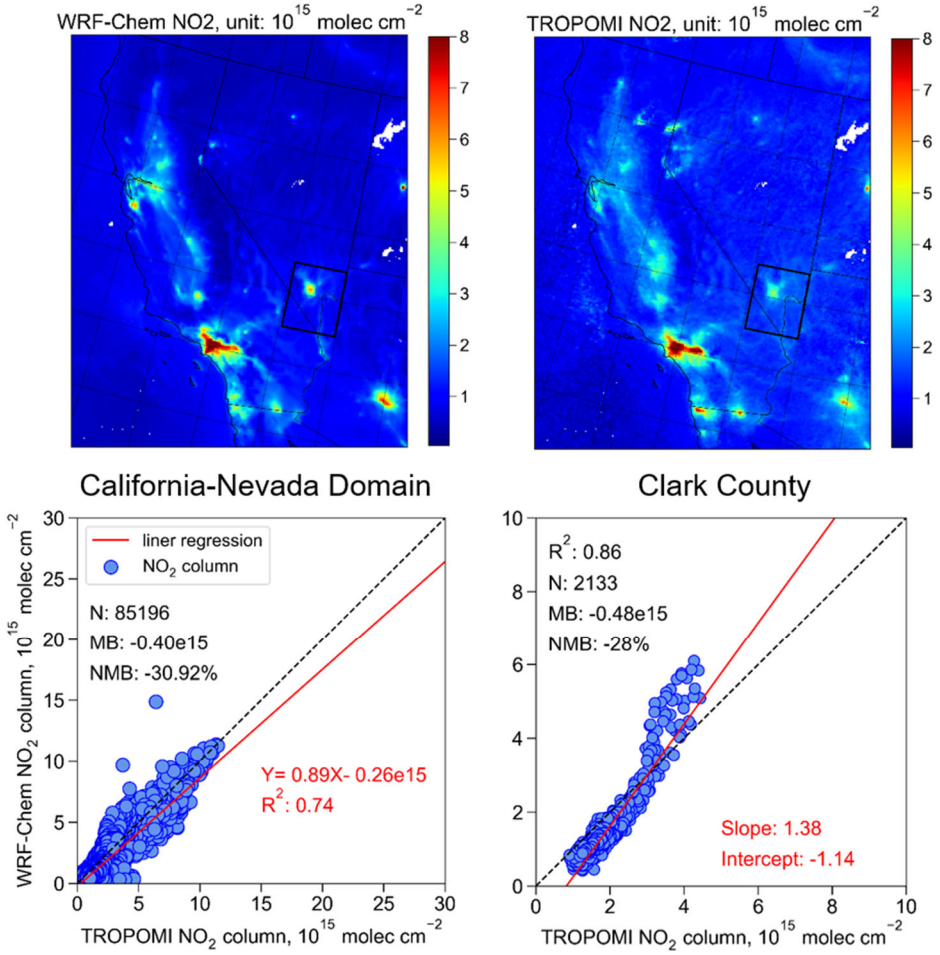

Figure 11-17. Evaluation of WRF-Chem (top left) with satellite TROPOMI tropospheric NO_2 VCD with (top right) for July 2021. Linear regression of WRF-Chem model versus TROPOMI NO_2 for (bottom left) California-Nevada domain and (bottom right) Clark County box shown as a black outline.

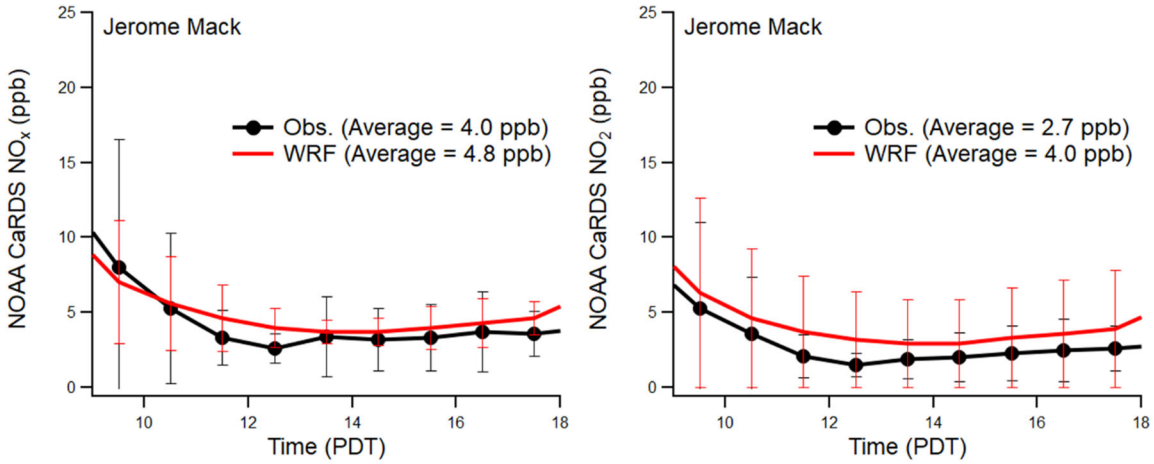

Figure 11-18. Evaluation of WRF-Chem (red lines) versus NOAA measurements (black lines) at the Jerome Mack ground site for NO_x and NO_2. Error bars reflect one standard deviation.

Biogenic Evaluation

As part of SUNVEx, the NOAA CSL mobile laboratory was driven outside of the city on 7 days (6/27, 6/28, 6/29, 7/28, 7/29, 7/30 and 7/31) specifically to assess biogenic emissions. Additionally, VOC instrumentation sampled biogenic emissions on two transit drives from Las Vegas to Los Angeles (8/2) and Los Angeles to Las Vegas (9/7). Coggon et al. [2021] demonstrated the utility of mobile lab drive data for evaluation of biogenic emissions in WRF-Chem at both urban and continental scales, and whose methodology is replicated here. Mobile lab observations are binned at 0.02 degrees x 0.02 degrees at 1-minute time resolution and matched to WRF-Chem using a nearest neighbor approach. Spatial maps of the mobile lab observations and WRF-Chem model are shown in the vicinity of Las Vegas (Figure 11-19) and for the transit drives to/from Los Angeles (Figure 11-20). The isoprene and monoterpene observations are from the PTR-ToF-MS. In urbanized portions of the domain, there is the potential for interferences from other species that load on masses detecting isoprene and monoterpenes. Thus, model-observation comparisons are focused on rural drives.

The drives outside of Las Vegas suggest that isoprene and monoterpene emissions in WRF-Chem could be overestimated by factors of 2.6 and 2.7, respectively (Figure 11-19). The Las Vegas-Los Angeles transit drives also show an overestimate of isoprene and monoterpenes by factors of 2.5 and ~10, respectively (Figure 11-20). BEIS v3.14 does employ a temperature cap at 315 K accounting for heat stress [*Pouliot and Pierce*, 2009]. To test the sensitivity of ozone to uncertainties to biogenic VOC emissions, a top down estimate is made by: (1) scaling down rural emissions in Clark County according to drives in the vicinity of Las Vegas, (2) scaling down California/Nevada emissions outside Clark County according to transit drives, and (3) scaling up South Coast air basin BVOC emissions according to the CalTech ground site measurements. Urban vegetation emissions in Las Vegas were left unadjusted given that WRF-Chem was already in reasonable agreement with observations at Jerome Mack.

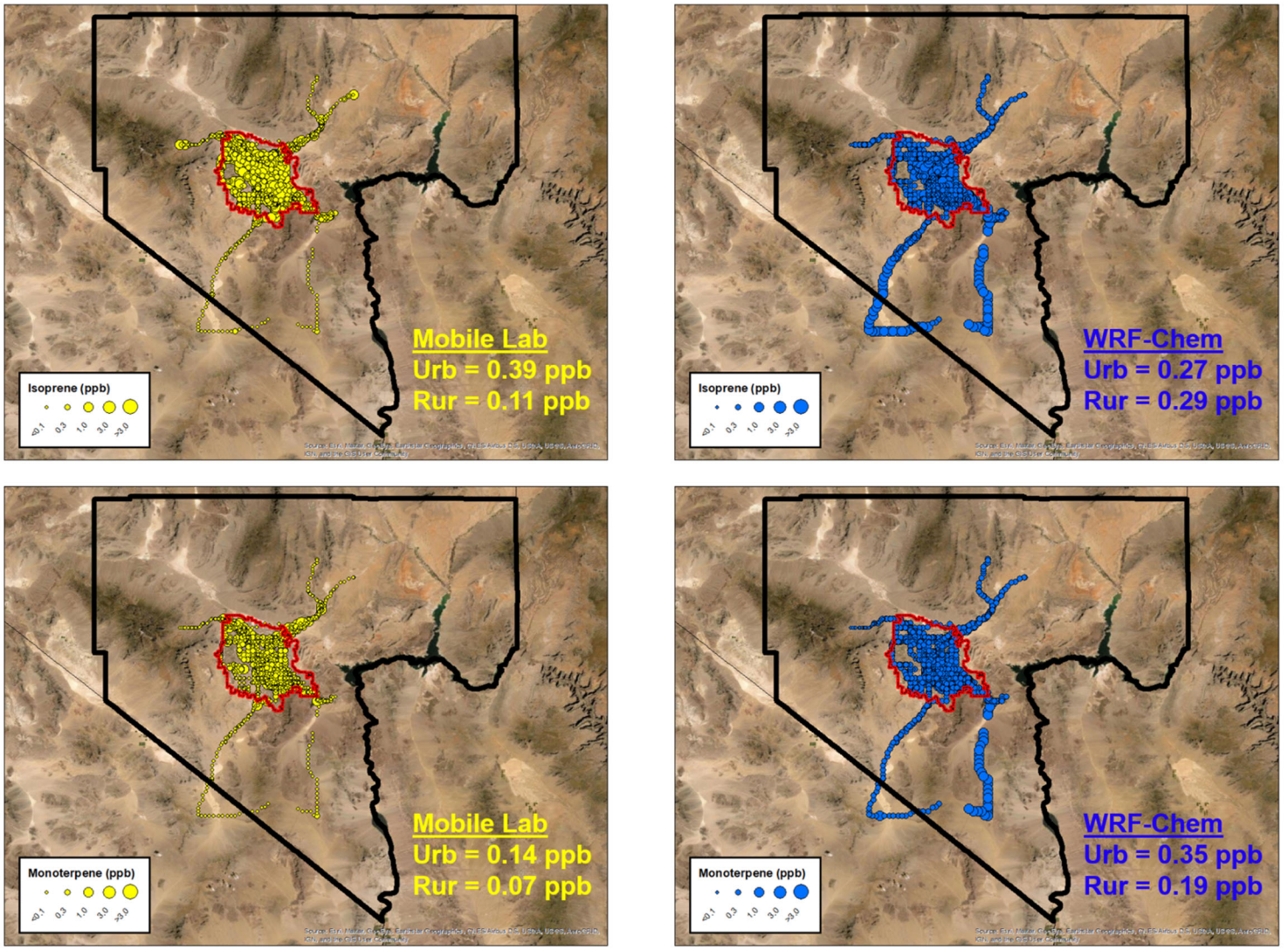

Figure 11-19. Evaluation of WRF-Chem (blue markers) versus NOAA mobile lab observations (yellow markers) in the vicinity of Las Vegas. Markers are sized according to their concentrations.

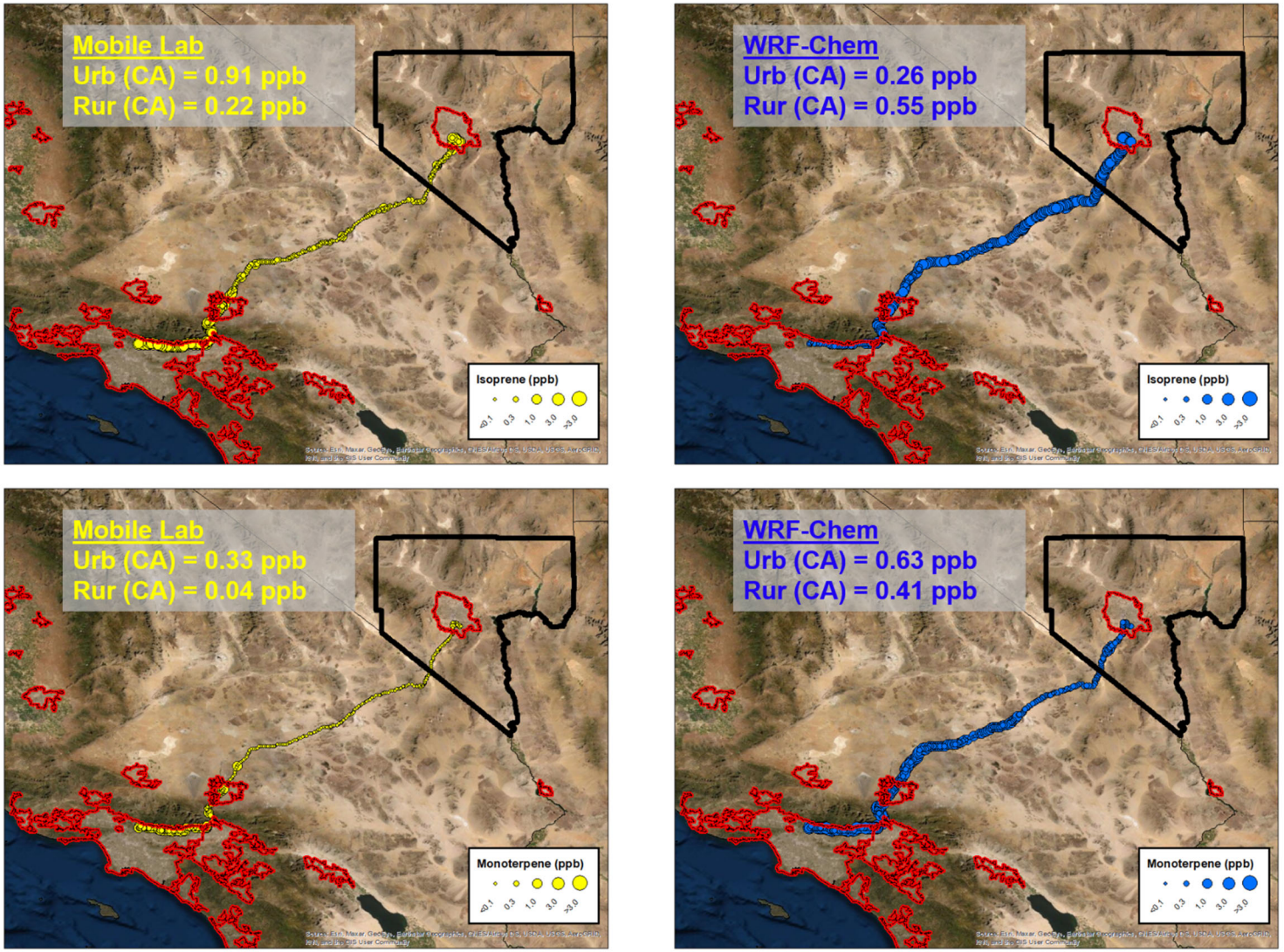

Figure 11-20. Evaluation of WRF-Chem (blue markers) versus NOAA mobile lab observations (yellow markers) on the Las Vegas-Los Angeles transit drives. Markers are sized according to their concentrations.

11.7 WRF-Chem Ozone Sensitivity Simulations

NO_x and VOC Sensitivity

Ozone sensitivity simulations are performed to assess the driving factors for high ozone in Las Vegas. Due to computational limitations, the sensitivity simulations are performed for a one-week period (7/5 – 7/12). This period was chosen to capture the growth of temperature associated with a heatwave over the Western US (Figure 11-11). Temperatures reached almost 320 K (or 117 ºF) over Clark County at the peak. The temperatures were so high that there is a gap in the NOAA CSL instrument data due to failure of the Jerome Mack air conditioning system. In this way, the WRF-Chem modeling complements the box modeling presented in Section 9 by filling in gaps. It is expected that such heat events will increase in the future due to a changing climate and affect ozone and its precursor emissions [*Meehl et al.*, 2018]. Thus, it is important to simulate NO_x and VOC sensitivity under such a heatwave episode, and provide insights on how emission control strategies might affect MDA8 ozone under future climate conditions.

Results presented in Figures 11-21 and 11-22 are focused on the two days with the highest ozone observed over Clark County (7/9 and 7/10), which also coincides with peak ozone across the broader California-Nevada domain (Figure 11-15). Though the baseline simulation of WRF-Chem performs well across the month of July for MDA8 ozone (median bias = +2.9 ppb, R^2 = 0.62), the upward bias in WRF-Chem doubles to ~5 ppb on these two days over Clark County. This could be due to WRF-Chem simulating more stagnant windspeeds than observed by the Doppler Lidar (Figure 11-10). Regionally, WRF-Chem performs better across the California-Nevada domain for these two days than across the whole month (median bias = +2.8 ppb, R^2 = 0.63) with a slight positive bias of ~2 ppb MDA8 ozone. Given the upward biases, the max values reported from WRF-Chem in Figures 11-21 and 11-22 are less instructive than the differences in MDAO3 relative to the baseline simulation (shown in parentheses). Model sensitivities are calculated using the maximum grid cell value within the Clark County boundary. The same is performed for the South Coast air basin to compare and contrast with Clark County.

Figure 11-21 shows model sensitivity simulations illustrating the role VOC emissions play on MDA8 ozone. Over Clark County, anthropogenic VOC emissions contribute +2.1 ppb to MDA8 ozone on these two heatwave days. Fossil fuel VOC emissions account for around half of the total and VCPs plus cooking the other half. The model is relatively insensitive to the top-down biogenic VOC emissions adjustment (Table 11-3), despite factor of ~3 reductions in Clark County. Unlike the box model (Figure 9-7), WRF-Chem exhibits relatively low sensitivity to anthropogenic VOC emissions on high heat days (July 9-10).

More work is needed to reconcile the differences between the 3D and box model. It is possible that high heat days may undergo different patterns of regional transport of ozone and oxidative chemistry than average July conditions. By contrast, the Los Angeles basin exhibits much stronger sensitivity to anthropogenic VOC emissions (+24 ppb to MDA8 ozone).

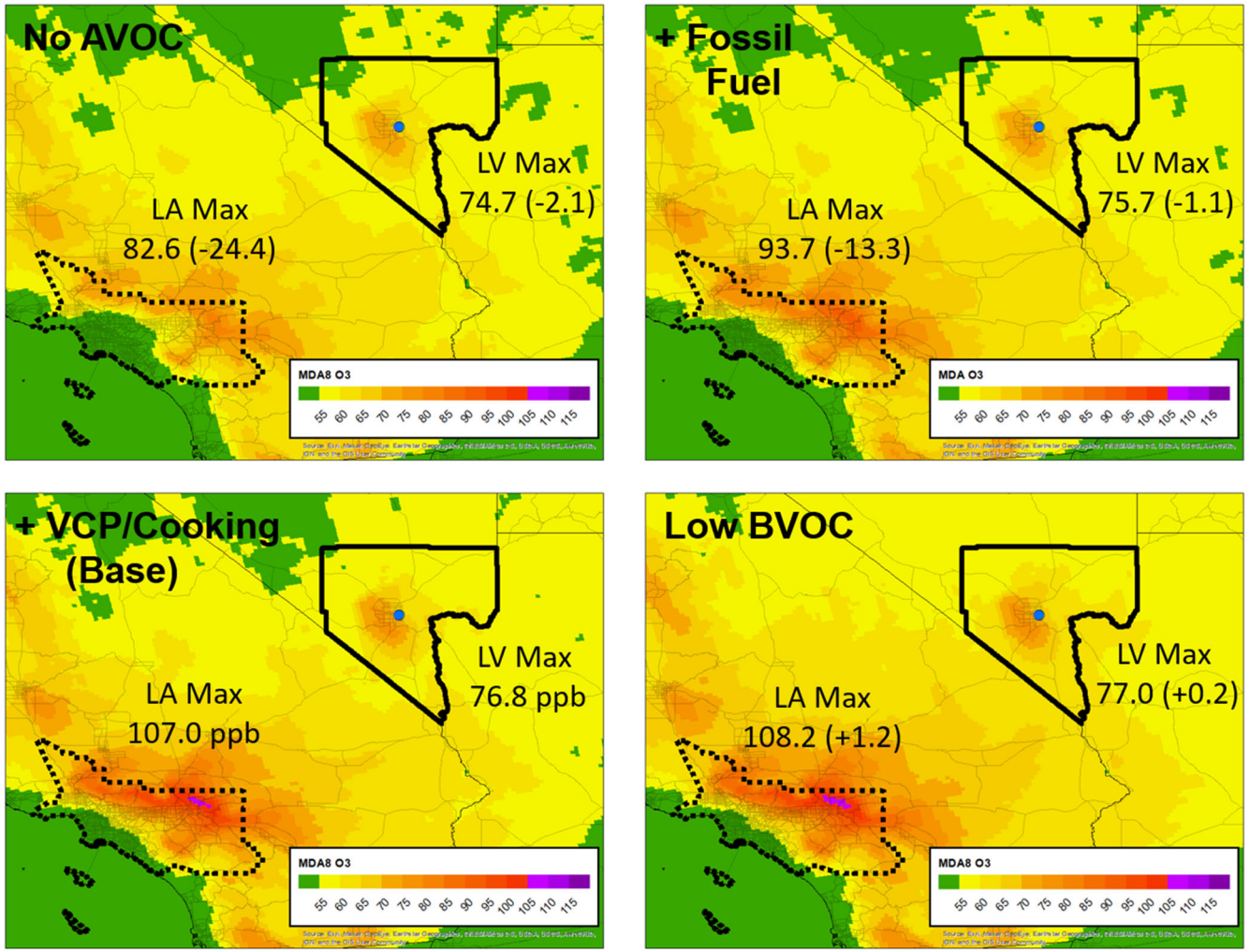

Figure 11-21. WRF-Chem model sensitivity cases of anthropogenic and biogenic VOC emissions on MDA8 ozone. Maps show the average of MDA8 ozone for July 9 and 10, 2021. Max values are shown for Clark County and South Coast air basin. Differences are calculated relative to the base case simulation shown.

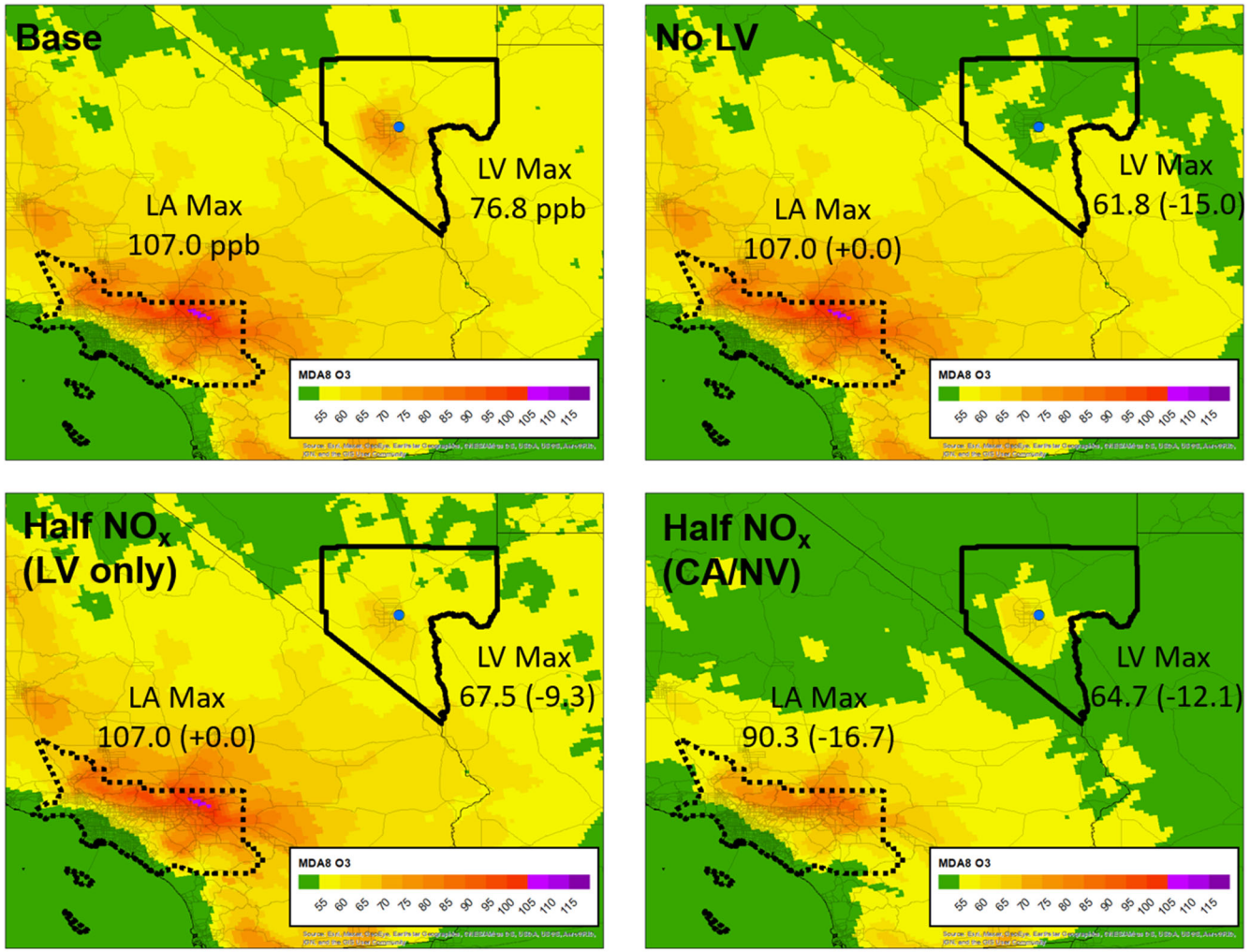

Figure 11-22. WRF-Chem model sensitivity cases of local Las Vegas and NO_x emissions on MDA8 ozone. Maps show the average of MDA8 ozone for July 9 and 10, 2021. Max values are shown for Clark County and South Coast air basin. Differences are calculated relative to the base case simulation shown.

Figure 11-22 shows model sensitivity simulations illustrating the role of local vs. non-local and NO_x emissions on Clark County ozone. The top right panel shows a sensitivity simulation where Clark County emissions are zeroed out for both NO_x and VOCs. The results suggest local emissions contribute +15 ppb to MDA8 ozone. Though the NOAA TOPAZ (Tunable Optical Profiler for Aerosol and oZone) differential absorption lidar was not deployed during SUNVEx 2021, the high incoming regional/background concentration is consistent with findings from FAST-LVOS [*Langford et al.*, 2022] and LVOS [*Langford et al.*, 2015], identifying that entrainment can contribute 50-55 ppb of MDA8 ozone. Two of the models utilized in Langford et al. [2022], RAQMS and the Rapid Refresh with Chemistry (RAP-Chem, https://rapidrefresh.noaa.gov/RAPchem/) are embedded in the WRF-Chem simulations performed here. RAQMS provides lateral boundary conditions of ozone to the contiguous US domain, which in turn provides initial and boundary conditions to the inner California-Nevada domain. Second, the physics settings of the NOAA CSL WRF-Chem setup mimics the RAP-Chem model (Table 11-1). To the extent transport and entrainment contribute to Las Vegas ozone, they should be represented in the current WRF-Chem setup.

The bottom row of Figure 11-22 shows NO_x sensitivity simulations performed in WRF-Chem. Halving NO_x emissions in only Clark County results in a reduction of MDA8 ozone by 9.3 ppb. This is similar to the effect in the box model (Figure 9-7) where if NO_x were halved, a 10.5 ppb reduction in ozone results. An additional experiment is performed halving NO_x emissions across the California-Nevada domain. Only combustion-related emissions in the contiguous US were adjusted down. Left unadjusted were international shipping lanes, Mexico, and agricultural soils. This sensitivity simulation represents the role of regional policies that control NO_x. California is banning the sale of new gasoline-powered cars by 2035. Further NO_x reductions are expected from turnover of the heavy-duty truck fleet equipped with selective catalytic reduction systems [*Yu et al.*, 2021]. The reductions in ozone over Southern California from halving NO_x are consistent with long-term ozone modeling by Kim et al. [2022], suggesting that Los Angeles is transitioning towards a NO_x-sensitive regime. Figure 11-22 suggests that there are local strategies that can be effective at lowering MDA8 ozone, and can augment regional actions to control NO_x.

Transported Wildfire Ozone

The above model sensitivity simulations for NO_x and VOC sensitivity did not include wildfire emissions. The sensitivity of MDA8 ozone to RAVE wildfire emissions is shown in Figure 11-23. The sensitivity simulation is performed within the contiguous US (12 km x 12 km) domain to see the broad scale features of Western wildfires. For July 2021, the mean MDA8 ozone increase is 7 ppb from wildfire smoke over Clark County. However, this model sensitivity should be treated with extreme caution. First, wildfire emissions can vary by 1-2 orders of magnitude [*Bela et al.*, 2022; *Stockwell et al.*, 2022], chemical mechanisms miss explicit chemistry needed to predict secondary species [*National Academies of Sciences*, 2022], and sub-grid turbulent and plume-rise processes are not well-represented [*Wang et al.*, 2021]. WRF-Chem already slightly over-predicts MDA ozone without wildfires, and thus inclusion would make over-predictions worse. For July 2021, the biggest increases in MDA ozone are in Northwest Nevada, which is consistent with under-prediction of tropospheric NO_2 in the baseline simulation without wildfires versus TROPOMI (Figure 11-17). Despite

the large uncertainties in simulating wildfires, Figure 11-23 highlights the role of wildfires and the need for further research on their impacts on air pollution in the Western US.

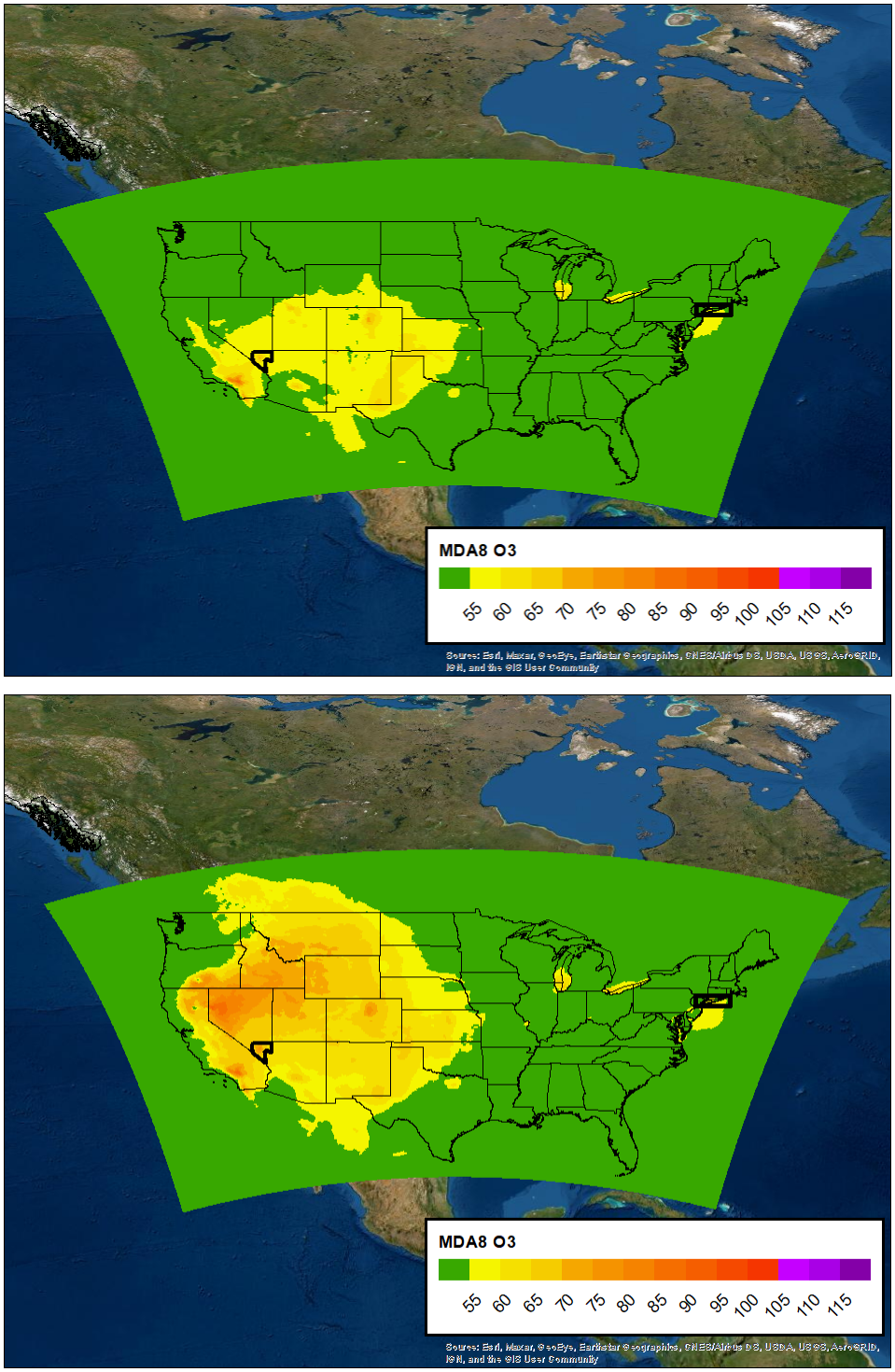

Figure 11-23. WRF-Chem model sensitivity case of RAVE wildfire emissions on MDA8 ozone. (top) WRF-Chem model without wildfires, and (bottom) with wildfire emissions. Maps show MDAO3 averaged over the month of July, 2021.

To summarize the key findings of the WRF-Chem modeling:

(1) Transported regional/background ozone remains a significant source of Las Vegas ozone during high heat events (~60 ppb MDA8 ozone);

(2) Halving NO_x emissions can be effective at reducing MDA8 ozone by ~10 ppb, and WRF-Chem results are consistent with the box model;

(3) The effectiveness of controlling anthropogenic VOC emissions is mixed, and WRF-Chem results are inconsistent with the box model. Further work is needed to better reconcile VOC sensitivity between the 3D and box model. Improving photolysis and chemistry, and biogenic VOC (urban and rural) emissions could help bring the two models into better agreement;

(4) WRF-Chem modeling suggests that wildfires in the Western US are potentially a significant source of ozone pollution in Clark County that requires further research and attention.

Conclusions:

The measurements and modeling efforts in summer 2021 showed that Las Vegas has different characteristics than most urban areas: (1) the Las Vegas Strip is an area of unusually high emissions of VCPs and cooking combined with mobile source emissions, (2) the strong dilution due to the high boundary layer during summer causes large amplitudes of the diurnal profiles with large mixing ratios at night and relatively cleaner daytime condition, and (3) in the surrounded desert mixing ratios drop of quickly outside the city.

The source apportionment showed that VCPs are the largest source of VOCs in the city followed by mobile source emissions, with cooking having a significant fraction of the emissions. Box and 3D modeling efforts show that ozone is sensitive to reductions in NOx and that regional and transported ozone is a significant source for ozone in Las Vegas.

References

Andreae, M. O. (2019), Emission of trace gases and aerosols from biomass burning - an updated assessment, *Atmos. Chem. Phys.*, *19*(13), 8523-8546, doi:10.5194/acp-19-8523-2019.

Arata, C., P. K. Misztal, Y. Tian, D. M. Lunderberg, K. Kristensen, A. Novoselac, M. E. Vance, D. K. Farmer, W. W. Nazaroff, and A. H. Goldstein (2021), Volatile organic compound emissions during HOMEChem, *Indoor Air*, *31*(6), 2099-2117, doi:https://doi.org/10.1111/ina.12906.

Arnold, S. T., A. A. Viggiano, and R. A. Morris (1998), Rate Constants and Product Branching Fractions for the Reactions of H3O+ and NO+ with C2−C12 Alkanes, *The Journal of Physical Chemistry A*, *102*(45), 8881-8887, doi:10.1021/jp9815457.

Bela, M. M., et al. (2022), Quantifying Carbon Monoxide Emissions on the Scale of Large Wildfires, *Geophys Res Lett*, *49*(3), doi:ARTN e2021GL095831 10.1029/2021GL095831.

Benjamin, M. T., M. Sudol, L. Bloch, and A. M. Winer (1996), Low-emitting urban forests: A taxonomic methodology for assigning isoprene and monoterpene emission rates, *Atmos Environ*, *30*(9), 1437-1452, doi:Doi 10.1016/1352-2310(95)00439-4.

Bishop, G. A., and M. J. Haugen (2018), The Story of Ever Diminishing Vehicle Tailpipe Emissions as Observed in the Chicago, Illinois Area, *Environ. Sci. Technol.*, *52*(13), 7587-7593, doi:10.1021/acs.est.8b00926.

Borbon, A., et al. (2013), Emission ratios of anthropogenic volatile organic compounds in northern mid-latitude megacities: Observations versus emission inventories in Los Angeles and Paris, *J. Geophys. Res.-Atmos.*, *118*(4), 2041-2057, doi:10.1002/jgrd.50059.

Breitenlechner, M., L. Fischer, M. Hainer, M. Heinritzi, J. Curtius, and A. Hansel (2017), PTR3: An Instrument for Studying the Lifecycle of Reactive Organic Carbon in the Atmosphere, *Analytical Chemistry*, *89*(11), 5824-5831, doi:10.1021/acs.analchem.6b05110.

Buhr, K., S. van Ruth, and C. Delahunty (2002), Analysis of volatile flavour compounds by Proton Transfer Reaction-Mass Spectrometry: fragmentation patterns and discrimination between isobaric and isomeric compounds, *International Journal of Mass Spectrometry*, *221*(1), 1-7, doi:https://doi.org/10.1016/S1387-3806(02)00896-5.

Calfapietra, C., S. Fares, F. Manes, A. Morani, G. Sgrigna, and F. Loreto (2013), Role of Biogenic Volatile Organic Compounds (BVOC) emitted by urban trees on ozone concentration in cities: A review, *Environmental Pollution*, *183*, 71-80, doi:https://doi.org/10.1016/j.envpol.2013.03.012.

Canonaco, F., M. Crippa, J. G. Slowik, U. Baltensperger, and A. S. H. Prévôt (2013), SoFi, an IGOR-based interface for the efficient use of the generalized multilinear engine (ME-2) for the source apportionment: ME-2 application to aerosol mass spectrometer data, *Atmos. Meas. Tech.*, *6*(12), 3649-3661, doi:10.5194/amt-6-3649-2013.

Cao, H. S., D. K. Henze, K. Cady-Pereira, B. C. McDonald, C. Harkins, K. Sun, K. W. Bowman, T. M. Fu, and M. O. Nawaz (2022), COVID-19 Lockdowns Afford the First Satellite-Based Confirmation That Vehicles Are an Under-recognized Source of Urban NH3 Pollution in Los Angeles, *Environ Sci Tech Let*, *9*(1), 3-9, doi:10.1021/acs.estlett.1c00730.

Coggon, M. M., et al. (2021), Volatile chemical product emissions enhance ozone and modulate urban chemistry, *Proceedings of the National Academy of Sciences of the United States of America*, *118*(32), doi:10.1073/pnas.2026653118.

Coggon, M. M., et al. (2018), Diurnal Variability and Emission Pattern of Decamethylcyclopentasiloxane (D-5) from the Application of Personal Care Products in Two North American Cities, *Environ. Sci. Technol.*, *52*(10), 5610-5618, doi:10.1021/acs.est.8b00506.
Coggon, M. M., et al. (2016), Emissions of nitrogen-containing organic compounds from the burning of herbaceous and arboraceous biomass: Fuel composition dependence and the variability of commonly used nitrile tracers, *Geophys. Res. Lett.*, *43*(18), 9903-9912, doi:10.1002/2016gl070562.
de Gouw, J. A., et al. (2018), Chemistry of Volatile Organic Compounds in the Los Angeles Basin: Formation of Oxygenated Compounds and Determination of Emission Ratios, *J. Geophys. Res.-Atmos.*, *123*(4), 2298-2319, doi:10.1002/2017jd027976.
de Gouw, J. A., C. Warneke, D. D. Parrish, J. S. Holloway, M. Trainer, and F. C. Fehsenfeld (2003), Emission sources and ocean uptake of acetonitrile (CH3CN) in the atmosphere, *J. Geophys. Res.*, *108*(D11), doi:doi:10.1029/2002JD002897.
Doumbia, T., et al. (2021), Changes in global air pollutant emissions during the COVID-19 pandemic: a dataset for atmospheric modeling, *Earth Syst Sci Data*, *13*(8), 4191-4206, doi:10.5194/essd-13-4191-2021.
EPA (2010), NONROAD2008a Model*Rep.*, Office of Transportation and Air Quality, U.S. Environmental Protection Agency.
Gkatzelis, G. I., M. M. Coggon, B. C. McDonald, J. Peischl, K. C. Aikin, J. B. Gilman, M. Trainer, and C. Warneke (2021a), Identifying Volatile Chemical Product Tracer Compounds in US Cities, *Environ. Sci. Technol.*, *55*(1), 188-199, doi:10.1021/acs.est.0c05467.
Gkatzelis, G. I., et al. (2021b), Observations Confirm that Volatile Chemical Products Are a Major Source of Petrochemical Emissions in US Cities, *Environ. Sci. Technol.*, *55*(8), 4332-4343, doi:10.1021/acs.est.0c05471.
Grell, G. A., S. E. Peckham, R. Schmitz, S. A. McKeen, G. Frost, W. C. Skamarock, and B. Eder (2005), Fully coupled "online" chemistry within the WRF model, *Atmos. Environ.*, *39*(37), 6957-6975.
Gueneron, M., M. H. Erickson, G. S. VanderSchelden, and B. T. Jobson (2015), PTR-MS fragmentation patterns of gasoline hydrocarbons, *International Journal of Mass Spectrometry*, *379*, 97-109, doi:https://doi.org/10.1016/j.ijms.2015.01.001.
Guenther, A. B., X. Jiang, C. L. Heald, T. Sakulyanontvittaya, T. Duhl, L. K. Emmons, and X. Wang (2012), The Model of Emissions of Gases and Aerosols from Nature version 2.1 (MEGAN2.1): an extended and updated framework for modeling biogenic emissions, *Geosci. Model Dev.*, *5*(6), 1471-1492, doi:10.5194/gmd-5-1471-2012.
Harkins, C., B. C. McDonald, D. K. Henze, and C. Wiedinmyer (2021), A fuel-based method for updating mobile source emissions during the COVID-19 pandemic, *Environ Res Lett*, *16*, doi:10.1088/1748-9326/ac0660.
Harley, R. A., S. C. Coulter-Burke, and T. S. Yeung (2000), Relating liquid fuel and headspace vapor composition for California reformulated gasoline samples containing ethanol, *Environ Sci Technol*, *34*(19), 4088-4094.
Harley, R. A., L. C. Marr, J. K. Lehner, and S. N. Giddings (2005), Changes in motor vehicle emissions on diurnal to decadal time scales and effects on atmospheric composition, *Environ. Sci. Technol.*, *39*(14), 5356-5362.

Hassler, B., et al. (2016), Analysis of long-term observations of NOx and CO in megacities and application to constraining emissions inventories, *Geophys Res Lett*, *43*(18), 9920-9930, doi:10.1002/2016gl069894.
Hayes, P. L., et al. (2015), Modeling the formation and aging of secondary organic aerosols in Los Angeles during CalNex 2010, *Atmos. Chem. Phys.*, *15*(10), 5773-5801, doi:10.5194/acp-15-5773-2015.
Hayes, P. L., et al. (2013), Organic aerosol composition and sources in Pasadena, California, during the 2010 CalNex campaign, *Journal of Geophysical Research: Atmospheres*, *118*(16), 9233-9257, doi:10.1002/jgrd.50530.
Hurley, J. F., E. Smiley, and G. Isaacman-VanWertz (2021), Modeled Emission of Hydroxyl and Ozone Reactivity from Evaporation of Fragrance Mixtures, *Environmental Science & Technology*, *55*(23), 15672-15679, doi:10.1021/acs.est.1c04004.
Jobson, B. T., M. L. Alexander, G. D. Maupin, and G. G. Muntean (2005), On-line analysis of organic compounds in diesel exhaust using a proton transfer reaction mass spectrometer (PTR-MS), *International Journal of Mass Spectrometry*, *245*(1), 78-89, doi:https://doi.org/10.1016/j.ijms.2005.05.009.
Karl, T., M. Striednig, M. Graus, A. Hammerle, and G. Wohlfahrt (2018), Urban flux measurements reveal a large pool of oxygenated volatile organic compound emissions, *Proc. Natl. Acad. Sci. U.S.A.*, *115*(6), 1186-1191, doi:10.1073/pnas.1714715115.
Kean, A. J., R. F. Sawyer, and R. A. Harley (2000), A fuel-based assessment of off-road diesel engine emissions, *J Air Waste Manage*, *50*(11), 1929-1939, doi:10.1080/10473289.2000.10464233.
Kim, S.-W., B. C. McDonald, S. Seo, K.-M. Kim, and M. Trainer (2022), Understanding the Paths of Surface Ozone Abatement in the Los Angeles Basin, *Journal of Geophysical Research: Atmospheres*, *127*(4), e2021JD035606, doi:https://doi.org/10.1029/2021JD035606.
Kim, S. W., et al. (2016), Modeling the weekly cycle of NOx and CO emissions and their impacts on O3 in the Los Angeles South Coast Air Basin during the CalNex 2010 field campaign, *J Geophys Res-Atmos*, *121*(3), 1340-1360, doi:10.1002/2015jd024292.
Klein, F., et al. (2016), Characterization of Gas-Phase Organics Using Proton Transfer Reaction Time-of-Flight Mass Spectrometry: Cooking Emissions, *Environ. Sci. Technol.*, *50*(3), 1243-1250, doi:10.1021/acs.est.5b04618.
Koss, A., et al. (2017), Observations of VOC emissions and photochemical products over US oil- and gas-producing regions using high-resolution H3O+ CIMS (PTR-ToF-MS), *Atmos. Meas. Tech.*, *10*(8), 2941-2968, doi:10.5194/amt-10-2941-2017.
Koss, A. R., et al. (2018), Non-methane organic gas emissions from biomass burning: identification, quantification, and emission factors from PTR-ToF during the FIREX 2016 laboratory experiment, *Atmos. Chem. Phys.*, *18*(5), 3299-3319, doi:10.5194/acp-18-3299-2018.
Krechmer, J., et al. (2018), Evaluation of a New Reagent-Ion Source and Focusing Ion–Molecule Reactor for Use in Proton-Transfer-Reaction Mass Spectrometry, *Analytical Chemistry*, *90*(20), 12011-12018, doi:10.1021/acs.analchem.8b02641.
Langford, A. O., et al. (2022), The Fires, Asian, and Stratospheric Transport-Las Vegas Ozone Study (FAST-LVOS), *Atmos Chem Phys*, *22*(3), 1707-1737, doi:10.5194/acp-22-1707-2022.

Langford, A. O., et al. (2015), An overview of the 2013 Las Vegas Ozone Study (LVOS): Impact of stratospheric intrusions and long-range transport on surface air quality, *Atmos Environ*, *109*, 305-322, doi:10.1016/j.atmosenv.2014.08.040.
Li, F. J., X. Y. Zhang, S. Kondragunta, X. M. Lu, I. Csiszar, and C. C. Schmidt (2022), Hourly biomass burning emissions product from blended geostationary and polar-orbiting satellites for air quality forecasting applications, *Remote Sens Environ*, *281*, doi:ARTN 113237
10.1016/j.rse.2022.113237.
Li, M., et al. (2021), Assessment of Updated Fuel-Based Emissions Inventories Over the Contiguous United States Using TROPOMI NO2 Retrievals, *J Geophys Res-Atmos*, *126*(24), doi:ARTN e2021JD035484
10.1029/2021JD035484.
McDonald, B. C., T. R. Dallmann, E. W. Martin, and R. A. Harley (2012), Long-term trends in nitrogen oxide emissions from motor vehicles at national, state, and air basin scales, *J Geophys Res-Atmos*, *117*, D00V18, doi:10.1029/2012jd018304.
McDonald, B. C., et al. (2018a), Volatile chemical products emerging as largest petrochemical source of urban organic emissions, *Science*, *359*(6377), 760-764, doi:10.1126/science.aaq0524.
McDonald, B. C., D. R. Gentner, A. H. Goldstein, and R. A. Harley (2013), Long-term trends in motor vehicle emissions in u.s. urban areas, *Environ. Sci. Technol.*, *47*(17), 10022-10031, doi:10.1021/es401034z.
McDonald, B. C., A. H. Goldstein, and R. A. Harley (2015), Long-term trends in California mobile source emissions and ambient concentrations of black carbon and organic aerosol, *Environ Sci Technol*, *49*(8), 5178-5188, doi:10.1021/es505912b.
McDonald, B. C., Z. C. McBride, E. W. Martin, and R. A. Harley (2014), High-resolution mapping of motor vehicle carbon dioxide emissions, *J Geophys Res-Atmos*, *119*(9), 5283-5298, doi:10.1002/2013jd021219.
McDonald, B. C., et al. (2018b), Modeling ozone in the Eastern U.S. using a fuel-based mobile source emissions inventory, *Environ Sci Technol*, *52*, 7360-7370, doi:10.1021/acs.est.8b00778.
Meehl, G. A., C. Tebaldi, S. Tilmes, J. F. Lamarque, S. Bates, A. Pendergrass, and D. Lombardozzi (2018), Future heat waves and surface ozone, *Environ Res Lett*, *13*(6), doi:Artn 064004
10.1088/1748-9326/Aabcdc.
National Academies of Sciences, E., and Medicine (2022), The Chemistry of Fires at the Wildland-Urban Interface*Rep.*, Washington, DC.
Paatero, P. (1999), The Multilinear Engine—A Table-Driven, Least Squares Program for Solving Multilinear Problems, Including the n-Way Parallel Factor Analysis Model, *Journal of Computational and Graphical Statistics*, *8*(4), 854-888, doi:10.1080/10618600.1999.10474853.
Pagonis, D., K. Sekimoto, and J. de Gouw (2019), A Library of Proton-Transfer Reactions of H3O+ Ions Used for Trace Gas Detection, *Journal of the American Society for Mass Spectrometry*, *30*(7), 1330-1335, doi:10.1021/jasms.8b06050.
Peischl, J., T. Ryerson, J. Holloway, D. Parrish, M. Trainer, G. Frost, K. Aikin, S. Brown, W. Dubé, and H. Stark (2010), A top-down analysis of emissions from selected Texas

power plants during TexAQS 2000 and 2006, *Journal of Geophysical Research: Atmospheres*, *115*(D16).
Peischl, J., et al. (2013), Quantifying sources of methane using light alkanes in the Los Angeles basin, California, *J. Geophys. Res.-Atmos.*, *118*(10), 4974-4990, doi:10.1002/jgrd.50413.
Pierce, T. C., C. Geron, G. Pouliot, E. Kinnee, and J. Vukovish (2002), Integration of the Biogenic Emissions Inventory System (BEIS3) into the Community Multiscale Air Quality (CMAQ) modeling system, paper presented at AMS 4th Urban Environment Symposium, Norfolk, VA.
Pouliot, G., and T. Pierce (2009), Integration of the Model of Emissions of Gases and Aerosols from Nature (MEGAN) into the CMAQ Modeling System*Rep.*, U.S. Environmental Protection Agency, Research Triangle Park, NC.
Schauer, J. J., M. J. Kleeman, G. R. Cass, and B. R. T. Simoneit (1999a), Measurement of Emissions from Air Pollution Sources. 1. C1 through C29 Organic Compounds from Meat Charbroiling, *Environmental Science & Technology*, *33*(10), 1566-1577, doi:10.1021/es980076j.
Schauer, J. J., M. J. Kleeman, G. R. Cass, and B. R. T. Simoneit (1999b), Measurement of emissions from air pollution sources. 1. C-1 through C-29 organic compounds from meat charbroiling, *Environ. Sci. Technol.*, *33*(10), 1566-1577, doi:10.1021/es980076j.
Sekimoto, K., S.-M. Li, B. Yuan, A. Koss, M. Coggon, C. Warneke, and J. de Gouw (2017), Calculation of the sensitivity of proton-transfer-reaction mass spectrometry (PTR-MS) for organic trace gases using molecular properties, *International Journal of Mass Spectrometry*, *421*, 71-94, doi:10.1016/j.ijms.2017.04.006.
Stockwell, C. E., et al. (2022), Airborne Emission Rate Measurements Validate Remote Sensing Observations and Emission Inventories of Western US Wildfires, *Environ. Sci. Technol.*, *56*(12), 7564-7577, doi:10.1021/acs.est.1c07121.
Stockwell, C. E., M. M. Coggon, G. I. Gkatzelis, J. Ortega, B. C. McDonald, J. Peischl, K. Aikin, J. B. Gilman, M. Trainer, and C. Warneke (2021), Volatile organic compound emissions from solvent- and water-borne coatings – compositional differences and tracer compound identifications, *Atmos. Chem. Phys.*, *21*(8), 6005-6022, doi:10.5194/acp-21-6005-2021.
Wang, S. Y., et al. (2021), Chemical Tomography in a Fresh Wildland Fire Plume: A Large Eddy Simulation (LES) Study, *J. Geophys. Res.-Atmos.*, *126*(18), doi:10.1029/2021jd035203.
Warneke, C., et al. (2010), Biogenic emission measurement and inventories determination of biogenic emissions in the eastern United States and Texas and comparison with biogenic emission inventories, *J. Geophys. Res.-Atmos.*, *115*, doi:D00f18 10.1029/2009jd012445.
Warneke, C., et al. (2013), Photochemical aging of volatile organic compounds in the Los Angeles basin: Weekday-weekend effect, *J. Geophys. Res.-Atmos.*, *118*(10), 5018-5028, doi:10.1002/jgrd.50423.
Warneke, C., et al. (2004), Comparison of daytime and nighttime oxidation of biogenic and anthropogenic VOCs along the New England coast in summer during New England Air Quality Study 2002, *J. Geophys. Res.-Atmos.*, *109*(D10), doi:doi:10.1029/2003JD004424.
Warneke, C., J. A. de Gouw, J. S. Holloway, J. Peischl, T. B. Ryerson, E. Atlas, D. Blake, M. Trainer, and D. D. Parrish (2012), Multiyear trends in volatile organic compounds in Los

Angeles, California: Five decades of decreasing emissions, *J. Geophs. Res.*, *117*(D21), 1-10, doi:10.1029/2012jd017899.
Warneke, C., J. A. de Gouw, W. C. Kuster, P. D. Goldan, and R. Fall (2003), Validation of Atmospheric VOC Measurements by Proton-Transfer- Reaction Mass Spectrometry Using a Gas-Chromatographic Preseparation Method, *Environmental Science & Technology*, *37*(11), 2494-2501, doi:10.1021/es026266i.
Warneke, C., et al. (2014), Volatile organic compound emissions from the oil and natural gas industry in the Uintah Basin, Utah: oil and gas well pad emissions compared to ambient air composition, *Atmos. Chem. Phys.*, *14*(20), 10977-10988, doi:10.5194/acp-14-10977-2014.
Warneke, C., et al. (2007), Determination of urban volatile organic compound emission ratios and comparison with an emissions database, *J. Geophys. Res.-Atmos.*, *112*(D10), D10S47, doi:10.1029/2006JD007930.
Wennberg, P. O., et al. (2012), On the Sources of Methane to the Los Angeles Atmosphere, *Environ. Sci. Technol.*, *46*(17), 9282-9289, doi:10.1021/es301138y.
Wild, R. J., W. P. Dubé, K. C. Aikin, S. J. Eilerman, J. A. Neuman, J. Peischl, T. B. Ryerson, and S. S. Brown (2017), On-road measurements of vehicle NO2/NOx emission ratios in Denver, Colorado, USA, *Atmos. Environ.*, *148*, 182-189, doi:https://doi.org/10.1016/j.atmosenv.2016.10.039.
Yu, K. A., B. C. McDonald, and R. A. Harley (2021), Evaluation of Nitrogen Oxide Emission Inventories and Trends for On-Road Gasoline and Diesel Vehicles, *Environ Sci Technol*, doi:10.1021/acs.est.1c00586.
Yuan, B., A. Koss, C. Warneke, J. B. Gilman, B. M. Lerner, H. Stark, and J. A. de Gouw (2016), A high-resolution time-of-flight chemical ionization mass spectrometer utilizing hydronium ions (H3O+ ToF-CIMS) for measurements of volatile organic compounds in the atmosphere, *Atmos. Meas. Tech.*, *9*(6), 2735-2752, doi:10.5194/amt-9-2735-2016.
Yuan, B., A. R. Koss, C. Warneke, M. Coggon, K. Sekimoto, and J. A. de Gouw (2017), Proton-Transfer-Reaction Mass Spectrometry: Applications in Atmospheric Sciences, *Chem. Rev.*, *117*(21), 13187-13229, doi:10.1021/acs.chemrev.7b00325.
Zhang, Y., et al. (2019), Six-year source apportionment of submicron organic aerosols from near-continuous highly time-resolved measurements at SIRTA (Paris area, France), *Atmos. Chem. Phys.*, *19*(23), 14755-14776, doi:10.5194/acp-19-14755-2019.

Appendix

Table A1. Summary of COVID-19 Pandemic Scaling Factor Data.

Sector	Base Inventory	SCC Codes	COVID Scaling	Spatial Adjustment
On-Road				
Gasoline	FIVE18	2200000000-2209999999	EIA Gas[a]	State
Diesel	FIVE18	2230000000-2239999999	EIA Dsl[b]	PADD
Non-Road				
Agriculture Diesel	FIVE18	2270005000-2270005999	EIA Dsl[b]	PADD
Non-ag Diesel	FIVE18	2270000000-2270004999 2270006000-2270099999	EIA Dsl[b]	PADD
Gasoline (marine)	FIVE18	2282005000-2282005025 2282010000-2282010025	EIA Gas[a]	PADD
Gasoline (2-str)	FIVE18	2260000000-2260010010	EIA Gas[a]	PADD
Gasoline (4-str)	FIVE18	2265000000-2265010010	EIA Gas[a]	PADD
Locomotives	NEI17	2285000000-2285008015	BTS[c]	US
Point				
Electricity Gen.	NEI17	10100101-10102101 20100101-20190099	CEMS[d]	Facility
Industrial Boilers				
Coal	NEI17	10200101-10200307	EIA Coal[e]	US
Oil	NEI17	10200401-10200506 20200101-20200109 20200401-20200506 20200901-20200909 20400101-20400499	EIA Oil[e]	US
Natural Gas	NEI17	10200601-10200604 20200201-20200256 20200702-20200714	EIA NG[e]	US
Commercial Boilers				
Oil	NEI17	10300401-10300505 20300101-20300109	EIA Oil[f]	US
Natural Gas	NEI17	10300601-10300603 20300201-20300209	EIA NG[f]	US

Table A1. Continued.

Sector	Base Inventory	SCC Codes	COVID Scaling	Spatial Adjustment
Industrial Processes				
Chemical	NEI17	30100101-30199999 30800101-30899999 40700401-42505102 64470010-68510001	DOC Chem.[g]	US
Food & Ag.	NEI17	30200101-30299999 62540023-62540024	DOC Farm[g]	US
Metals & Mining	NEI17	30300001-30599999 30900198-30999999	DOC Metals[g]	US
Refinery & Bulk Terminals	NEI17	30600102-30699999 40301001-40400279 40400401-40400498	DOC Petrol.[g]	US
Pulp, Paper, & Construction	NEI17 NEI17	30700101-30799999 31100102-31100299	DOC Lumber & Const.[g]	US
Machinery & Electrical	NEI17	31299999-31399999	DOC Mach.[g]	US
Automotive	NEI17	31400901-31499999	DOC Motor[g]	US
Apparel	NEI17	32099997-33088801	DOC Apparel[g]	US
Oil & Gas Prod.	FOG18	31000101-31088811 40400300-40400340	DrillingInfo[h]	Facility
Point VCPs				
Ind. Degreasing	VCP18	40100201-40188898	DOC Chem.[g]	US
Ind. Coatings	VCP18	40200101-40200601 40200801-40299998 49000101-49099998	DOC Chem.[g]	US
Ind. Adhesives	VCP18	40200701-40200712	DOC Chem.[g]	US
Printing Inks	VCP18	40500204-40500806	DOC Chem.[g]	US
Airports	NEI17	2265008005-2275001000	BTS[i]	US

Table A1. Continued.

Sector	Base Inventory	SCC Codes	COVID Scaling	Spatial Adjustment
Area				
Industrial Boilers				
Coal	NEI17	2102001000-2102002000	EIA Coal[e]	US
Oil	NEI17	2102004000-2102005000 2102011000	EIA Oil[e]	US
Natural Gas	NEI17	2102006000-2102007000 2102010000	EIA NG[e]	US
Biomass	NEI17	2102008000	EIA Bio[e]	US
Commercial Boilers				
Coal	NEI17	2103001000-2103002000	EIA Coal[f]	US
Oil	NEI17	2103004000-2103005000 2103011000	EIA Oil[f]	US
Natural Gas	NEI17	2103006000-2103007000	EIA NG[f]	US
Biomass	NEI17	2103008000	EIA Bio[f]	US
Residential Boilers				
Coal	NEI17	2104001000-2104002000	EIA Coal[j]	US
Oil	NEI17	2104004000 2104011000	EIA Oil[j]	US
Natural Gas	NEI17	2104006000-2104007000	EIA NG[j]	US
Biomass	NEI17	2104008100-2104009000	EIA Bio[j]	US
Aviation	NEI17	2275087000	BTS[i]	US
Comm. Marine Dsl	NEI17	2280002101-2280002204	DOC[k]	US
Comm. Marine Res.	NEI17	2280003103-2280003204	DOC[k]	US
Rail Equipment	NEI17	2285002006-2285002010	DOC[k]	US

Table A1. Continued.

Sector	Base Inventory	SCC Codes	COVID Scaling	Spatial Adjustment
Industrial Processes				
Chemical	NEI17	2301000000-2301030000 2308000000	DOC Chem.[g]	US
Food & Ag	NEI17	2302000000-2302080002	DOC Grocery[g]	US
Metals & Mining	NEI17	2304000000-2305000000 2309000000 2325000000-2325060000	DOC Metals[g]	US
Refineries	NEI17	2306010000-2306010100	DOC Petrol.[g]	US
Pulp, Paper, & Construction	NEI17	2307000000 2311010000-2311030000	DOC Lumber & Const.[g]	US
Machinery	NEI17	2312000000	DOC Mach.[g]	US
Misc. Industry	NEI17	2399000000-2399010000	--	US
Oil & Gas (onshore)	FOG18	2310000220-2310001000 2310010100-2310011600 2310020000-2310021803 2310023000-2310111701 2310121100-2310121700 2310300220-2310421603	DrillingInfo[h]	US
Oil & Gas (offshore)	NEI17	2310002000-2310002421 2310012000-2310012526 2310022000-2310022506 2310112401 2310122100	DOC Petrol.[g]	US
Storage & Trans.	NEI17	2505010000-2525000000	DOC Petrol.[g]	US
Agriculture	NEI17	2801000000-2801000008 2801520000-2801700099	--	US
Crop	NEI17	2801500000-2801500600	--	US
Burning	NEI17	2805001000-2807030000	--	US
Livestock				

Table A1. Continued.

Sector	Base Inventory	SCC Codes	COVID Scaling	Spatial Adjustment
Area VCPs				
Arch. Coatings	VCP18	2401001000 2460400000-2460500000	DOC Retail[l]	US
Ind. Coatings	VCP18	2401005000-2401200000	DOC Retail[l]	US
Ind. Degreasing	VCP18	2415000000	DOC Retail[l]	US
Printing Inks	VCP18	2425000000-2425040000	DOC Retail[l]	US
Ind. Adhesives	VCP18	2440020000	DOC Retail[l]	US
Personal Care	VCP18	2460100000	DOC Retail[l]	US
Cleaning	VCP18	2420000000-2420000999 2460200000	DOC Retail[l]	US
Cons. Adhesives	VCP18	2460600000	DOC Retail[l]	US
Cons. Pesticides	VCP18	2460800000	DOC Retail[l]	US
Ag. Pesticides	VCP18	2461800001-2461850000	DOC Retail[l]	US
Waste	NEI17	2601000000-2680003000	--	US
Dust	NEI17	2294000000-2296000000	--	US
Miscellaneous	NEI17	2810003000-2862000000	--	US

a. Monthly gasoline sales data from the US Energy Information Administration, see Harkins et al.[2021].
b. Monthly diesel sales data from the US Energy Information Administration at, see Harkins et al.[2021].
c. Total monthly carloads and intermodal rail containers from the Bureau of Transportation Statistics: https://data.bts.gov/Research-and-Statistics/Freight-Rail-Traffic-Intermodal-Units/ejmp-u4kv, https://data.bts.gov/Research-and-Statistics/Freight-Rail-Traffic-Carloads/uyr2-7q4x
d. Continuous emissions monitoring data can be found at: https://ampd.epa.gov/ampd/
e. Monthly energy usage by the industrial sector can be found from the US Energy Information Administration in Table 2.4 at: https://www.eia.gov/totalenergy/data/monthly/index.php

f. Monthly energy usage by the commercial sector can be found from the US Energy Information Administration in Table 2.3 at: https://www.eia.gov/totalenergy/data/monthly/index.php
g. Monthly whole sale trade data can be found at Department of Commerce US Census Bureau: https://www.census.gov/wholesale/index.html
h. Well-level production and drilling data from Enverus DrillingInfo database.
i. Total monthly miles flown by US passenger and cargo airlines from Bureau of Transportation Statistics: https://www.transtats.bts.gov/TRAFFIC/
j. Monthly energy usage by the residential sector can be found from the US Energy Information Administration in Table 2.2 at: https://www.eia.gov/totalenergy/data/monthly/index.php
k. Total weight in monthly foreign trade (imports + exports) on vessels by US Port District from the US Census Bureau (Exhibit 1 and Exhibit 4): https://www.census.gov/foreign-trade/Press-Release/ft920_index.html#2020
l. Monthly retail sales from the US Census Bureau: https://www.census.gov/econ/currentdata/dbsearch?program=MRTS&startYear=1992&endYear=2020&categories=446&dataType=SM&geoLevel=US&adjusted=1&notAdjusted=1&submit=GET+DATA&releaseScheduleId=